UNIVERSITY OF CALIFORNIA
RIVERSIDE

Functionalization of Nanostructures by Surface Engineering

A Dissertation submitted in partial satisfaction
of the requirements for the degree of

Doctor of Philosophy

in

Chemistry

by

Wenjing Xu

December 2017

Dissertation Committee:
Dr. Yadong Yin, Chairperson
Dr. Ludwig Bartels
Dr. Jingsong Zhang

The Dissertation of Wenjing Xu is approved:

Committee Chairperson

University of California, Riverside

Acknowledgements

Looking back to the day that I first arrived at United States, the five-years I spent on the Ph.D study was like a glance. Time flies, but memories last forever. At the harvesting season, I would like to express my deepest love and thanks to my mentor, collaborators, colleagues, friends and family.

First, the inmost gratitude is given to my mentor Prof. Yadong Yin. My first step into scientific research was like a baby, energetic but knowing nothing. Yadong is like a father, he taught me to speak (presentation), write (publish scientific work), walk (do research) and think scientifically with all his genius heart and endless patient. He passed all his knowledge and life experience to me with no conservation. Without him, I could not achieve any of the accomplishments today.

Besides my advisor, I am also very grateful to the rest of committee: Prof. Ludwig Bartels and Prof. Jingsong Zhang, for their insightful comments and encouragement, but also for the hard questions which incented me to widen my research from various perspectives.

My sincere thanks also go to Prof. Christopher Bardeen and Prof Richard Hooley for the collaborations on the project of chemical switch. Without their precious support, it would not be possible to conduct this research.

I thank my fellow labmates in UCR Yin group for the discussions, for the sleepless nights we were working together before deadlines, and for all the fun we had in the past five years. My most special appreciations are given to Prof. Mingyang Xing, Dr. Mingsheng Wang, Dr. Aiqin Gao, Dr. Fenglei Lyu for the closest collaboration on research projects and supreme contribution to my achievements. I am also very thankful to Le He, Yiding Liu, Yaocai Bai, Ji Feng, Xiaojing Wang, Zhiwei Li, Fan Yang, Rashed Aleisa, Chaolumen Wu, Qingsong Fan for sharing the happiness and sorrow in research and life. I would also like to express my greatest thanks to the visiting members for their most beautiful heart and caring to me, even we only spent one or two years together: Lan Peng, Ke Tang, Prof. Jingbin Zeng, Prof. Qinqin Liu, Prof. Aiwei Tang, Prof. Guangsheng Wang, Prof. Guocheng Lyu, Prof. Xiong Yin, Prof. Yongxiang Wang, Mingfu Gong, Yun Liu, Shichuan Li, Qianqian Shang, Lulu Long, Chunyu Zhou, Jian Liu, Jian Zhang, Shuai Zhou, Panpan Xu, Wenwen Yin, Jinxing Chen, Xiaojun Zeng, Zhenyuan Liu, Yubo Tan, Zhouhui Xia, Fenglian Qi, Bo Li, Dong Ye, Ming Wu, Prof. Xiaoliang Zhang and all the past and present group members.

Most importantly, I would like to thank my family for standing by my side with no conditions and all those support throughout my graduate study and life: my father Shiping Xu, my mother Guiqin Lyu, my father-in-law Xinhua Chen and my mother-in-law Fengzhen Zhang. Parents give our life and nourish our growth with all their love. They are the ones who are the most proud of us whenever we gain some progress. Most

of all, I would like to express my thank and love to my husband Xi Chen for his help and supporting in research and endless love, caring, accompanying and commitment in life.

Copyright Acknowledgements

Dedication

To my parents Shiping Xu, Guiqin Lyu and my love Xi Chen

ABSTRACT OF THE DISSERTATION

Functionalization of Nanostructures by Surface Engineering

by

Wenjing Xu

Doctor of Philosophy, Graduate Program in Chemistry
University of California, Riverside, December 2017
Dr. Yadong Yin, Chairperson

All nanomaterials share a common feature of large surface-to-volume ratio, making their surfaces the dominant player in many physical and chemical processes. By means of surface engineering such as ligands bonding, defects engineering and incorporation, the intrinsic physical properties including energy band gap, surface wettability and adhesion have been regulated, which greatly impact their applications in catalysis, optical device and biomedicine. Herein, I summarized my five-years research work on the fabrication of functional nanostructures by surface engineering.

Through bonding of surface ligands, large mechanical deformations and changes to overall particle morphology during chemical transformations have been overcome. Specifically, via stabilization with strong coordinating capping ligands, we demonstrate the effectiveness of this method by transforming β-FeOOH nanorods into magnetic Fe_3O_4 nanorods, which are known to be difficult to produce directly. The surface-

protected conversion strategy is believed to represent a general self-templating method for nanocrystal synthesis, as confirmed by applying it to the chemical conversion of nanostructures of other morphologies (spheres, rods, cubes, and plates) and compositions (hydroxides, oxides, and metal organic frameworks). In addition to chemical transformation, the method was found effective to create oxygen vacancies, which provide more active sites and promote faster exchange of intermediates and electrons. The as prepared cobalt oxide nanoplates manifest oxygen evolution reaction (OER) overpotential as low as 306 mV at 10 mA/cm^2 in 1 M KOH, which is superior to the values of most reported Co-based electrocatalysts.

Surface defect engineering is further explored in the advanced oxidation processes. We discover that metal sulfides (MoS_2, WS_2, Cr_2S_3, CoS, PbS or ZnS) could serve as excellent co-catalysts to greatly increase the efficiency of H_2O_2 decomposition and significantly decrease the required dosage of H_2O_2 and Fe^{2+} in AOPs. The unsaturated S atoms on the surface of metal sulfides can capture protons in the solution to form H_2S, and expose metallic active sites with reductive property to accelerate the rate-limiting step of Fe^{3+}/Fe^{2+} conversion. This discovery is expected to drive great advances in the use of AOPs for large-scale practical applications such as environmental remediation.

The ability to engineer surface patches holds great importance for functionalization of nanostructures. We demonstrate shape switching of patchy particles via fine-tuning of the spreading coefficient upon post-treatment process. When heated above glass transition

temperature, the polymer patches would melt and reconfigure themselves according to the new established spreading coefficient, which holds potentials for many new applications in optics, catalysis and self-assembly.

Moreover, functional nanostructures of noble metal are prepared by surface dewetting. This study reports a novel confined-space thermal dewetting strategy for the fabrication of Au nanocups with tunable diameter, height, and size of cup opening. With strong scattering in near infrared, the Au nanocups exhibit superior efficiency as contrast agents for spectral-domain optical coherence tomography imaging. This confined-space thermal dewetting strategy is scalable and general, and can be potentially extended to the synthesis of novel anisotropic nanostructures of various compositions that are difficult to produce by conventional wet chemical or physical methods, thus opening up opportunities for many new applications.

At last, we develop a colloidal system with bistability based on the surface adhesion. In a dynamical colloidal dispersion, a bistable system has two stable equilibrium states with local minima of potential energy separated by a local maximum. We prepare amine-functionalized superparamagnetic particles, which can switch between assembled state and dispersion state upon external stimuli. Since the energy barrier between the two stable states is determined by electrostatic potential, which highly depends on surface charges, pH dependent bistability is achieved by managing $[H^+]$ related to protonation of amino groups.

Table of Contents

List of Figures

List of Tables

List of Scheme

Chapter 1

Overview of Surface Engineering and Application of Functional Nanomaterials

1.1 Introduction of Surface Engineering

Nanomaterials refer to a natural, incidental or manufactured material containing particles, in an unbound state or as an aggregate or as an agglomerate, where one or more external dimensions is in the size range of 1-100 nm. Nanomaterials are developed to exhibit novel characteristics (such as increased strength, chemical reactivity or conductivity) compared to their bulk counterparts. In a bulk solid, the concentration of surface atoms is very low, making its contribution to material properties negligible. However, with the decrease of size to nanoscale, the surface-to-volume ratios have been greatly increased, as a result, surface of nanomaterials started playing a dominant role in material properties, functionalities and applications, which makes surface engineering one of the most effective method to fabrication functional nanomaterials.

Strategies of surface engineering include surface ligands bonding,[1] defect engineering,[2] incorporation[3] and patching.[4] Traditionally, surface engineering has established that the surfaces of large crystals can lower their energy by moving surface atoms away from

lattice sites in the process of surface reconstruction, dangling bonds can introduction new electronic states, and foreign molecules can alter the energy and reactivity of a crystal surface.[5] The set of ligands that attached to the surface of nanoparticles forms a capping layer that screens the particle from its environment, and controls nucleation and growth kinetics during synthesis.[6] Ligands can also influence the optical and electronic properties of the nanomaterials and provide steric or electrostatic stabilization of the colloidal dispersion.[7]

Defects exist widely in materials and are well accepted to tailor the intrinsic properties of materials, even with an extremely low concentration.[8] Through defect engineering, the energy band is effectively regulated. Widely used strategies for defect engineering include pits digging, oxygen-vacancy controlling and heteroatom substitution.[9] Surface defects can enhance the orbital hybridization, change electron density near Fermi level, and bring more dangling bonds and unsaturated coordination, the magnetic and electronic properties such as band gap and conductivity have been greatly altered to enhance the performance.[10-11]

Incorporation of multiple functional materials together not only simply adding up the advantages and functions of different parts, but also revealing new and enhanced benefits due to the abundant new interfaces and bondings between the phases, which can greatly impact on optical, electronic, magnetic and stable properties of the nanomaterials.[12-14]

Patching surface with functional patches is another effective method to engineer the surface properties of nanomaterials. Surface patches can be functional materials or ligands. Through tuning the properties, the number or the area of patches, the surface charge distribution, magnetic dipolar interaction and wettability have been regulated.[15-17] With such anisotropic morphology or surface properties, patchy particles are regards as a class of unique building blocks for self-assembly. [18-19] If stimuli-responsive patches are functionalized on the surface, smart materials with responsive, reconfigurable or reversible properties can be achieved.[20-21]

In a word, surface engineering, including surface ligands binding, defect engineering, incorporation and patching, pave a new effective way to modulate the intrinsic physical properties that are vital for mitigating fundamental problems in the current stage for diverse practical applications of functional nanomaterials (as illustrated in Figure 1.1).

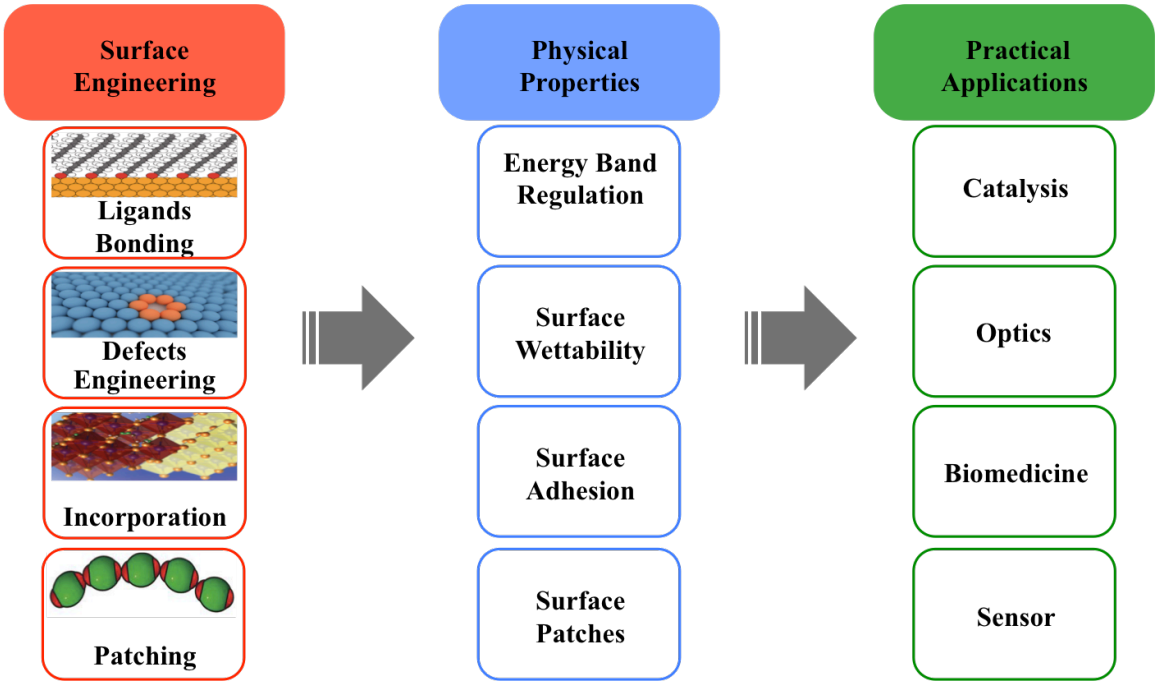

Figure 1.1. Schematic illustration of surface engineering strategies for the fabrication of functional nanomaterials with intrinsic physical properties and their applications.

Commensurate with the surface engineering strategies, hundreds if not thousands of synthetic recipes are available for crafting the size, morphology, physical and surface properties of colloidal building blocks. Large quantities with ever improving monodispersity has been achieved for fabrication of nanospheres,[22-25] dimers,[26-31] plates,[32-35] rods,[36-40] cubes, [41-45]polyhedrons[46-51] and complex structures[5, 52-54] made from wide range of materials including metals, semiconductors, oxides, MOFs and polymers. Beyond the extension of understandings, surface engineering has also been heralded as the practical means of nano/microstructral fabrication for optical devices,[55-61] sensors,[62-64] electronics, [65]catalysts[66-67] and drug delivery.[68]

In this chapter, I would like to present a general introduction of surface engineering of functional nanomaterials from fundamental studies to applications. In **Section 1.2** techniques of surface engineering, its recent advances, applications will be introduced. Although impressive progress has been achieved in surface engineering, there are some great challenges facing the research field, which will be discussed in **Section 1.3**. Finally, the scope of this dissertation will be presented in Section **1.4**.

1.2 Functionalization of Nanostructures by Surface Engineering

1.2.1 Surface Ligands Binding

Surface ligands – molecules that bind to the surface with surfactant-ligand duality – are an essential component of nanomaterial synthesis, processing and applications. Typically, nanoparticles are synthesized in solution phase with the head of surface ligands anchoring on the surface of nanoparticle and hydrocarbon tail directing away from it. If surface ligands selectively bind to certain facets of a growing nanocrystal, they reduce the surface energy of these facets relative to others.[69] The ligand layer can also block delivery of new reagents to the surface of nanocrystal.[5] These thermodynamic and kinetic factors are widely used for the synthesis of nanoparticles with anisotropic structures such as rods, plates or polyhedrons. For example, in their pioneer works, Alivisatos et al. have reported the synthesis of CdSe nanorods by managing the kinetics of the reaction.[70] Our group also explored the seeded growth of Ag nanoplates by selective ligand adhesion of citrate ligands on the basal facets to block overgrowth and only allowing growth in the lateral direction.[71]

Surface ligands also influence the optical and electronic properties of nanoparticles. While dispersed in solution, the surface of the nanoparticle is stabilized by the surface

ligands either by the electrostatic repulsive interaction originated from the surface charge or the steric repulsive force from the long polymer chains. Upon exposed to external stimuli such as variations of temperature, pH or ionic strength, the physical properties of the surface ligands have been changed, which greatly affect the arrangement and interaction between particles, as a result, the electronic or optical properties of the nanoparticles are changed. For example, our group demonstrated reversible thermoreponsive tuning of plasmon coupling of Au nanoparticles by manipulating the electrostatic interaction through the temperature dependent zeta potential of the surface ligand (BSPP).[72] Moreover, with the addition of salt such as sodium chloride, which screens the surface charge of surface ligands, assembly of Au nanoparticles is also observed with apparent red shift in the extinction spectra.[73]

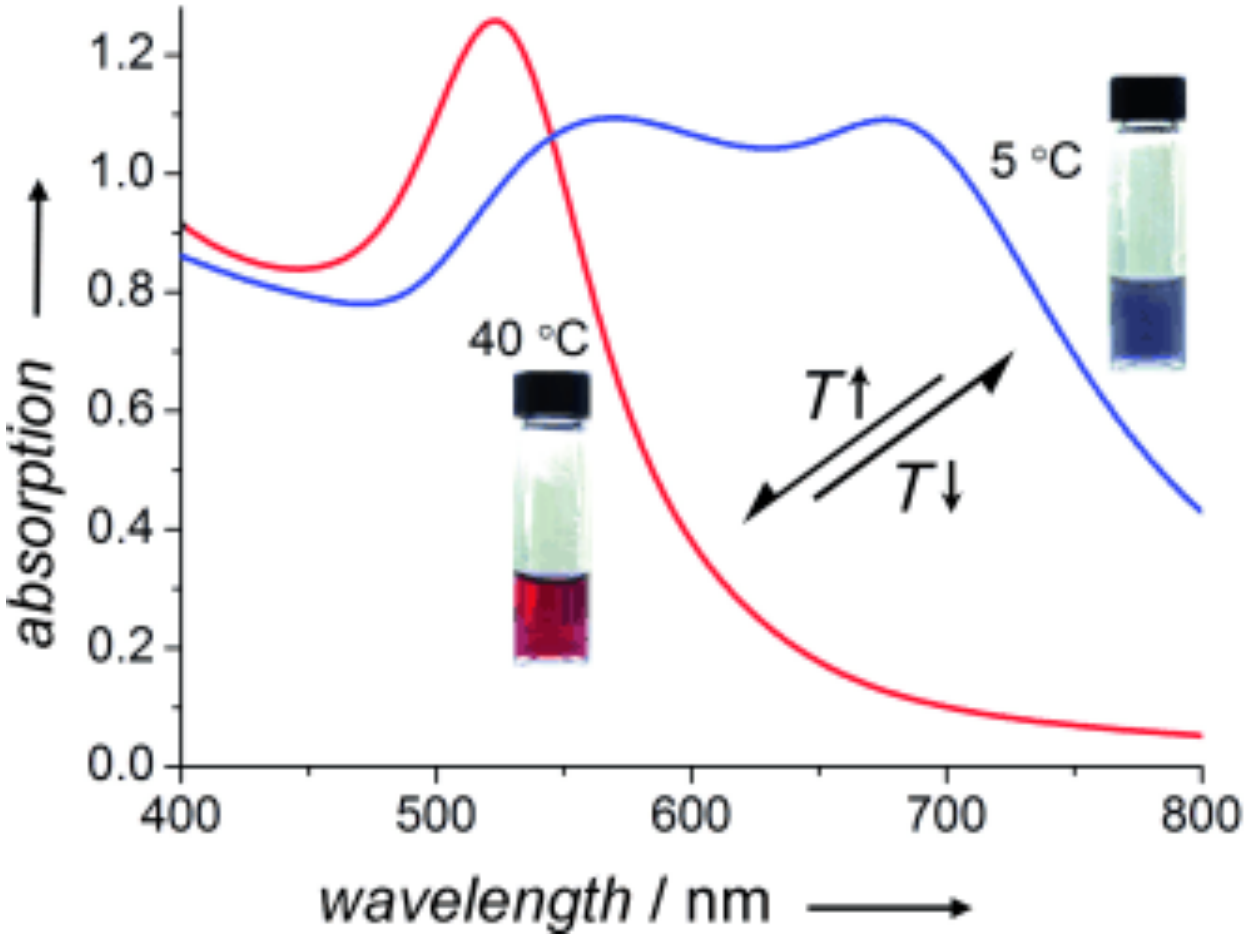

Figure 1.2. Schematic illustration of thermoresponsive assembly of Au nanoparticles assisted by the surface ligands. Reprint with permission from Ref. 72 © 2012 WILEY-VCH Verlag GmbH & Co. KGaA, Weinheim

1.2.2 Defect Engineering

Defects widely exist on the surface of nanocrystals with abundant dangling bonds and unsaturated coordinations, which have a great impact on the magnetic and electronic properties of nanomaterials.[4] With highly reactive sites around the defects, the intrinsic physical properties of nanomaterials, such as energy band gap, adsorption and desorption energy, electron density, coordination, interaction with surroundings and etc. are varied, which hold great importance for their applications in catalysis.[74] The techniques for defect engineering include pit digging, oxygen vacancies control and heteroatom substitution.[75-78]

The introduction of pits provides a feasible approach to enhance the degree of surface defect via bring more dangling bonds and unsaturated coordination atoms to the surface. Xie et al. have developed an ultrafast open space transformation strategy and successfully synthesized three-atom-layer thin CeO_2 sheets with 20% pits occupancy.[79] As expected, the presence of coordination-unsaturated cerium sites in pit-rich CeO_2 nanosheets not only increases the density of hole carriers ensuring fast diffusion, but also reduce activation barrier and decrease the catalyst poisoning change, both of which resulted in an obvious enhance of catalytic performance in CO oxidation with respect to the defect-free ultrathin CeO_2 sheets and the bulk counterpart.

Oxygen vacancies near the surface also play a key role in catalytic process because of an increasing number of active sites around these defects, a weaker metal-oxygen bond yielding faster exchange of intermediates and more efficient electron transfer induced by the vacancies[80-82]. Dai et al. have developed a plasma-engraving strategy to generate oxygen vacancies on the surface of Co_3O_4.[82] The oxygen-vacancy-enriched cobalt oxides showed improved electronic conductivity and more active defects for oxygen elevolution reaction (OER). Compared to pristine Co_3O_4, the engraved Co_3O_4 exhibits a much higher current density and a lower onset potential. Xie et al have performed DFT calculation to understand the contribution of oxygen vacancies.[83] According to their report, the existence of an oxygen vacancy could decrease the hindrance from the adsorption of H_2O and increase the reactivity with observing the delocalized O 2p orbital around the defects as shown in Figure 1.3.

Beside oxygen vacancy, heteroatom substitution with controllable disorder can also realize the electronic structure regulation of the functional nanopaterials. Our group has reported a colloidal synthesis method to prepare barium-doped TiO_2 nanocrystals, which show highly reversible light-responsive color switching of redox dyes with excellent cycling performance and high switching rate.[77] The excellent performance can be contributed to the Ba doping, which serves as effective sacrificial electron donors (SEDs) to scavenge the holes photogenerated by TiO_2 nanocrystals under UV irradiation and subsequently promote the reduction of dyes. Defects around the dopants can effectively promote the separation of electrons and holes during the photocatalytic reaction of TiO_2.

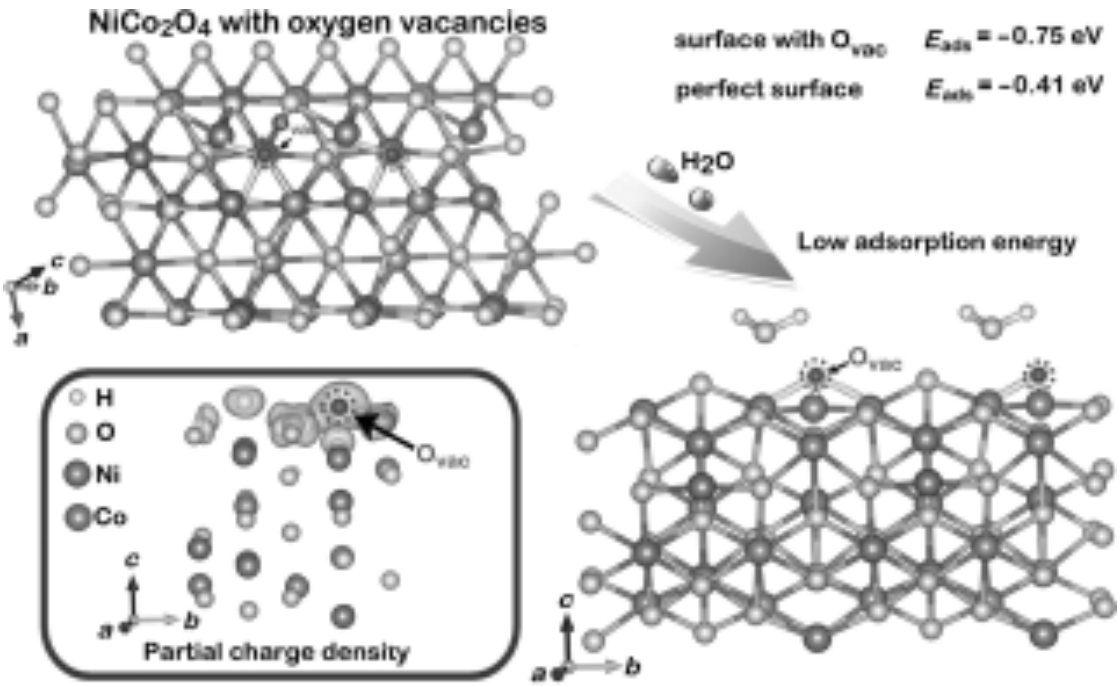

Figure 1.3. Schematic illustration of the adsorption of H_2O molecules onto the spinel structure and the partial charge density of $NiCo_2O_4$ with oxygen vacancies. Reprint with permission from Ref. 82 © 2015 WILEY-VCH Verlag GmbH & Co. KGaA, Weinheim

1.2.3 Surface Incorporation

Surface incorporation is regard as a direct mean of combining advantages or functionalities of materials together.[84] Surprisingly, in addition to simply adding up the desired properties in the nanocomposites, newly arisen and enhanced functions are observed due to the abundant interfaces, which facilitate mass or electron transfer during chemical reactions, as a result, their performance has been greatly enhanced.[85]

Our group has reported fully alloyed Ag/Au nanospheres with high compositional homogeneity prepared by annealing at high temperatures, which show large extinction cross sections, extremely narrow bandwidths and remarkable stability in harsh chemical environments.[3] Ag nanoparticles are known possessing stronger surface plasmon resonance than Au, but their applications have been limited by their poor chemical stability. However, through the incorporation of chemically inert plasmonic metal such as Au to the nanostructures of Ag by fully alloying, stable plasmonic nanostructures are prepared.

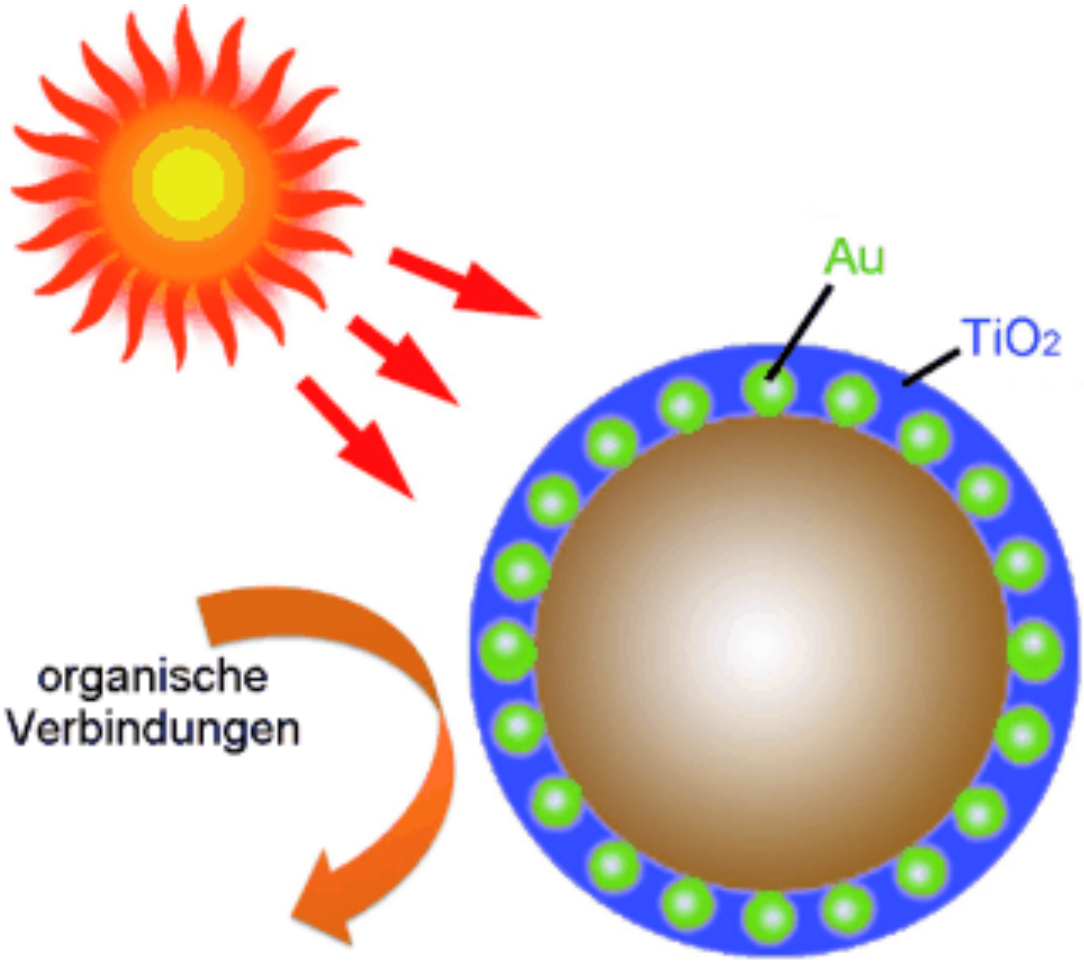

Figure 1.4. Schematically illustration of photocatalysis by Au/TiO_2 composites. Reprint with permission from Ref. 12 © 2011 WILEY-VCH Verlag GmbH & Co. KGaA, Weinheim

In addition to alloying with Ag to improve stability, Au is also incorporated to TiO_2 shell to enhance the photocatalytic performance (Figure 1.4).[12] Our group has reported a colloidal synthesis method by combining simple sol-gel and calcination processes to prepare the Au/TiO_2 nanocomposites. Due to the plasmonic properties of Au particles, the photocatalytic performance of TiO_2 in visible light has been enhanced. With abundant interfaces between Au and TiO_2, the efficiency of charge separation and transport has been largely improved and the rate of recombination of electron and hole is decreased with metal decoration serving as an electron reservoir.

1.2.4 Surface Patches

Patching surface of nanoparticles with functional patches is another mean of surface engineering. Unlike isotropic spherical colloidal particles, patchy particles are a class of unique building blocks, which possess anisotropic morphology or surface properties and enable directional interaction upon assembly.[15, 86] With the development of synthetic strategies, Janus particles with amphiphlic, opposite charges, isotropically magnetic and electronic dipolar surfaces have been fabricated.[87] Thus, the self-assembly of Janus particles into programmable structures with complex morphologies and functionalities has been made possible.[88-89] Weck et al. have reported a colloidal method to synthesize shape-shifting patchy particles, which change patch shape between concave and convex features induced by solvents (Figure 1.5).[90] With such unique properties, these particles can be assembled into chained, branched, zigzag and cyclic colloidal superstructures by capillary bridging.

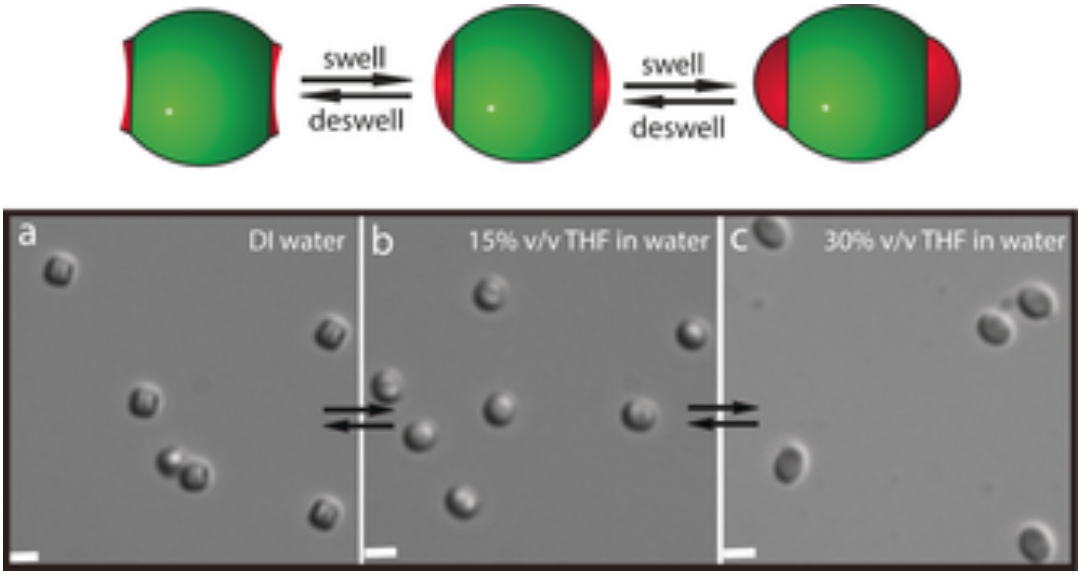

Figure 1.5. Schematic illustration and optical images of shape switching patchy particles. Reprint with permission from Ref. 90 © 2017 WILEY-VCH Verlag GmbH & Co. KGaA, Weinheim

1.3 Challenges in the Application of Functional Nanomaterials

The major challenges in the application of functional nanomaterials are aggregation, morphology deformation and recycling. Generally, an intrinsic shortcoming of nano-sized materials is their distinct tendency to form aggregates due to the high surface energy.[91] When the nanoparticles aggregate together, their exposed surface area is largely decreased, which, to a great extent, restrict their applications especially in catalysis, which requires large active surface area. Moreover, for the application of nanoparticles in programmable assembly, good dispersity and reversibility, which allows the building blocks adjusting direction and position within the assemblies, are also the key prerequisites. A widely used way to avoid aggregations is modifying the surface of nanoparticles by stabilizers or surfactants. On one hand, through building up charges by the surface ligands, the aggregations between particles can be countered by interparticle electrostatic repulsive interaction. On the other hand, even without surface charges, surface ligands can also provide hindrance repulsive interaction when the particles get closer to each other. As long as the balance between attractive and repulsive interactions can be built up before the short range Van der Waals force starts dominate, the aggregations of nanoparticles can be overcome.

Despite the advantages of nanomaterials with large surface area with large number of active sites and high reactivity, their morphologies are easily deformed due to the fast

reaction rate and chemical conversion. Accompanying the losing of surface structures during the chemical reaction, the functions of nanomaterials have been greatly compromised. For instant, in electrocatalytic system, two-dimensional ultrathin nanostructure is regarded as an effective catalyst with large exposed surface area and short diffusion pathways for electrons and ions. However, during the electrocatalytic reaction, the ultrathin nanostructure can be easily broke due to the expansion caused by insertion of ions and valance changes during chemical conversion. Moreover, if defect engineering is performed on the nanostructures to further enhance the performance, the deformation of morphology is also evitable. Thus, how to conserve the morphology especially the surface structure of nanomaterial holds significant importance for its practical applications.

With impressive small sizes beyond the scope of human eyes, the collecting and recycling of nanomaterials after using is critical to safety and environment. One way to solve this problem is incorporation of magnetic or electronic ingredients into the nanocomposites, through which the post recycle is facilitated utilizing external magnetic or electronic fields. The challenges of this method is development of synthetic strategies for such nanocomposites, which is not easy considering the mismatch of functional materials with the magnetic or electronic additions. Another solution may be developing the stimuli responsive nanomaterials, which keep dispersion when performing the function but aggregate during post collection upon the stimuli such as pH, temperature,

light and etc. The challenges here should be how to build up a system that can reversibly switch between the dispersion and aggregated states.

Above all, taking the key points of aggregation, morphology deformation and recycle into consideration is crucial when we develop new materials and implement them in practical applications. Hard as they may, challenges also open new opportunities and guidance for the designing of functional nanomaterials.

1.4 Scope of This Thesis

The surface engineering and fabrication of functional nanomaterials in an efficient and cost-effective way is an important topic due to their practical applications in various fields. This dissertation discusses our efforts in the surface engineering of nanomaterials and their application in catalysis, electrochemistry, data storage and optical device. Based on the principles of surface engineering, we first proposed new methods of surface engineering to fabricate functional nanomaterials followed by the mechanism study on the supreme surface properties of the materials. At last, demonstrate the application of the prepared functional material in catalysis, data storage, display and ect.

When nanocrystals are made to undergo chemical transformations, there are often accompanying large mechanical deformations and changes to overall particle morphology. These effects can constrain development of multistep synthetic methods through loss of well-defined particle morphology and functionality. In Chapter 2, we demonstrated a surface protection strategy for solution phase chemical conversion of colloidal nanostructures that allows for preservation of overall particle morphology despite large volume changes. Specifically, via stabilization with strong coordinating capping ligands on the surface, we demonstrated the transforming β-FeOOH nanorods into magnetic Fe_3O_4 nanorods. The mechanism of surface protection was then studied. At last, the surface-protected conversion strategy was generalized to the chemical

conversion of nanostructures of other morphologies (spheres, rods, cubes, and plates) and compositions (hydroxides, oxides, and metal organic frameworks).

In Chapter 3, porous cobalt oxide nanoplates enriched with oxygen vacancies are synthesized using a ligand-assisted polyol reduction method. With the aid of surface ligands, this method enables large-scale synthesis that offers superior uniformity, solution dispersity and controllable concentration of oxygen vacancies on surface. The large surface area of porous cobalt oxide nanoplates together with enriched oxygen vacancies provide more active sites, which promotes faster exchange of intermediates and more efficient electron transfer. At last, the prepared catalysts were applied to the electrocatalytic process. The as prepared cobalt oxide nanoplates manifest oxygen evolution reaction (OER) overpotential as low as 306 mV at 10 mA/cm^2 in 1 M KOH, which is superior to the values of most reported Co-based electrocatalysts.

Advanced Oxidation Processes (AOPs) are widely proposed for treating persistent pollutants by the •OH radicals generated from the decomposition of H_2O_2. Their broad applications in practical settings, however, have been hampered by the low efficiency of H_2O_2 decomposition. Although catalysts such as Fe^{2+} are often used, the overall efficiency of H_2O_2 decomposition is still considerably low so that a large dosage of H_2O_2 and catalyst (e.g. Fe^{2+}) are required, which not only make the AOPs too expensive for large-scale industrial applications but also lead to sludge formation and consequently catalyst poisoning. In Chapter 4, we report that metal sulfides (MoS_2, WS_2, Cr_2S_3, CoS,

PbS or ZnS) can serve as excellent co-catalysts to greatly increase the efficiency of H_2O_2 decomposition and significantly decrease the required dosage of H_2O_2 and Fe^{2+} in AOPs. The co-catalytic performance can be attributed to the surface defects of the cocatalysts. In details, the unsaturated S atoms on the surface of metal sulfides can be captured by protons in the solution to form H_2S, and expose metallic active sites with reductive property to accelerate the rate-limiting step of Fe^{3+}/Fe^{2+} conversion. The efficiency of the AOPs involving metal sulfide co-catalysts can be further enhanced by illumination with visible light thanks to the light-induced sensitization of organic pollutants. This discovery is expected to drive great advances in the use of AOPs for large-scale practical applications such as environmental remediation.

In Chapter 5, we demonstrate shape switching of patchy particles via fine-tuning of the spreading coefficient upon post-treatment process. When heated above glass transition temperature, the polymer patches would melt and reconfigure themselves according to the new established spreading coefficient. Since the spreading coefficient is determined by the three interfacial tensions between the silica core, polymer shell and dispersion environment, systematical study of the effect of each interfacial tension is carried out. When dispersed in different solvents, upon post-heating, the core-shell structured particles transform to dimer structures with polymer patches of different size and contact angle attached to the surface. More precise control has been accomplished utilizing solvent mixtures with different volume ratios. Originated from the thermodynamic stable nature of spreading coefficient in pursuing minimal surface energy, reversible shape

switching by alternating solvents has been achieved. When the shape reconfiguration process is quenched before reaching the equilibrium state, the quantity of patches is managed, revealing more complex three-dimensional organization of the particles, such as triangle bipyramid, tetrahedron and octahedron. In addition to achieving the variations of patchy shape parameters such as contact area, contact angle, curvature and quantity, the selective functionalization of the patchy particles is realized by depositing Pt nanoparticles on specific area of the silica core, which is complimentary to the shape of polymer patches. Utilizing the anisotropic surface property of the functional patchy particles, Pt shells with different thickness, depth and opening sizes have been fabricated, which hold potentials for many new applications in optics, catalysis and self-assembly.

In Chapter 6, we report a novel confined-space thermal dewetting strategy for the fabrication of Au nanocups with tunable diameter, height, and size of cup opening. Upon heating, dewetting of Au liquid between two SiO_2 interfaces is initiated. The nanocup morphology is defined by the cup-shaped void space created by a yolk–shell silica template that spontaneously takes an eccentric configuration during annealing. With strong scattering in near infrared, the Au nanocups exhibit superior efficiency as contrast agents for spectral-domain optical coherence tomography imaging. At last, the prepared Au nanocups are applied to the biological system as the contrast agent and achieve great enhancement of the chicken tissue in OCT imaging.

Colloidal bistability: In a dynamical colloidal dispersion, the system has two stable equilibrium states with local minima of potential energy separated by a local maximum. In Chapter 7, we have prepared amino-functionalized superparamagnetic particles, which can switch the adhesion between the surfaces of neighboring particles upon external stimuli. Specifically, when the system is turned "ON" with magnetic stimulus, nanoparticles self-assembled into chain structures through NH_2-catalyzed condensation of silanol groups to form siloxane bonds between particles. Upon turned "OFF" by thermal agitation, assemblies would disassemble to dispersed state due to the hydrolysis of siloxane bonds. Since the energy barrier between the two stable states is determined by electrostatic potential, which highly depends on surface charges, pH dependent bistability is achieved by managing $[H^+]$ related to the protonation of amino groups. With such stimuli-responsive system, rewritable data storage is demonstrated with the bistable particles.

1.5 References

1. Xu, W.; Wang, M.; Li, Z.; Wang, X.; Wang, Y.; Xing, M.; Yin, Y., Chemical Transformation of Colloidal Nanostructures with Morphological Preservation by Surface-Protection with Capping Ligands. *Nano Lett.* **2017,** *17* (4), 2713-2718.

2. Xu, W.; Lyu, F.; Bai, Y.; Gao, A.; Feng, J.; Cai, Z.; Yin, Y., Porous cobalt oxide nanoplates enriched with oxygen vacancies for oxygen evolution reaction. *Nano Energy* **2018,** *43*, 110-116.

3. Liu, K.; Bai, Y.; Zhang, L.; Yang, Z.; Fan, Q.; Zheng, H.; Yin, Y.; Gao, C., Porous Au–Ag Nanospheres with High-Density and Highly Accessible Hotspots for SERS Analysis. *Nano Lett.* **2016,** *16* (6), 3675-3681.

4. Araki, T.; Serra, F.; Tanaka, H., Defect science and engineering of liquid crystals under geometrical frustration. *Soft Matter* **2013,** *9* (34), 8107-8120.

5. Liu, Y.; Tang, A.; Zhang, Q.; Yin, Y., Seed-Mediated Growth of Anatase TiO2 Nanocrystals with Core–Antenna Structures for Enhanced Photocatalytic Activity. *J. Am. Chem. Soc.* **2015,** *137* (35), 11327-11339.

6. Ithurria, S.; Tessier, M. D.; Mahler, B.; Lobo, R. P. S. M.; Dubertret, B.; Efros, A. L., Colloidal nanoplatelets with two-dimensional electronic structure. *Nat. Mater.* **2011,** *10*, 936.

7. Boles, M. A.; Ling, D.; Hyeon, T.; Talapin, D. V., The surface science of nanocrystals. *Nat. Mater.* **2016,** *15*, 141.

8. Guo, Y.; Xu, K.; Wu, C.; Zhao, J.; Xie, Y., Surface chemical-modification for engineering the intrinsic physical properties of inorganic two-dimensional nanomaterials. *Chem. Soc. Rev.* **2015,** *44* (3), 637-646.

9. Wang, H.; Zhang, J.; Hang, X.; Zhang, X.; Xie, J.; Pan, B.; Xie, Y., Half-Metallicity in Single-Layered Manganese Dioxide Nanosheets by Defect Engineering. *Angew. Chem., Int. Ed.* **2015,** *54* (4), 1195-1199.

10. Wang, J.; Li, K.; Zhong, H.-x.; Xu, D.; Wang, Z.-l.; Jiang, Z.; Wu, Z.-j.; Zhang, X.-b., Synergistic Effect between Metal–Nitrogen–Carbon Sheets and NiO Nanoparticles for Enhanced Electrochemical Water-Oxidation Performance. *Angew. Chem., Int. Ed.* **2015,** *54* (36), 10530-10534.

11. Hu, H.; Guan, B.; Xia, B.; Lou, X. W., Designed Formation of Co3O4/NiCo2O4 Double-Shelled Nanocages with Enhanced Pseudocapacitive and Electrocatalytic Properties. *J. Am. Chem. Soc.* **2015,** *137* (16), 5590-5595.

12. Zhang, Q.; Lima, D. Q.; Lee, I.; Zaera, F.; Chi, M.; Yin, Y., A Highly Active Titanium Dioxide Based Visible-Light Photocatalyst with Nonmetal Doping and Plasmonic Metal Decoration. *Angew. Chem.* **2011,** *123* (31), 7226-7230.

13. Lyu, F.; Bai, Y.; Li, Z.; Xu, W.; Wang, Q.; Mao, J.; Wang, L.; Zhang, X.; Yin, Y., Self-Templated Fabrication of CoO–MoO2 Nanocages for Enhanced Oxygen Evolution. *Adv. Funct. Mater.* **2017,** *27* (34), 1702324-n/a.

14. Ma, M.; Zhang, K.; Li, P.; Jung, M. S.; Jeong, M. J.; Park, J. H., Dual Oxygen and Tungsten Vacancies on a WO3 Photoanode for Enhanced Water Oxidation. *Angew. Chem., Int. Ed.* **2016,** *55* (39), 11819-11823.

15. Wang, Y.; Wang, Y.; Breed, D. R.; Manoharan, V. N.; Feng, L.; Hollingsworth, A. D.; Weck, M.; Pine, D. J., Colloids with valence and specific directional bonding. *Nature* **2012,** *491* (7422), 51-55.

16. Wang, M.; Yin, Y., Magnetically Responsive Nanostructures with Tunable Optical Properties. *J. Am. Chem. Soc.* **2016,** *138* (20), 6315-6323.

17. Tu, F.; Lee, D., Shape-Changing and Amphiphilicity-Reversing Janus Particles with pH-Responsive Surfactant Properties. *J. Am. Chem. Soc.* **2014,** *136* (28), 9999-10006.

18. Walther, A.; Müller, A. H. E., Janus Particles: Synthesis, Self-Assembly, Physical Properties, and Applications. *Chem. Rev.* **2013,** *113* (7), 5194-5261.

19. Zhang, J.; Grzybowski, B. A.; Granick, S., Janus Particle Synthesis, Assembly, and Application. *Langmuir* **2017,** *33* (28), 6964-6977.

20. Youssef, M.; Hueckel, T.; Yi, G.-R.; Sacanna, S., Shape-shifting colloids via stimulated dewetting. *Nat. Commun.* **2016,** *7*, 12216.

21. Wang, H.; Li, B.; Yodh, A. G.; Zhang, Z., Stimuli-Responsive Shape Switching of Polymer Colloids by Temperature-Sensitive Absorption of Solvent. *Angew. Chem., Int. Ed.* **2016,** *55* (34), 9952-9955.

22. Ge, J.; Hu, Y.; Yin, Y., Highly Tunable Superparamagnetic Colloidal Photonic Crystals. *Angew. Chem., Int. Ed.* **2007,** *46* (39), 7428-7431.

23. Mayoral, R.; Requena, J.; Moya, J. S.; López, C.; Cintas, A.; Miguez, H.; Meseguer, F.; Vázquez, L.; Holgado, M.; Blanco, Á., 3D Long-range ordering in ein SiO2 submicrometer-sphere sintered superstructure. *Adv. Mater.* **1997,** *9* (3), 257-260.

24. Xu, X.; Asher, S. A., Synthesis and Utilization of Monodisperse Hollow Polymeric Particles in Photonic Crystals. *J. Am. Chem. Soc.* **2004,** *126* (25), 7940-7945.

25. Míguez, H.; Meseguer, F.; López, C.; Mifsud, A.; Moya, J. S.; Vázquez, L., Evidence of FCC Crystallization of SiO2 Nanospheres. *Langmuir* **1997,** *13* (23), 6009-6011.

26. Sacanna, S.; Rossi, L.; Pine, D. J., Magnetic Click Colloidal Assembly. *J. Am. Chem. Soc.* **2012,** *134* (14), 6112-6115.

27. Park, J.-G.; Forster, J. D.; Dufresne, E. R., High-Yield Synthesis of Monodisperse Dumbbell-Shaped Polymer Nanoparticles. *J. Am. Chem. Soc.* **2010,** *132* (17), 5960-5961.

28. Rahman, M. M.; Montagne, F.; Fessi, H.; Elaissari, A., Anisotropic magnetic microparticles from ferrofluid emulsion. *Soft Matter* **2011,** *7* (4), 1483-1490.

29. Chen, T.; Yang, M.; Wang, X.; Tan, L. H.; Chen, H., Controlled Assembly of Eccentrically Encapsulated Gold Nanoparticles. *J. Am. Chem. Soc.* **2008,** *130* (36), 11858-11859.

30. Chen, T.; Chen, G.; Xing, S.; Wu, T.; Chen, H., Scalable Routes to Janus Au−SiO2 and Ternary Ag−Au−SiO2 Nanoparticles. *Chem. Mat.* **2010,** *22* (13), 3826-3828.

31. Ge, J.; Hu, Y.; Zhang, T.; Yin, Y., Superparamagnetic Composite Colloids with Anisotropic Structures. *J. Am. Chem. Soc.* **2007,** *129* (29), 8974-8975.

32. Hu, Y.; Ge, J.; Zhang, T.; Yin, Y., A Blown Film Process to Disk-Shaped Polymer Ellipsoids. *Adv. Mater.* **2008,** *20* (23), 4599-4602.

33. Zhang, Q.; Li, N.; Goebl, J.; Lu, Z.; Yin, Y., A Systematic Study of the Synthesis of Silver Nanoplates: Is Citrate a "Magic" Reagent? *J. Am. Chem. Soc.* **2011,** *133* (46), 18931-18939.

34. Gao , C.; Lu , Z.; Liu , Y.; Zhang, Q.; Chi, M.; Cheng, Q.; Yin, Y., Highly Stable Silver Nanoplates for Surface Plasmon Resonance Biosensing. *Angew. Chem., Int. Ed.* **2012,** *51* (23), 5629-5633.

35. Wang, G.; Tao, S.; Liu, Y.; Guo, L.; Qin, G.; Ijiro, K.; Maeda, M.; Yin, Y., High-yield halide-free synthesis of biocompatible Au nanoplates. *Chem. Commun.* **2016,** *52* (2), 398-401.

36. Jana, N. R.; Gearheart, L.; Murphy, C. J., Wet Chemical Synthesis of High Aspect Ratio Cylindrical Gold Nanorods. *J. Phys. Chem. B* **2001,** *105* (19), 4065-4067.

37. Hu, J.; Odom, T. W.; Lieber, C. M., Chemistry and Physics in One Dimension: Synthesis and Properties of Nanowires and Nanotubes. *Acc. Chem. Res.* **1999,** *32* (5), 435-445.

38. Gao, C.; Zhang, Q.; Lu, Z.; Yin, Y., Templated Synthesis of Metal Nanorods in Silica Nanotubes. *J. Am. Chem. Soc.* **2011,** *133* (49), 19706-19709.

39. Wang, C.; Zhang, Z.; Yang, G.; Chen, Q.; Yin, Y.; Jin, M., Creation of Controllable High-Density Defects in Silver Nanowires for Enhanced Catalytic Property. *Nano Lett.* **2016,** *16* (9), 5669-5674.

40. Liu, B.; Aydil, E. S., Growth of Oriented Single-Crystalline Rutile TiO2 Nanorods on Transparent Conducting Substrates for Dye-Sensitized Solar Cells. *J. Am. Chem. Soc.* **2009,** *131* (11), 3985-3990.

41. Sun, Y.; Xia, Y., Shape-Controlled Synthesis of Gold and Silver Nanoparticles. *Science* **2002,** *298* (5601), 2176-2179.

42. Sherry, L. J.; Chang, S.-H.; Schatz, G. C.; Van Duyne, R. P.; Wiley, B. J.; Xia, Y., Localized Surface Plasmon Resonance Spectroscopy of Single Silver Nanocubes. *Nano Lett.* **2005,** *5* (10), 2034-2038.

43. Skrabalak, S. E.; Chen, J.; Sun, Y.; Lu, X.; Au, L.; Cobley, C. M.; Xia, Y., Gold Nanocages: Synthesis, Properties, and Applications. *Acc. Chem. Res.* **2008,** *41* (12), 1587-1595.

44. Gou, L.; Murphy, C. J., Solution-Phase Synthesis of Cu2O Nanocubes. *Nano Lett.* **2003,** *3* (2), 231-234.

45. Fan, F.-R.; Liu, D.-Y.; Wu, Y.-F.; Duan, S.; Xie, Z.-X.; Jiang, Z.-Y.; Tian, Z.-Q., Epitaxial Growth of Heterogeneous Metal Nanocrystals: From Gold Nano-octahedra to Palladium and Silver Nanocubes. *J. Am. Chem. Soc.* **2008,** *130* (22), 6949-6951.

46. Niu, W.; Zheng, S.; Wang, D.; Liu, X.; Li, H.; Han, S.; Chen, J.; Tang, Z.; Xu, G., Selective Synthesis of Single-Crystalline Rhombic Dodecahedral, Octahedral, and Cubic Gold Nanocrystals. *J. Am. Chem. Soc.* **2009,** *131* (2), 697-703.

47. Cao, H.; Qian, X.; Wang, C.; Ma, X.; Yin, J.; Zhu, Z., High Symmetric 18-Facet Polyhedron Nanocrystals of Cu7S4 with a Hollow Nanocage. *J. Am. Chem. Soc.* **2005,** *127* (46), 16024-16025.

48. Brittman, S.; Gao, H.; Garnett, E. C.; Yang, P., Absorption of Light in a Single-Nanowire Silicon Solar Cell Decorated with an Octahedral Silver Nanocrystal. *Nano Lett.* **2011,** *11* (12), 5189-5195.

49. Kuo, C.-H.; Huang, M. H., Facile Synthesis of Cu2O Nanocrystals with Systematic Shape Evolution from Cubic to Octahedral Structures. *J. Phys. Chem. C* **2008,** *112* (47), 18355-18360.

50. Henzie, J.; Grünwald, M.; Widmer-Cooper, A.; Geissler, P. L.; Yang, P., Self-assembly of uniform polyhedral silver nanocrystals into densest packings and exotic superlattices. *Nat. Mater.* **2012,** *11* (2), 131-137.

51. Yang, P., Surface chemistry: Crystal cuts on the nanoscale. *Nature* **2012,** *482* (7383), 41-42.

52. Chen, M.; Zhou, S.; You, B.; Wu, L., A Novel Preparation Method of Raspberry-like PMMA/SiO2 Hybrid Microspheres. *Macromolecules* **2005,** *38* (15), 6411-6417.

53. Mahmoud; Tabor, C. E.; El-Sayed, M. A.; Ding, Y.; Wang, Z. L., A New Catalytically Active Colloidal Platinum Nanocatalyst: The Multiarmed Nanostar Single Crystal. *J. Am. Chem. Soc.* **2008,** *130* (14), 4590-4591.

54. Hao, F.; Nehl, C. L.; Hafner, J. H.; Nordlander, P., Plasmon Resonances of a Gold Nanostar. *Nano Lett.* **2007,** *7* (3), 729-732.

55. Ge, J.; Yin, Y., Magnetically Tunable Colloidal Photonic Structures in Alkanol Solutions. *Adv. Mater.* **2008,** *20* (18), 3485-3491.

56. Ge, J.; Goebl, J.; He, L.; Lu, Z.; Yin, Y., Rewritable Photonic Paper with Hygroscopic Salt Solution as Ink. *Adv. Mater.* **2009,** *21* (42), 4259-4264.

57. Ge, J.; Lee, H.; He, L.; Kim, J.; Lu, Z.; Kim, H.; Goebl, J.; Kwon, S.; Yin, Y., Magnetochromatic Microspheres: Rotating Photonic Crystals. *J. Am. Chem. Soc.* **2009,** *131* (43), 15687-15694.

58. Zorba, S.; Maxwell, R. T.; Farah, C.; He, L.; Ye, M.; Yin, Y., Superparamagnetic Magnetite Nanoparticle Superstructures for Optical Modulation/Chopping. *J. Phys. Chem. C* **2010,** *114* (41), 17868-17873.

59. Kim, J.; Song, Y.; He, L.; Kim, H.; Lee, H.; Park, W.; Yin, Y.; Kwon, S., Real-Time Optofluidic Synthesis of Magnetochromatic Microspheres for Reversible Structural Color Patterning. *Small* **2011,** *7* (9), 1163-1168.

60. Wang, M.; He, L.; Hu, Y.; Yin, Y., Magnetically rewritable photonic ink based on superparamagnetic nanochains. *J. Mater. Chem. C* **2013,** *1* (38), 6151-6156.

61. Kim, H.; Ge, J.; Kim, J.; Choi, S.-e.; Lee, H.; Lee, H.; Park, W.; Yin, Y.; Kwon, S., Structural colour printing using a magnetically tunable and lithographically fixable photonic crystal. *Nat Photon* **2009,** *3* (9), 534-540.

62. Xuan, R.; Wu, Q.; Yin, Y.; Ge, J., Magnetically assembled photonic crystal film for humidity sensing. *J. Mater. Chem.* **2011,** *21* (11), 3672-3676.

63. He, L.; Hu, Y.; Wang, M.; Yin, Y., Determination of Solvation Layer Thickness by a Magnetophotonic Approach. *ACS Nano* **2012,** *6* (5), 4196-4202.

64. Han, X.; Liu, Y.; Yin, Y., Colorimetric Stress Memory Sensor Based on Disassembly of Gold Nanoparticle Chains. *Nano Lett.* **2014,** *14* (5), 2466-2470.

65. Cui, Y.; Lieber, C. M., Functional Nanoscale Electronic Devices Assembled Using Silicon Nanowire Building Blocks. *Science* **2001,** *291* (5505), 851-853.

66. Ge, J.; Huynh, T.; Hu, Y.; Yin, Y., Hierarchical Magnetite/Silica Nanoassemblies as Magnetically Recoverable Catalyst–Supports. *Nano Lett.* **2008,** *8* (3), 931-934.

67. Zhang, Q.; Joo, J.-B.; Lu, Z.; Dahl, M.; Oliveira, D. Q. L.; Ye, M.; Yin, Y., Self-assembly and photocatalysis of mesoporous TiO2 nanocrystal clusters. *Nano Res.* **2011,** *4* (1), 103-114.

68. Ferrari, M., Nanogeometry: Beyond drug delivery. *Nat Nano* **2008,** *3* (3), 131-132.

69. Yin, Y.; Alivisatos, A. P., Colloidal nanocrystal synthesis and the organic–inorganic interface. *Nature* **2004,** *437*, 664.

70. Peng, X.; Manna, L.; Yang, W.; Wickham, J.; Scher, E.; Kadavanich, A.; Alivisatos, A. P., Shape control of CdSe nanocrystals. *Nature* **2000,** *404*, 59.

71. Liu, Y.; Han, X.; He, L.; Yin, Y., Thermoresponsive Assembly of Charged Gold Nanoparticles and Their Reversible Tuning of Plasmon Coupling. *Angew. Chem., Int. Ed.* **2012,** *51* (26), 6373-6377.

72. Han, X.; Goebl, J.; Lu, Z.; Yin, Y., Role of Salt in the Spontaneous Assembly of Charged Gold Nanoparticles in Ethanol. *Langmuir* **2011,** *27* (9), 5282-5289.

73. Tao, L.; Lin, C.-Y.; Dou, S.; Feng, S.; Chen, D.; Liu, D.; Huo, J.; Xia, Z.; Wang, S., Creating coordinatively unsaturated metal sites in metal-organic-frameworks as efficient electrocatalysts for the oxygen evolution reaction: Insights into the active centers. *Nano Energy* **2017,** *41* (Supplement C), 417-425.

74. Xie, J.; Zhang, J.; Li, S.; Grote, F.; Zhang, X.; Zhang, H.; Wang, R.; Lei, Y.; Pan, B.; Xie, Y., Controllable Disorder Engineering in Oxygen-Incorporated MoS2 Ultrathin Nanosheets for Efficient Hydrogen Evolution. *J. Am. Chem. Soc.* **2013,** *135* (47), 17881-17888.

75. Zhuang, L.; Ge, L.; Yang, Y.; Li, M.; Jia, Y.; Yao, X.; Zhu, Z., Ultrathin Iron-Cobalt Oxide Nanosheets with Abundant Oxygen Vacancies for the Oxygen Evolution Reaction. *Adv. Mater.* **2017,** *29* (17), 1606793.

76. Wang, W.; Ye, Y.; Feng, J.; Chi, M.; Guo, J.; Yin, Y., Enhanced Photoreversible Color Switching of Redox Dyes Catalyzed by Barium-Doped TiO2 Nanocrystals. *Angew. Chem., Int. Ed.* **2015,** *54* (4), 1321-1326.

77. Han, D.; Jiang, B.; Feng, J.; Yin, Y.; Wang, W., Photocatalytic Self-Doped SnO2−x Nanocrystals Drive Visible-Light-Responsive Color Switching. *Angew. Chem., Int. Ed.* **2017,** *56* (27), 7792-7796.

78. Sun, Y.; Liu, Q.; Gao, S.; Cheng, H.; Lei, F.; Sun, Z.; Jiang, Y.; Su, H.; Wei, S.; Xie, Y., Pits confined in ultrathin cerium(IV) oxide for studying catalytic centers in carbon monoxide oxidation. *Nat. Commun.* **2013,** *4*, 2899.

79. Kim, J.; Yin, X.; Tsao, K.-C.; Fang, S.; Yang, H., Ca2Mn2O5 as Oxygen-Deficient Perovskite Electrocatalyst for Oxygen Evolution Reaction. *J. Am. Chem. Soc.* **2014,** *136* (42), 14646-14649.

80. Petrie, J. R.; Jeen, H.; Barron, S. C.; Meyer, T. L.; Lee, H. N., Enhancing Perovskite Electrocatalysis through Strain Tuning of the Oxygen Deficiency. *J. Am. Chem. Soc.* **2016,** *138* (23), 7252-7255.

81. Xu, L.; Jiang, Q.; Xiao, Z.; Li, X.; Huo, J.; Wang, S.; Dai, L., Plasma-Engraved Co3O4 Nanosheets with Oxygen Vacancies and High Surface Area for the Oxygen Evolution Reaction. *Angew. Chem., Int. Ed.* **2016,** *55* (17), 5277-5281.

82. Bao, J.; Zhang, X.; Fan, B.; Zhang, J.; Zhou, M.; Yang, W.; Hu, X.; Wang, H.; Pan, B.; Xie, Y., Ultrathin Spinel-Structured Nanosheets Rich in Oxygen Deficiencies for Enhanced Electrocatalytic Water Oxidation. *Angew. Chem., Int. Ed.* **2015,** *54* (25), 7399-7404.

83. Wang, Q.; Shang, L.; Shi, R.; Zhang, X.; Waterhouse, G. I. N.; Wu, L.-Z.; Tung, C.-H.; Zhang, T., 3D carbon nanoframe scaffold-immobilized Ni3FeN nanoparticle electrocatalysts for rechargeable zinc-air batteries' cathodes. *Nano Energy* **2017,** *40* (Supplement C), 382-389.

84. Zhao, Y.; Jia, X.; Chen, G.; Shang, L.; Waterhouse, G. I. N.; Wu, L.-Z.; Tung, C.-H.; O'Hare, D.; Zhang, T., Ultrafine NiO Nanosheets Stabilized by TiO2 from Monolayer NiTi-LDH Precursors: An Active Water Oxidation Electrocatalyst. *J. Am. Chem. Soc.* **2016,** *138* (20), 6517-6524.

85. Zhang; Glotzer, S. C., Self-Assembly of Patchy Particles. *Nano Lett.* **2004,** *4* (8), 1407-1413.

86. Jiang, S.; Chen, Q.; Tripathy, M.; Luijten, E.; Schweizer, K. S.; Granick, S., Janus Particle Synthesis and Assembly. *Adv. Mater.* **2010,** *22* (10), 1060-1071.

87. Perro, A.; Duguet, E.; Lambert, O.; Taveau, J.-C.; Bourgeat-Lami, E.; Ravaine, S., A Chemical Synthetic Route towards "Colloidal Molecules". *Angew. Chem., Int. Ed.* **2009,** *48* (2), 361-365.

88. Velev, O. D., Self-Assembly of Unusual Nanoparticle Crystals. *Science* **2006,** *312* (5772), 376-377.

89. Zheng, X.; Liu, M.; He, M.; Pine, D. J.; Weck, M., Shape-Shifting Patchy Particles. *Angew. Chem., Int. Ed.* **2017,** *56* (20), 5507-5511.

90. Bai, C.; Liu, M., Implantation of nanomaterials and nanostructures on surface and their applications. *Nano Today* **2012,** *7* (4), 258-281.

Chapter 2

Chemical Transformation of Colloidal Nanostructures with Morphological Preservation by Surface-Protection with Capping Ligands

2.1 Introduction

Chemical transformation has been developed as an effective means for producing colloidal nanostructures that are difficult to grow directly.[41, 92-105] As chemical reactions of nanocrystals involve changes in composition, crystal structure or phase, the transformation processes often lead to significant alternation to the original morphology of the nanocrystals. While in some cases the morphology change is pursued in order to create new structures, in many other cases one often wishes to maintain the original morphology.[106-109] A good example is the synthesis of magnetic iron oxide nanorods, which have recently attracted significant attention as building blocks for fundamental studies in colloidal self-assembly,[110-111] and for technological uses such as biomedical applications in magnetic resonance imaging (MRI) contrast enhancement,[112-114] targeted drug delivery,[115-116] medical diagnose and therapy,[117] and bioseparation.[118] Despite the great progress in colloidal synthesis of nanostructures, there are still no effective

procedures that can be used to directly synthesize magnetic iron oxide nanorods, in either magnetite or maghemite phase, with considerably high degree of control over the size and uniformity. We and other groups have therefore employed alternative methods by converting β-FeOOH and α-Fe_2O_3 nanorods or nanoellipsoids, which are rather easy to synthesize, into magnetic nanorods under hydrogen atmosphere at high temperatures.[110, 119-120] However, due to the high temperatures involved and the change in chemical composition and crystal structure during the process, the nanorods morphology cannot be preserved without additional measures such as coating the precursor nanorods with a protective hard shell, e.g. silica.[92, 119, 121] In such a scheme, the procedures for producing satisfactory coatings and for removing them after reduction are rather complicated and often add significant hindrance for large scale production. In addition, the chemistry for inorganic coating needs to be compatible with and optimized for the specific materials to be reduced. Therefore, the development of a more straightforward conversion method for fabricating magnetic iron oxide nanorods with well-defined morphology is of particular importance. Such a method, if it can be easily generalized, will have more significant impact to the field of nanocrystal synthesis as more nanostructures could be conveniently produced through chemical conversion routes.

Here we report a surface-protected conversion approach that can help to maintain the particle morphology during the chemical transformation of β-FeOOH nanorods into Fe_3O_4 nanorods. The approach is simple and effective, and more importantly, it can be generalized to preserving morphology during chemical transformations of other

nanostructures. The key in the surface protection concept is an effective capping ligand, which can stabilize the surface of nanocrystals and prevent their significant morphology change during chemical transformation. A relevant concept was proposed in our previous work on surface-protected etching, where silica and titania microspheres were capped with polymeric ligands and then etched by an appropriate etchant. Hollow shells with well-defined spherical morphologies were obtained as the result of preferential etching of the materials from the interior.[13] While the prior studies focused on making hollow shells, the particles were amorphous submicrometer objects with no phase or compositional changes during the etching process. In this work, we show that the surface protection concept can be greatly generalized to stabilizing the overall morphology of crystalline structures with dimension of nanometer scale. The conversion requires no coating of hard templates, and the protection can be achieved by simply mixing the nanostructures with appropriate capping ligands.

2.2 Materials and Methods

2.2.1 Materials

$FeCl_3 \bullet 6H_2O$, DEG, polyvinylpyrrolidone (PVP) (Mw.40000), potassium ferricyanide, 35% HCl, sodium citrate, urea, $KMnO_4$, hydrazine hydrate (hydrazine 64%), sodium acetate (NaAc), trisodium citrate (TSC), poly(acrylic acid) (PAA), poly(acrylic acid sodium salt) (PAASS), poly(sodium 4-styrenesulfonate) (PSS), CTAB and SDS were purchased from Sigma Aldrich. Distilled water was used in all experiments. All chemicals were directly used as received without further treatment.

2.2.2 Synthesis of 110 nm β-FeOOH nanorods:[110]

The synthesis of β-FeOOH nanorods is based on a previously reported method with minor revision. 4 mmol $FeCl_3 \bullet 6H_2O$ was dissolved in 40 ml water and centrifuged at 11000 rpm for 3 min to remove the undissolved precipitates. Then the supernatant was transferred into a three neck round bottom flask, and was heated to 87°C for 18 hours. The final product was washed by H_2O for several times, and was collected by centrifugation. At last, the precipitate was dispersed in 12 ml water.

2.2.3 PAA surface modification on the β-FeOOH nanorods:

To approximately 1 ml β-FeOOH solution mentioned above, 20 ml water and 1 ml of 7.2 mg/ml PAA solution were added. After magnetic stirring overnight, the product was firstly centrifuged at 11000 rpm for 5 min to remove the excess PAA. Afterwards, the particles were washed with water for several times, and were concentrated in 2 ml DEG for future use.

2.2.4 Synthesis of 200 nm β-FeOOH nanorods:[122]

0.04M $FeCl_3$ aqueous solution was aged at room temperature for 3 months. The product was removed by centrifugation and washed with water for twice and then dispersed in DEG for future use.

2.2.5 Synthesis of 200 nm Prussian blue nanocubes:[123]

The synthesis was followed a previously reported method. Basically, 113.4 mg potassium ferricyanide and 3 g of PVP (Mw.40000) were added to 40 ml 0.1 M HCl solution. After stirring at room temperature for 30 min, the system was heating to 80°C for 20 hours. The blue product was then collected by centrifugation and dispersed in DEG for future use.

2.2.6 Synthesis of 200 nm Fe_2O_3 clusters:[124]

In a typical synthesis, 0.5 g of $FeCl_3 \bullet 6H_2O$, 1.2 g of sodium citrate and 0.4 g of urea were dissolved in 50 ml distilled H2O. Then 0.3 g of poly (acrylic acid sodium salt) was added to the solution under magnetic stirring until it was all dissolved. The solution was then transferred into a 60 ml Teflon-lined autoclave, which was sealed and heated at 200°C for 3 hours. The red color product was collected by centrifugation and dispersed in DEG for future use.

2.2.7 Synthesis of 200 nm $Mn(OH)_2$ nanoplates:[125]

In a typical synthesis, 0.316 g of $KMnO_4$ was dissolved in 40 ml distilled water under magnetic stirring followed by the addition of 5 ml hydrazine hydrate (hydrazine 64%). The color changed from purple to brown. And then the solution was transferred to a 60 ml Teflon-lined autoclave, which was sealed and heated at 120°C for 12 hours. The product is white precipitate, which was washed with water for several times and dispersed in DEG for future use.

2.2.8 Synthesis of 600 nm β-FeOOH nanorods:[126]

To synthesize the 600 nm β-FeOOH nanorods, an aqueous solution of 0.1 M $FeCl_3 \bullet 6H_2O$ and 0.06 M HCl was heated in oven at 87°C for 24 hours. And then the solution was washed with water for several times and dispersed in DEG for the next step.

2.2.9 Surface protected conversion via polyol process

Under the protection of Nitrogen, 60 ml DEG containing desired capping ligand was heated to 220 °C, followed by the injection of a certain nanoparticle/DEG solution. Samples during the conversion after certain time intervals were collected in order to investigate the surface protected reduction process. Before TEM characterization, samples were washed with mixture solution of ethanol and water for several times.

2.2.10 Characterization

The morphologies were characterized using a Tecnai T12 transmission electron microscope (TEM). The HRTEM and SAED were characterized by transmission electron microscopy (JEM-2100, JEOL). The crystal phases of the products were characterized with an X-ray diffractometer (XRD, EMPYREAM, PANalytical, Cu-Kα radiation), in a range 2 theta from 20° to 80°. All Fourier transform infrared (FTIR) spectra were performed by Brucker Alpha FT-IR spectrometer in form of powder. Magnetic property

of Fe3O4 nanorods was determined by using a Lakeshore vibrating sample magnetometer, Model 142A, with Model 642 Electromagnet power supple and Model EM4 HV electromagnet. The concentration of iron ions was analyzed with Perkin-Elmer Optima 7300DV ICP-OES apparatus that combined an SCD detector and an echelle optical system. The chemical state and electronic state of the elements on the surface were measured with X-ray photoelectron spectroscopy (AXIS ULTRA).

2.3 Results and Discussion

We chose non-magnetic β-FeOOH nanorods as the starting material, which was synthesized through a hydrothermal method reported previously.[110] An aqueous dispersion of the β-FeOOH nanorods was injected into diethylene glycol (DEG) solution pre-heated at 220°C. DEG was chosen as the reducing agent because reduction in a solution phase of polyol could help eliminate close contact of the nanoparticles and reduce the possibility of aggregation and coalescence, which were commonly encountered during the high-temperature H_2 reduction of solid phase. Moreover, in contrast to the cases of rapid reduction under H_2, the mild reducing power of polyols could allow convenient control over the conversion by fine tuning the reaction time and temperature.

2.3.1 Choice of Capping Ligands

Initially, various ligands were chosen to perform DEG reduction. In a typical synthesis, β-FeOOH solution was injected into the hot DEG solution containing different kinds of capping ligands and heated at 220°C for 2 hours. Subsequently, the products were collected and characterized by transmission electron microscope (TEM). As illustrated in the TEM images in Figure 2.1, without any capping ligand, β-FeOOH nanorods quickly lost their original shape and formed large aggregation during the phase transition from β-FeOOH to Fe_3O_4 (also see Figure 2.2). Similarly, in the presence of a typically used

capping ligand cetyltrimethylammonium bromide (CTAB), the original morphology was lost as well since there was no strong interaction between the CTAB and β-FeOOH surface. However, when sodium dodecyl sulfate (SDS), another popular ligand with a weak coordination group of SO_4^{2-} to iron cations, the morphological deformation was greatly relieved with merely small portion of fragments. By further introducing other capping ligands with stronger coordination interactions with iron cations, particularly those containing one or more carboxyl groups such as sodium acetate (NaAc), trisodium citrate (TSC), poly(acrylic acid) (PAA) and poly(acrylic acid sodium salt) (PAASS), the morphological deformation of β-FeOOH nanorods during phase transition could be almost completely suppressed. In addition, polymeric capping ligands containing other functional groups such as poly(sodium 4-styrenesulfonate) (PSS) and polyvinylpyrrolidone (PVP) showed ability of effective protection as well, confirming our understanding of the need for strong capping ligands for successful surface-protected conversion.

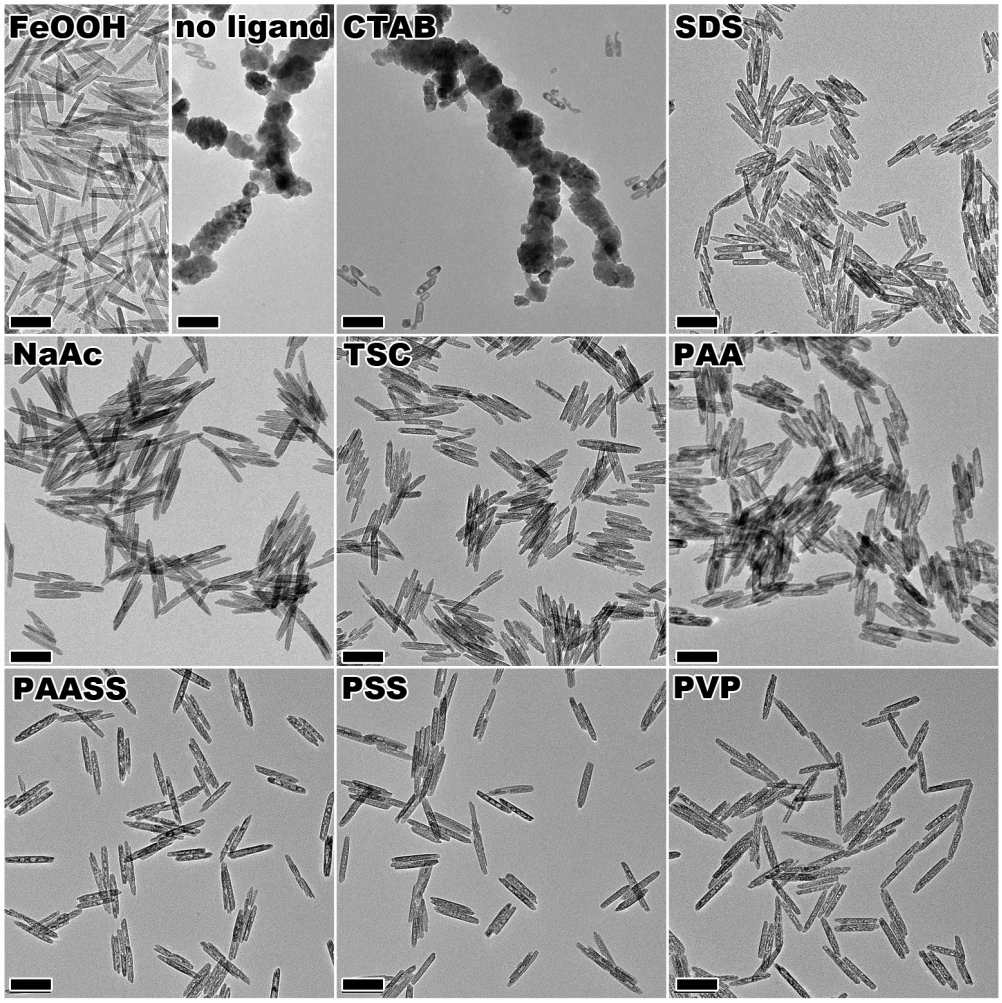

Figure 2.1. TEM images of original β-FeOOH nanorods and the products of their reduction in DEG in the presence of various capping ligands such as CTAB, SDS, NaAc, TSC, PAA, PAASS, PSS, and PVP. All scale bars are 100 nm.

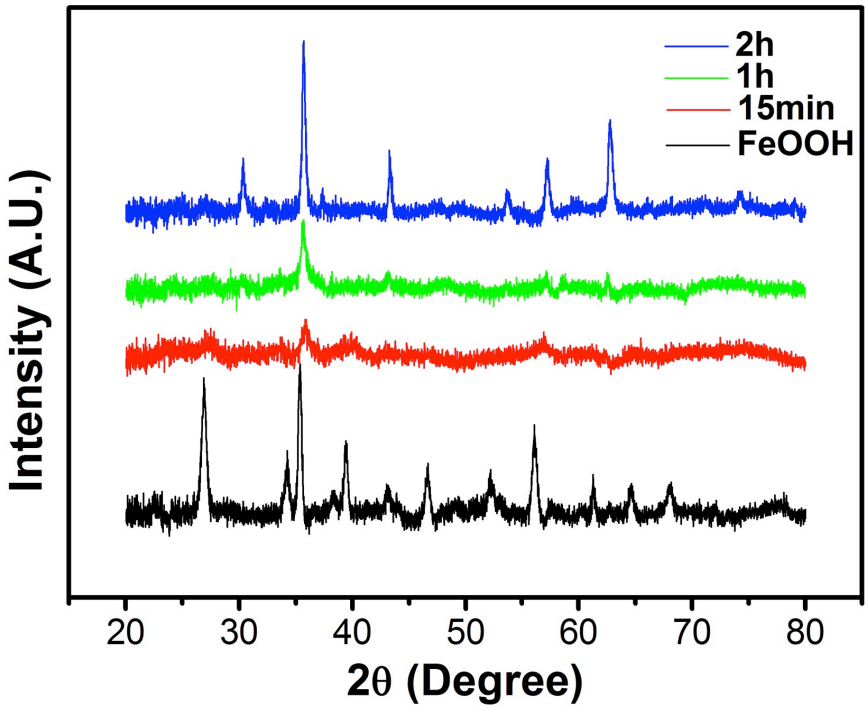

Figure 2.2. XRD patterns of (from bottom to top) the original β-FeOOH nanorods and the samples after reduction for 15 min, 1 and 2 h without any surface protection.

2.3.2 Surface-Protected Conversion of FeOOH

The surface-protected conversion was then studied in detail using PAA as a model ligand. The as-synthesized β-FeOOH nanorods exhibited well-defined rod-like morphology with a uniform size distribution. The average length of a typical nanorod sample is around 110 nm and average width approximately 20 nm (Figure 2.3a). To study the phase transition process, upon a certain time of incubation, the reaction was quenched to room temperature at different points in time (1, 4 and 8 h) and the respective intermediates were examined by TEM (shown in Figure 2.3b-d). Conversion started very quickly when the nanorods were reduced by DEG at 220°C, producing small pores which coalesced and grew bigger over time (Figure 2.4). The nanorods appeared to be noticeably porous after ~1 h of reaction, and hollow after ~ 4 h. Significantly, the overall morphology of the hollow nanorods changed very little upon continued heating for ~8 h, only showing slight increase in hollowness inside the shell. This is very different from the case without ligand protection, where the formation of large pores eventually led to collapse of the structure of the nanorods. The tubular nanorods showed uneven shell thickness, with the thinner regions of ~ 3 nm. By measuring the dimensions in the TEM image, the void volume is roughly estimated around 65%. Another important feature here is that the surface-protected nanorods remain high colloidal stability throughout the heating process (Figure 2.5), demonstrating the strong binding of the polymeric ligands to the nanorods surface. The transformation process was then characterized by high-resolution TEM (HRTEM). As shown in figure 2.3e-h, the phase transformed from β-FeOOH with d-

space value of 5.24 Å to Fe_3O_4 with d-space value of 2.53 Å. After 1-h reduction, the major phase is still β-FeOOH, the formation of pores is only caused by the thermal dehydration reaction. Later, a mixture of β-FeOOH and Fe_3O_4 was observed in the 4 h sample with β-FeOOH as the shell and Fe_3O_4 as the interior, which suggested that the reduction occurred inside first.

Subsequently, the phase transition process was further confirmed by X-ray diffraction (XRD) measurement. Figure 2.3i shows the XRD patterns of the original sample and those underwent surface-protected reduction for 1, 4 and 8 h. All diffraction peaks in the black curve for the starting material can be indexed to β-FeOOH (JCPDS Card No. 75-1594). Some characteristic peaks (i.e. at 35°) of β-FeOOH are very close to Fe_3O_4, but a sharp peak at 27°, corresponding to the (130) reflection from β-FeOOH, is suitable to monitor the disappearance of β-FeOOH. As shown in the 1-h curve, during the reduction process, the peak at 27° became broader with decreasing intensity, which illustrated the conversion of β-FeOOH phase with decreased crystallinity. The crystalline domain size is estimated around 6.8 nm by following Scherrer's equation. At the same time, the (220) peak for magnetite appeared at 30°, and grew sharper over 8 hours, demonstrating the formation of magnetite with good crystallinity. We concluded that β-FeOOH was fully converted to magnetite in 8 hours based on the absence of the characteristic peak of β-FeOOH at 27° in the 8-h curve. To distinguish magnetite (Fe_3O_4) from maghemite (γ-Fe_2O_3) with identical XRD patterns, we performed Fourier transform infrared spectroscopy (FTIR) on the 8-h sample. As shown in Figure 2.6 in the supporting

information, the peak positioned at 560 cm^{-1} corresponds to the Fe-O stretching mode of the tetrahedral and octahedral sites that belong to magnetite; in contrast, the Fe-O absorption peak in maghemite appears around 630 cm^{-1}.[127-128] Accordingly, the XRD results are very consistent with the HRTEM results.

We also investigated the magnetic behavior of the final product magnetite nanorods by characterizing the field dependence of magnetization. The magnetic hysteresis loop of the magnetite nanorods measured at 300 K was illustrated in Figure 2.3j. Their saturation magnetization (Ms) was 40 emu/g. The coercivity was less than 2 Oe, which could be categorized as superparamagnetic, given a typical superparamagnetic limit of 30 Oe.[129]

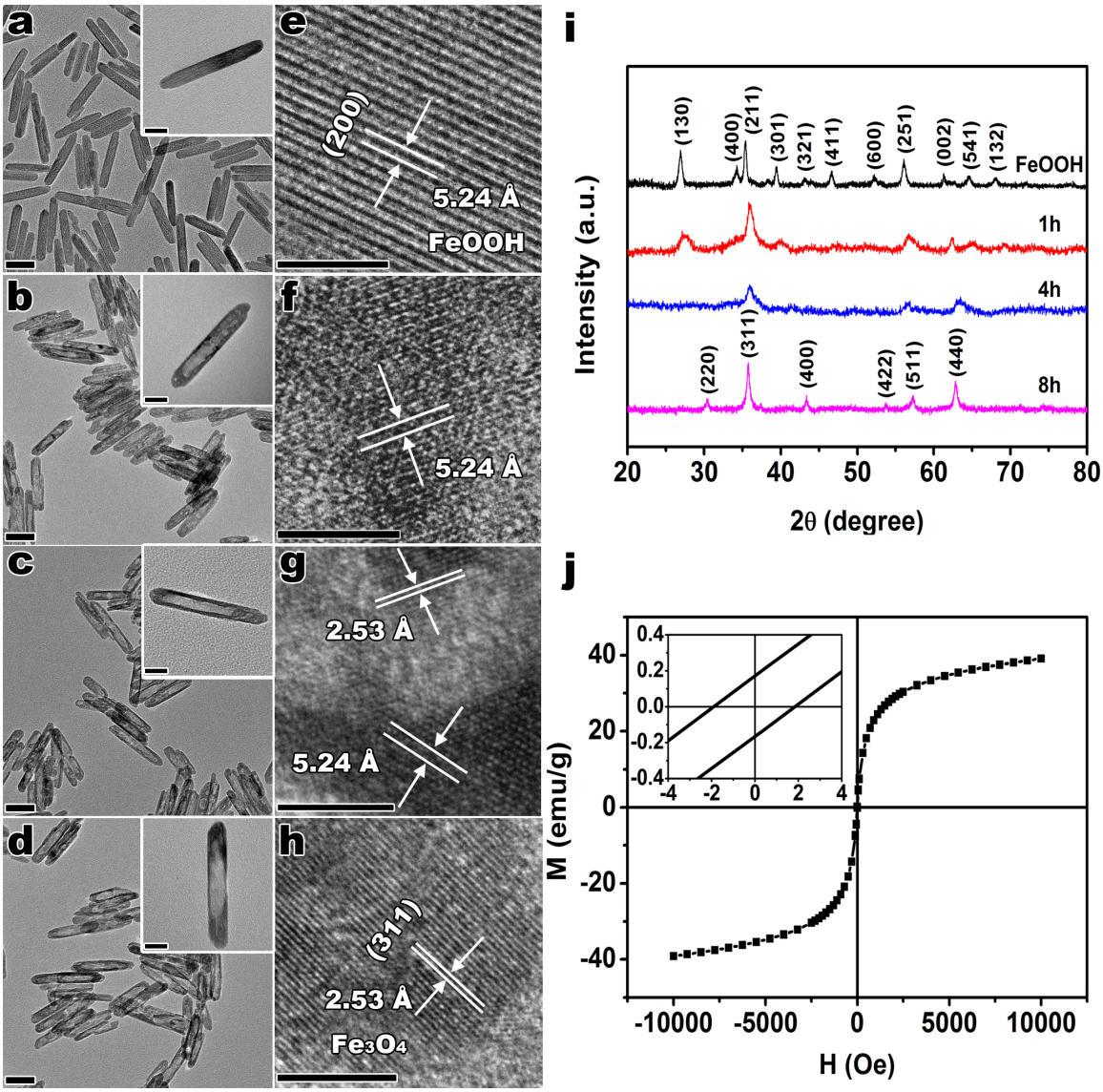

Figure 2.3. a-d) TEM images of β-FeOOH, β-FeOOH reduced for 1, 4 and 8 h respectively (scale bars: 50 nm, insets: 20 nm) and e-h) corresponding HRTEM images of select area (scale bars: 5 nm); i) XRD; j) Mass magnetization M as a function of applied external field H for the dried 8 h magnetite measured at 300K (inset: expanded low-field curve).

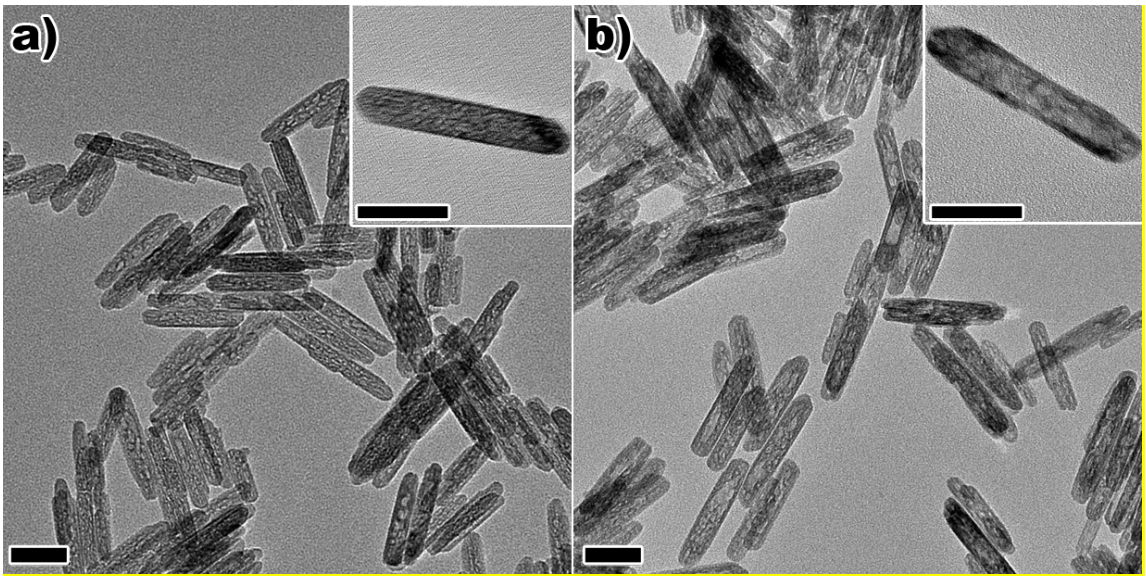

Figure 2.4. Reduction of PAA modified β-FeOOH nanorods in DEG for a) 1 min; b) 15 min. Scale bars: 50 nm.

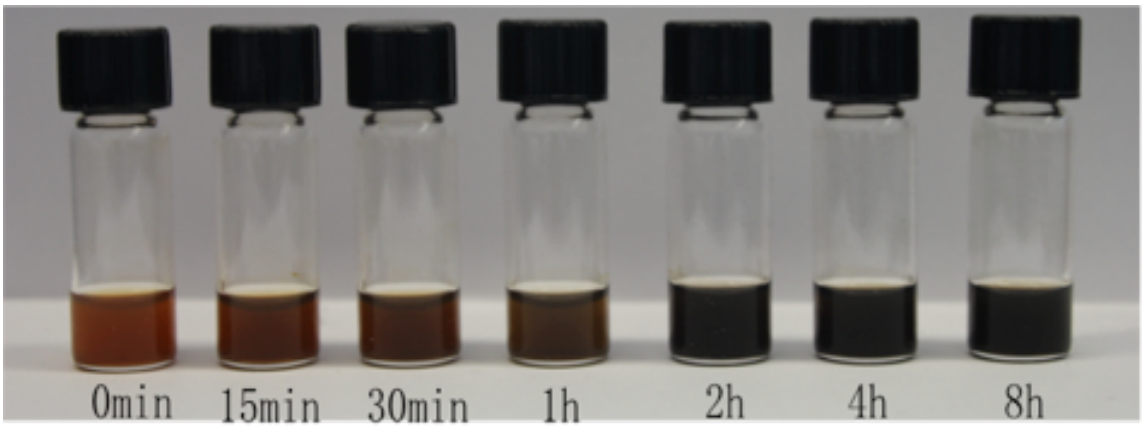

Figure 2.5. Digital photo of β-FeOOH nanorod dispersion in DEG during the conversion process.

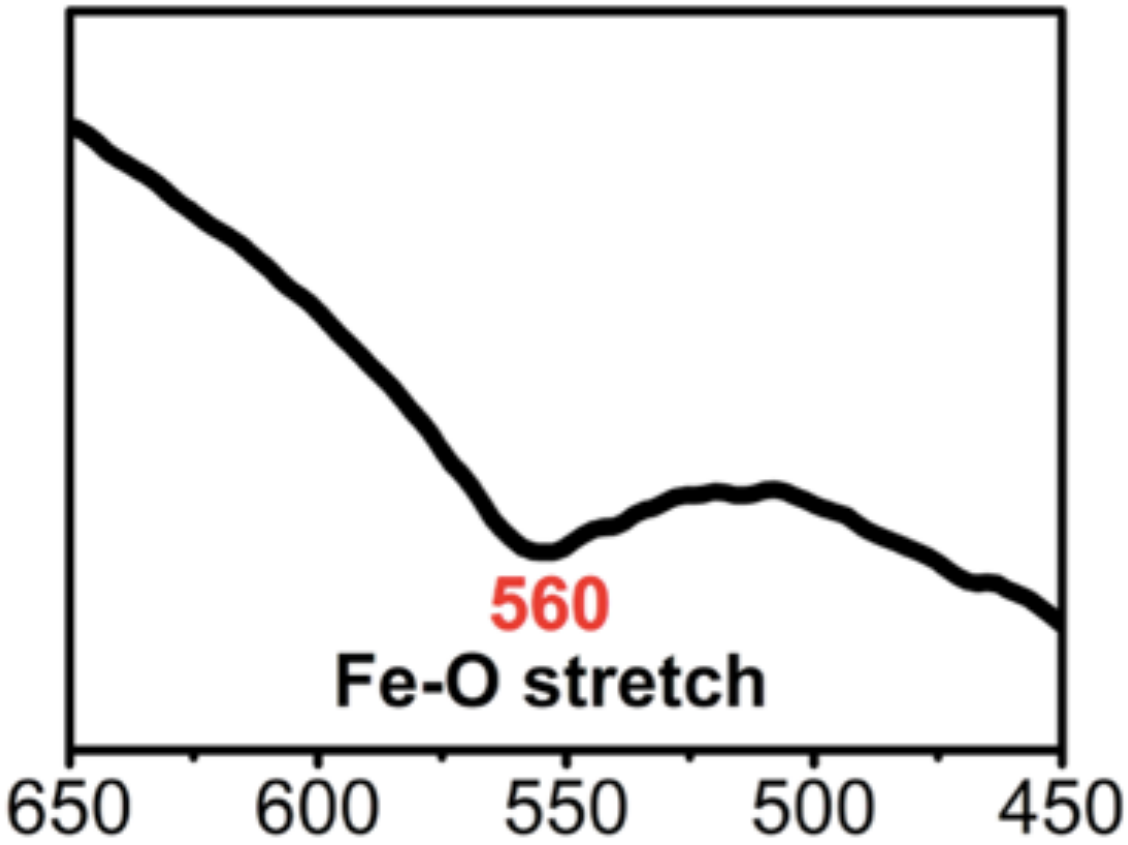

Figure 2.6. FTIR spectrum of Fe_3O_4 nanorods synthesized through reduction of β-FeOOH nanorods by 8 h. The peak positioned at 560 cm^{-1} corresponds to the Fe-O stretching mode of the tetrahedral and octahedral sites of magnetite.

2.3.3 The Role of Capping Ligands

In this conversion process, PAA plays a crucial role in maintaining both the colloidal and structural stability. Firstly, its strong binding to the nanorod surface enables high dispersity in polar solvents such as water and ethanol, aiding applications in areas such as bioimaging and drug delivery. Secondly and more importantly, PAA acts as a surface protection ligand to maintain the morphology of nanorods during the phase transition. Through the strong coordination interaction between the iron cations and multiple carboxyl groups, PAA acts as a multidendate ligand on the surface of the nanorods, preventing the surface from breaking down by DEG. The formation of hollow nanorods is due to the volume shrinkage caused by mass losing from β-FeOOH to Fe_3O_4 and more importantly originated from the condensation from β-FeOOH with a low density of 3 g/cm^3 to a denser magnetite phase with a density of 5.2 g/cm^3. Accordingly, the theoretical volume shrinkage is calculated around 50 %. Since the surface is protected by PAA, the volume change can only be achieved by voiding the interior space of the nanorods. After β-FeOOH is completely converted to Fe_3O_4, no more volume changes take place and final product magnetite tubular nanorods are formed. Moreover, compared to the theoretical volume shrinkage (50%), the measured one (65%) is slightly higher, which may contribute to the dissolving of iron ion by DEG.[130]

We verified the binding of PAA to β-FeOOH by analyzing the composition of the nanorods via FTIR. FTIR spectra of dry powders of PAA and the as-synthesized β-

FeOOH were first measured as references. As illustrated in Figure 2.7a, PAA showed a strong peak around 1700 cm^{-1}, corresponding to the typical stretching of C=O double bonds of the carboxyl groups (black curve). As-synthesized β-FeOOH showed a characteristic peak at 3400 cm^{-1} due to the hydroxyl group of β-FeOOH (green curve). After surface modification by PAA, β-FeOOH nanorod sample was washed with water for several times to remove the excess amount of PAA before drying for FTIR measurement. The PAA modified β-FeOOH sample showed typical IR peaks of both the carboxyl groups and hydroxyl groups (blue curve), indicating its successful surface binding to the nanorod surface. The FTIR measurement on the sample reduced in DEG for 8 hours (pink curve) also suggested the presence of carboxyl groups, further confirming the strong bonding of PAA on Fe_3O_4 surfaces.

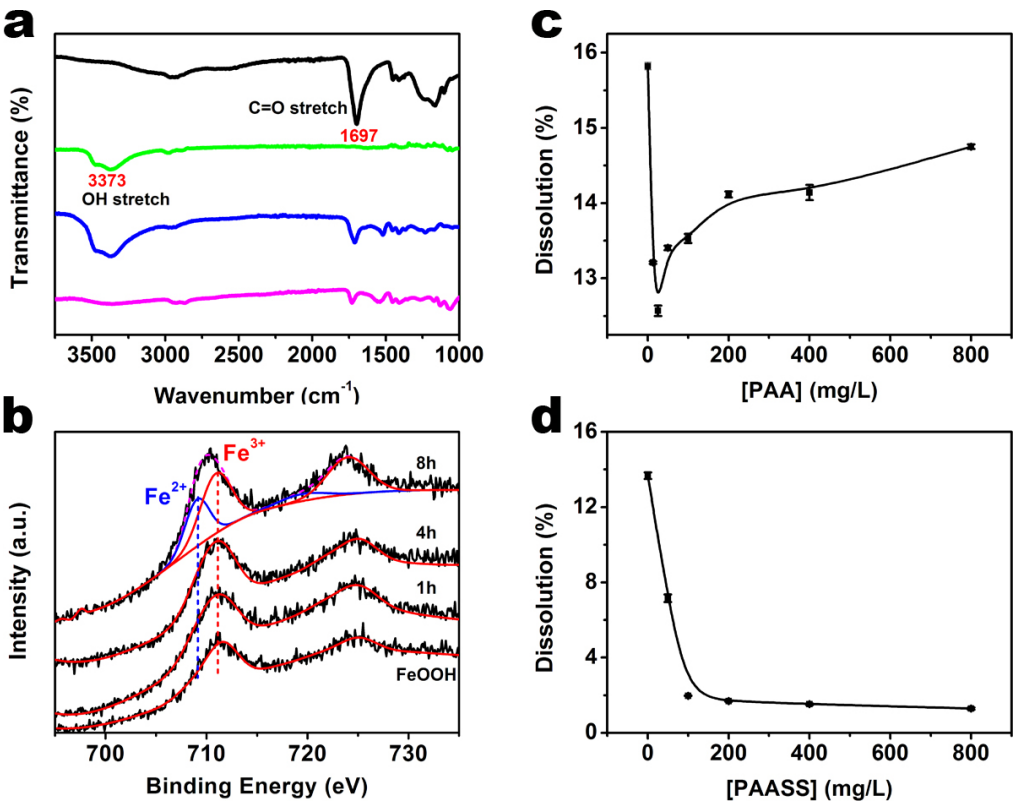

Figure 2.7. a) FTIR of PAA, β-FeOOH, PAA modified β-FeOOH and β-FeOOH reduced for 8 h (from top to down); b) Fe 2p XPS spectra of β-FeOOH, 1, 4 and 8 h; c) ICP-OES of Fe ion with different concentration of PAA (0, 25, 50, 100, 200, 400 and 800 mg/L); d) ICP-OES of Fe ion with different concentration of PAASS (0, 50, 100, 200, 400 and 800 mg/L).

To further demonstrate that the surface layer is occupied by the capping ligands and the reduction reaction is initiated from the interior, β-FeOOH and β-FeOOH reduced by DEG for different lengths of time were then studied by X-ray photoelectron spectroscopy (XPS). The fine-scanned Fe 2p XPS spectra were shown in Figure 2.7b. In the spectra of β-FeOOH, 1- and 4-h samples, the peaks of Fe $2p_{3/2}$ and Fe $2p_{1/2}$ were located at round 711.5 and 725 eV respectively, which indicated the Fe^{3+} oxidation state. Whereas the peaks of Fe $2p_{3/2}$ and Fe $2p_{1/2}$ were located at round 710 and 724 eV for the 8-h sample. The shift of peaks to lower binding energy can be attributed to the reduction of Fe^{3+} to Fe^{2+}. To get further insight into the surface properties, the 8-h curve was fitted by Gaussian-Lorentz functions to investigate the electronic states of Fe atoms. The two fitted peaks for Fe $2p_{2/3}$ were found to be Fe^{3+} (B.E. 711.5 eV) and Fe^{2+} (B.E. 709.7 eV) respectively, indicating Fe_3O_4 chemical nature, consistent with the XRD result. However, in the XPS spectra of 4-h sample, only Fe^{3+} peaks were observed, demonstrating no reduction of Fe^{3+} on the surface. Considering that 4-h sample showed characteristic peaks of Fe_3O_4 in the XRD pattern, we could conclude that only the interior of β-FeOOH has been preferentially reduced to Fe_3O_4, whereas the surface remains β-FeOOH since it is occupied by the capping ligand. By further extending the reduction time to 8 h, the reduction of Fe^{3+} to Fe^{2+} was also achieved on the surface, indicating more complete conversion of β-FeOOH to Fe_3O_4. To elucidate the components of the surface, fine-scanned O 1s XPS spectra were analyzed and shown in figure 2.8. The peak centered at 531 eV can be assigned to Fe-OH originated from lattices, which confirmed its β-FeOOH nature. Moreover, the peak area of Fe-$OH_{lattice}$ decreased with the increase of reduction

time, indicating the dehydration of β-FeOOH to iron oxide on the surface upon high-temperature treatment. Afterwards, the importance of PAA was further revealed by inductively coupled plasma optical emission spectrometry (ICP-OES) measurements. In a typical synthesis process, one batch of β-FeOOH was evenly divided into 7 aliquots and then each aliquot was hot injected into the DEG solutions containing different amount of PAA. After 1-h reaction, the survived components were removed by centrifugation and the dissolved Fe ion in the supernatant was collected and analyzed by ICP-OES (Figure 2.7c). For bare β-FeOOH rods without any ligand protection, 16% of the Fe species have been dissolved by DEG. However, with slight addition of PAA, the dissolution amount decreased below 13% when the concentration of PAA in DEG increased to around 50 mg/L, demonstrating the good protection ability of PAA. Nevertheless, the protection from PAA is not infinite. By extensively increasing the concentration to 800 mg/L, the dissolution amount was increased to around 15% instead, due to the relatively low pH induced by larger amount of PAA. However, the etching effect originated from PAA can be resolved by using the basic sodium salt of PAA. As illustrated in Figure 2.7d，the dissolved Fe ion decreased to 2% and remained constant when the concentration of PAASS was above 100 mg/L.

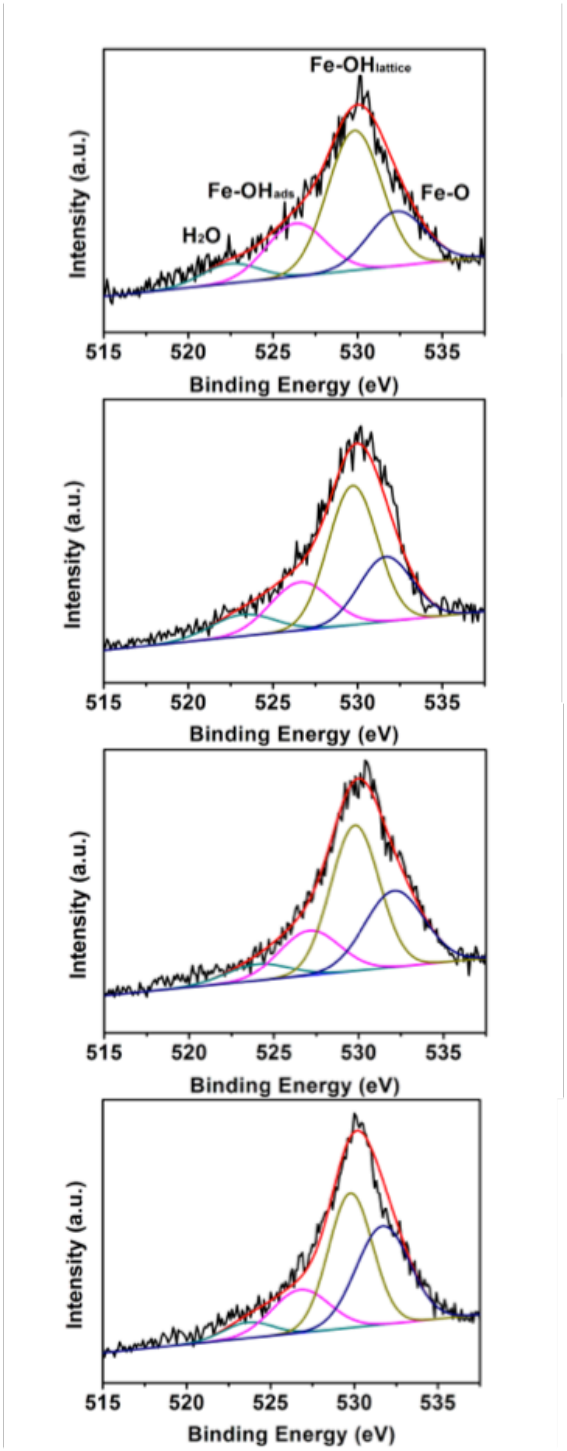

Figure 2.8. O 1s XPS spectra of β-FeOOH nanorods before and after reduction for 1, 4 and 8 h (From top to bottom).

2.3.4 Versatility of the Surface-Protected Conversion Method

To demonstrate its versatility, the surface-protected conversion method has been extended to materials of various phases and morphologies, such as longer β-FeOOH nanorods, α-Fe_2O_3 spherical nanoclusters, Prussian blue (PB) nanocubes and $Mn(OH)_2$ nanoplates. As shown in Figures 2.9a and b, uniform β-FeOOH nanorods of 200 nm in length were successfully converted to magnetite phases with well-maintained morphology after 4-h reduction, which was confirmed by XRD measurements. Through surface-protected reduction, magnetic magnetite hollow spheres were fabricated by surface-protected conversion of nonmagnetic hematite nanospheres for 4 h. As shown in Figure 2.9f, the volume shrinkage caused by phase transition was mediated by forming pores in the nanoshells. The surface-protected conversion method is also applicable to metal organic frameworks other than metal oxides, as demonstrated in Figures 2.9c and 2.9g where PB nanocubes were converted into hollow nanoboxes. Finally, $Mn(OH)_2$ nanoplates were converted to porous MnO nanoplates via thermal decomposition, during which the morphology of the hexagonal plate was maintained. These examples clearly demonstrated that the surface-protected conversion method could be regarded as a general method that can be used for the chemical transformation of nanostructures of various compositions in either crystalline or amorphous phases.

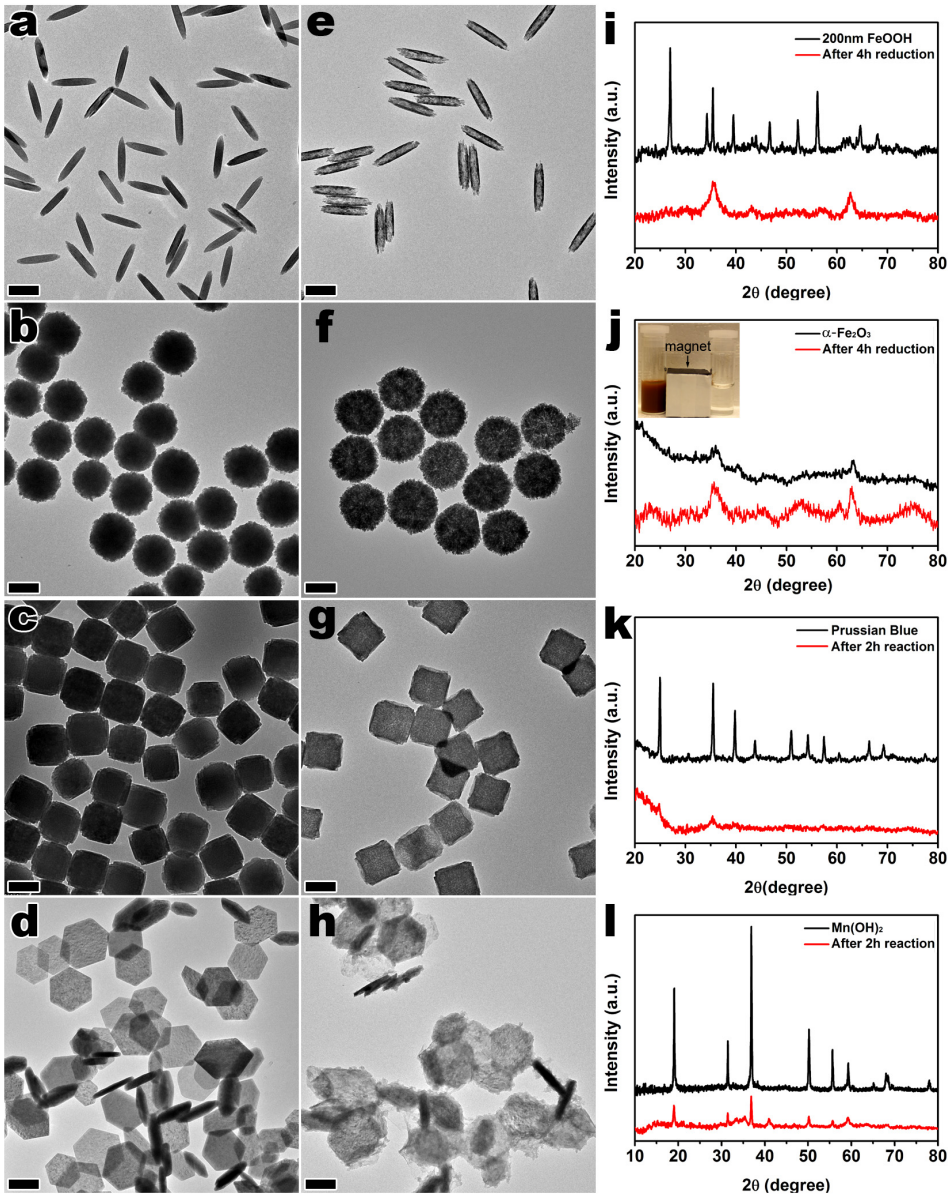

Figure 2.9. (a-h) TEM images of 200 nm β-FeOOH nanorods, α-Fe_2O_3 nanospheres, PB nanocubes and $Mn(OH)_2$ nanoplates before (a-d) and after (e-h) surface-protected conversion. (i-l) The corresponding XRD patterns to the samples at left. The inset in (j) shows the digital photo of magnetic separation of iron oxide before (left) and after (right) reduction. All scale bars are 200 nm.

2.4 Conclusion

In summary, we report here a surface-protected conversion strategy to overcome the morphological deformation such as disintegration and coalescence during the chemical transformation of nanostructures. Using non-magnetic β-FeOOH nanorods as a model, we show that surface protection by strong coordinating capping ligands could enable their successful conversion into magnetic Fe_3O_4 tubular nanorods with well-maintained shapes during their reduction in DEG. This work has its immediate significance in providing a very robust and convenient solution phase process for the synthesis of colloidal magnetite nanorods with well controlled morphology, considering the important applications of such anisotropic magnetic nanostructures and the challenges in their direct production. Conceptually, it also renews our understanding of the protection function of capping ligands not only in nanostructure growth, but also in their chemical reactions, which may involve drastic compositional and morphological changes. More importantly, the principle of surface protection described here can be widely used for conserving morphology of nanostructures of various compositions during their chemical reactions, and therefore greatly promote chemical transformation as a general and powerful tool for nanostructure synthesis.

2.5 References

1. Xu, W.; Wang, M.; Li, Z.; Wang, X.; Wang, Y.; Xing, M.; Yin, Y., Chemical Transformation of Colloidal Nanostructures with Morphological Preservation by Surface-Protection with Capping Ligands. *Nano Lett.* **2017,** *17* (4), 2713-2718.

2. Xu, W.; Lyu, F.; Bai, Y.; Gao, A.; Feng, J.; Cai, Z.; Yin, Y., Porous cobalt oxide nanoplates enriched with oxygen vacancies for oxygen evolution reaction. *Nano Energy* **2018,** *43*, 110-116.

3. Liu, K.; Bai, Y.; Zhang, L.; Yang, Z.; Fan, Q.; Zheng, H.; Yin, Y.; Gao, C., Porous Au–Ag Nanospheres with High-Density and Highly Accessible Hotspots for SERS Analysis. *Nano Lett.* **2016,** *16* (6), 3675-3681.

4. Araki, T.; Serra, F.; Tanaka, H., Defect science and engineering of liquid crystals under geometrical frustration. *Soft Matter* **2013,** *9* (34), 8107-8120.

5. Liu, Y.; Tang, A.; Zhang, Q.; Yin, Y., Seed-Mediated Growth of Anatase TiO2 Nanocrystals with Core–Antenna Structures for Enhanced Photocatalytic Activity. *J. Am. Chem. Soc.* **2015,** *137* (35), 11327-11339.

6. Ithurria, S.; Tessier, M. D.; Mahler, B.; Lobo, R. P. S. M.; Dubertret, B.; Efros, A. L., Colloidal nanoplatelets with two-dimensional electronic structure. *Nat. Mater.* **2011,** *10*, 936.

7. Boles, M. A.; Ling, D.; Hyeon, T.; Talapin, D. V., The surface science of nanocrystals. *Nat. Mater.* **2016,** *15*, 141.

8. Guo, Y.; Xu, K.; Wu, C.; Zhao, J.; Xie, Y., Surface chemical-modification for engineering the intrinsic physical properties of inorganic two-dimensional nanomaterials. *Chem. Soc. Rev.* **2015,** *44* (3), 637-646.

9. Wang, H.; Zhang, J.; Hang, X.; Zhang, X.; Xie, J.; Pan, B.; Xie, Y., Half-Metallicity in Single-Layered Manganese Dioxide Nanosheets by Defect Engineering. *Angew. Chem., Int. Ed.* **2015,** *54* (4), 1195-1199.

10. Wang, J.; Li, K.; Zhong, H.-x.; Xu, D.; Wang, Z.-l.; Jiang, Z.; Wu, Z.-j.; Zhang, X.-b., Synergistic Effect between Metal–Nitrogen–Carbon Sheets and NiO Nanoparticles for Enhanced Electrochemical Water-Oxidation Performance. *Angew. Chem., Int. Ed.* **2015,** *54* (36), 10530-10534.

11. Hu, H.; Guan, B.; Xia, B.; Lou, X. W., Designed Formation of Co3O4/NiCo2O4 Double-Shelled Nanocages with Enhanced Pseudocapacitive and Electrocatalytic Properties. *J. Am. Chem. Soc.* **2015,** *137* (16), 5590-5595.

12. Zhang, Q.; Lima, D. Q.; Lee, I.; Zaera, F.; Chi, M.; Yin, Y., A Highly Active Titanium Dioxide Based Visible-Light Photocatalyst with Nonmetal Doping and Plasmonic Metal Decoration. *Angew. Chem.* **2011,** *123* (31), 7226-7230.

13. Lyu, F.; Bai, Y.; Li, Z.; Xu, W.; Wang, Q.; Mao, J.; Wang, L.; Zhang, X.; Yin, Y., Self-Templated Fabrication of CoO–MoO2 Nanocages for Enhanced Oxygen Evolution. *Adv. Funct. Mater.* **2017,** *27* (34), 1702324-n/a.

14. Ma, M.; Zhang, K.; Li, P.; Jung, M. S.; Jeong, M. J.; Park, J. H., Dual Oxygen and Tungsten Vacancies on a WO3 Photoanode for Enhanced Water Oxidation. *Angew. Chem., Int. Ed.* **2016,** *55* (39), 11819-11823.

15. Wang, Y.; Wang, Y.; Breed, D. R.; Manoharan, V. N.; Feng, L.; Hollingsworth, A. D.; Weck, M.; Pine, D. J., Colloids with valence and specific directional bonding. *Nature* **2012,** *491* (7422), 51-55.

16. Wang, M.; Yin, Y., Magnetically Responsive Nanostructures with Tunable Optical Properties. *J. Am. Chem. Soc.* **2016,** *138* (20), 6315-6323.

17. Tu, F.; Lee, D., Shape-Changing and Amphiphilicity-Reversing Janus Particles with pH-Responsive Surfactant Properties. *J. Am. Chem. Soc.* **2014,** *136* (28), 9999-10006.

18. Walther, A.; Müller, A. H. E., Janus Particles: Synthesis, Self-Assembly, Physical Properties, and Applications. *Chem. Rev.* **2013,** *113* (7), 5194-5261.

19. Zhang, J.; Grzybowski, B. A.; Granick, S., Janus Particle Synthesis, Assembly, and Application. *Langmuir* **2017,** *33* (28), 6964-6977.

20. Youssef, M.; Hueckel, T.; Yi, G.-R.; Sacanna, S., Shape-shifting colloids via stimulated dewetting. *Nat. Commun.* **2016,** *7*, 12216.

21. Wang, H.; Li, B.; Yodh, A. G.; Zhang, Z., Stimuli-Responsive Shape Switching of Polymer Colloids by Temperature-Sensitive Absorption of Solvent. *Angew. Chem., Int. Ed.* **2016,** *55* (34), 9952-9955.

22. Ge, J.; Hu, Y.; Yin, Y., Highly Tunable Superparamagnetic Colloidal Photonic Crystals. *Angew. Chem., Int. Ed.* **2007,** *46* (39), 7428-7431.

23. Mayoral, R.; Requena, J.; Moya, J. S.; López, C.; Cintas, A.; Miguez, H.; Meseguer, F.; Vázquez, L.; Holgado, M.; Blanco, Á., 3D Long-range ordering in ein SiO2 submicrometer-sphere sintered superstructure. *Adv. Mater.* **1997,** *9* (3), 257-260.

24. Xu, X.; Asher, S. A., Synthesis and Utilization of Monodisperse Hollow Polymeric Particles in Photonic Crystals. *J. Am. Chem. Soc.* **2004,** *126* (25), 7940-7945.

25. Míguez, H.; Meseguer, F.; López, C.; Mifsud, A.; Moya, J. S.; Vázquez, L., Evidence of FCC Crystallization of SiO2 Nanospheres. *Langmuir* **1997,** *13* (23), 6009-6011.

26. Sacanna, S.; Rossi, L.; Pine, D. J., Magnetic Click Colloidal Assembly. *J. Am. Chem. Soc.* **2012,** *134* (14), 6112-6115.

27. Park, J.-G.; Forster, J. D.; Dufresne, E. R., High-Yield Synthesis of Monodisperse Dumbbell-Shaped Polymer Nanoparticles. *J. Am. Chem. Soc.* **2010,** *132* (17), 5960-5961.

28. Rahman, M. M.; Montagne, F.; Fessi, H.; Elaissari, A., Anisotropic magnetic microparticles from ferrofluid emulsion. *Soft Matter* **2011,** *7* (4), 1483-1490.

29. Chen, T.; Yang, M.; Wang, X.; Tan, L. H.; Chen, H., Controlled Assembly of Eccentrically Encapsulated Gold Nanoparticles. *J. Am. Chem. Soc.* **2008,** *130* (36), 11858-11859.

30. Chen, T.; Chen, G.; Xing, S.; Wu, T.; Chen, H., Scalable Routes to Janus Au−SiO2 and Ternary Ag−Au−SiO2 Nanoparticles. *Chem. Mat.* **2010,** *22* (13), 3826-3828.

31. Ge, J.; Hu, Y.; Zhang, T.; Yin, Y., Superparamagnetic Composite Colloids with Anisotropic Structures. *J. Am. Chem. Soc.* **2007,** *129* (29), 8974-8975.

32. Hu, Y.; Ge, J.; Zhang, T.; Yin, Y., A Blown Film Process to Disk-Shaped Polymer Ellipsoids. *Adv. Mater.* **2008,** *20* (23), 4599-4602.

33. Zhang, Q.; Li, N.; Goebl, J.; Lu, Z.; Yin, Y., A Systematic Study of the Synthesis of Silver Nanoplates: Is Citrate a "Magic" Reagent? *J. Am. Chem. Soc.* **2011,** *133* (46), 18931-18939.

34. Gao , C.; Lu , Z.; Liu , Y.; Zhang, Q.; Chi, M.; Cheng, Q.; Yin, Y., Highly Stable Silver Nanoplates for Surface Plasmon Resonance Biosensing. *Angew. Chem., Int. Ed.* **2012,** *51* (23), 5629-5633.

35. Wang, G.; Tao, S.; Liu, Y.; Guo, L.; Qin, G.; Ijiro, K.; Maeda, M.; Yin, Y., High-yield halide-free synthesis of biocompatible Au nanoplates. *Chem. Commun.* **2016,** *52* (2), 398-401.

36. Jana, N. R.; Gearheart, L.; Murphy, C. J., Wet Chemical Synthesis of High Aspect Ratio Cylindrical Gold Nanorods. *J. Phys. Chem. B* **2001,** *105* (19), 4065-4067.

37. Hu, J.; Odom, T. W.; Lieber, C. M., Chemistry and Physics in One Dimension: Synthesis and Properties of Nanowires and Nanotubes. *Acc. Chem. Res.* **1999,** *32* (5), 435-445.

38. Gao, C.; Zhang, Q.; Lu, Z.; Yin, Y., Templated Synthesis of Metal Nanorods in Silica Nanotubes. *J. Am. Chem. Soc.* **2011,** *133* (49), 19706-19709.

39. Wang, C.; Zhang, Z.; Yang, G.; Chen, Q.; Yin, Y.; Jin, M., Creation of Controllable High-Density Defects in Silver Nanowires for Enhanced Catalytic Property. *Nano Lett.* **2016,** *16* (9), 5669-5674.

40. Liu, B.; Aydil, E. S., Growth of Oriented Single-Crystalline Rutile TiO2 Nanorods on Transparent Conducting Substrates for Dye-Sensitized Solar Cells. *J. Am. Chem. Soc.* **2009,** *131* (11), 3985-3990.

41. Sun, Y.; Xia, Y., Shape-Controlled Synthesis of Gold and Silver Nanoparticles. *Science* **2002,** *298* (5601), 2176-2179.

42. Sherry, L. J.; Chang, S.-H.; Schatz, G. C.; Van Duyne, R. P.; Wiley, B. J.; Xia, Y., Localized Surface Plasmon Resonance Spectroscopy of Single Silver Nanocubes. *Nano Lett.* **2005,** *5* (10), 2034-2038.

43. Skrabalak, S. E.; Chen, J.; Sun, Y.; Lu, X.; Au, L.; Cobley, C. M.; Xia, Y., Gold Nanocages: Synthesis, Properties, and Applications. *Acc. Chem. Res.* **2008,** *41* (12), 1587-1595.

44. Gou, L.; Murphy, C. J., Solution-Phase Synthesis of Cu2O Nanocubes. *Nano Lett.* **2003,** *3* (2), 231-234.

45. Fan, F.-R.; Liu, D.-Y.; Wu, Y.-F.; Duan, S.; Xie, Z.-X.; Jiang, Z.-Y.; Tian, Z.-Q., Epitaxial Growth of Heterogeneous Metal Nanocrystals: From Gold Nano-octahedra to Palladium and Silver Nanocubes. *J. Am. Chem. Soc.* **2008,** *130* (22), 6949-6951.

46. Niu, W.; Zheng, S.; Wang, D.; Liu, X.; Li, H.; Han, S.; Chen, J.; Tang, Z.; Xu, G., Selective Synthesis of Single-Crystalline Rhombic Dodecahedral, Octahedral, and Cubic Gold Nanocrystals. *J. Am. Chem. Soc.* **2009,** *131* (2), 697-703.

47. Cao, H.; Qian, X.; Wang, C.; Ma, X.; Yin, J.; Zhu, Z., High Symmetric 18-Facet Polyhedron Nanocrystals of Cu7S4 with a Hollow Nanocage. *J. Am. Chem. Soc.* **2005,** *127* (46), 16024-16025.

48. Brittman, S.; Gao, H.; Garnett, E. C.; Yang, P., Absorption of Light in a Single-Nanowire Silicon Solar Cell Decorated with an Octahedral Silver Nanocrystal. *Nano Lett.* **2011,** *11* (12), 5189-5195.

49. Kuo, C.-H.; Huang, M. H., Facile Synthesis of Cu2O Nanocrystals with Systematic Shape Evolution from Cubic to Octahedral Structures. *J. Phys. Chem. C* **2008,** *112* (47), 18355-18360.

50. Henzie, J.; Grünwald, M.; Widmer-Cooper, A.; Geissler, P. L.; Yang, P., Self-assembly of uniform polyhedral silver nanocrystals into densest packings and exotic superlattices. *Nat. Mater.* **2012,** *11* (2), 131-137.

51. Yang, P., Surface chemistry: Crystal cuts on the nanoscale. *Nature* **2012,** *482* (7383), 41-42.

52. Chen, M.; Zhou, S.; You, B.; Wu, L., A Novel Preparation Method of Raspberry-like PMMA/SiO2 Hybrid Microspheres. *Macromolecules* **2005,** *38* (15), 6411-6417.

53. Mahmoud; Tabor, C. E.; El-Sayed, M. A.; Ding, Y.; Wang, Z. L., A New Catalytically Active Colloidal Platinum Nanocatalyst: The Multiarmed Nanostar Single Crystal. *J. Am. Chem. Soc.* **2008,** *130* (14), 4590-4591.

54. Hao, F.; Nehl, C. L.; Hafner, J. H.; Nordlander, P., Plasmon Resonances of a Gold Nanostar. *Nano Lett.* **2007,** *7* (3), 729-732.

55. Ge, J.; Yin, Y., Magnetically Tunable Colloidal Photonic Structures in Alkanol Solutions. *Adv. Mater.* **2008,** *20* (18), 3485-3491.

56. Ge, J.; Goebl, J.; He, L.; Lu, Z.; Yin, Y., Rewritable Photonic Paper with Hygroscopic Salt Solution as Ink. *Adv. Mater.* **2009,** *21* (42), 4259-4264.

57. Ge, J.; Lee, H.; He, L.; Kim, J.; Lu, Z.; Kim, H.; Goebl, J.; Kwon, S.; Yin, Y., Magnetochromatic Microspheres: Rotating Photonic Crystals. *J. Am. Chem. Soc.* **2009,** *131* (43), 15687-15694.

58. Zorba, S.; Maxwell, R. T.; Farah, C.; He, L.; Ye, M.; Yin, Y., Superparamagnetic Magnetite Nanoparticle Superstructures for Optical Modulation/Chopping. *J. Phys. Chem. C* **2010,** *114* (41), 17868-17873.

59. Kim, J.; Song, Y.; He, L.; Kim, H.; Lee, H.; Park, W.; Yin, Y.; Kwon, S., Real-Time Optofluidic Synthesis of Magnetochromatic Microspheres for Reversible Structural Color Patterning. *Small* **2011,** *7* (9), 1163-1168.

60. Wang, M.; He, L.; Hu, Y.; Yin, Y., Magnetically rewritable photonic ink based on superparamagnetic nanochains. *J. Mater. Chem. C* **2013,** *1* (38), 6151-6156.

61. Kim, H.; Ge, J.; Kim, J.; Choi, S.-e.; Lee, H.; Lee, H.; Park, W.; Yin, Y.; Kwon, S., Structural colour printing using a magnetically tunable and lithographically fixable photonic crystal. *Nat Photon* **2009,** *3* (9), 534-540.

62. Xuan, R.; Wu, Q.; Yin, Y.; Ge, J., Magnetically assembled photonic crystal film for humidity sensing. *J. Mater. Chem.* **2011,** *21* (11), 3672-3676.

63. He, L.; Hu, Y.; Wang, M.; Yin, Y., Determination of Solvation Layer Thickness by a Magnetophotonic Approach. *ACS Nano* **2012,** *6* (5), 4196-4202.

64. Han, X.; Liu, Y.; Yin, Y., Colorimetric Stress Memory Sensor Based on Disassembly of Gold Nanoparticle Chains. *Nano Lett.* **2014,** *14* (5), 2466-2470.

65. Cui, Y.; Lieber, C. M., Functional Nanoscale Electronic Devices Assembled Using Silicon Nanowire Building Blocks. *Science* **2001,** *291* (5505), 851-853.

66. Ge, J.; Huynh, T.; Hu, Y.; Yin, Y., Hierarchical Magnetite/Silica Nanoassemblies as Magnetically Recoverable Catalyst–Supports. *Nano Lett.* **2008,** *8* (3), 931-934.

67. Zhang, Q.; Joo, J.-B.; Lu, Z.; Dahl, M.; Oliveira, D. Q. L.; Ye, M.; Yin, Y., Self-assembly and photocatalysis of mesoporous TiO2 nanocrystal clusters. *Nano Res.* **2011,** *4* (1), 103-114.

68. Ferrari, M., Nanogeometry: Beyond drug delivery. *Nat Nano* **2008,** *3* (3), 131-132.

69. Yin, Y.; Alivisatos, A. P., Colloidal nanocrystal synthesis and the organic–inorganic interface. *Nature* **2004,** *437*, 664.

70. Peng, X.; Manna, L.; Yang, W.; Wickham, J.; Scher, E.; Kadavanich, A.; Alivisatos, A. P., Shape control of CdSe nanocrystals. *Nature* **2000,** *404*, 59.

71. Liu, Y.; Han, X.; He, L.; Yin, Y., Thermoresponsive Assembly of Charged Gold Nanoparticles and Their Reversible Tuning of Plasmon Coupling. *Angew. Chem., Int. Ed.* **2012,** *51* (26), 6373-6377.

72. Han, X.; Goebl, J.; Lu, Z.; Yin, Y., Role of Salt in the Spontaneous Assembly of Charged Gold Nanoparticles in Ethanol. *Langmuir* **2011,** *27* (9), 5282-5289.

73. Tao, L.; Lin, C.-Y.; Dou, S.; Feng, S.; Chen, D.; Liu, D.; Huo, J.; Xia, Z.; Wang, S., Creating coordinatively unsaturated metal sites in metal-organic-frameworks as efficient electrocatalysts for the oxygen evolution reaction: Insights into the active centers. *Nano Energy* **2017,** *41* (Supplement C), 417-425.

74. Xie, J.; Zhang, J.; Li, S.; Grote, F.; Zhang, X.; Zhang, H.; Wang, R.; Lei, Y.; Pan, B.; Xie, Y., Controllable Disorder Engineering in Oxygen-Incorporated MoS2 Ultrathin Nanosheets for Efficient Hydrogen Evolution. *J. Am. Chem. Soc.* **2013,** *135* (47), 17881-17888.

75. Zhuang, L.; Ge, L.; Yang, Y.; Li, M.; Jia, Y.; Yao, X.; Zhu, Z., Ultrathin Iron-Cobalt Oxide Nanosheets with Abundant Oxygen Vacancies for the Oxygen Evolution Reaction. *Adv. Mater.* **2017,** *29* (17), 1606793.

76. Wang, W.; Ye, Y.; Feng, J.; Chi, M.; Guo, J.; Yin, Y., Enhanced Photoreversible Color Switching of Redox Dyes Catalyzed by Barium-Doped TiO2 Nanocrystals. *Angew. Chem., Int. Ed.* **2015,** *54* (4), 1321-1326.

77. Han, D.; Jiang, B.; Feng, J.; Yin, Y.; Wang, W., Photocatalytic Self-Doped SnO2−x Nanocrystals Drive Visible-Light-Responsive Color Switching. *Angew. Chem., Int. Ed.* **2017,** *56* (27), 7792-7796.

78. Sun, Y.; Liu, Q.; Gao, S.; Cheng, H.; Lei, F.; Sun, Z.; Jiang, Y.; Su, H.; Wei, S.; Xie, Y., Pits confined in ultrathin cerium(IV) oxide for studying catalytic centers in carbon monoxide oxidation. *Nat. Commun.* **2013,** *4*, 2899.

79. Kim, J.; Yin, X.; Tsao, K.-C.; Fang, S.; Yang, H., Ca2Mn2O5 as Oxygen-Deficient Perovskite Electrocatalyst for Oxygen Evolution Reaction. *J. Am. Chem. Soc.* **2014,** *136* (42), 14646-14649.

80. Petrie, J. R.; Jeen, H.; Barron, S. C.; Meyer, T. L.; Lee, H. N., Enhancing Perovskite Electrocatalysis through Strain Tuning of the Oxygen Deficiency. *J. Am. Chem. Soc.* **2016,** *138* (23), 7252-7255.

81. Xu, L.; Jiang, Q.; Xiao, Z.; Li, X.; Huo, J.; Wang, S.; Dai, L., Plasma-Engraved Co3O4 Nanosheets with Oxygen Vacancies and High Surface Area for the Oxygen Evolution Reaction. *Angew. Chem., Int. Ed.* **2016,** *55* (17), 5277-5281.

82. Bao, J.; Zhang, X.; Fan, B.; Zhang, J.; Zhou, M.; Yang, W.; Hu, X.; Wang, H.; Pan, B.; Xie, Y., Ultrathin Spinel-Structured Nanosheets Rich in Oxygen Deficiencies for Enhanced Electrocatalytic Water Oxidation. *Angew. Chem., Int. Ed.* **2015,** *54* (25), 7399-7404.

83. Wang, Q.; Shang, L.; Shi, R.; Zhang, X.; Waterhouse, G. I. N.; Wu, L.-Z.; Tung, C.-H.; Zhang, T., 3D carbon nanoframe scaffold-immobilized Ni3FeN nanoparticle electrocatalysts for rechargeable zinc-air batteries' cathodes. *Nano Energy* **2017,** *40* (Supplement C), 382-389.

84. Zhao, Y.; Jia, X.; Chen, G.; Shang, L.; Waterhouse, G. I. N.; Wu, L.-Z.; Tung, C.-H.; O'Hare, D.; Zhang, T., Ultrafine NiO Nanosheets Stabilized by TiO2 from Monolayer NiTi-LDH Precursors: An Active Water Oxidation Electrocatalyst. *J. Am. Chem. Soc.* **2016,** *138* (20), 6517-6524.

85. Zhang; Glotzer, S. C., Self-Assembly of Patchy Particles. *Nano Lett.* **2004,** *4* (8), 1407-1413.

86. Jiang, S.; Chen, Q.; Tripathy, M.; Luijten, E.; Schweizer, K. S.; Granick, S., Janus Particle Synthesis and Assembly. *Adv. Mater.* **2010,** *22* (10), 1060-1071.

87. Perro, A.; Duguet, E.; Lambert, O.; Taveau, J.-C.; Bourgeat-Lami, E.; Ravaine, S., A Chemical Synthetic Route towards "Colloidal Molecules". *Angew. Chem., Int. Ed.* **2009,** *48* (2), 361-365.

88. Velev, O. D., Self-Assembly of Unusual Nanoparticle Crystals. *Science* **2006,** *312* (5772), 376-377.

89. Zheng, X.; Liu, M.; He, M.; Pine, D. J.; Weck, M., Shape-Shifting Patchy Particles. *Angew. Chem., Int. Ed.* **2017,** *56* (20), 5507-5511.

90. Bai, C.; Liu, M., Implantation of nanomaterials and nanostructures on surface and their applications. *Nano Today* **2012,** *7* (4), 258-281.

91. Wang, X.; Feng, J.; Bai, Y.; Zhang, Q.; Yin, Y., Synthesis, Properties, and Applications of Hollow Micro-/Nanostructures. *Chem. Rev.* **2016,** *116* (18), 10983-11060.

92. Zhang, W.; Zhao, Y.; Malgras, V.; Ji, Q.; Jiang, D.; Qi, R.; Ariga, K.; Yamauchi, Y.; Liu, J.; Jiang, J.-S.; Hu, M., Synthesis of Monocrystalline Nanoframes of Prussian Blue Analogues by Controlled Preferential Etching. *Angew. Chem., Int. Ed.* **2016,** *55* (29), 8228-8234.

93. Han, L.; Yu, X.-Y.; Lou, X. W., Formation of Prussian-Blue-Analog Nanocages via a Direct Etching Method and their Conversion into Ni–Co-Mixed Oxide for Enhanced Oxygen Evolution. *Adv. Mater.* **2016,** *28* (23), 4601-4605.

94. Avci, C.; Ariñez-Soriano, J.; Carné-Sánchez, A.; Guillerm, V.; Carbonell, C.; Imaz, I.; Maspoch, D., Post-Synthetic Anisotropic Wet-Chemical Etching of Colloidal Sodalite ZIF Crystals. *Angew. Chem., Int. Ed.* **2015,** *54* (48), 14417-14421.

95. Kandambeth, S.; Venkatesh, V.; Shinde, D. B.; Kumari, S.; Halder, A.; Verma, S.; Banerjee, R., Self-templated chemically stable hollow spherical covalent organic framework. *Nat. Commun.* **2015,** *6*, 6786.

96. Oh, M. H.; Yu, T.; Yu, S.-H.; Lim, B.; Ko, K.-T.; Willinger, M.-G.; Seo, D.-H.; Kim, B. H.; Cho, M. G.; Park, J.-H.; Kang, K.; Sung, Y.-E.; Pinna, N.; Hyeon, T., Galvanic Replacement Reactions in Metal Oxide Nanocrystals. *Science* **2013,** *340* (6135), 964-968.

97. Yin, Y.; Rioux, R. M.; Erdonmez, C. K.; Hughes, S.; Somorjai, G. A.; Alivisatos, A. P., Formation of Hollow Nanocrystals Through the Nanoscale Kirkendall Effect. *Science* **2004,** *304* (5671), 711-714.

98. Son, D. H.; Hughes, S. M.; Yin, Y.; Paul Alivisatos, A., Cation Exchange Reactions in Ionic Nanocrystals. *Science* **2004,** *306* (5698), 1009-1012.

99. Jeong, U.; Camargo, P. H. C.; Lee, Y. H.; Xia, Y., Chemical transformation: a powerful route to metal chalcogenide nanowires. *J. Mater. Chem.* **2006,** *16* (40), 3893-3897.

100. Ibáñez, M.; Cabot, A., All Change for Nanocrystals. *Science* **2013,** *340* (6135), 935-936.

101. Sadtler, B.; Demchenko, D. O.; Zheng, H.; Hughes, S. M.; Merkle, M. G.; Dahmen, U.; Wang, L. W.; Alivisatos, A. P., Selective Facet Reactivity during Cation Exchange in Cadmium Sulfide Nanorods. *J. Am. Chem. Soc.* **2009,** *131* (14), 5285-5293.

102. Xia, Y.; Li, W.; Cobley, C. M.; Chen, J.; Xia, X.; Zhang, Q.; Yang, M.; Cho, E. C.; Brown, P. K., Gold Nanocages: From Synthesis to Theranostic Applications. *Acc. Chem. Res.* **2011,** *44* (10), 914-924.

103. González, E.; Arbiol, J.; Puntes, V. F., Carving at the Nanoscale: Sequential Galvanic Exchange and Kirkendall Growth at Room Temperature. *Science* **2011,** *334* (6061), 1377-1380.

104. Jones, M. R.; Osberg, K. D.; Macfarlane, R. J.; Langille, M. R.; Mirkin, C. A., Templated Techniques for the Synthesis and Assembly of Plasmonic Nanostructures. *Chem. Rev.* **2011,** *111* (6), 3736-3827.

105. Yin, Y.; Erdonmez, C.; Aloni, S.; Alivisatos, A. P., Faceting of Nanocrystals during Chemical Transformation: From Solid Silver Spheres to Hollow Gold Octahedra. *J. Am. Chem. Soc.* **2006,** *128* (39), 12671-12673.

106. Chou, N. H.; Schaak, R. E., Shape-controlled conversion of beta-Sn nanocrystals into intermetallic M-Sn (M = Fe, Co, Ni, Pd) nanocrystals. *J. Am. Chem. Soc.* **2007,** *129* (23), 7339-7345.

107. Saruyama, M.; So, Y. G.; Kimoto, K.; Taguchi, S.; Kanemitsu, Y.; Teranishi, T., Spontaneous Formation of Wurzite-CdS/Zinc Blende-CdTe Heterodimers through a Partial Anion Exchange Reaction. *J. Am. Chem. Soc.* **2011,** *133* (44), 17598-17601.

108. Moon, G. D.; Ko, S.; Xia, Y.; Jeong, U., Chemical Transformations in Ultrathin Chalcogenide Nanowires. *ACS Nano* **2010,** *4* (4), 2307-2319.

109. Wang, M.; He, L.; Xu, W.; Wang, X.; Yin, Y., Magnetic Assembly and Field-Tuning of Ellipsoidal-Nanoparticle-Based Colloidal Photonic Crystals. *Angew. Chem., Int. Ed.* **2015,** *54* (24), 7077-7081.

110. Hill, L. J.; Richey, N. E.; Sung, Y.; Dirlam, P. T.; Griebel, J. J.; Lavoie-Higgins, E.; Shim, I. B.; Pinna, N.; Willinger, M. G.; Vogel, W.; Benkoski, J. J.; Char, K.; Pyun, J., Colloidal Polymers from Dipolar Assembly of Cobalt-Tipped CdSe@CdS Nanorods. *ACS Nano* **2014,** *8* (4), 3272-3284.

111. Jun, Y. W.; Lee, J. H.; Cheon, J., Chemical design of nanoparticle probes for high-performance magnetic resonance imaging. *Angew. Chem., Int. Ed.* **2008,** *47* (28), 5122-5135.

112. Na, H. B.; Song, I. C.; Hyeon, T., Inorganic Nanoparticles for MRI Contrast Agents. *Adv. Mater.* **2009,** *21* (21), 2133-2148.

113. Lee, H.; Lee, E.; Kim, D. K.; Jang, N. K.; Jeong, Y. Y.; Jon, S., Antibiofouling polymer-coated superparamagnetic iron oxide nanoparticles as potential magnetic resonance contrast agents for in vivo cancer imaging. *J. Am. Chem. Soc.* **2006,** *128* (22), 7383-7389.

114. Lee, J. E.; Lee, N.; Kim, H.; Kim, J.; Choi, S. H.; Kim, J. H.; Kim, T.; Song, I. C.; Park, S. P.; Moon, W. K.; Hyeon, T., Uniform Mesoporous Dye-Doped Silica Nanoparticles Decorated with Multiple Magnetite Nanocrystals for Simultaneous Enhanced Magnetic Resonance Imaging, Fluorescence Imaging, and Drug Delivery. *J. Am. Chem. Soc.* **2010,** *132* (2), 552-557.

115. Pan, J.; Zhang, J. C.; Wang, L. L.; Wan, D., Synthesis of iron oxide coated fluoridated HAp/Ln(3+) (Ln = Eu or Tb) nanocomposites for biological applications. *Chem. Commun.* **2014,** *50* (90), 14010-14012.

116. Liang, H.; Zhang, X. B.; Lv, Y. F.; Gong, L.; Wang, R. W.; Zhu, X. Y.; Yang, R. H.; Tan, W. H., Functional DNA-Containing Nanomaterials: Cellular Applications in Biosensing, Imaging, and Targeted Therapy. *Acc. Chem. Res.* **2014,** *47* (6), 1891-1901.

117. Ma, C.; Li, C. Y.; He, N. Y.; Wang, F.; Ma, N. N.; Zhang, L. M.; Lu, Z. X.; Ali, Z.; Xi, Z. J.; Li, X. L.; Liang, G. F.; Liu, H. N.; Deng, Y.; Xu, L. J.; Wang, Z. F., Preparation and Characterization of Monodisperse Core-Shell Fe3O4 @ SiO2 Microspheres and Its Application for Magnetic Separation of Nucleic Acids from E. coli BL21. *J. Biomed. Nanotechnol.* **2012,** *8* (6), 1000-1005.

118. Piao, Y.; Kim, J.; Na, H. B.; Kim, D.; Baek, J. S.; Ko, M. K.; Lee, J. H.; Shokouhimehr, M.; Hyeon, T., Wrap-bake-peel process for nanostructural transformation from beta-FeOOH nanorods to biocompatible iron oxide nanocapsules. *Nat. Mater.* **2008,** *7* (3), 242-247.

119. Zhenmeng, P.; Mingzai, W.; Ying, X.; Jun, W.; Qianwang, C., Synthesis of Magnetite Nanorods through Reduction of β-FeOOH. *Chemistry Letters* **2005,** *34* (5), 636-637.

120. Wang, M.; Gao, C.; He, L.; Lu, Q.; Zhang, J.; Tang, C.; Zorba, S.; Yin, Y., Magnetic Tuning of Plasmonic Excitation of Gold Nanorods. *J. Am. Chem. Soc.* **2013,** *135* (41), 15302-15305.

121. Maeda, Y.; Hachisu, S., Schiller layers in β-ferric oxyhydroxide sol as an order—disorder phase separating system. *Colloids and Surfaces* **1983,** *6* (1), 1-16.

122. Hu, M.; Furukawa, S.; Ohtani, R.; Sukegawa, H.; Nemoto, Y.; Reboul, J.; Kitagawa, S.; Yamauchi, Y., Synthesis of Prussian Blue Nanoparticles with a Hollow Interior by Controlled Chemical Etching. *Angew. Chem., Int. Ed.* **2012,** *51* (4), 984-988.

123. Zou, B.; Liu, Y.; Wang, Y., Facile synthesis of highly water-dispersible and monodispersed Fe3O4 hollow microspheres and their application in water treatment. *RSC Advances* **2013,** *3* (45), 23327-23334.

124. Zhang, X.; Xing, Z.; Wang, L.; Zhu, Y.; Li, Q.; Liang, J.; Yu, Y.; Huang, T.; Tang, K.; Qian, Y.; Shen, X., Synthesis of MnO@C core-shell nanoplates with controllable shell thickness and their electrochemical performance for lithium-ion batteries. *J. Mater. Chem.* **2012,** *22* (34), 17864-17869.

125. Wang, M.; He, L.; Zorba, S.; Yin, Y., Magnetically Actuated Liquid Crystals. *Nano Lett.* **2014,** *14* (7), 3966-3971.

126. Xiong, Y.; Ye, J.; Gu, X.; Chen, Q.-w., Synthesis and Assembly of Magnetite Nanocubes into Flux-Closure Rings. *J. Phys. Chem. C* **2007,** *111* (19), 6998-7003.

127. Nasrazadani, S.; Raman, A., The application of infrared spectroscopy to the study of rust systems—II. Study of cation deficiency in magnetite (Fe3O4) produced during its transformation to maghemite (γ-Fe2O3) and hematite (α-Fe2O3). *Corrosion Science* **1993,** *34* (8), 1355-1365.

128. Ge, J.; Hu, Y.; Biasini, M.; Beyermann, W. P.; Yin, Y., Superparamagnetic Magnetite Colloidal Nanocrystal Clusters. *Angew. Chem., Int. Ed.* **2007,** *46* (23), 4342-4345.

129. Fievet, F.; Lagier, J. P.; Blin, B.; Beaudoin, B.; Figlarz, M., Homogeneous and heterogeneous nucleations in the polyol process for the preparation of micron and submicron size metal particles. *Solid State Ionics* **1989,** *32*, 198-205.

130. Katsounaros, I.; Cherevko, S.; Zeradjanin, A. R.; Mayrhofer, K. J. J., Oxygen Electrochemistry as a Cornerstone for Sustainable Energy Conversion. *Angew. Chem., Int. Ed.* **2014,** *53* (1), 102-121.

131. Liu, Y.; Cheng, H.; Lyu, M.; Fan, S.; Liu, Q.; Zhang, W.; Zhi, Y.; Wang, C.; Xiao, C.; Wei, S.; Ye, B.; Xie, Y., Low Overpotential in Vacancy-Rich Ultrathin CoSe2 Nanosheets for Water Oxidation. *J. Am. Chem. Soc.* **2014,** *136* (44), 15670-15675.

132. Tung, C.-W.; Hsu, Y.-Y.; Shen, Y.-P.; Zheng, Y.; Chan, T.-S.; Sheu, H.-S.; Cheng, Y.-C.; Chen, H. M., Reversible adapting layer produces robust single-crystal electrocatalyst for oxygen evolution. *Nat Commun* **2015,** *6*.

133. Wang, J.; Tang, H.; Wang, H.; Yu, R.; Wang, D., Multi-shelled hollow micro-/nanostructures: promising platforms for lithium-ion batteries. *Mater. Chem. Front.* **2017,** *1* (3), 414-430.

134. Long, X.; Li, J.; Xiao, S.; Yan, K.; Wang, Z.; Chen, H.; Yang, S., A Strongly Coupled Graphene and FeNi Double Hydroxide Hybrid as an Excellent Electrocatalyst for the Oxygen Evolution Reaction. *Angew. Chem., Int. Ed.* **2014,** *53* (29), 7584-7588.

135. Jiang, N.; You, B.; Sheng, M.; Sun, Y., Electrodeposited Cobalt-Phosphorous-Derived Films as Competent Bifunctional Catalysts for Overall Water Splitting. *Angew. Chem., Int. Ed.* **2015,** *54* (21), 6251-6254.

136. Zhu, Y.; Zhou, W.; Chen, Z.-G.; Chen, Y.; Su, C.; Tadé, M. O.; Shao, Z., SrNb0.1Co0.7Fe0.2O3−δ Perovskite as a Next-Generation Electrocatalyst for Oxygen Evolution in Alkaline Solution. *Angew. Chem., Int. Ed.* **2015,** *54* (13), 3897-3901.

137. Lim, B.; Jiang, M.; Camargo, P. H. C.; Cho, E. C.; Tao, J.; Lu, X.; Zhu, Y.; Xia, Y., Pd-Pt Bimetallic Nanodendrites with High Activity for Oxygen Reduction. *Science* **2009,** *324* (5932), 1302-1305.

138. Danilovic, N.; Subbaraman, R.; Chang, K. C.; Chang, S. H.; Kang, Y.; Snyder, J.; Paulikas, A. P.; Strmcnik, D.; Kim, Y. T.; Myers, D.; Stamenkovic, V. R.; Markovic, N. M., Using Surface Segregation To Design Stable Ru-Ir Oxides for the Oxygen Evolution Reaction in Acidic Environments. *Angew. Chem., Int. Ed.* **2014,** *53* (51), 14016-14021.

139. Exner, K. S.; Anton, J.; Jacob, T.; Over, H., Controlling Selectivity in the Chlorine Evolution Reaction over RuO2-Based Catalysts. *Angew. Chem., Int. Ed.* **2014,** *53* (41), 11032-11035.

140. Qi, J.; Lai, X.; Wang, J.; Tang, H.; Ren, H.; Yang, Y.; Jin, Q.; Zhang, L.; Yu, R.; Ma, G.; Su, Z.; Zhao, H.; Wang, D., Multi-shelled hollow micro-/nanostructures. *Chem. Soc. Rev.* **2015,** *44* (19), 6749-6773.

141. Guo, S.; Yang, Y.; Liu, N.; Qiao, S.; Huang, H.; Liu, Y.; Kang, Z., One-step synthesis of cobalt, nitrogen-codoped carbon as nonprecious bifunctional electrocatalyst for oxygen reduction and evolution reactions. *Sci Bull* **2016,** *61* (1), 68-77.

142. Chen, S.; Duan, J.; Jaroniec, M.; Qiao, S. Z., Three-Dimensional N-Doped Graphene Hydrogel/NiCo Double Hydroxide Electrocatalysts for Highly Efficient Oxygen Evolution. *Angew. Chem., Int. Ed.* **2013,** *52* (51), 13567-13570.

143. Tang, C.; Cheng, N.; Pu, Z.; Xing, W.; Sun, X., NiSe Nanowire Film Supported on Nickel Foam: An Efficient and Stable 3D Bifunctional Electrode for Full Water Splitting. *Angew. Chem., Int. Ed.* **2015,** *54* (32), 9351-9355.

144. Liu, G.; Li, P.; Zhao, G.; Wang, X.; Kong, J.; Liu, H.; Zhang, H.; Chang, K.; Meng, X.; Kako, T.; Ye, J., Promoting Active Species Generation by Plasmon-Induced Hot-Electron Excitation for Efficient Electrocatalytic Oxygen Evolution. *J. Am. Chem. Soc.* **2016,** *138* (29), 9128-9136.

145. Lyu, F.; Bai, Y.; Wang, Q.; Wang, L.; Zhang, X.; Yin, Y., Phase-controllable synthesis of cobalt hydroxide for electrocatalytic oxygen evolution. *Dalton Trans.* **2017**.

146. Wang, J.; Yang, N.; Tang, H.; Dong, Z.; Jin, Q.; Yang, M.; Kisailus, D.; Zhao, H.; Tang, Z.; Wang, D., Accurate Control of Multishelled Co3O4 Hollow Microspheres as High-Performance Anode Materials in Lithium-Ion Batteries. *Angew. Chem., Int. Ed.* **2013,** *52* (25), 6417-6420.

147. Wang, Y.; Zhang, Y.; Liu, Z.; Xie, C.; Feng, S.; Liu, D.; Shao, M.; Wang, S., Layered Double Hydroxide Nanosheets with Multiple Vacancies Obtained by Dry

Exfoliation as Highly Efficient Oxygen Evolution Electrocatalysts. *Angew. Chem., Int. Ed.* **2017,** *56* (21), 5867-5871.

148. Gong, M.; Li, Y.; Wang, H.; Liang, Y.; Wu, J. Z.; Zhou, J.; Wang, J.; Regier, T.; Wei, F.; Dai, H., An Advanced Ni–Fe Layered Double Hydroxide Electrocatalyst for Water Oxidation. *J. Am. Chem. Soc.* **2013,** *135* (23), 8452-8455.

149. Yan, D.; Li, Y.; Huo, J.; Chen, R.; Dai, L.; Wang, S., Defect Chemistry of Nonprecious-Metal Electrocatalysts for Oxygen Reactions. *Adv. Mater.*, 1606459-n/a.

150. Chhowalla, M.; Shin, H. S.; Eda, G.; Li, L.-J.; Loh, K. P.; Zhang, H., The chemistry of two-dimensional layered transition metal dichalcogenide nanosheets. *Nat Chem* **2013,** *5* (4), 263-275.

151. Huang, X.; Tan, C.; Yin, Z.; Zhang, H., 25th Anniversary Article: Hybrid Nanostructures Based on Two-Dimensional Nanomaterials. *Adv. Mater.* **2014,** *26* (14), 2185-2204.

152. Fan, H.; Huang, X.; Shang, L.; Cao, Y.; Zhao, Y.; Wu, L.-Z.; Tung, C.-H.; Yin, Y.; Zhang, T., Controllable Synthesis of Ultrathin Transition-Metal Hydroxide Nanosheets and their Extended Composite Nanostructures for Enhanced Catalytic Activity in the Heck Reaction. *Angew. Chem., Int. Ed.* **2016,** *55* (6), 2167-2170.

153. Xiao, X.; Song, H.; Lin, S.; Zhou, Y.; Zhan, X.; Hu, Z.; Zhang, Q.; Sun, J.; Yang, B.; Li, T.; Jiao, L.; Zhou, J.; Tang, J.; Gogotsi, Y., Scalable salt-templated synthesis of two-dimensional transition metal oxides. *Nat Commun* **2016,** *7*, 11296.

154. Tang, H.; Hessel, C. M.; Wang, J.; Yang, N.; Yu, R.; Zhao, H.; Wang, D., Two-dimensional carbon leading to new photoconversion processes. *Chem. Soc. Rev.* **2014,** *43* (13), 4281-4299.

155. Wang, Q.; Shang, L.; Shi, R.; Zhang, X.; Zhao, Y.; Waterhouse, G. I. N.; Wu, L.-Z.; Tung, C.-H.; Zhang, T., NiFe Layered Double Hydroxide Nanoparticles on Co,N-Codoped Carbon Nanoframes as Efficient Bifunctional Catalysts for Rechargeable Zinc–Air Batteries. *Adv. Energy Mater.*, 1700467-n/a.

156. Cheng, F.; Zhang, T.; Zhang, Y.; Du, J.; Han, X.; Chen, J., Enhancing Electrocatalytic Oxygen Reduction on MnO2 with Vacancies. *Angew. Chem., Int. Ed.* **2013,** *52* (9), 2474-2477.

157. Ling, T.; Yan, D.-Y.; Jiao, Y.; Wang, H.; Zheng, Y.; Zheng, X.; Mao, J.; Du, X.-W.; Hu, Z.; Jaroniec, M.; Qiao, S.-Z., Engineering surface atomic structure of single-crystal cobalt (II) oxide nanorods for superior electrocatalysis. *Nat. Commun.* **2016,** *7*, 12876.

158. Liu, Z.; Zhao, Z.; Wang, Y.; Dou, S.; Yan, D.; Liu, D.; Xia, Z.; Wang, S., In Situ Exfoliated, Edge-Rich, Oxygen-Functionalized Graphene from Carbon Fibers for Oxygen Electrocatalysis. *Adv. Mater.* **2017,** *29* (18), 1606207-n/a.

159. Rodriguez, J. A.; Hanson, J. C.; Frenkel, A. I.; Kim, J. Y.; Pérez, M., Experimental and Theoretical Studies on the Reaction of H2 with NiO: Role of O Vacancies and Mechanism for Oxide Reduction. *J. Am. Chem. Soc.* **2002,** *124* (2), 346-354.

160. Liu, Z.; Ma, R.; Osada, M.; Takada, K.; Sasaki, T., Selective and Controlled Synthesis of α- and β-Cobalt Hydroxides in Highly Developed Hexagonal Platelets. *J. Am. Chem. Soc.* **2005,** *127* (40), 13869-13874.

161. Jia, C.-J.; Schwickardi, M.; Weidenthaler, C.; Schmidt, W.; Korhonen, S.; Weckhuysen, B. M.; Schüth, F., Co3O4–SiO2 Nanocomposite: A Very Active Catalyst for CO Oxidation with Unusual Catalytic Behavior. *J. Am. Chem. Soc.* **2011,** *133* (29), 11279-11288.

162. Liao, L.; Zhang, Q.; Su, Z.; Zhao, Z.; Wang, Y.; Li, Y.; Lu, X.; Wei, D.; Feng, G.; Yu, Q.; Cai, X.; Zhao, J.; Ren, Z.; Fang, H.; Robles-Hernandez, F.; Baldelli, S.; Bao, J., Efficient solar water-splitting using a nanocrystalline CoO photocatalyst. *Nat Nano* **2014,** *9* (1), 69-73.

163. Lou, Y.; Ma, J.; Cao, X.; Wang, L.; Dai, Q.; Zhao, Z.; Cai, Y.; Zhan, W.; Guo, Y.; Hu, P.; Lu, G.; Guo, Y., Promoting Effects of In2O3 on Co3O4 for CO Oxidation: Tuning O2 Activation and CO Adsorption Strength Simultaneously. *ACS Catalysis* **2014,** *4* (11), 4143-4152.

164. Mei, W.; Huang, J.; Zhu, L.; Ye, Z.; Mai, Y.; Tu, J., Synthesis of porous rhombus-shaped Co3O4 nanorod arrays grown directly on a nickel substrate with high electrochemical performance. *J. Mater. Chem.* **2012,** *22* (18), 9315-9321.

165. Deng, D.; Xing, X.; Chen, N.; Li, Y.; Wang, Y., Hydrothermal synthesis of β-Co(OH)2 nanoplatelets: A novel catalyst for CO oxidation. *J. Phys. Chem. Solids* **2017,** *100* (Supplement C), 107-114.

166. Ge, Y.; Kan, K.; Yang, Y.; Zhou, L.; Jing, L.; Shen, P.; Li, L.; Shi, K., Highly mesoporous hierarchical nickel and cobalt double hydroxide composite: fabrication, characterization and ultrafast NOx gas sensors at room temperature. *J. Mater. Chem. A* **2014,** *2* (14), 4961-4969.

167. Wang, H.; Qing, C.; Guo, J.; Aref, A. A.; Sun, D.; Wang, B.; Tang, Y., Highly conductive carbon-CoO hybrid nanostructure arrays with enhanced electrochemical

performance for asymmetric supercapacitors. *J. Mater. Chem. A* **2014,** *2* (30), 11776-11783.

168. Cong, Y.; Zhang, J.; Chen, F.; Anpo, M., Synthesis and Characterization of Nitrogen-Doped TiO2 Nanophotocatalyst with High Visible Light Activity. *J. Phys. Chem. C* **2007,** *111* (19), 6976-6982.

169. Song, F.; Hu, X., Ultrathin Cobalt–Manganese Layered Double Hydroxide Is an Efficient Oxygen Evolution Catalyst. *J. Am. Chem. Soc.* **2014,** *136* (47), 16481-16484.

170. Stoerzinger, K. A.; Qiao, L.; Biegalski, M. D.; Shao-Horn, Y., Orientation-Dependent Oxygen Evolution Activities of Rutile IrO2 and RuO2. *J. Phys. Chem. Lett.* **2014,** *5* (10), 1636-1641.

171. McCrory, C. C. L.; Jung, S.; Peters, J. C.; Jaramillo, T. F., Benchmarking Heterogeneous Electrocatalysts for the Oxygen Evolution Reaction. *J. Am. Chem. Soc.* **2013,** *135* (45), 16977-16987.

172. Bergmann, A.; Martinez-Moreno, E.; Teschner, D.; Chernev, P.; Gliech, M.; de Araújo, J. F.; Reier, T.; Dau, H.; Strasser, P., Reversible amorphization and the catalytically active state of crystalline Co3O4 during oxygen evolution. *Nat. Commun.* **2015,** *6*, 8625.

173. Wang, Y.; Zhou, T.; Jiang, K.; Da, P.; Peng, Z.; Tang, J.; Kong, B.; Cai, W.-B.; Yang, Z.; Zheng, G., Reduced Mesoporous Co3O4 Nanowires as Efficient Water Oxidation Electrocatalysts and Supercapacitor Electrodes. *Adv. Energy Mater.* **2014,** *4* (16), 1400696-1400703.

174. Song, F.; Hu, X., Exfoliation of layered double hydroxides for enhanced oxygen evolution catalysis. *Nat. Commun.* **2014,** *5*, 4477.

175. Gao, M.; Sheng, W.; Zhuang, Z.; Fang, Q.; Gu, S.; Jiang, J.; Yan, Y., Efficient Water Oxidation Using Nanostructured α-Nickel-Hydroxide as an Electrocatalyst. *J. Am. Chem. Soc.* **2014,** *136* (19), 7077-7084.

176. Wu, L.; Li, Q.; Wu, C. H.; Zhu, H.; Mendoza-Garcia, A.; Shen, B.; Guo, J.; Sun, S., Stable Cobalt Nanoparticles and Their Monolayer Array as an Efficient Electrocatalyst for Oxygen Evolution Reaction. *J. Am. Chem. Soc.* **2015,** *137* (22), 7071-7074.

177. Pera-Titus, M.; García-Molina, V.; Baños, M. A.; Giménez, J.; Esplugas, S., Degradation of chlorophenols by means of advanced oxidation processes: a general review. *Applied Catalysis B: Environmental* **2004,** *47* (4), 219-256.

178. Zhang, C.; Ou, Y.; Lei, W.-X.; Wan, L.-S.; Ji, J.; Xu, Z.-K., CuSO4/H2O2-Induced Rapid Deposition of Polydopamine Coatings with High Uniformity and Enhanced Stability. *Angewandte Chemie* **2016,** *128* (9), 3106-3109.

179. De Laat, J.; Le, T. G., Effects of chloride ions on the iron(III)-catalyzed decomposition of hydrogen peroxide and on the efficiency of the Fenton-like oxidation process. *Applied Catalysis B: Environmental* **2006,** *66* (1–2), 137-146.

180. Pham, A. L.-T.; Doyle, F. M.; Sedlak, D. L., Kinetics and efficiency of H2O2 activation by iron-containing minerals and aquifer materials. *Water Research* **2012,** *46* (19), 6454-6462.

181. A.R., D.; N., K.; E., G.; Y., G., Removal of COD from Oil Recovery Industry Wastewater by the Advanced Oxidation Processes (AOP) Based on H_2O_2. *Global NEST Journal* **2008,** *10* (1), 31-38.

182. Ronak, S.; Shweta, V., Fenton's Reagent for the Treatment of Pharmaceutical Industry Wastewater *International Journal of Science and Research* **2015,** *4* (7), 3093-3096.

183. Li, T.; Zhao, Z.; Wang, Q.; Xie, P.; Ma, J., Strongly enhanced Fenton degradation of organic pollutants by cysteine: An aliphatic amino acid accelerator outweighs hydroquinone analogues. *Water Research* **2016,** *105*, 479-486.

184. Sekaran, G.; Karthikeyan, S.; Evvie, C.; Boopathy, R.; Maharaja, P., Oxidation of refractory organics by heterogeneous Fenton to reduce organic load in tannery wastewater. *Clean Technologies and Environmental Policy* **2013,** *15* (2), 245-253.

185. A., S.; V., K., Behavior of Steels against Corrosion in Peroxide Solutions. *J. Mater. Environ. Sci* **2011,** *3* (1), 76-84.

186. Wang, M.; Fang, G.; Liu, P.; Zhou, D.; Ma, C.; Zhang, D.; Zhan, J., Fe3O4@β-CD nanocomposite as heterogeneous Fenton-like catalyst for enhanced degradation of 4-chlorophenol (4-CP). *Applied Catalysis B: Environmental* **2016,** *188*, 113-122.

187. Ma, J. H.; Song, W. J.; Chen, C. C.; Ma, W. H.; Zhao, J. C.; Tang, Y. L., Fenton degradation of organic compounds promoted by dyes under visible irradiation. *Environmental Science & Technology* **2005,** *39* (15), 5810-5815.

188. Ma, J. H.; Ma, W. H.; Song, W. J.; Chen, C. C.; Tang, Y. L.; Zhao, J. C.; Huang, Y. P.; Xu, Y. M.; Zang, L., Fenton degradation of organic pollutants in the presence of low-molecular-weight organic acids: Cooperative effect of quinone and visible light. *Environmental Science & Technology* **2006,** *40* (2), 618-624.

189. De Luca, A.; Dantas, R. F.; Esplugas, S., Study of Fe(III)-NTA chelates stability for applicability in photo-Fenton at neutral pH. *Applied Catalysis B: Environmental* **2015,** *179*, 372-379.

190. Gazi, S.; Rajakumar, A.; Singh, N. D. P., Photodegradation of organic dyes in the presence of [Fe(III)-salen]Cl complex and H2O2 under visible light irradiation. *Journal of Hazardous Materials* **2010,** *183* (1), 894-901.

191. Qin, Y. X.; Song, F. H.; Ai, Z. H.; Zhang, P. P.; Zhang, L. Z., Protocatechuic Acid Promoted Alachlor Degradation in Fe(III)/H2O2 Fenton System. *Environmental Science & Technology* **2015,** *49* (13), 7948-7956.

192. Qian, Y.; Yin, X. P.; Lin, H.; Rao, B.; Brooks, S. C.; Liang, L. Y.; Gu, B. H., Why Dissolved Organic Matter Enhances Photodegradation of Methylmercury. *Environmental Science & Technology Letters* **2014,** *1* (10), 426-431.

193. Jiang, C.; Garg, S.; Waite, T. D., Hydroquinone-Mediated Redox Cycling of Iron and Concomitant Oxidation of Hydroquinone in Oxic Waters under Acidic Conditions: Comparison with Iron-Natural Organic Matter Interactions. *Environmental Science & Technology* **2015,** *49* (24), 14076-14084.

194. Boles, M. A.; Ling, D.; Hyeon, T.; Talapin, D. V., The surface science of nanocrystals. *Nat Mater* **2016,** *15* (2), 141-153.

195. Guo, S.; Zhu, Y.; Yan, Y.; Min, Y.; Fan, J.; Xu, Q., Holey structured graphitic carbon nitride thin sheets with edge oxygen doping via photo-Fenton reaction with enhanced photocatalytic activity. *Applied Catalysis B: Environmental* **2016,** *185*, 315-321.

196. Li, M.; Qiang, Z.; Pulgarin, C.; Kiwi, J., Accelerated methylene blue (MB) degradation by Fenton reagent exposed to UV or VUV/UV light in an innovative micro photo-reactor. *Applied Catalysis B: Environmental* **2016,** *187* (Supplement C), 83-89.

197. Hems, R. F.; Hsieh, J. S.; Slodki, M. A.; Zhou, S.; Abbatt, J. P. D., Suppression of OH Generation from the Photo-Fenton Reaction in the Presence of α-Pinene Secondary Organic Aerosol Material. *Environmental Science & Technology Letters* **2017**.

198. Mak, K. F.; Lee, C.; Hone, J.; Shan, J.; Heinz, T. F., Atomically Thin ${\mathrm{MoS}}_{2}$: A New Direct-Gap Semiconductor. *Physical Review Letters* **2010,** *105* (13), 136805.

199. Liu, C.; Kong, D.; Hsu, P.-C.; Yuan, H.; Lee, H.-W.; Liu, Y.; Wang, H.; Wang, S.; Yan, K.; Lin, D.; Maraccini, P. A.; Parker, K. M.; Boehm, A. B.; Cui, Y., Rapid water disinfection using vertically aligned MoS2 nanofilms and visible light. *Nat Nano* **2016,** *11*, 1098-1104.

200. Wiedau-Pazos, M.; Goto, J. J.; Rabizadeh, S.; Gralla, E. B.; Roe, J. A.; Lee, M. K.; Valentine, J. S.; Bredesen, D. E., Altered Reactivity of Superoxide Dismutase in Familial Amyotrophic Lateral Sclerosis. *Science* **1996,** *271* (5248), 515-518.

201. Xing, M. Y.; Zhang, J. L.; Qiu, B. C.; Tian, B. Z.; Anpo, M.; Che, M., A Brown Mesoporous TiO2-x/MCF Composite with an Extremely High Quantum Yield of Solar Energy Photocatalysis for H-2 Evolution. *Small* **2015,** *11* (16), 1920-1929.

202. Tan, C.; Zhang, H., Epitaxial Growth of Hetero-Nanostructures Based on Ultrathin Two-Dimensional Nanosheets. *Journal of the American Chemical Society* **2015,** *137* (38), 12162-12174.

203. ScraceT; TsaiY; BarmanB; SchweidenbackL; PetrouA; KioseoglouG; OzfidanI; KorkusinskiM; HawrylakP, Magnetoluminescence and valley polarized state of a two-dimensional electron gas in WS2 monolayers. *Nat Nano* **2015,** *10* (7), 603-607.

204. Jarosz, A. P.; Yep, T.; Mutus, B., Microplate-Based Colorimetric Detection of Free Hydrogen Sulfide. *Anal. Chem.* **2013,** *85* (7), 3638-3643.

205. Voiry, D.; Fullon, R.; Yang, J.; de Carvalho Castro e Silva, C.; Kappera, R.; Bozkurt, I.; Kaplan, D.; Lagos, M. J.; Batson, P. E.; Gupta, G.; Mohite, A. D.; Dong, L.; Er, D.; Shenoy, V. B.; Asefa, T.; Chhowalla, M., The role of electronic coupling between substrate and 2D MoS2 nanosheets in electrocatalytic production of hydrogen. *Nat Mater* **2016,** *15*, 1003-1009.

206. Li, H.; Tsai, C.; Koh, A. L.; Cai, L.; Contryman, A. W.; Fragapane, A. H.; Zhao, J.; Han, H. S.; Manoharan, H. C.; Abild-Pedersen, F.; Norskov, J. K.; Zheng, X., Activating and optimizing MoS2 basal planes for hydrogen evolution through the formation of strained sulphur vacancies. *Nat Mater* **2016,** *15* (1), 48-53.

207. Ye, G.; Gong, Y.; Lin, J.; Li, B.; He, Y.; Pantelides, S. T.; Zhou, W.; Vajtai, R.; Ajayan, P. M., Defects Engineered Monolayer MoS2 for Improved Hydrogen Evolution Reaction. *Nano Letters* **2016,** *16* (2), 1097-1103.

208. Tsai, C.; Li, H.; Park, S.; Park, J.; Han, H. S.; Nørskov, J. K.; Zheng, X.; Abild-Pedersen, F., Electrochemical generation of sulfur vacancies in the basal plane of MoS(2) for hydrogen evolution. *Nature Communications* **2017,** *8*, 15113.

209. Cai, L.; He, J.; Liu, Q.; Yao, T.; Chen, L.; Yan, W.; Hu, F.; Jiang, Y.; Zhao, Y.; Hu, T.; Sun, Z.; Wei, S., Vacancy-Induced Ferromagnetism of MoS2 Nanosheets. *J. Am. Chem. Soc.* **2015,** *137* (7), 2622-2627.

210. Twu, J.; Dutta, P. K., Raman spectroscopic studies of intercalated molybdate ions in layered metal hydroxides. *Chem. Mat.* **1992,** *4* (2), 398-401.

211. Guifeng, C.; Xiaolin, S.; Lixiu, G.; Jianwei, C.; Hui, Z.; Shijie, W.; Jisheng, P.; Junguang, T., Defect assisted coupling of a MoS 2 /TiO 2 interface and tuning of its electronic structure. *Nanotechnol.* **2016,** *27* (35), 355203.

212. Tang, H.; Wang, J.; Yin, H.; Zhao, H.; Wang, D.; Tang, Z., Growth of Polypyrrole Ultrathin Films on MoS2 Monolayers as High-Performance Supercapacitor Electrodes. *Adv. Mater.* **2015,** *27* (6), 1117-1123.

213. Hameed, B. H.; Lee, T. W., Degradation of malachite green in aqueous solution by Fenton process. *Journal of Hazardous Materials* **2009,** *164* (2–3), 468-472.

214. Boles, M. A.; Engel, M.; Talapin, D. V., Self-Assembly of Colloidal Nanocrystals: From Intricate Structures to Functional Materials. *Chem. Rev.* **2016,** *116* (18), 11220-11289.

215. Whitesides, G. M.; Grzybowski, B., Self-Assembly at All Scales. *Science* **2002,** *295* (5564), 2418-2421.

216. van Blaaderen, A., CHEMISTRY: Colloidal Molecules and Beyond. *Science* **2003,** *301* (5632), 470-471.

217. Du, J.; O'Reilly, R. K., Anisotropic particles with patchy, multicompartment and Janus architectures: preparation and application. *Chem. Soc. Rev.* **2011,** *40* (5), 2402-2416.

218. Walker, D. A.; Leitsch, E. K.; Nap, R. J.; Szleifer, I.; Grzybowski, B. A., Geometric curvature controls the chemical patchiness and self-assembly of nanoparticles. *Nat Nano* **2013,** *8* (9), 676-681.

219. Reculusa, S.; Mingotaud, C.; Bourgeat-Lami, E.; Duguet, E.; Ravaine, S., Synthesis of Daisy-Shaped and Multipod-like Silica/Polystyrene Nanocomposites. *Nano Lett.* **2004,** *4* (9), 1677-1682.

220. Reculusa, S.; Poncet-Legrand, C.; Ravaine, S.; Mingotaud, C.; Duguet, E.; Bourgeat-Lami, E., Syntheses of Raspberrylike Silica/Polystyrene Materials. *Chem. Mat.* **2002,** *14* (5), 2354-2359.

221. Sheu, H. R.; El-Aasser, M. S.; Vanderhoff, J. W., Phase separation in polystyrene latex interpenetrating polymer networks. *J. Polym. Sci., Part A: Polym. Chem.* **1990,** *28* (3), 629-651.

222. van Blaaderen, A., Materials Science: Colloids get complex. *Nature* **2006,** *439* (7076), 545-546.

223. Klinger, D.; Wang, C. X.; Connal, L. A.; Audus, D. J.; Jang, S. G.; Kraemer, S.; Killops, K. L.; Fredrickson, G. H.; Kramer, E. J.; Hawker, C. J., A Facile Synthesis of Dynamic, Shape-Changing Polymer Particles. *Angew. Chem., Int. Ed.* **2014,** *53* (27), 7018-7022.

224. Brochard-Wyart, F.; Di Meglio, J. M.; Quere, D.; De Gennes, P. G., Spreading of nonvolatile liquids in a continuum picture. *Langmuir* **1991,** *7* (2), 335-338.

225. Park, J. M., Core-Shell Polymerization with Hydrophilic Polymer Cores. *Korea Polym. J.* **2001,** *9* (1), 51-65.

226. Bigall, N. C.; Härtling, T.; Klose, M.; Simon, P.; Eng, L. M.; Eychmüller, A., Monodisperse Platinum Nanospheres with Adjustable Diameters from 10 to 100 nm: Synthesis and Distinct Optical Properties. *Nano Lett.* **2008,** *8* (12), 4588-4592.

227. Gao, A.; Xu, W.; Ponce de León, Y.; Bai, Y.; Gong, M.; Xie, K.; Park, B. H.; Yin, Y., Controllable Fabrication of Au Nanocups by Confined-Space Thermal Dewetting for OCT Imaging. *Adv. Mater.* **2017**, 1701070-n/a.

228. Feng, L.; Wu, X.; Ren, L.; Xiang, Y.; He, W.; Zhang, K.; Zhou, W.; Xie, S., Well-Controlled Synthesis of Au@Pt Nanostructures by Gold-Nanorod-Seeded Growth. *Chem. Eur. J.* **2008,** *14* (31), 9764-9771.

229. Extrand, C. W.; Moon, S. I., Contact Angles on Spherical Surfaces. *Langmuir* **2008,** *24* (17), 9470-9473.

230. Yang, G.-W.; Wu, G.-P.; Chen, X.; Xiong, S.; Arges, C. G.; Ji, S.; Nealey, P. F.; Lu, X.-B.; Darensbourg, D. J.; Xu, Z.-K., Directed Self-Assembly of Polystyrene-b-poly(propylene carbonate) on Chemical Patterns via Thermal Annealing for Next Generation Lithography. *Nano Lett.* **2017,** *17* (2), 1233-1239.

231. Xia, Y.; Gates, B.; Yin, Y.; Lu, Y., Monodispersed Colloidal Spheres: Old Materials with New Applications. *Adv. Mater.* **2000,** *12* (10), 693-713.

232. Yin, Y.; Xia, Y., Self-Assembly of Spherical Colloids into Helical Chains with Well-Controlled Handedness. *J. Am. Chem. Soc.* **2003,** *125* (8), 2048-2049.

233. Wang, J.; Hu, Y.; Deng, R.; Xu, W.; Liu, S.; Liang, R.; Nie, Z.; Zhu, J., Construction of multifunctional photonic crystal microcapsules with tunable shell structures by combining microfluidic and controlled photopolymerization. *Lab on a Chip* **2012,** *12* (16), 2795-2798.

234. Grzelczak, M.; Vermant, J.; Furst, E. M.; Liz-Marzán, L. M., Directed Self-Assembly of Nanoparticles. *ACS Nano* **2010,** *4* (7), 3591-3605.

235. Steinbach, G.; Nissen, D.; Albrecht, M.; Novak, E. V.; Sanchez, P. A.; Kantorovich, S. S.; Gemming, S.; Erbe, A., Bistable self-assembly in homogeneous colloidal systems for flexible modular architectures. *Soft Matter* **2016,** *12* (10), 2737-2743.

236. Hu, Y.; He, L.; Yin, Y., Magnetically Responsive Photonic Nanochains. *Angew. Chem., Int. Ed.* **2011,** *50* (16), 3747-3750.

237. Zhang, Q.; Janner, M.; He, L.; Wang, M.; Hu, Y.; Lu, Y.; Yin, Y., Photonic Labyrinths: Two-Dimensional Dynamic Magnetic Assembly and in Situ Solidification. *Nano Lett.* **2013,** *13* (4), 1770-1775.

238. Mirkin, C. A.; Letsinger, R. L.; Mucic, R. C.; Storhoff, J. J., A DNA-based method for rationally assembling nanoparticles into macroscopic materials. *Nature* **1996,** *382* (6592), 607-609.

239. Derjaguin, B., On the repulsive forces between charged colloid particles and on the theory of slow coagulation and stability of lyophobe sols. *J. Chem. Soc. Faraday Trans.* **1940,** *35* (0), 203-215.

240. Carman, P. C., Constitution of colloidal silica. *J. Chem. Soc. Faraday Trans.* **1940,** *36* (0), 964-973.

241. Verwey, E. J. W., Theory of the Stability of Lyophobic Colloids. *J. Phys. Colloid Chem.* **1947,** *51* (3), 631-636.

242. Depasse, J.; Watillon, A., The stability of amorphous colloidal silica. *J. Colloid Interface Sci.* **1970,** *33* (3), 430-438.

243. Zhang, H.; Wang, D., Controlling the Growth of Charged-Nanoparticle Chains through Interparticle Electrostatic Repulsion. *Angew. Chem.* **2008,** *120* (21), 4048-4051.

244. Wang, Y.; Chen, G.; Yang, M.; Silber, G.; Xing, S.; Tan, L. H.; Wang, F.; Feng, Y.; Liu, X.; Li, S.; Chen, H., A systems approach towards the stoichiometry-controlled hetero-assembly of nanoparticles. *Nat. Commun.* **2010,** *1*, 87.

245. He, L.; Hu, Y.; Han, X.; Lu, Y.; Lu, Z.; Yin, Y., Assembly and Photonic Properties of Superparamagnetic Colloids in Complex Magnetic Fields. *Langmuir* **2011,** *27* (22), 13444-13450.

Chapter 3

Porous Cobalt Oxide Nanoplates Enriched with Oxygen Vacancies for Oxygen Evolution Reaction

3.1 Introduction

Electrochemical water oxidation, also known as oxygen evolution reaction (OER), plays an important role in many technologies relevant to energy conversion and storage.[74, 131-134] However, OER is kinetically sluggish and requires a high overpotential, due to the stepwise four-electron oxidation process.[135-137] Although noble metal and noble metal oxides such as RuO_2 and IrO_2 are currently regarded as the most active electrocatalyst, their scarcity and high cost have seriously impeded their large-scale applications.[138-142] Accordingly, the exploration of abundant, highly efficient, and economic alternatives for water splitting is crucial in terms of solving global energy crisis and environmental challenges. Recently, earth-abundant and environmentally friendly transition-metals-based oxides (Co, Ni, Fe) have exhibited superior performance in OER catalysis due to their reasonable reactivity and stability.[10, 13, 84, 143-148] However, their electrocatalytic activity still underperforms the benchmark of IrO_2 and RuO_2.[149] Therefore, the development of robust and economic routes to achieve highly active transition-metal-

based catalysts will contribute greatly towards various OER relevant fields.

Increasing the reactivity and number of active sites are two effective means to improve electrocatalytic performance.[80-82, 150] Ultra-thin two dimensional (2D) transition metal oxides (TMOs) were therefore chosen as the starting material, due to their large surface area, exposed active sites, and short diffusion lengths of ions and electrons.[83, 85, 148, 151-156] To further improve their electrocatalytic performance, it is imperative to enhance the reactivity of active sites on the surface of 2D TMOs. Recently, the incorporation of oxygen vacancies has been found to remarkably increase the reactivity of active sites, leading to significant improvement of OER performance.[76, 82-83, 157-159] However, the most commonly used method of creating oxygen vacancies, i.e., reduction under high-temperature annealing, is accompanied by morphological deformation and severe aggregation, which may then greatly decrease the effective surface area.[160] Due to the high reaction rate at high temperatures, fine-tuning of concentration of oxygen vacancies is extremely difficult to achieve. To this end, a novel wet chemical synthesis strategy that enables large-scale synthesis of homogenous 2D ultrathin nanostructures with fine-tuning concentration of oxygen vacancies would represent a great breakthrough that may allow us to combine advantages of high specific surface area and highly reactive sites.

Herein, we report a ligand-assisted polyol reduction method that allows successful conversion of $Co(OH)_2$ nanoplates into CoO_x with well-maintained morphology and at the same time offers an opportunity for effectively creation of oxygen vacancies of

controllable concentration on surface. More specifically, $Co(OH)_2$ nanoplates, which can be easily prepared through the hydrolysis of $CoCl_2$, are modified with polyacrylic acid (PAA) through the coordination interaction between cobalt cations and the carboxyl groups. With multiple carboxyl groups, PAA forms a crosslinked network on the surface of $Co(OH)_2$, which allows the transformation of $Co(OH)_2$ nanoplates through polyol reduction in diethylene glycol (DEG) at relatively high temperature without losing their original plate morphology.[1] This seemingly simply procedure has subtly solved the most challenging problem of simultaneously fabricating 2D nanostructures and generating oxygen vacancies. The chemical conversion strategy makes it possible to produce CoO_x nanocrystals, which usually do not grow two-dimensionally due to the limitation of its intrinsic crystal symmetry, with a plate morphology by taking advantage of the shape of the $Co(OH)_2$ precursor. The phase transition from $Co(OH)_2$ to CoO_x is accompanied by volume shrinkage, which causes the formation of pores on the nanoplates and further increases the effective surface area. In addition, the mild solution-phase reduction reaction allows convenient scale up for mass production, and enables effective creation of oxygen vacancies in a controllable manner while avoids typically used high-temperature hydrogen reduction method, which could cause severe aggregation of nanoplates. More importantly, the resulting oxygen-vacancy-rich nanoplates show excellent catalytic performance, manifesting OER overpotential as low as 306 mV at 10 mA/cm^2.

3.2 Materials and Methods

3.2.1 Chemicals

Cobalt (II) chloride hexahydrate, PVP (Mw. 55000), hexamethylenetetramine (HMT), diethylene glycol (DEG), polyacrylic acid (PAA) (Mw. 1800), KOH, Nafion and isopropanol were purchased from Sigma-Aldrich and ethanol (200 proof) was purchased from Decon Laboratories. All chemicals were used as purchased without further purification.

3.2.2 Synthesis of $Co(OH)_2$ nanoplates

The synthesis of $Co(OH)_2$ nanoplates was based on a previous report with slight modifications.[161] In a typical synthesis, 0.48 g $CoCl_2 \cdot 6H_2O$, 0.2 g PVP (Mw. 55000), and 0.28 g hexamethylenetetramine (HMT) were dissolved in 80 ml of a 9:1 mixture of deionized H_2O and ethanol. The reaction solution was then refluxed at about 95 °C for 2 hours. The nanoplates were then isolated by centrifugation and washed with water several times.

3.2.3 Surface modification of $Co(OH)_2$ nanoplates

The surface of $Co(OH)_2$ nanoplates were functionalized with poly(acrylic acid) (PAA) at first. In a typical procedure, 30 mg of $Co(OH)_2$ and 1 mL PAA solution (7.2 mg/mL) were added to 20 mL of deionized water under sonication. The mixture was then stirred for 12 hours to allow the functionalization of nanoplates. Afterwards, the excess PAA in the solution was removed by centrifugation and the $Co(OH)_2$ nanoplates were dispersed in 2 mL diethylene glycol (DEG).

3.3.4 Surface protected reduction of $Co(OH)_2$ nanoplates

In a three-neck flask, 30 mL DEG was heated up to 220°C under N_2 atmosphere. Then, 2 mL DEG solution of $Co(OH)_2$ was injected into the hot DEG solution with magnetic stirring. After incubation for a certain length of time, the product was collected by centrifugation and washed with ethanol/H_2O mixture solution several times.

3.3.5 Calcination of $Co(OH)_2$ nanoplates

30 mg of as-prepared $Co(OH)_2$ was placed in a crucible and calcined in an oven at 300 °C for 2 hours under Ar atmosphere. The temperature was increased at 2.5 °C /min and the flow rate of Ar is 40 cm^3/min.

3.3.6 Characterization

The morphology of the initial $Co(OH)_2$ nanoplates, CoO, is prepared with surface protected reduction method and calcination, characterized by using a Tecnai T12 transmission electron microscope. The large-scale images of the samples were analyzed with a scanning electron microscope XL30-FEG. The crystal phases of the products were examined with X-ray diffraction (Bruker SMART APEX2), in a range of 2θ from 5 to 80°. The concentration of cobalt ions was analyzed with Perkin-Elmer Optima 7300DV ICP-OES apparatus, which combined an SCD detector and an echelle optical system. All FTIR spectra were characterized by Nicolet 6700. The chemical state and electronic state of the elements on the surface were measured with X-ray photoelectron spectroscopy (AXIS ULTRA).

3.3.7 Electrochemical measurements

The electrochemical tests were conducted on a Princeton VersaSTAT 4 electrochemical workstation with a typical three-electrode cell. The three-electrode cell is composed of: a glassy carbon working electrode, a platinum foil counter electrode and a saturated calomel reference electrode. For the working electrode preparation, catalysts (5 mg) and Nafion solution (50 μL) were added to the mixture solution of isopropanol (250 μL) and water (750 μL), followed by sonication to achieve a good dispersion. Then the dispersed catalysts were casted on the glassy carbon (3 mm in diameter) with 0.5 mg/cm^2. The linear sweep voltammetry curves were recorded at a scan rate of 5 mV/s. Chronopotentiometry curve was obtained at a constant current density of 5 mA/cm^2. Cyclic voltammetry curves were recorded at a scan rate of 50 mV/s. The conversion of potential against RHE was based on the following equation

$$E_{RHE} = E_{SCE} + 0.244 + 0.059 \times pH$$

3.3 Results and Discussion

3.3.1 Synthesis of Oxygen Vacancies Enriched Cobalt Oxides Nanoplates

α-$Co(OH)_2$ hexagonal nanoplates were synthesized with a previously reported method with minor revision.[161] Typical transmission electron microscopy (TEM) image shown in Figure 3.1A reveals an almost perfect hexagonal plate-like structure with width in the range of 1-2 μm. These plates are uniform and thin with a thickness of around 15 nm as illustrated in the scanning electron microscope (SEM) image in Figure 3.2. The corresponding selected-area electron diffraction (SAED) pattern (Figure 3.1E) exhibited perfect hexagonally arranged diffraction spots, which can be readily indexed as the two-dimensional in-plane reflection with [001] crystal planes on the surface. Subsequently, the classic polyol process was performed through hot injection of the nanoplates into DEG at 220 °C. The reaction was quenched to room temperature at different points in time (1, 2 and 4 h) and the respective intermediates were separated by centrifugation and examined using TEM (shown in Figure 3.1B-D). The surface structure of the hexagonal platelets was well maintained during the chemical transformation while the interior part became more and more porous, due to the volume shrinkage caused by the dehydration of $Co(OH)_2$ and phase transition. As shown in Figure 3.1F-H, the corresponding SAED patterns changed rapidly upon DEG reduction, indicating the phase transition. X-Ray Diffraction (XRD) analyses, as shown in Figure 3.1I-J, helped clarify the component of $Co(OH)_2$ before and after reduction during the phase transition process. In Figure 3.1I,

the as-synthesized $Co(OH)_2$ shows two prominent reflection peaks in the XRD pattern, including 003 and 006 reflections of the hydrotalcite-like structure. With its green color, the sample can be determined as α-$Co(OH)_2$.[161] The samples upon reduction show three predominant peaks corresponding to the 111, 200 and 220 facets of CoO phase (JCPDS No. 43-1004) (Figure 3.1J). As the reduction time increases from 1 h to 4 h, the diffraction peaks become sharper and narrower, indicating more complete conversion from $Co(OH)_2$ to CoO and improved crystallinity. Further confirmation of the phase transition can be seen from the high-resolution TEM (HRTEM) images in Figure 3.3 of supporting information. As shown in Figure 3.3A-C, CoO phase with d-spacing of (111) planes with 0.25 nm was observed after DEG reduction for 1, 2 and 4h.

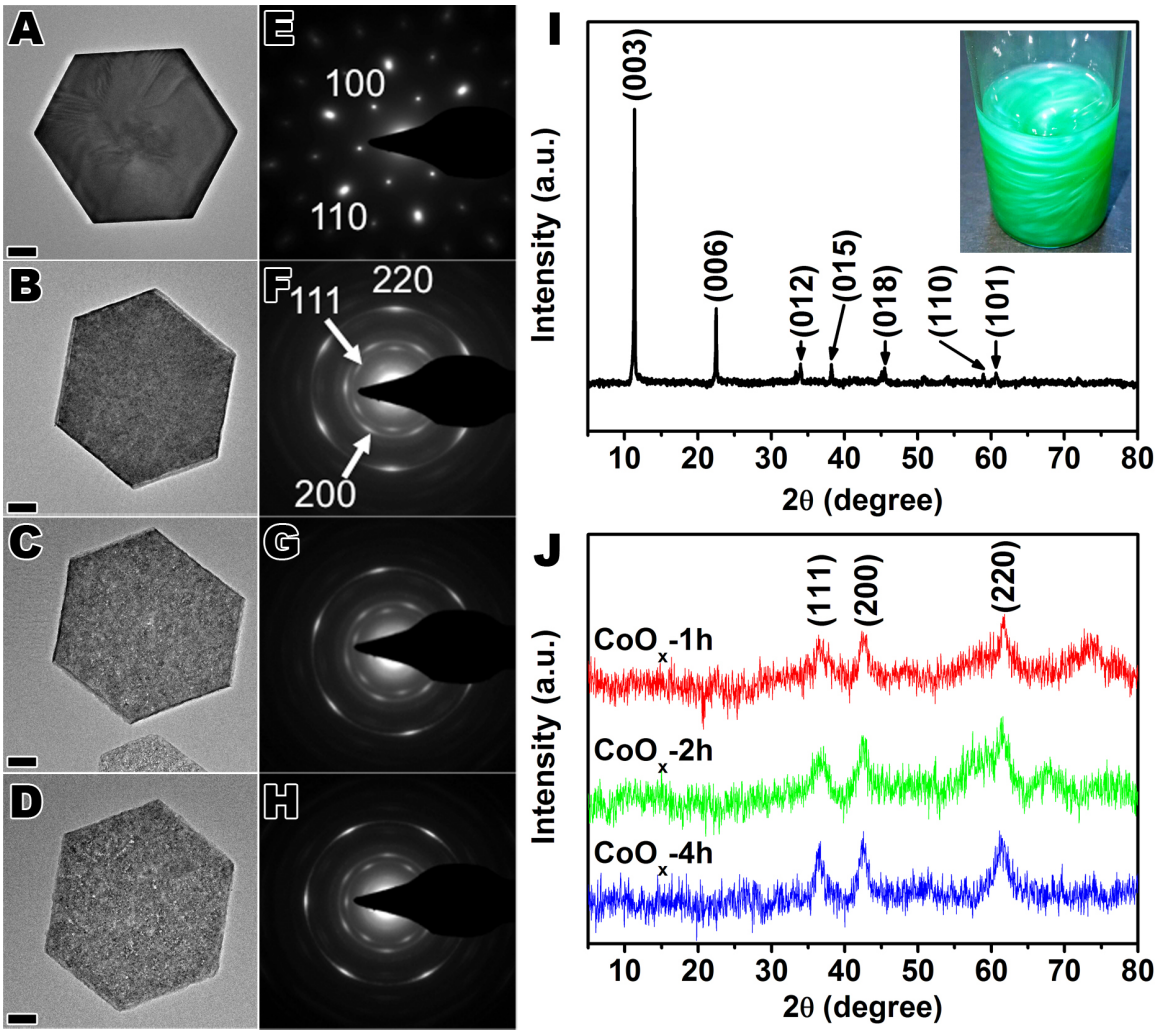

Figure 3.1. (A-D) TEM images of α-$Co(OH)_2$ and CoO obtained after reduction for 1, 2 and 4 h (scale bar: 500 nm). (E-H) Corresponding SAED patterns and (I-J) XRD patterns of (I) α-$Co(OH)_2$ (Inset: digital photo of $Co(OH)_2$), and (J) CoOx obtained after reduction time of 1 (red), 2 (green) and 4 h (blue).

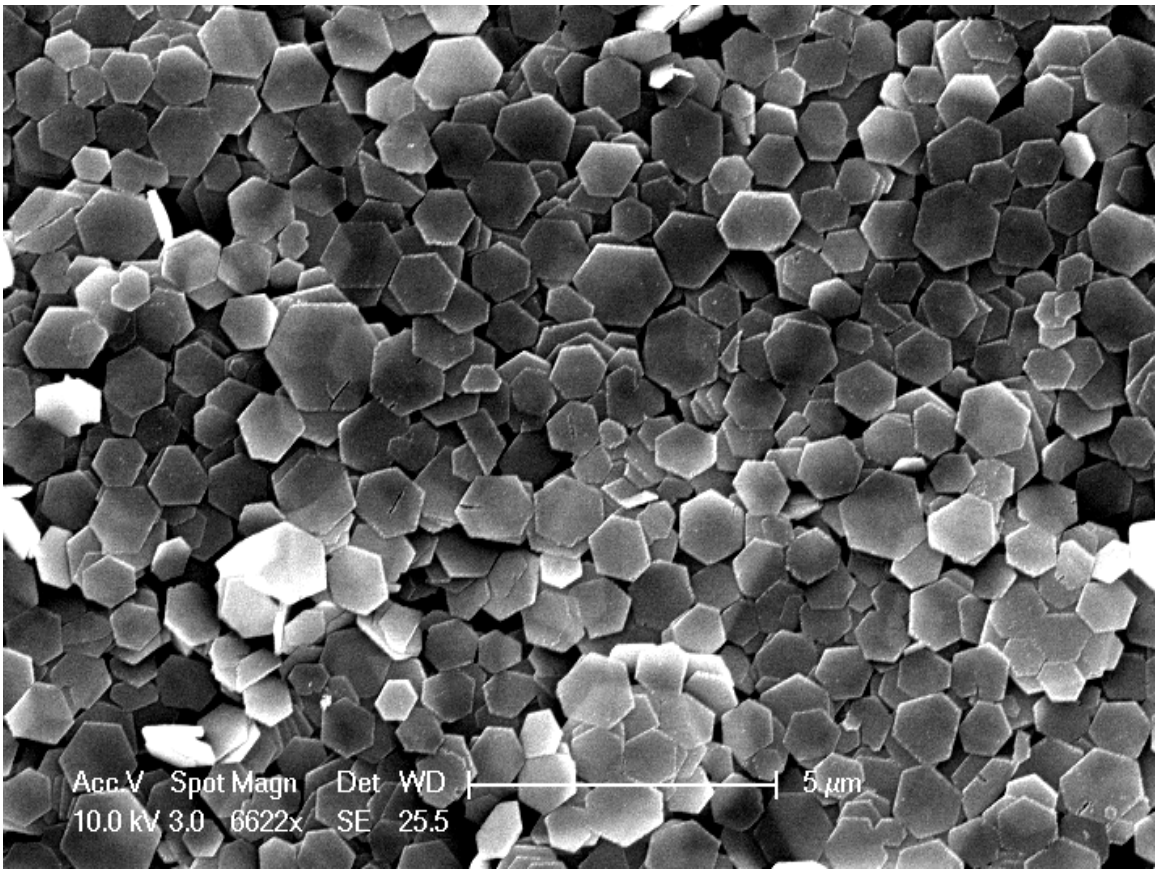

Figure 3.2. SEM image of $Co(OH)_2$

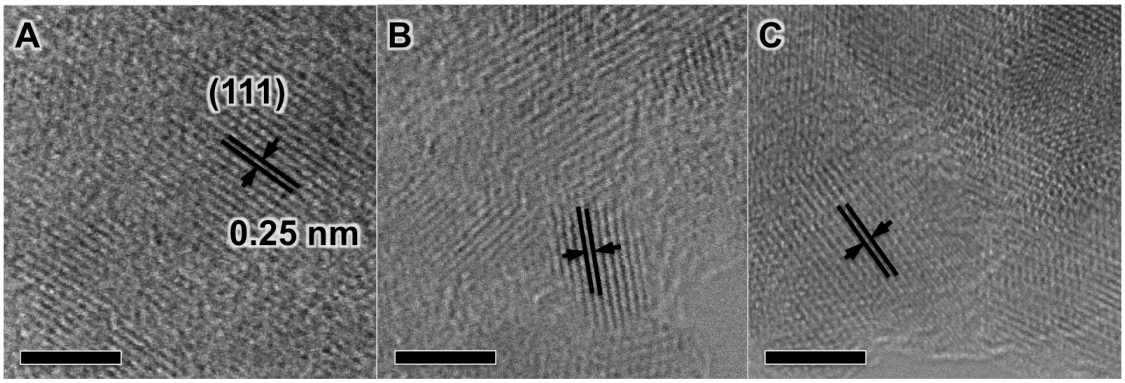

Figure 3.3. HRTEM images of CoO produced by DEG reduction for A)1, B) 2 and C) 4h. Scale bars: 20 nm.

3.3.2 The Role of PAA

The role PAA played during surface protected reduction process was studied by Fourier transform infrared spectroscopy (FTIR), and inductively coupled plasma optical emission spectrometry (ICP-OES). To verify the coordination interaction between the carboxyl groups of PAA and Co ions, FTIR was performed for PAA, bare $Co(OH)_2$ and PAA modified $Co(OH)_2$. As shown in Figure 3.4A, PAA displays a strong peak around 1700 cm^{-1}, which corresponds to the typical stretching mode of C=O double bonds of the carboxyl group. The as-synthesized $Co(OH)_2$ without any surfactant displays a characteristic peak at 3400 cm^{-1} originated from the hydroxyl group of cobalt hydroxide. After PAA modification, a new peak emerges at 1560 cm^{-1} in the spectrum. Considering that the electrons around C=O could be pulled towards the metal atom during coordination, resulting in low electron density around C=O, reduced stiffness of C=O bond, and decreased stretching frequency, it is reasonable to assume that the peak around 1560 cm^{-1} is caused by carboxyl groups of PAA, which confirms the coordination interaction between PAA and cobalt cations. The importance of PAA to the reduction reaction was revealed by ICP-OES measurement. In a typical synthesis process, one batch of $Co(OH)_2$ was evenly divided into 6 aliquots and each aliquot was injected into the hot DEG solutions which contain different amounts of PAA. After a one-hour reaction, the surviving components were removed by centrifugation and the dissolved Co ions in the supernatant was collected and analyzed by ICP-OES. Without any protection, 24% of the Co species in $Co(OH)_2$ was dissolved by DEG. Figure 3.5 details the

dissolving process by TEM. The surface of the $Co(OH)_2$ platelets were quickly corrupted within 15 min of the reaction and almost lost their original shape within an hour. By increasing the time to 4 hours, the majority of the sample was dissolved. However, when the concentration of PAA in DEG was increased to around 200 mg/L, the dissolution amount was dramatically decreased to below 6%; which demonstrated the adequate protection ability of PAA. However, due to the acidity of PAA, increasing the PAA to 400 mg/L increased dissolution to 15%. The protection and etching effect were further confirmed by TEM and SEM imaging of samples (Figure 3.6). The samples prepared in 100 and 400 mg/L PAA/DEG solutions appear more porous in the TEM images and with lighter contrast in the SEM images, indicating a smaller thickness caused by dissolving and etching, which is consistent with the ICP-OES results.

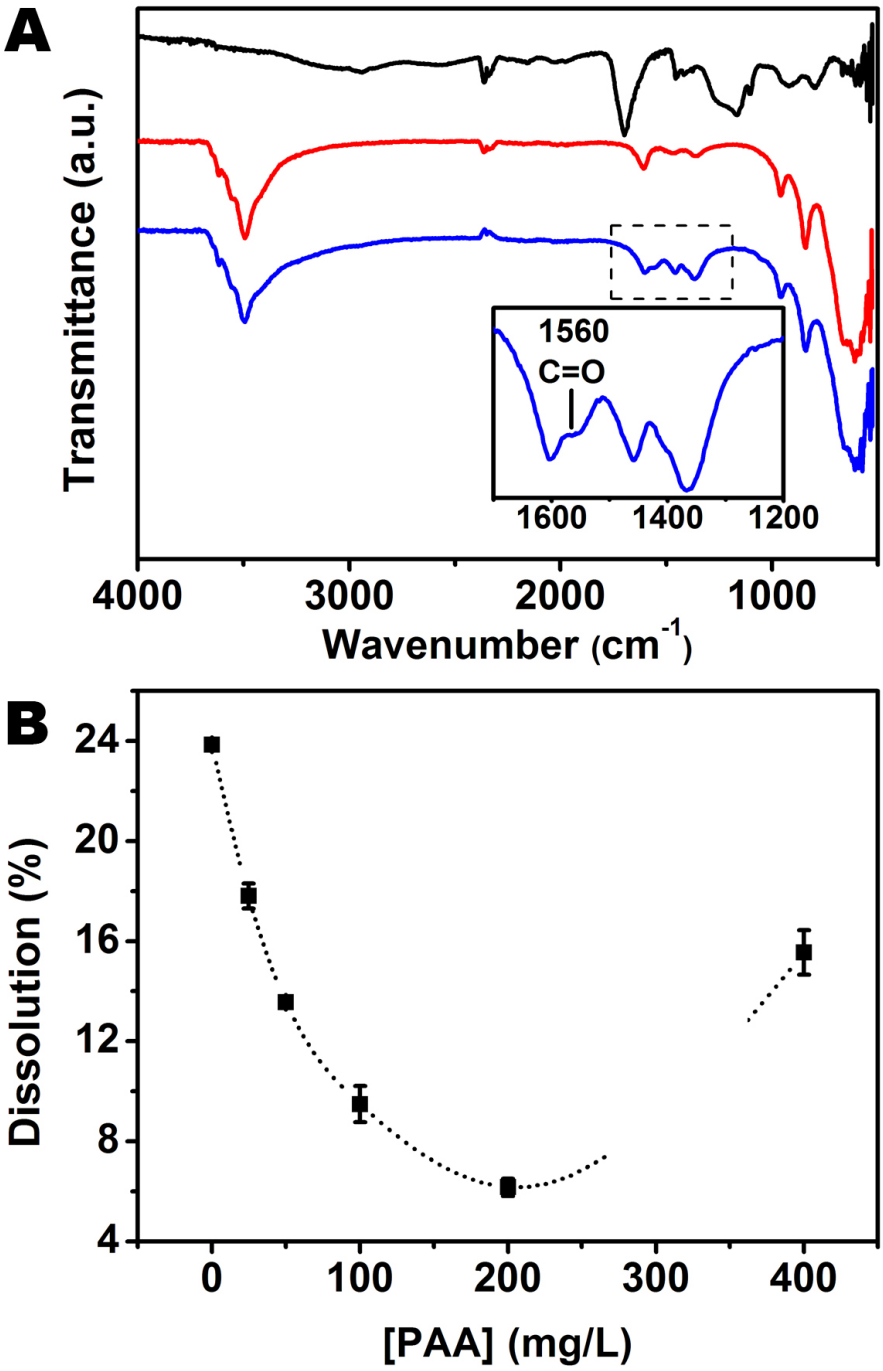

Figure 3.4. (A) FTIR of PAA (black), $Co(OH)_2$ (red) and $Co(OH)_2$ after PAA surface modification (blue). The inset is enlarged C=O peak of PAA modified $Co(OH)_2$. (B) ICP-OES analysis of cobalt ions that dissolved in DEG after 1 h reduction with different PAA concentration.

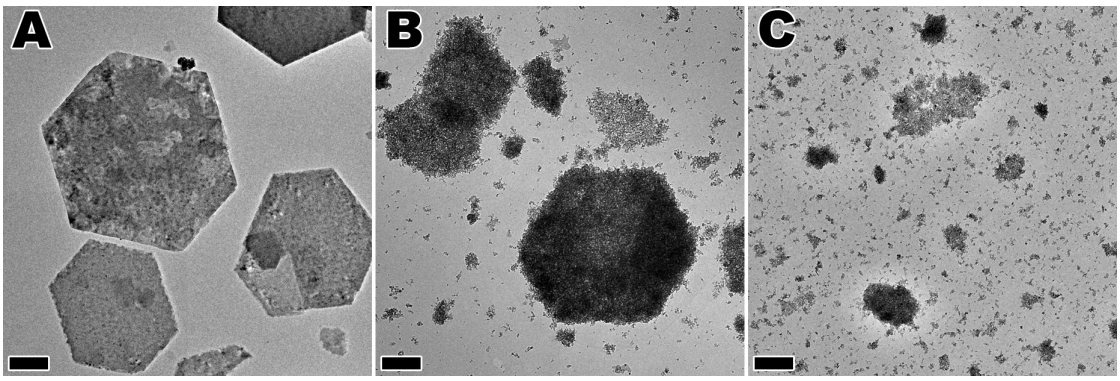

Figure 3.5. Reduction of $Co(OH)_2$ without any protection for (A) 15 min, (B) 1 h and (C) 4 h. (scale bar: 500 nm)

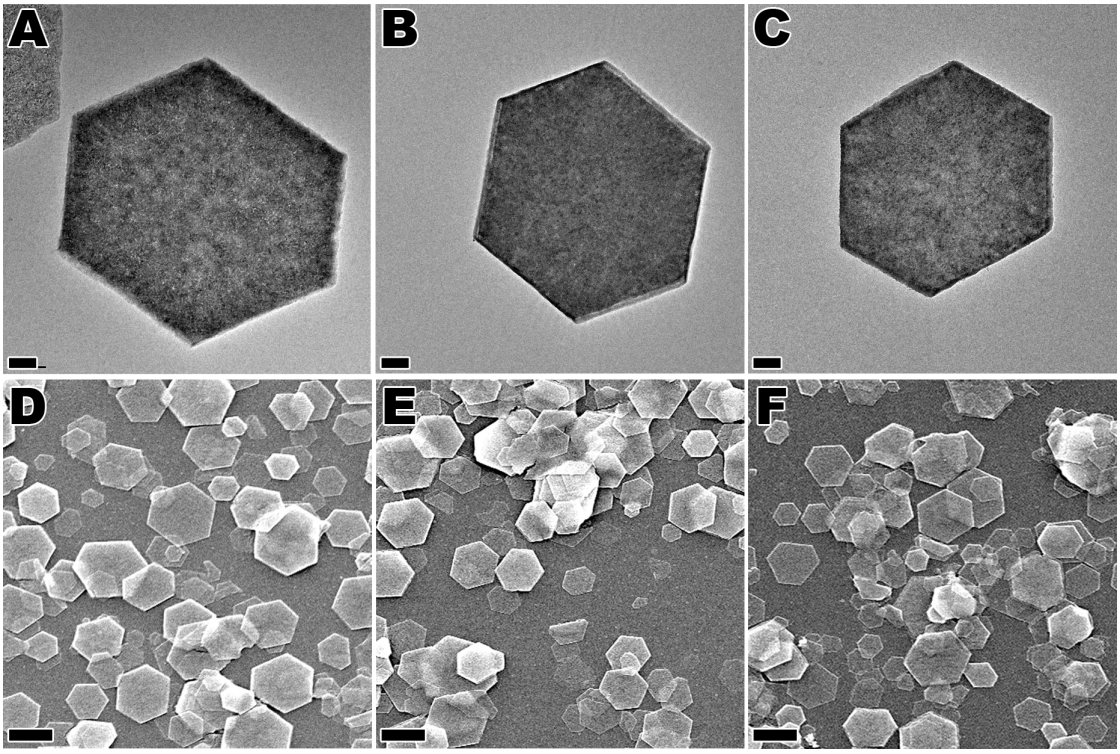

Figure 3.6. TEM and corresponding SEM images of $Co(OH)_2$ reduced for 1 h in different concentration of PAA/DEG solutions (A, D) 100 mg/L, (B, E) 200 mg/L, (C, F) 400 mg/L (scale bar of TEM: 200 nm, scale bar of SEM: 1 μm).

3.3.3 Characterization of Oxygen Vacancies

To highlight the unique advantage of the ligand-assisted polyol reduction method, cobalt oxide was directly synthesized through calcination (CoO-cal) at 300°C for 2h in Ar as a control sample (Figure 3.7), and then compared with CoO_X samples prepared with DEG reduction for different lengths of time by X-ray photoelectron spectroscopy (XPS) analysis. The fine-scanned Co 2p XPS spectra are given in Figure 3.8A, displaying peaks of Co $2p_{3/2}$ and Co $2p_{1/2}$ at approximately 780 and 796 eV, respectively. The two satellite peaks centered at approximately 786 and 803 eV, which belong to Co^{2+} oxidation sate, confirming their CoO chemical nature.[162-164] To get further insight of the surface properties, we fit the curves by Gaussian-Lorentz functions to investigate the electronic states of Co atoms. The two fitted peaks for Co $2p_{2/3}$ could be assigned to Co^{3+} (B.E. 779 eV) and Co^{2+} (B.E. 781 eV).[165] The appearance of Co^{3+} could be attributed to inevitable oxidation during the synthesis of the nanostructures, which has been observed previously.[166] Compared to pristine $Co(OH)_2$ (Figure 3.9), the relative atomic ratio of Co^{2+}/Co^{3+} on the surface of CoO-cal is barely affected. However, the Co^{2+}/Co^{3+} ratio of catalysts prepared by the polyol reduction method was dramatically increased, indicating the generation of oxygen vacancies on the surface, which could then be further confirmed by the fine-scanned O 1s XPS spectra. CoO-cal shows two oxygen peaks in the O 1s spectra whereas CoOx (15min, 1, 2, 4 h) shows four oxygen peaks. In detail, the peaks at 529, 531, 532 and 534 eV are associated with Co-O bonds, hydroxyl species, oxygen vacancies or defects (O_{vac}) and surface adsorbed water molecules.[14, 167-168] The absence of

a peak at 532 eV in CoO-cal spectra indicates that CoO-cal lacks oxygen defects on its surface, which is also the case of pristine $Co(OH)_2$ (Figure 3.9). However, the large O_{vac} peak areas for CoO_x in Figure 3.8B(ii-v) demonstrate that the ligand-assisted polyol reduction method is very effective in creating oxygen vacancies on the surface. Additionally, the calculated atomic concentration of O_{vac}/O demonstrates that by simply extending the reduction time from 15min to 4 h, the concentration of O_{vac} on surface can be increased from 13% to 31%. This is also consistent with the atomic ratio decrease of Co^{2+}/Co^{3+} in the Co spectra. It is worth noting that the calculated concentration of oxygen vacancies reflects the surface structure only, whereas the relative concentration of the oxygen vacancies of the bulk is believed to be much smaller.[169]

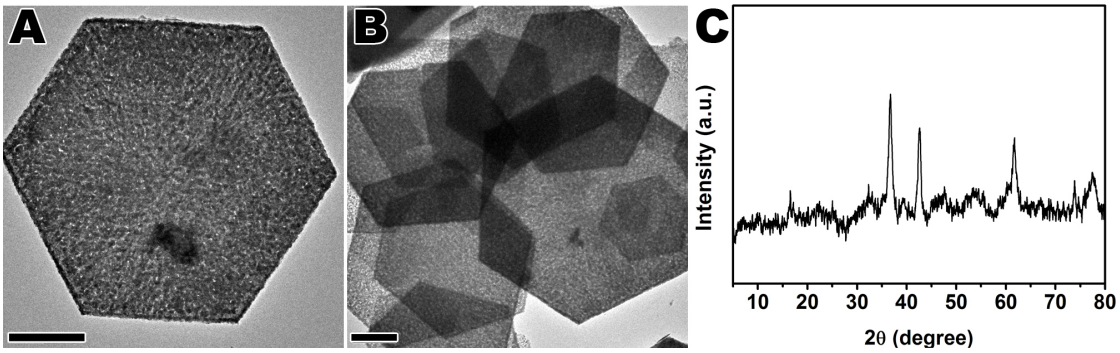

Figure 3.7. (A) High magnification TEM image of CoO prepared by calcination and (B) corresponding low magnification TEM image (scale bar: 1 μm). (C) Corresponding XRD pattern of the CoO.

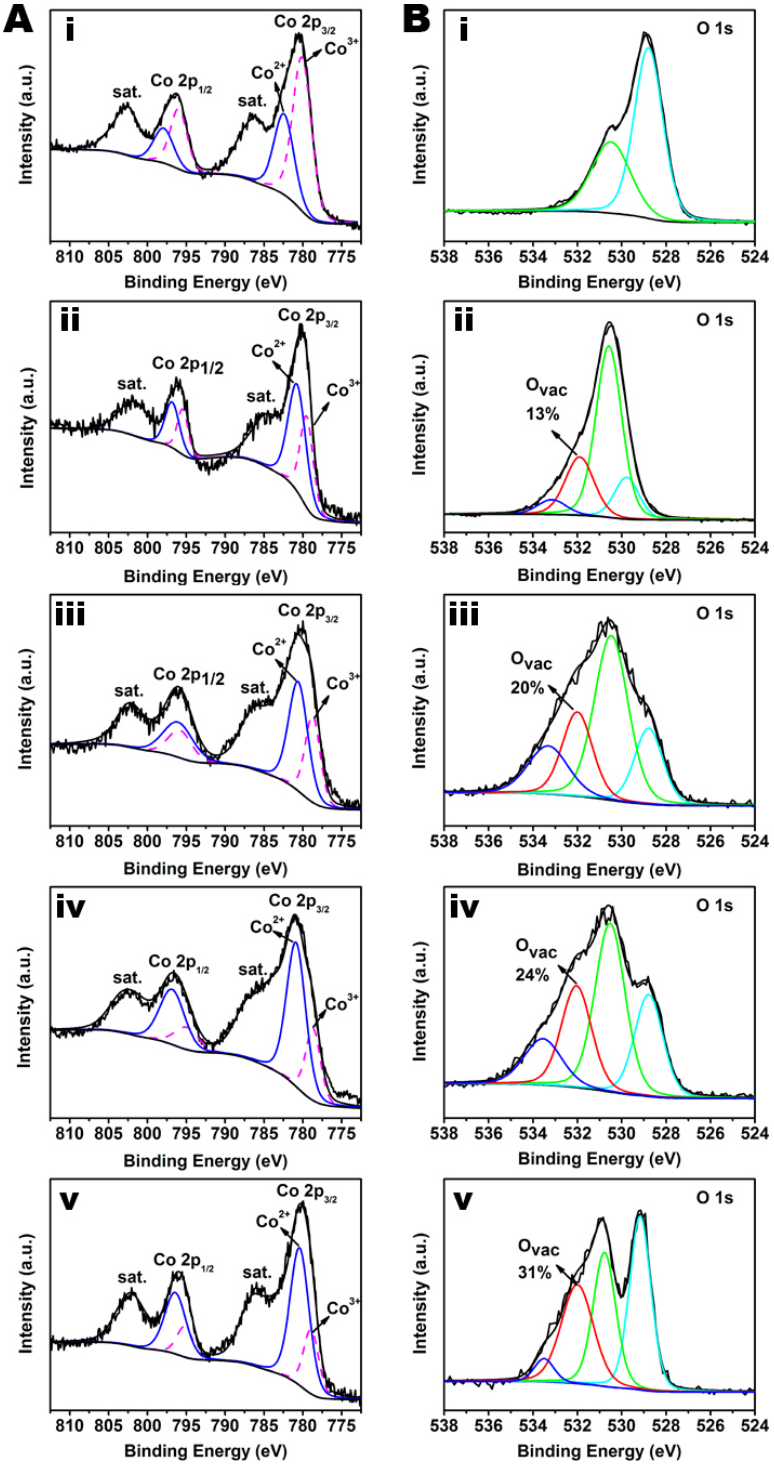

Figure 3.8. (A) Co 2p XPS spectra and (B) O 1s XPS spectra of (i) CoO-cal, (ii) CoO_x-15min, (iii) CoO_x-1h, (iv) CoO_x-2h, and (v) CoO_x-4h.

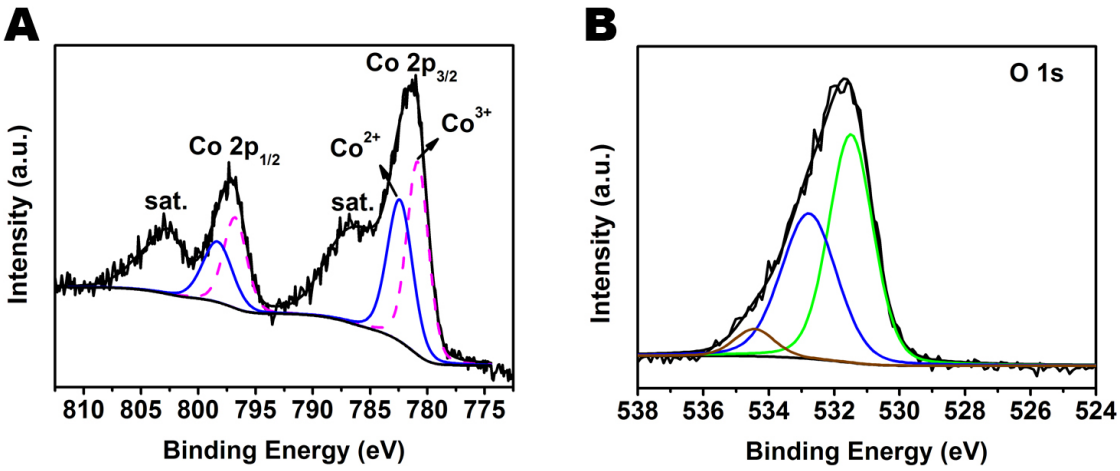

Figure 3.9. (A) Co 2p XPS spectrum and (B) O 1s XPS spectrum of $Co(OH)_2$.

3.3.4 Electrocatalytic Performance of the Catalysts

Subsequently, the OER performance of oxygen-vacancy-enriched cobalt oxides was evaluated using a standard three-electrode system in 1M KOH. To minimize the capacitive current, a slow scan rate of 5 mV/s was applied to obtain the polarization curves. As shown in Figure 3.10A, the onset potential for OER on CoO_x-4h is 1.54 V, versus the reversible hydrogen electrode (RHE), which has the lowest onset potential of the six samples and the best OER performance. The overpotential values of the six samples at a current density of 10 mA/cm^2 are illustrated in Figure 3.10B. The pristine $Co(OH)_2$ and cobalt oxide prepared by calcination displayed overpotentials above 340 mV, while the cobalt oxides with increasing oxygen vacancy exhibited significant decrease in overpotentials. The lowest overpotential was achieved by CoO_x-4h at only 306 mV, making it one of the best cobalt based OER electrocatalysts reported (Table 3.1).[11, 83, 158, 170-174] Moreover, the corresponding current densities of the six samples at the overpotential of 330 mV are presented in Figure 3.10C. CoO_x-4h showed the highest current density of 21 mA/cm^2, which was about 3 times larger than the pristine $Co(OH)_2$ and CoO-cal. The enhanced activity could be attributed to the large surface area and high concentration of oxygen vacancies of CoO_x-4h. Further activity evaluation could be seen from Tafel plots (Figure 3.10D). The Tafel slope of CoO_x enriched with oxygen vacancies was calculated to be approximately 65 mV/dec, which was much smaller than the $Co(OH)_2$ (97 mV/dec) and CoO-cal (90 mV/dec); this indicated that faster OER kinetics can be achieved by introducing oxygen vacancies. The activities of CoO_x-4h,

CoO-cal and $Co(OH)_2$ were also expressed in apparent turnover frequencies (TOFs), assuming that all the metal ions in the nanoplates were active (Table 3.2).[175-177] Furthermore, to evaluate the durability of the catalysts, the chronopotentiometry curve was measured for CoO_x enriched with oxygen vacancies. As illustrated in Figure 3.10E, there is no significant increase in the potential during continuous electrolysis, verifying its reliable stability. High activity with reliable stability enables the wide application of oxygen-vacancy-enriched CoO_x. To gain a deeper understanding of the superior OER performance of CoO_x-4h, cyclic voltammetry (CV) measurements of CoO_x-4h, CoO-cal and $Co(OH)_2$ were performed over a potential range of 1.05 to 1.55 V (v.s. RHE). As shown in Figure 3.10F, for both electrodes, two distinct pairs of redox peaks are observed around 1.15 and 1.45 V, which could be assigned to the Co(III)/Co(II) and Co(IV)/Co(III) conversion process. The increase of oxidation current at higher potential (>1.5 V) is attributed to the water oxidation reaction. Compared to the pristine $Co(OH)_2$, the CoO_x-4h shows a negatively shifted oxidation peak around 1.15 V, indicating the easier formation of Co(III); therefore, demonstrating the higher reactivity of the active sites for OER, which could be attributed to the oxygen vacancies. Moreover, the dramatically increased current density of CoO_x-4h over the entire potential range suggests a much larger electrochemically active surface area. To further confirm the stability of the catalyst, CoO_x-4h after OER cycling was characterized by XPS to verify the valence of cobalt ion and the concentration of oxygen vacancies. As shown in Figure 3.11, neither obvious change of Co^{3+}/Co^{2+} ratio nor concentration of oxygen vacancies were observed, demonstrating good stability of our catalyst.

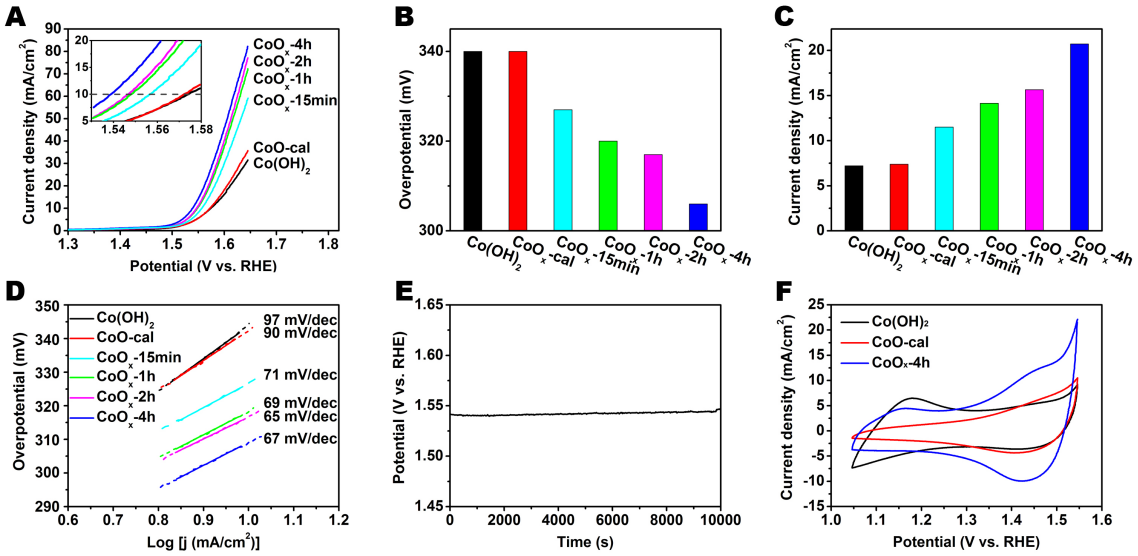

Figure 3.10. (A) LSV curves of the samples. Inset: enlargement of the region near onset. Comparison of (B) overpotential required for a current density of 10 mA/cm^2, (C) current density at an overpotential of 330 mV. (D) Corresponding Tafel plots of the samples. (E) Potential versus time data on a CoO_x-4h electrode for 10000 s at constant current density of 5 mA/cm^2. (F) CVs of $Co(OH)_2$, CoO-cal and CoO_x-4h.

Table 3.1. Comparison of OER performance of CoO_x-4h to recent reported cobalt-based electrocatalysts.

Catalyst	**Electrolyte**	**Overpotential @10mA/cm^2**	**Loading (mg/cm^2)**	**References**
CoMn LDH	1 M KOH	324 mV	0.142	*J. Am. Chem. Soc.,* **2014**,*136*,16481.
Reduced Co_3O_4	1 M KOH	380 mV	0.136	*Adv. Energy Mater.*, **2014**, *4*, 1400696.
Co_3O_4/$NiCo_2O_4$	1 M KOH	340 mV	1	*J. Am. Chem. Soc.*, **2015**, *137*, 5590.
$NiCo_2O_4$ nanosheets	1 M KOH	320 mV	0.285	*Angew. Chem.,* **2015**, *127*, 7507.
Co_3O_4 @ CoO	1 M KOH	430 mV	0.077	*Nat. Commun.,* **2015**, *6*, 8625
CoO nanorods	1 M KOH	330 mV	0.19	*Nat. Commun.,* **2016**, *7*,12876
RuO_2	0.1 M KOH	411 mV	Not given	*J. Phys. Chem. Lett.,* **2014,** *5*, 1636
IrO_2	1 M KOH	338 mV	Not given	*J. Am. Chem. Soc.,* **2013,***135*, 16977
CoO_x-4h nanoplates	**1 M KOH**	**306 mV**	**0.5**	**This work**

Calculation of TOF: The turnover frequency (TOF) value is calculated as follows:[175-177]

$$\mathrm{TOF} = \frac{\mathrm{jS}}{4\mathrm{nF}}$$

Where j is measured current density (mA/cm^2), S is the geometric area of glassy carbon electrode (0.07065 cm^2 for 3 mm glassy carbon electrode), n is the moles of active materials deposited on the working electrode, F is the Faradic constant (96485 C/mol).

Table 3.2. TOFs of CoO_x-4h, $Co(OH)_2$ and CoO-cal at different overpotentials.

	300 mV	320 mV	350 mV
CoO_x-4h	0.0030	0.0056	0.012
$Co(OH)_2$	0.0016	0.0027	0.0054
CoO-cal	0.0013	0.0021	0.0044

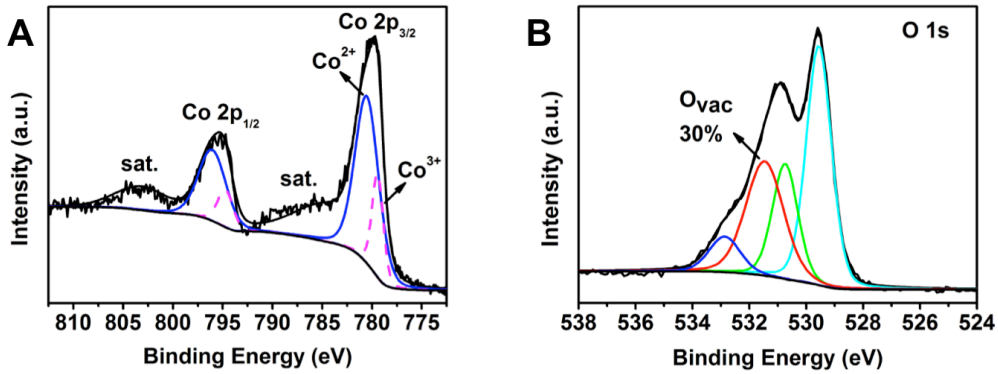

Figure 3.11. (A) Co 2p XPS spectrum and (B) O 1s XPS spectrum of Co_xO-4h after OER cyclings.

3.3.5 Role of Oxygen Vacancies in OER

According to these results, the enhanced OER performance of CoO_x prepared through the ligand-assisted polyol reduction method can be attributed to the synergistic effect of the large surface area and abundant surface oxygen vacancies. The 2D ultrathin nanoplate-like structure of CoO_x provides large surface area, abundant active sites and short diffusion lengths for ions and electrons. Previous work and DFT calculations have confirmed that the oxygen vacancies near the surface lowers the adsorption energy of H_2O and increases active sites around these defects. Oxygen vacancies also enable weaker metal-oxygen bonds to yield faster exchange of intermediates and electrons.[76, 82-83, 148] To elucidate the more important role of oxygen vacancies, the effect of surface area was studied. Firstly, Brunauer-Emmett-Teller (BET) surface area measuring was performed on CoO-cal and CoO_x-4h. As shown in N_2 adsorption/desorption isothermals in Figure 3.12, CoO-cal and CoO_x-4h showed similar surface area of 51.54 and 30.36 m^2/g respectively. However, in the absence of oxygen vacancies, CoO-cal was found to be inferior to CoO_x-4h in catalytic performance. Thus, the improvement of the OER performance upon prolonging the reduction time can be attributed to the increased concentration of oxygen vacancies. Moreover, the relationship between reduction time, oxygen vacancies and OER performance was plotted in Figure 3.13, which further confirmed that oxygen vacancies played a more important role in the superior OER performance of CoO_x-4h.

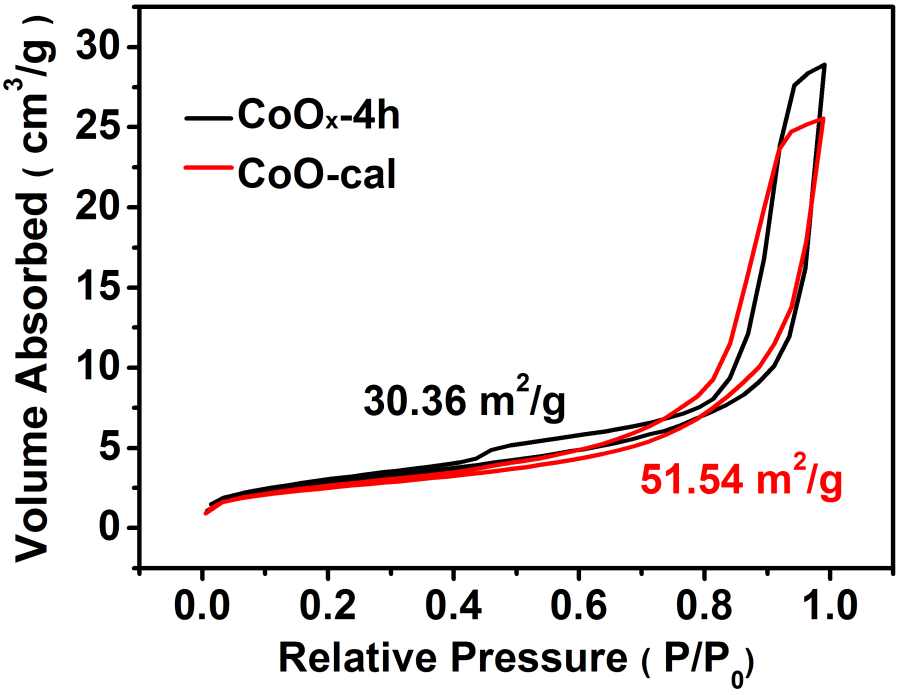

Figure 3.12. N_2 adsorption/desorption isotherms of CoO_x-4h (black curve) and CoO-cal (red curve) and corresponding BET surface area of 30.36 and 51.54 m^2/g.

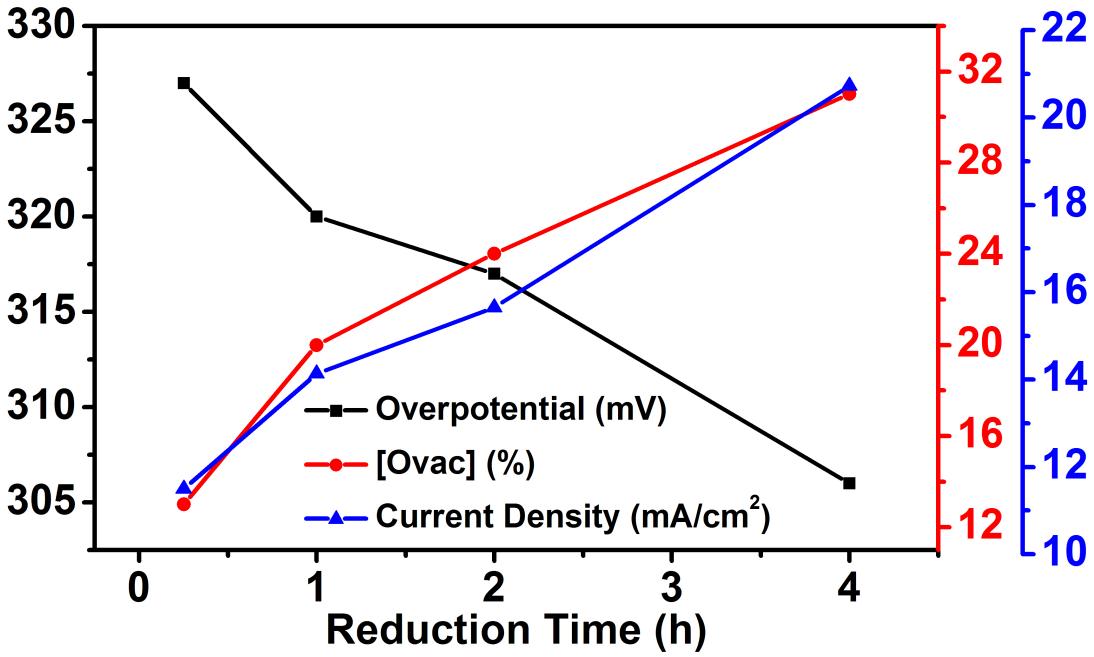

Figure 3.13. Relation between reduction time and concentration of oxygen vacancies (red), overpotentials (black) and current densities (blue).

3.4 Conclusions

In summary, we have developed a ligand-assisted polyol reduction method to produce well-defined cobalt oxide porous nanoplates enriched with controllable oxygen vacancies, which exhibit remarkable OER performance. With the help of a coordinating polymer ligand, the polyol reduction reaction enables successful conversion of $Co(OH)_2$ nanoplates into CoO_x with greatly suppressed morphological deformation and at the same time allows the creation of oxygen vacancies on the nanoplates surface. The concentration of the oxygen vacancies on surface could be conveniently controlled by the reduction time, reaching 31%, which is rarely reported. The large surface area originated from the 2D porous structure and the abundant active sites due to oxygen vacancies are extremely beneficial for OER performance, achieving overpotential values as low as 306 mV at 10 mA/cm^2. Besides providing a new high-performance OER catalyst, this work also proposes a general and scalable strategy to create controllable concentration of oxygen vacancies on the surface of nanoscale materials while preventing significant morphological changes during phase transition.

3.5 References

1. Katsounaros, I.; Cherevko, S.; Zeradjanin, A. R.; Mayrhofer, K. J. J., Oxygen Electrochemistry as a Cornerstone for Sustainable Energy Conversion. *Angew. Chem., Int. Ed.* **2014,** *53* (1), 102-121.

2. Liu, Y.; Cheng, H.; Lyu, M.; Fan, S.; Liu, Q.; Zhang, W.; Zhi, Y.; Wang, C.; Xiao, C.; Wei, S.; Ye, B.; Xie, Y., Low Overpotential in Vacancy-Rich Ultrathin CoSe2 Nanosheets for Water Oxidation. *J. Am. Chem. Soc.* **2014,** *136* (44), 15670-15675.

3. Tung, C.-W.; Hsu, Y.-Y.; Shen, Y.-P.; Zheng, Y.; Chan, T.-S.; Sheu, H.-S.; Cheng, Y.-C.; Chen, H. M., Reversible adapting layer produces robust single-crystal electrocatalyst for oxygen evolution. *Nat Commun* **2015,** *6*.

4. Wang, J.; Tang, H.; Wang, H.; Yu, R.; Wang, D., Multi-shelled hollow micro-/nanostructures: promising platforms for lithium-ion batteries. *Mater. Chem. Front.* **2017,** *1* (3), 414-430.

5. Tao, L.; Lin, C.-Y.; Dou, S.; Feng, S.; Chen, D.; Liu, D.; Huo, J.; Xia, Z.; Wang, S., Creating coordinatively unsaturated metal sites in metal-organic-frameworks as efficient electrocatalysts for the oxygen evolution reaction: Insights into the active centers. *Nano Energy* **2017,** *41* (Supplement C), 417-425.

6. Long, X.; Li, J.; Xiao, S.; Yan, K.; Wang, Z.; Chen, H.; Yang, S., A Strongly Coupled Graphene and FeNi Double Hydroxide Hybrid as an Excellent Electrocatalyst for the Oxygen Evolution Reaction. *Angew. Chem., Int. Ed.* **2014,** *53* (29), 7584-7588.

7. Jiang, N.; You, B.; Sheng, M.; Sun, Y., Electrodeposited Cobalt-Phosphorous-Derived Films as Competent Bifunctional Catalysts for Overall Water Splitting. *Angew. Chem., Int. Ed.* **2015,** *54* (21), 6251-6254.

8. Zhu, Y.; Zhou, W.; Chen, Z.-G.; Chen, Y.; Su, C.; Tadé, M. O.; Shao, Z., SrNb0.1Co0.7Fe0.2O3−δ Perovskite as a Next-Generation Electrocatalyst for Oxygen Evolution in Alkaline Solution. *Angew. Chem., Int. Ed.* **2015,** *54* (13), 3897-3901.

9. Lim, B.; Jiang, M.; Camargo, P. H. C.; Cho, E. C.; Tao, J.; Lu, X.; Zhu, Y.; Xia, Y., Pd-Pt Bimetallic Nanodendrites with High Activity for Oxygen Reduction. *Science* **2009,** *324* (5932), 1302-1305.

10. Danilovic, N.; Subbaraman, R.; Chang, K. C.; Chang, S. H.; Kang, Y.; Snyder, J.; Paulikas, A. P.; Strmcnik, D.; Kim, Y. T.; Myers, D.; Stamenkovic, V. R.; Markovic, N.

M., Using Surface Segregation To Design Stable Ru-Ir Oxides for the Oxygen Evolution Reaction in Acidic Environments. *Angew. Chem., Int. Ed.* **2014,** *53* (51), 14016-14021.

11. Exner, K. S.; Anton, J.; Jacob, T.; Over, H., Controlling Selectivity in the Chlorine Evolution Reaction over RuO2-Based Catalysts. *Angew. Chem., Int. Ed.* **2014,** *53* (41), 11032-11035.

12. Qi, J.; Lai, X.; Wang, J.; Tang, H.; Ren, H.; Yang, Y.; Jin, Q.; Zhang, L.; Yu, R.; Ma, G.; Su, Z.; Zhao, H.; Wang, D., Multi-shelled hollow micro-/nanostructures. *Chem. Soc. Rev.* **2015,** *44* (19), 6749-6773.

13. Guo, S.; Yang, Y.; Liu, N.; Qiao, S.; Huang, H.; Liu, Y.; Kang, Z., One-step synthesis of cobalt, nitrogen-codoped carbon as nonprecious bifunctional electrocatalyst for oxygen reduction and evolution reactions. *Sci Bull* **2016,** *61* (1), 68-77.

14. Chen, S.; Duan, J.; Jaroniec, M.; Qiao, S. Z., Three-Dimensional N-Doped Graphene Hydrogel/NiCo Double Hydroxide Electrocatalysts for Highly Efficient Oxygen Evolution. *Angew. Chem., Int. Ed.* **2013,** *52* (51), 13567-13570.

15. Tang, C.; Cheng, N.; Pu, Z.; Xing, W.; Sun, X., NiSe Nanowire Film Supported on Nickel Foam: An Efficient and Stable 3D Bifunctional Electrode for Full Water Splitting. *Angew. Chem., Int. Ed.* **2015,** *54* (32), 9351-9355.

16. Wang, J.; Li, K.; Zhong, H.-x.; Xu, D.; Wang, Z.-l.; Jiang, Z.; Wu, Z.-j.; Zhang, X.-b., Synergistic Effect between Metal–Nitrogen–Carbon Sheets and NiO Nanoparticles for Enhanced Electrochemical Water-Oxidation Performance. *Angew. Chem., Int. Ed.* **2015,** *54* (36), 10530-10534.

17. Liu, G.; Li, P.; Zhao, G.; Wang, X.; Kong, J.; Liu, H.; Zhang, H.; Chang, K.; Meng, X.; Kako, T.; Ye, J., Promoting Active Species Generation by Plasmon-Induced Hot-Electron Excitation for Efficient Electrocatalytic Oxygen Evolution. *J. Am. Chem. Soc.* **2016,** *138* (29), 9128-9136.

18. Lyu, F.; Bai, Y.; Wang, Q.; Wang, L.; Zhang, X.; Yin, Y., Phase-controllable synthesis of cobalt hydroxide for electrocatalytic oxygen evolution. *Dalton Trans.* **2017**.

19. Wang, J.; Yang, N.; Tang, H.; Dong, Z.; Jin, Q.; Yang, M.; Kisailus, D.; Zhao, H.; Tang, Z.; Wang, D., Accurate Control of Multishelled Co3O4 Hollow Microspheres as High-Performance Anode Materials in Lithium-Ion Batteries. *Angew. Chem., Int. Ed.* **2013,** *52* (25), 6417-6420.

20. Wang, Y.; Zhang, Y.; Liu, Z.; Xie, C.; Feng, S.; Liu, D.; Shao, M.; Wang, S., Layered Double Hydroxide Nanosheets with Multiple Vacancies Obtained by Dry Exfoliation as Highly Efficient Oxygen Evolution Electrocatalysts. *Angew. Chem., Int.*

Ed. **2017,** *56* (21), 5867-5871.

21. Wang, Q.; Shang, L.; Shi, R.; Zhang, X.; Waterhouse, G. I. N.; Wu, L.-Z.; Tung, C.-H.; Zhang, T., 3D carbon nanoframe scaffold-immobilized Ni3FeN nanoparticle electrocatalysts for rechargeable zinc-air batteries' cathodes. *Nano Energy* **2017,** *40* (Supplement C), 382-389.

22. Lyu, F.; Bai, Y.; Li, Z.; Xu, W.; Wang, Q.; Mao, J.; Wang, L.; Zhang, X.; Yin, Y., Self-Templated Fabrication of CoO–MoO2 Nanocages for Enhanced Oxygen Evolution. *Adv. Funct. Mater.* **2017,** *27* (34), 1702324-n/a.

23. Gong, M.; Li, Y.; Wang, H.; Liang, Y.; Wu, J. Z.; Zhou, J.; Wang, J.; Regier, T.; Wei, F.; Dai, H., An Advanced Ni–Fe Layered Double Hydroxide Electrocatalyst for Water Oxidation. *J. Am. Chem. Soc.* **2013,** *135* (23), 8452-8455.

24. Kim, J.; Yin, X.; Tsao, K.-C.; Fang, S.; Yang, H., Ca2Mn2O5 as Oxygen-Deficient Perovskite Electrocatalyst for Oxygen Evolution Reaction. *J. Am. Chem. Soc.* **2014,** *136* (42), 14646-14649.

25. Petrie, J. R.; Jeen, H.; Barron, S. C.; Meyer, T. L.; Lee, H. N., Enhancing Perovskite Electrocatalysis through Strain Tuning of the Oxygen Deficiency. *J. Am. Chem. Soc.* **2016,** *138* (23), 7252-7255.

26. Xu, L.; Jiang, Q.; Xiao, Z.; Li, X.; Huo, J.; Wang, S.; Dai, L., Plasma-Engraved Co3O4 Nanosheets with Oxygen Vacancies and High Surface Area for the Oxygen Evolution Reaction. *Angew. Chem., Int. Ed.* **2016,** *55* (17), 5277-5281.

27. Yan, D.; Li, Y.; Huo, J.; Chen, R.; Dai, L.; Wang, S., Defect Chemistry of Nonprecious-Metal Electrocatalysts for Oxygen Reactions. *Adv. Mater.*, 1606459-n/a.

28. Chhowalla, M.; Shin, H. S.; Eda, G.; Li, L.-J.; Loh, K. P.; Zhang, H., The chemistry of two-dimensional layered transition metal dichalcogenide nanosheets. *Nat Chem* **2013,** *5* (4), 263-275.

29. Huang, X.; Tan, C.; Yin, Z.; Zhang, H., 25th Anniversary Article: Hybrid Nanostructures Based on Two-Dimensional Nanomaterials. *Adv. Mater.* **2014,** *26* (14), 2185-2204.

30. Fan, H.; Huang, X.; Shang, L.; Cao, Y.; Zhao, Y.; Wu, L.-Z.; Tung, C.-H.; Yin, Y.; Zhang, T., Controllable Synthesis of Ultrathin Transition-Metal Hydroxide Nanosheets and their Extended Composite Nanostructures for Enhanced Catalytic Activity in the Heck Reaction. *Angew. Chem., Int. Ed.* **2016,** *55* (6), 2167-2170.

31. Xiao, X.; Song, H.; Lin, S.; Zhou, Y.; Zhan, X.; Hu, Z.; Zhang, Q.; Sun, J.; Yang,

B.; Li, T.; Jiao, L.; Zhou, J.; Tang, J.; Gogotsi, Y., Scalable salt-templated synthesis of two-dimensional transition metal oxides. *Nat Commun* **2016,** *7*, 11296.

32. Bao, J.; Zhang, X.; Fan, B.; Zhang, J.; Zhou, M.; Yang, W.; Hu, X.; Wang, H.; Pan, B.; Xie, Y., Ultrathin Spinel-Structured Nanosheets Rich in Oxygen Deficiencies for Enhanced Electrocatalytic Water Oxidation. *Angew. Chem., Int. Ed.* **2015,** *54* (25), 7399-7404.

33. Tang, H.; Hessel, C. M.; Wang, J.; Yang, N.; Yu, R.; Zhao, H.; Wang, D., Two-dimensional carbon leading to new photoconversion processes. *Chem. Soc. Rev.* **2014,** *43* (13), 4281-4299.

34. Zhao, Y.; Jia, X.; Chen, G.; Shang, L.; Waterhouse, G. I. N.; Wu, L.-Z.; Tung, C.-H.; O'Hare, D.; Zhang, T., Ultrafine NiO Nanosheets Stabilized by TiO2 from Monolayer NiTi-LDH Precursors: An Active Water Oxidation Electrocatalyst. *J. Am. Chem. Soc.* **2016,** *138* (20), 6517-6524.

35. Wang, Q.; Shang, L.; Shi, R.; Zhang, X.; Zhao, Y.; Waterhouse, G. I. N.; Wu, L.-Z.; Tung, C.-H.; Zhang, T., NiFe Layered Double Hydroxide Nanoparticles on Co,N-Codoped Carbon Nanoframes as Efficient Bifunctional Catalysts for Rechargeable Zinc–Air Batteries. *Adv. Energy Mater.*, 1700467-n/a.

36. Cheng, F.; Zhang, T.; Zhang, Y.; Du, J.; Han, X.; Chen, J., Enhancing Electrocatalytic Oxygen Reduction on MnO2 with Vacancies. *Angew. Chem., Int. Ed.* **2013,** *52* (9), 2474-2477.

37. Ling, T.; Yan, D.-Y.; Jiao, Y.; Wang, H.; Zheng, Y.; Zheng, X.; Mao, J.; Du, X.-W.; Hu, Z.; Jaroniec, M.; Qiao, S.-Z., Engineering surface atomic structure of single-crystal cobalt (II) oxide nanorods for superior electrocatalysis. *Nat. Commun.* **2016,** *7*, 12876.

38. Zhuang, L.; Ge, L.; Yang, Y.; Li, M.; Jia, Y.; Yao, X.; Zhu, Z., Ultrathin Iron-Cobalt Oxide Nanosheets with Abundant Oxygen Vacancies for the Oxygen Evolution Reaction. *Adv. Mater.* **2017,** *29* (17), 1606793.

39. Liu, Z.; Zhao, Z.; Wang, Y.; Dou, S.; Yan, D.; Liu, D.; Xia, Z.; Wang, S., In Situ Exfoliated, Edge-Rich, Oxygen-Functionalized Graphene from Carbon Fibers for Oxygen Electrocatalysis. *Adv. Mater.* **2017,** *29* (18), 1606207-n/a.

40. Rodriguez, J. A.; Hanson, J. C.; Frenkel, A. I.; Kim, J. Y.; Pérez, M., Experimental and Theoretical Studies on the Reaction of H2 with NiO: Role of O Vacancies and Mechanism for Oxide Reduction. *J. Am. Chem. Soc.* **2002,** *124* (2), 346-354.

41. Xu, W.; Wang, M.; Li, Z.; Wang, X.; Wang, Y.; Xing, M.; Yin, Y., Chemical Transformation of Colloidal Nanostructures with Morphological Preservation by Surface-Protection with Capping Ligands. *Nano Lett.* **2017,** *17* (4), 2713-2718.

42. Liu, Z.; Ma, R.; Osada, M.; Takada, K.; Sasaki, T., Selective and Controlled Synthesis of α- and β-Cobalt Hydroxides in Highly Developed Hexagonal Platelets. *J. Am. Chem. Soc.* **2005,** *127* (40), 13869-13874.

43. Jia, C.-J.; Schwickardi, M.; Weidenthaler, C.; Schmidt, W.; Korhonen, S.; Weckhuysen, B. M.; Schüth, F., Co3O4–SiO2 Nanocomposite: A Very Active Catalyst for CO Oxidation with Unusual Catalytic Behavior. *J. Am. Chem. Soc.* **2011,** *133* (29), 11279-11288.

44. Liao, L.; Zhang, Q.; Su, Z.; Zhao, Z.; Wang, Y.; Li, Y.; Lu, X.; Wei, D.; Feng, G.; Yu, Q.; Cai, X.; Zhao, J.; Ren, Z.; Fang, H.; Robles-Hernandez, F.; Baldelli, S.; Bao, J., Efficient solar water-splitting using a nanocrystalline CoO photocatalyst. *Nat Nano* **2014,** *9* (1), 69-73.

45. Lou, Y.; Ma, J.; Cao, X.; Wang, L.; Dai, Q.; Zhao, Z.; Cai, Y.; Zhan, W.; Guo, Y.; Hu, P.; Lu, G.; Guo, Y., Promoting Effects of In2O3 on Co3O4 for CO Oxidation: Tuning O2 Activation and CO Adsorption Strength Simultaneously. *ACS Catalysis* **2014,** *4* (11), 4143-4152.

46. Mei, W.; Huang, J.; Zhu, L.; Ye, Z.; Mai, Y.; Tu, J., Synthesis of porous rhombus-shaped Co3O4 nanorod arrays grown directly on a nickel substrate with high electrochemical performance. *J. Mater. Chem.* **2012,** *22* (18), 9315-9321.

47. Deng, D.; Xing, X.; Chen, N.; Li, Y.; Wang, Y., Hydrothermal synthesis of β-Co(OH)2 nanoplatelets: A novel catalyst for CO oxidation. *J. Phys. Chem. Solids* **2017,** *100* (Supplement C), 107-114.

48. Ge, Y.; Kan, K.; Yang, Y.; Zhou, L.; Jing, L.; Shen, P.; Li, L.; Shi, K., Highly mesoporous hierarchical nickel and cobalt double hydroxide composite: fabrication, characterization and ultrafast NOx gas sensors at room temperature. *J. Mater. Chem. A* **2014,** *2* (14), 4961-4969.

49. Wang, H.; Qing, C.; Guo, J.; Aref, A. A.; Sun, D.; Wang, B.; Tang, Y., Highly conductive carbon-CoO hybrid nanostructure arrays with enhanced electrochemical performance for asymmetric supercapacitors. *J. Mater. Chem. A* **2014,** *2* (30), 11776-11783.

50. Ma, M.; Zhang, K.; Li, P.; Jung, M. S.; Jeong, M. J.; Park, J. H., Dual Oxygen and Tungsten Vacancies on a WO3 Photoanode for Enhanced Water Oxidation. *Angew. Chem., Int. Ed.* **2016,** *55* (39), 11819-11823.

51. Cong, Y.; Zhang, J.; Chen, F.; Anpo, M., Synthesis and Characterization of Nitrogen-Doped TiO2 Nanophotocatalyst with High Visible Light Activity. *J. Phys. Chem. C* **2007,** *111* (19), 6976-6982.

52. Song, F.; Hu, X., Ultrathin Cobalt–Manganese Layered Double Hydroxide Is an Efficient Oxygen Evolution Catalyst. *J. Am. Chem. Soc.* **2014,** *136* (47), 16481-16484.

53. Hu, H.; Guan, B.; Xia, B.; Lou, X. W., Designed Formation of Co3O4/NiCo2O4 Double-Shelled Nanocages with Enhanced Pseudocapacitive and Electrocatalytic Properties. *J. Am. Chem. Soc.* **2015,** *137* (16), 5590-5595.

54. Stoerzinger, K. A.; Qiao, L.; Biegalski, M. D.; Shao-Horn, Y., Orientation-Dependent Oxygen Evolution Activities of Rutile IrO2 and RuO2. *J. Phys. Chem. Lett.* **2014,** *5* (10), 1636-1641.

55. McCrory, C. C. L.; Jung, S.; Peters, J. C.; Jaramillo, T. F., Benchmarking Heterogeneous Electrocatalysts for the Oxygen Evolution Reaction. *J. Am. Chem. Soc.* **2013,** *135* (45), 16977-16987.

56. Bergmann, A.; Martinez-Moreno, E.; Teschner, D.; Chernev, P.; Gliech, M.; de Araújo, J. F.; Reier, T.; Dau, H.; Strasser, P., Reversible amorphization and the catalytically active state of crystalline Co3O4 during oxygen evolution. *Nat. Commun.* **2015,** *6*, 8625.

57. Wang, Y.; Zhou, T.; Jiang, K.; Da, P.; Peng, Z.; Tang, J.; Kong, B.; Cai, W.-B.; Yang, Z.; Zheng, G., Reduced Mesoporous Co3O4 Nanowires as Efficient Water Oxidation Electrocatalysts and Supercapacitor Electrodes. *Adv. Energy Mater.* **2014,** *4* (16), 1400696-1400703.

58. Song, F.; Hu, X., Exfoliation of layered double hydroxides for enhanced oxygen evolution catalysis. *Nat. Commun.* **2014,** *5*, 4477.

59. Gao, M.; Sheng, W.; Zhuang, Z.; Fang, Q.; Gu, S.; Jiang, J.; Yan, Y., Efficient Water Oxidation Using Nanostructured α-Nickel-Hydroxide as an Electrocatalyst. *J. Am. Chem. Soc.* **2014,** *136* (19), 7077-7084.

60. Wu, L.; Li, Q.; Wu, C. H.; Zhu, H.; Mendoza-Garcia, A.; Shen, B.; Guo, J.; Sun, S., Stable Cobalt Nanoparticles and Their Monolayer Array as an Efficient Electrocatalyst for Oxygen Evolution Reaction. *J. Am. Chem. Soc.* **2015,** *137* (22), 7071-7074.

Chapter 4

Metal Sulfides as Excellent Co-catalysts for H_2O_2 Decomposition in Advanced Oxidation Processes

4.1 Introduction

Advanced Oxidation Processes (AOPs) have been widely used for the removal of persistent pollutants from contaminated water by the •OH radicals generated from the decomposition of H_2O_2[178-179]. As the efficiency of the decomposition of H_2O_2 is very low, it usually operates in the presence of catalysts such as Fe^{2+} or Cu^{2+} ions. A conventional AOP involving Fe^{2+}/H_2O_2 proceeds through the following equations:

$$Fe^{2+}+H_2O_2 \rightarrow Fe^{3+}+OH^-+\bullet OH \qquad k_1 = (40 \sim 80\ L\cdot mol^{-1}\cdot s^{-1}) \qquad (1)$$

$$Fe^{3+}+H_2O_2 \rightarrow Fe^{2+}+\bullet O_2H+H^+ \qquad k_2 = (9.1\times 10^{-7}\ L\cdot mol^{-1}\cdot s^{-1}) \qquad (2)$$

$$Fe^{3+}+\bullet O_2H \rightarrow Fe^{2+}+O_2+H^+ \qquad k_3 = (0.33 \sim 2.1\times 10^{6}\ L\cdot mol^{-1}\cdot s^{-1}) \qquad (3)$$

The rate-limiting step of Eq. (2) determines the overall efficiency of this reaction, which is still low even with the assistance of the catalysts, so that a large quantity of H_2O_2 and catalysts are required, making the AOPs too expensive for large-scale applications in wastewater treatment[180-181]. For practical industrial settings, a large amount of Fe^{2+} (18~410 mmol/L) and H_2O_2 (30~6000 mmol/L) are generally required in order to produce •OH of sufficient concentrations[178, 182-184]. Owing to the high efficiency of Eq.

(1) but low efficiency of Eq. (2), an excessive amount of Fe^{3+} ions are generated, which leads to the formation of sludge (iron cement) and therefore catalyst poisoning[185]. On the other hand, too much H_2O_2 used in the AOPs will corrode the equipment and greatly increase the operating costs[186]. Many efforts have been made to optimize the AOPs and particularly the efficiency of Eq. (2), for example by adding various materials as "co-catalysts" for enhancing the generation of •OH[187-189]. However, nearly all the previous reports on co-catalytic AOPs focused on the use of organic matters as the co-catalysts, including nitrilotriacetic acid[190], salen[191], protocatechuic acid[192], quinone-hydroquinone analogues[189], and cysteine[184, 193], etc., which acted as iron chelators or promoters to prevent iron (III) from precipitation and accelerate the Fe^{3+}/Fe^{2+} conversion. Unfortunately, the organic co-catalysts would easily cause secondary pollution and make it very difficult to achieve complete mineralization of the organic molecules (with total organic carbon (TOC) degradation rate of below 20%)[184]. Furthermore, the AOPs with organic co-catalysts were difficult to maintain a stable activity due to the self-degradation induced by the oxidation of the co-catalysts by •OH[194]. It is therefore of great economic and environmental interests to develop inorganic co-catalysts, which usually have a higher chemical stability than the organic matters[195], for improving the overall efficiency of AOPs by maximizing the decomposition efficiency of H_2O_2 and minimizing the required dosage of H_2O_2 and Fe^{2+} species. In addition to co-catalysts, light illumination has also been incorporated into AOPs to promote the efficiency. Up to now, ultraviolet light has been used in most of such efforts as it is more energetic than visible light[196-198],

which however also brings additional problems such as harmful effect to human health and increased processing cost.

Herein, we report that metal sulfides (MoS_2, WS_2, Cr_2S_3, CoS, PbS or ZnS) can serve as excellent co-catalysts to greatly increase the efficiency of H_2O_2 decomposition and significantly decrease the consumption of H_2O_2 (0.4 mmol/L) and Fe^{2+} (0.07 mmol/L) in AOPs. The unsaturated S atoms on the surface of metal sulfides can capture protons from the solution to form H_2S, and at the same time expose reductive metallic active sites to greatly accelerate the rate-limiting step of Fe^{3+}/Fe^{2+} conversion. More interestingly, we find that the efficiency of the AOPs involving metal sulfide co-catalysts can be further enhanced by illumination with visible light, thanks to the light-induced sensitization of organic pollutants. In particular, by adding MoS_2 as the co-catalyst for AOPs, the reaction rate constant (*K*a) for the degradation of rhodamine B (RhB) increased by 18.5 times than that of the conventional AOPs, and the TOC degradation rate can remain 90% even after repeated reactions for 10 cycles. Furthermore, this cost-effective system can directly decrease the Chemical Oxygen Demand (COD) of actual wastewater from 10400 mg/L to 360 mg/L at a record low dosage of H_2O_2 and Fe^{2+}, greatly enhancing the value of AOPs for the practical applications of H_2O_2–based AOP technologies.

4.2 Materials and Methods

4.2.1 Materials

Commercial MoS_2 (purchased from Aladdin (< 2 μm; other metal sulfides were all purchased from Aladdin,) and Alfa Alfa Aesar (~ 30 μm)), commercial WS_2 (purchased from Strem Chemicals), commercial TiO_2 (purchased from Acros Organics, anatase), distilled water, hydrogen peroxide (30% wt), rhodamine B (RhB), ferrous sulfate ($FeSO_4 \cdot 7H_2O$). All the chemicals are used without further purification.

4.2.2 Metal Sulfides Co-catalytic AOPs

A certain amount of commercial metal sulfides such as MoS_2 was added into 100 mL RhB, phenol (20 mg/L), or actual wastewater solution (COD: 10400 mg/L, purchased from the chemical industrial wastewater) and followed by 20 seconds ultrasonic treatment to make it dispersion. And then 0.002 g $FeSO_4 \cdot 7H_2O$ was added into the solution. After the pH value being fixed at 3.8～4.0 by the adjustment of HCl (0.1 M), 4.0 μL H_2O_2 (30% wt) was added into the solution by the pipette. The above mixed

solution was placed in the dark or irradiated with the tungsten lamp (> 420 nm, 1000W) or the mercury lamp (300W, ~365 nm) for different time. The comparison experiment of conventional AOPs was carried out by using the similar procedure in the absence of MoS_2.

4.2.3 Detection of Generated •OH

The number of the •OH generated during the MoS_2 co-catalytic AOPs was detected by the measurement of the PL signal of hydroxybenzoic acid resulted from the capturing of •OH by the benzoic acid (Supplementary Fig. 7). The details are as follows: 0.030 g MoS_2, 0.002 g $FeSO_4 \cdot 7H_2O$ and a certain amount of benzoic acid (0.2 mmol/L) were mixed into 100 mL H_2O. And then, 4.0 μL H_2O_2 (30% wt) was added into the solution by the pipette. After shaking for 10 seconds by the vortex, the mixed solution was placed under the visible light irradiation for 30 min. The solution was filtered, and the filtrate was measured by the photoluminescence (PL) emission spectroscopy to indirectly measure the amount of •OH (excitation wavelength: 412 nm).

On the other side, 4.0 μL H_2O_2 and a certain amount of benzoic acid (0.2 mmol/L) were mixed with 100 mL H_2O. The mixed solution was reflux at 90 ^oC for 130 min to make the H_2O_2 to be completely decomposed into •OH, which was captured by the benzoic acid

to form the hydroxybenzoic acid with PL signal (Supplementary Fig. 8a). After the reflux, the solution was detected by the PL to calculate the decomposition efficiency of H_2O_2 in the MoS_2 co-catalytic AOPs by the PL intensity division in Supplementary Fig. 8b.

4.2.4 Apparent Kinetic Model

Typically, in our Fenton system, the rate Equation can be described as follows:

$$V = -(dc/dt) = K \cdot [Fe^{2+}]^a [H_2O_2]^b [MoS_2]^c$$

or expressed in terms of logarithms:

$$\lg(-dc/dt) = \lg K + a\lg[Fe^{2+}] + b\lg[H_2O_2] + c\lg[MoS_2]$$

Where *a, b, c* are reaction orders, respectively. *K* represents the total reaction rate constant. Herein, we have specifically analyzed three parameters: the concentration of $FeSO_4 \cdot 7H_2$, H_2O_2 and MoS_2. Assuming that the initial concentration of MoS_2 is $[MoS_2]_0$ in system, the concentration of ferrous ion is $[Fe^{2+}]_0$, the concentration of H_2O_2 is $[H_2O_2]_0$, the rate at t = 0 can be expressed as follows:

$$V = -(dc/dt) = K [Fe^{2+}]_0^a [H_2O_2]_0^b [MoS_2]_0^c$$

or in terms of logarithms：

$-\lg(dc/dt) = \lg K + a\lg[Fe^{2+}]_0 + b\lg[H_2O_2]_0 + c\lg[MoS_2]_0$

We employed a series of different concentrations of ferrous ions in RhB solution, but with the same concentrations of MoS_2 and H_2O_2. Then we record RhB concentration versus time curve. We can get the equations of these curves, which use "t" as independent variable and "c" as the dependent variable in the equation, respectively. And we find the derivative of the equation when t = 0, which is equal to –lg(dc/dt) at different $[Fe^{2+}]_0$. Meanwhile, we can get a group of related data, and -lg(dc/dt) is versus to $\lg[Fe^{2+}]_0$.

Since the amounts of MoS_2 and H_2O_2 are fixed, the $\lg K + b[H_2O_2]_0 + c[MoS_2]_0$ is a constant. Thus –lg(dc/dt) is linear to $\lg[Fe^{2+}]_0$. We can get a straight line, using $\lg[Fe^{2+}]_0$ as abscissa, and -lg(dc/dt) is used as Y-axis. The slope is "*a*", and the intercept is "$\lg K + b[H_2O_2]_0 + c[MoS_2]_0$".

Similarly, we can get the data of "*b*", "$\lg K + a\lg[Fe^{2+}]_0 + c[MoS_2]_0$", "*c*" and "$\lg K + a\lg[Fe^{2+}]_0 + b[H_2O_2]_0$", thereby we can get the value of *K*. Accordingly, we can obtain the apparent kinetic equation of MoS_2 co-catalytic AOPs for the degradation of RhB. The details of calculations and results are shown in Supplementary Fig. 4 and Supplementary Table 1-3.

4.2.5 Characterization

The transmission electron microscopy (TEM) was conducted on a JEOL JEM-2100EX electron microscope, operated at an accelerating voltage of 200 kV. The surface morphologies were observed by scanning electron microscopy (SEM, JEOL.JSM-6360LV). The concentration of the pollutant was measured using a UV–vis spectrophotometer (Shimadzu, UV-2450). Raman measurements were performed at room temperature using a Via^{+} Reflex Raman spectrometer with the excitation wavelength of 514 nm. The intensity of hydroxyl radicals was measured by using luminescence spectrometry (Cary Eclipse) at room temperature under the excitation light at 412 nm. X-ray diffraction measurements (XRD) were performed with a Rigaku Ultima IV (Cu Ka radiation, λ = 1.5406 Å) in the range of 10-80^{o} (2θ). The dissolving of iron cements and MoS_2 were measured by the inductively coupled plasma optical emission spectrometry (ICP-OES, Perkin-Elmer Optima 7300DV ICP-OES apparatus combined an SCD detector and an echelle optical system). The X-band EPR spectra were recorded at room temperature (Varian E-112).

4.3 Results and Discussion

4.3.1 Metal Sulfides Co-catalytic AOPs Performance

We found that commercial 2H-type MoS_2 (< 2 μm, Fig. 4.1) without any additional treatment could serve as a co-catalyst to significantly promote the Fe^{2+}-catalyzed decomposition of H_2O_2. As AOPs are always considered as complex systems and many factors can affect their performance, we first carried out systematic studies to reveal the great impact of MoS_2 to the catalytic performance. Specifically, we used the degradation of RhB as a model reaction and investigated a number of factors that may have influences on AOPs performance, such as the pH value, light irradiation, and dosages of MoS_2, $FeSO_4$, and H_2O_2 (Fig. 4.2). Careful kinetic measurements (Fig. 4.3) revealed that the reaction orders, both in the dark and under the light irradiation when using [MoS_2], were obviously higher than those of [H_2O_2] and [$FeSO_4$] (Eqs. 4,5), indicating that increasing the amount of MoS_2 was much more effective than that of either H_2O_2 or Fe^{2+} in improving the reaction rates of AOPs. It is worth mentioning that the activity for the MoS_2 co-catalytic AOPs under the visible light irradiation is obviously better than that in the dark, owing to the sensitization of RhB by light which is beneficial to the Fe^{2+}/Fe^{3+} cycle. Although significant enhancement can already be obtained in dark, performing the reaction under visible light irradiation may further improve the oxidation power of AOPs.

The apparent kinetic equation in the dark is:

$$V = -\lg(dc/dt) = 7.583\ [FeSO_4]^{-0.76635}[H_2O_2]^{0.30728}[MoS_2]^{0.83229} \qquad (4)$$

And the apparent kinetic equation in the visible light is:

$$V = -\lg(dc/dt) = 9.101\ [FeSO_4]^{-0.76674}[H_2O_2]^{0.25557}[MoS_2]^{0.82500} \qquad (5)$$

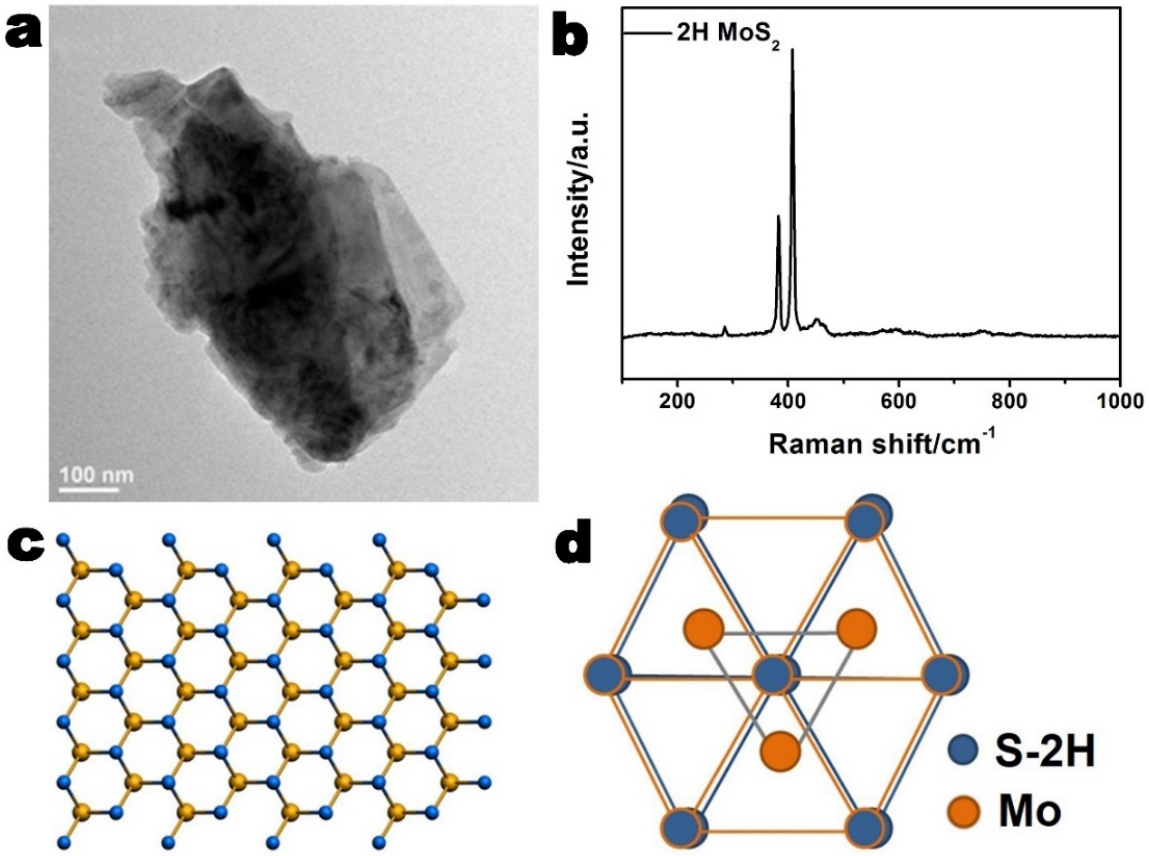

Figure 4.1 | Microstructure characterization of commercial MoS_2. a, TEM image for the commercial MoS_2 (< 2 μm). **b**, Raman spectrum for the commercial MoS_2 (< 2 μm). **c**, Monolayer of 2H-allotropes of MoS_2 composed of prismatic units MoS_6 (the top views are depicted). **d**, Schematic structural model corresponding to the 2H-structure.

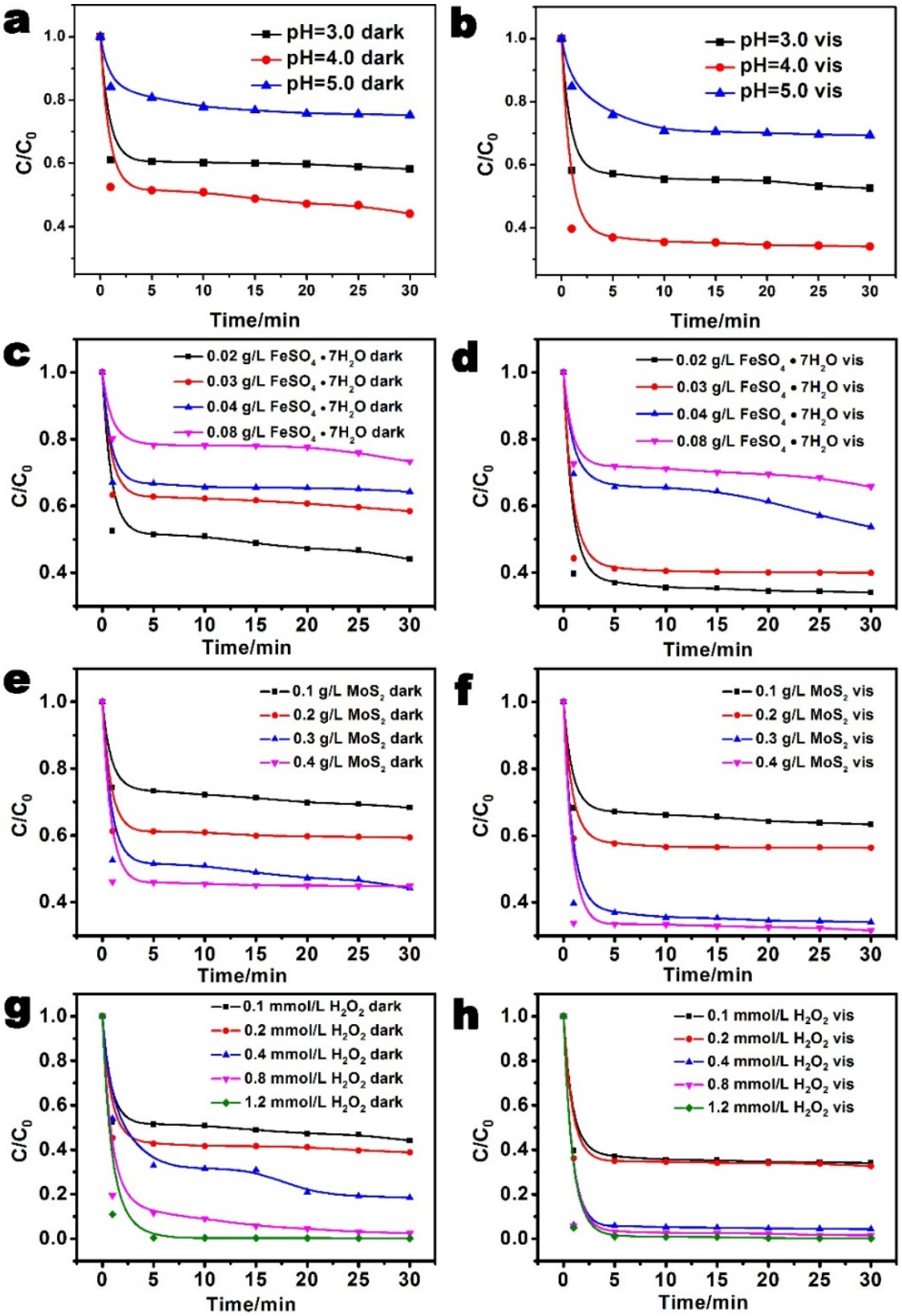
a
pH=3.0 dark
pH=4.0 dark
pH=5.0 dark
b
pH=3.0 vis
pH=4.0 vis
pH=5.0 vis
c
0.02 g/L FeSO4 • 7H2O dark
0.03 g/L FeSO4 • 7H2O dark
0.04 g/L FeSO4 • 7H2O dark
0.08 g/L FeSO4 • 7H2O dark
d
0.02 g/L FeSO4 • 7H2O vis
0.03 g/L FeSO4 • 7H2O vis
0.04 g/L FeSO4 • 7H2O vis
0.08 g/L FeSO4 • 7H2O vis
e
0.1 g/L MoS2 dark
0.2 g/L MoS2 dark
0.3 g/L MoS2 dark
0.4 g/L MoS2 dark
f
0.1 g/L MoS2 vis
0.2 g/L MoS2 vis
0.3 g/L MoS2 vis
0.4 g/L MoS2 vis
g
0.1 mmol/L H2O2 dark
0.2 mmol/L H2O2 dark
0.4 mmol/L H2O2 dark
0.8 mmol/L H2O2 dark
1.2 mmol/L H2O2 dark
h
0.1 mmol/L H2O2 vis
0.2 mmol/L H2O2 vis
0.4 mmol/L H2O2 vis
0.8 mmol/L H2O2 vis
1.2 mmol/L H2O2 vis
C/C0
Time/min

Figure 4.2 | Investigation on the influence factors in the MoS_2 co-catalytic AOPs. a-b, Effect of pH value on the activity of MoS_2 co-catalytic AOPs in the dark (**a**) or under the visible light (**b**) irradiation (100 mL solution included 0.02 g/L $FeSO_4 \cdot 7H_2O$, 0.1 mmol/L H_2O_2, 0.3 g/L MoS_2 and 20 mg/L RhB, which was adjusted the pH value by adding the 0.1 M HCl and irradiated under the visible light (λ > 420 nm) for 30 minutes). **c-d**, Effect of the dosage of initial $FeSO_4 \cdot 7H_2O$ (0.02 g/L, 0.03 g/L, 0.04 g/L, 0.08 g/L) on the activity of AOPs in the dark (**c**) or under the visible light (**d**) irradiation (pH=4, MoS_2: 0.3 g/L, H_2O_2: 0.1 mmol/L; λ> 420 nm). **e-f**, Effect of the dosage of MoS_2 (0.1 g/L, 0.2 g/L, 0.3 g/L, 0.4 g/L) on the activity of AOPs in the dark (**e**) or under the visible light (**f**) irradiation (pH=4, $FeSO_4 \cdot 7H_2O$: 0.02 g/L, H_2O_2: 0.1 mmol/L; λ> 420 nm). **g-h**, Effect of the dosage of initial H_2O_2 (0.1 mmol/L, 0.2 mmol/L, 0.4 mmol/L, 0.8 mmol/L, 1.2 mmol/L) on the activity of AOPs in the dark (**g**) or under the visible light (**h**) irradiation (pH=4, $FeSO_4 \cdot 7H_2O$: 0.02 g/L, MoS_2: 0.3 g/L; λ> 420 nm).

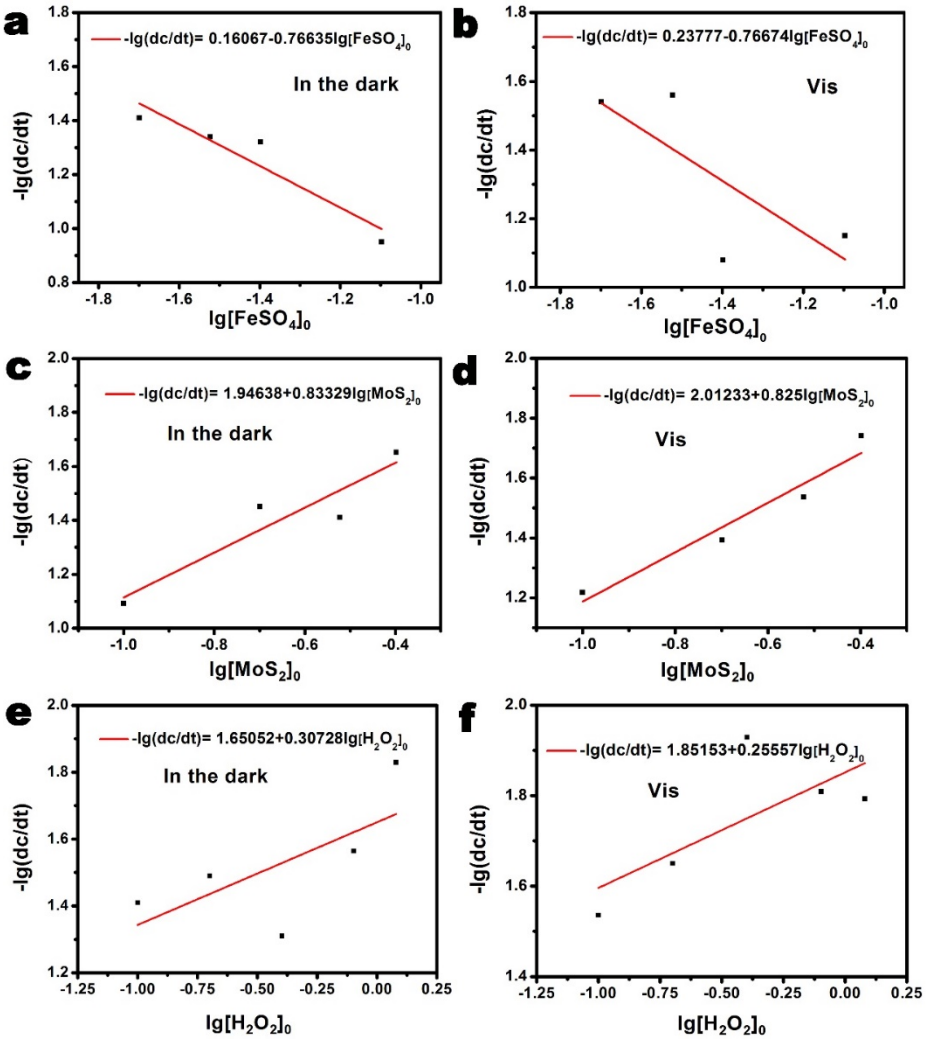

Figure 4.3 | Apparent kinetic calculation. **a**, The fitting line between –lg(dc/dt) and $lg[Fe^{2+}]_0$, in the dark. **b**, The fitting line between –lg(dc/dt) and $lg[Fe^{2+}]_0$, under the visible light irradiation. **c**, The fitting line between –lg(dc/dt) and $lg[MoS_2]_0$, in the dark. **d**, The fitting line between –lg(dc/dt) and $lg[MoS_2]_0$, under the visible light irradiation. **e**, The fitting line between –lg(dc/dt) and $lg[H_2O_2]_0$, in the dark. **f,** The fitting line between –lg(dc/dt) and $lg[H_2O_2]_0$, under the visible light irradiation.

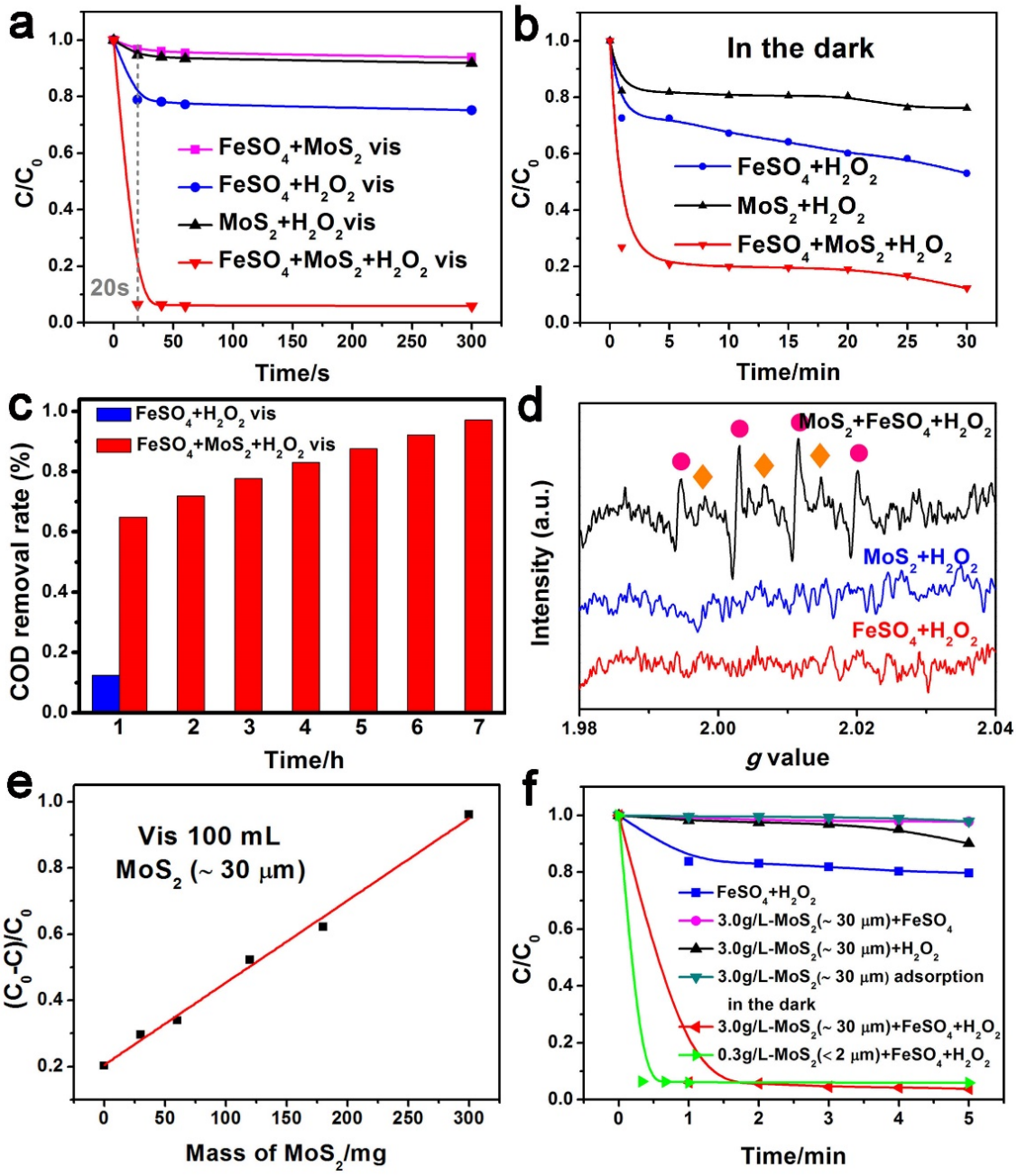
a
C/C0
Time/s
FeSO4+MoS2 vis
FeSO4+H2O2 vis
MoS2+H2O2vis
FeSO4+MoS2+H2O2 vis
20s
b
In the dark
C/C0
Time/min
FeSO4+H2O2
MoS2+H2O2
FeSO4+MoS2+H2O2
c
COD removal rate (%)
Time/h
FeSO4+H2O2 vis
FeSO4+MoS2+H2O2 vis
d
Intensity (a.u.)
g value
MoS2+FeSO4+H2O2
MoS2+H2O2
FeSO4+H2O2
e
Vis 100 mL
MoS2 (~ 30 μm)
(C0-C)/C0
Mass of MoS2/mg
f
C/C0
Time/min
FeSO4+H2O2
3.0g/L-MoS2(~ 30 μm)+FeSO4
3.0g/L-MoS2(~ 30 μm)+H2O2
3.0g/L-MoS2(~ 30 μm) adsorption in the dark
3.0g/L-MoS2(~ 30 μm)+FeSO4+H2O2
0.3g/L-MoS2(< 2 μm)+FeSO4+H2O2

Figure 4.4 | MoS_2 co-catalytic AOPs performance under different conditions. a, Degradation of RhB by AOPs under visible light illumination (λ> 420 nm) under the optimal conditions: 100 mL aqueous solution; 0.02 g/L $Fe(SO_4)\cdot 7H_2O$ (if present), 0.3 g/L MoS_2 (< 2 μm, if present), 0.4 mmol/L H_2O_2, and 20 mg/L RhB. **b**, Degradation of RhB by AOPs in dark for the degradation of RhB under the optimal conditions. **c**, Visible light-driven degradation of real wastewater (fine chemical wastewater) using MoS_2+$FeSO_4$+H_2O_2 AOP system under the optimal conditions (original COD of 10400 mg/L, 0.4 mmol/L H_2O_2 + 0.07 mmol/L Fe^{2+}). **d**. EPR spectra for the detection of •OH in the presence of 5,5-Dimethyl-1-Pyrrolidine-N-oxide (DMPO) at room temperature. **e**, Effect of amount of MoS_2 (~ 30 μm) on the degradation rate of RhB under the visible irradiation for 5 minutes. **f**, Activity comparison of AOPs with differently sized MoS_2 particles as the co-catalyts.

Using the above results, we fixed the optimal reaction conditions as follows: to a 100 mL of water containing 20 mg/L RhB, we added 0.002 g $FeSO_4 \cdot 7H_2O$ (0.07 mmol/L), 0.030 g MoS_2, 0.004 mL H_2O_2 (0.4 mmol/L), and then irradiated the solution with visible light ($\lambda > 420$ nm) for 5 minutes (Fig. 4.4a). Not surprisingly, the RhB was degraded almost completely within 20 seconds, while less than 30% of RhB was decomposed even after 300 s of irradiation in a control experiment where MoS_2 was absent. The degradation of RhB by the MoS_2 and H_2O_2 combination was negligible because the indirect bandgap of multilayered commercial MoS_2 could not drive direct decomposition of H_2O_2 into •OH under visible light irradiation[199-200]. The low activity of $FeSO_4$+MoS_2 in the absence of H_2O_2 confirmed that H_2O_2 was the source of •OH. It is important to highlight that even in the absence of light irradiation the MoS_2 still showed a significant co-catalytic activity in AOPs for the degradation of RhB, which is much better than that of $FeSO_4$+H_2O_2 and MoS_2+H_2O_2 systems (Fig. 4.4b). The enhanced UV-light-driven activity for the degradation of RhB is another indication of the co-catalytic activity of MoS_2 in AOPs (Fig. 4.5). In addition to RhB, MoS_2 can also co-catalyze AOPs for the decomposition of other pollutants, such as the colorless phenol (Fig. 4.6), suggesting its broad applicability for catalytic degradation of organics in wastewater.

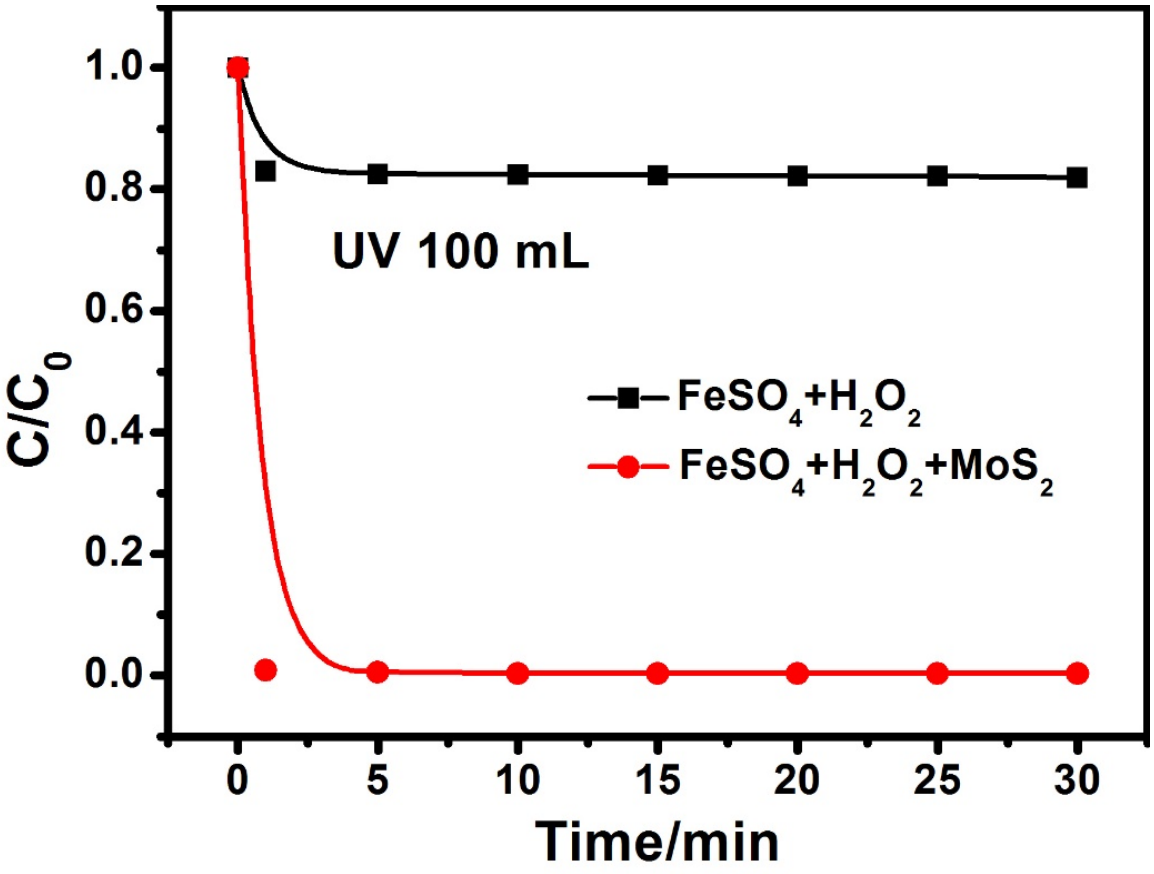

Figure 4.5 | UV light (~365 nm) driven MoS_2 (< 2 μm) co-catalytic AOPs for the degradation of RhB (20 mg/L) under the optimal conditions.

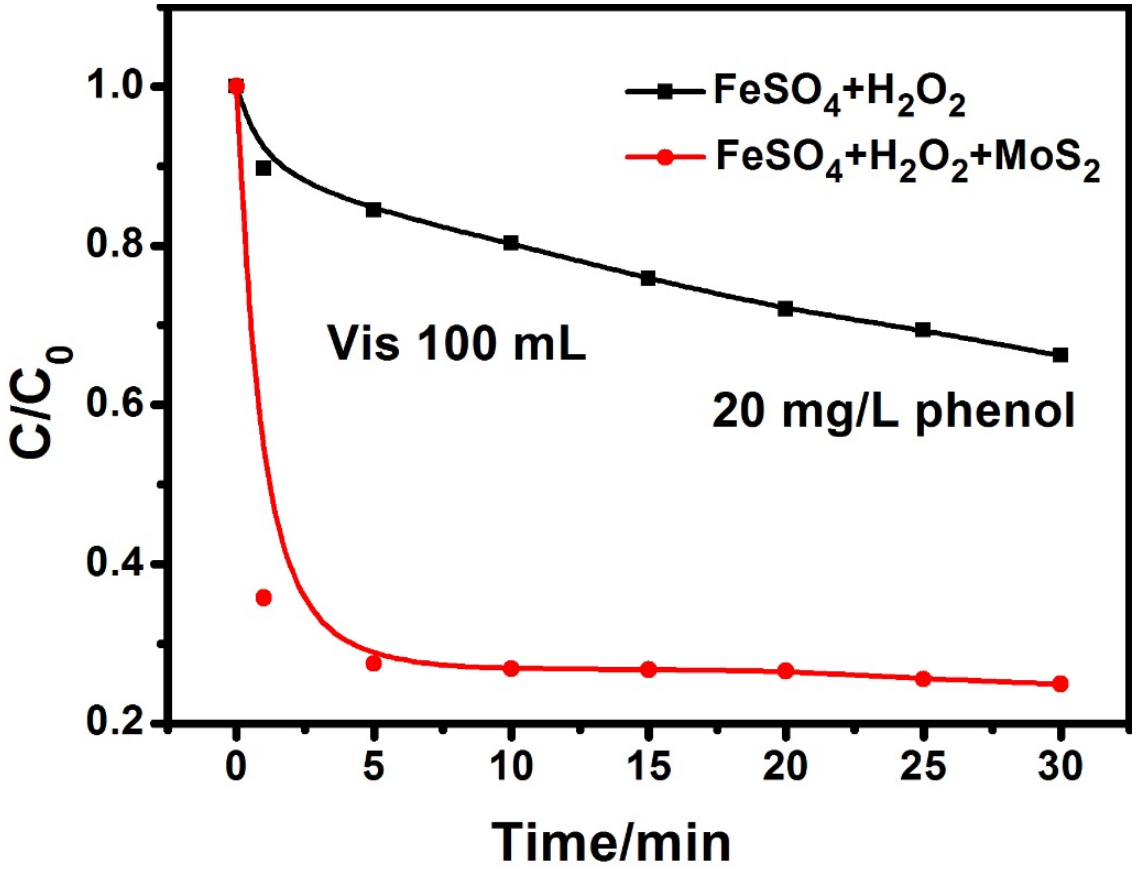

Figure 4.6 | Visible light (λ> 420 nm) driven MoS_2 (< 2 μm) co-catalytic AOPs for the degradation of phenol (20 mg/L) under the optimal conditions.

To further highlight the potential of MoS_2 co-catalytic system for the treatment of real wastewater, we carried out the degradation of fine chemical (benzenoid) wastewater (from a fine chemical factory) which has an original COD of 10400 mg/L (Fig. 4.4c). After 1-h irradiation, the COD removal rate by MoS_2+$FeSO_4$+H_2O_2 has been increased to 65% which was much higher than the case without MoS_2 (12%). And the COD can be further decreased to 360 mg/L after 7-h irradiation, which has reached the China National Grade III water quality discharge standard (GB4287: 500 mg/L). To the best of our knowledge, the MoS_2+$FeSO_4$+H_2O_2 system has set a new record for the cost-effective treatment of wastewater with a high original COD (> 10000 mg/L) using such a low dosage of H_2O_2 and Fe^{2+}. Compared with the very weak electron paramagnetic resonance (EPR) signals over MoS_2+H_2O_2 and $FeSO_4$+H_2O_2 systems, the MoS_2+$FeSO_4$+H_2O_2 system displayed the characteristic quartet signals of •OH (Fig. 4.4d)[201], supporting the observation of efficient co-catalytic activity of MoS_2 for the decomposition of H_2O_2. The yield of •OH in AOPs was measured by recording the increase in the photoluminescence (PL) signal of hydroxybenzoic acid resulting from the capture of •OH by the benzoic acid[202]. Compared to the data of $FeSO_4$+H_2O_2 and $FeSO_4$+MoS_2, the $FeSO_4$+MoS_2+H_2O_2 solution exhibited a significantly enhanced PL signal (Fig. 4.7), which further confirmed the co-catalytic effect of MoS_2 on the conversion of H_2O_2 into •OH. The decomposition efficiency of H_2O_2 represents an important index to evaluate the performance of AOPs. We heated a 0.4 mmol/L solution of H_2O_2 to decompose the H_2O_2 into •OH completely.

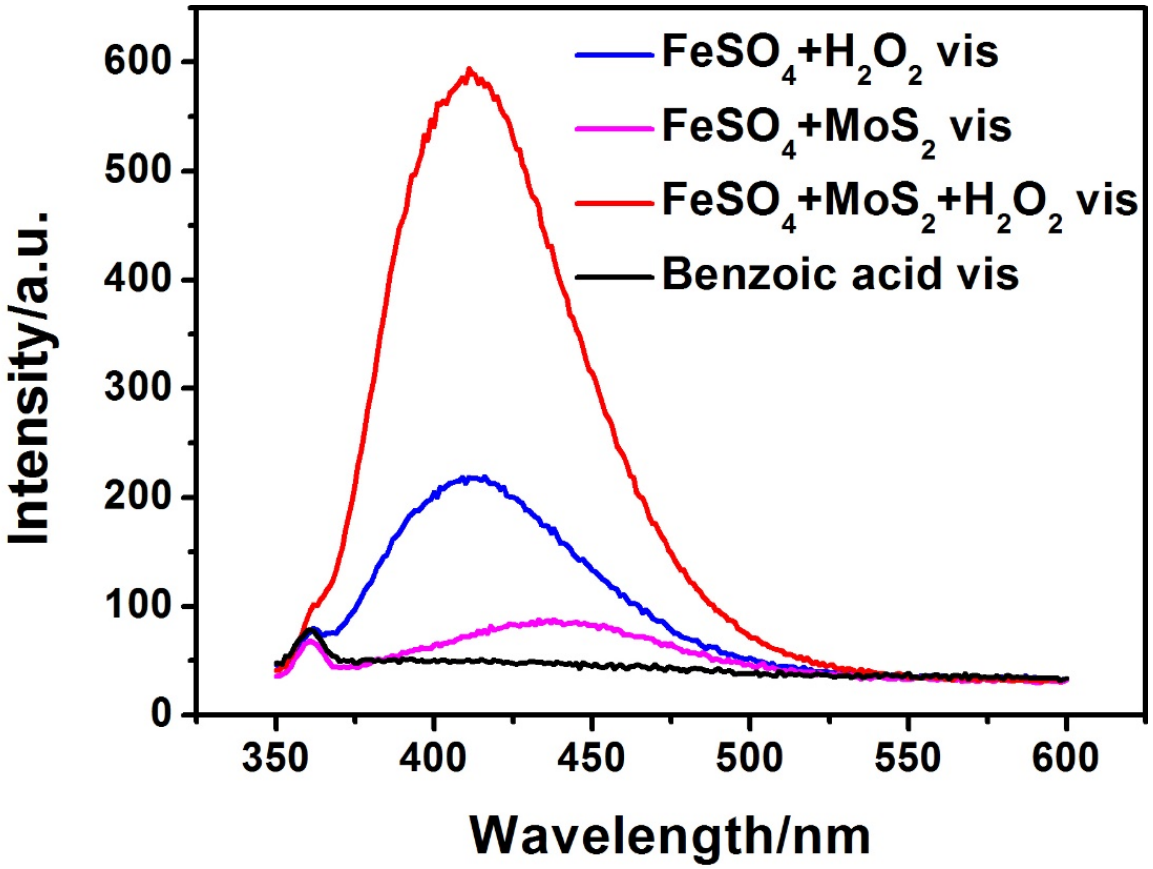

Figure 4.7 | Photoluminescence spectra of blank benzoic acid and benzoic acid mixed with different solutions under the visible light irradiation for 5 minutes.

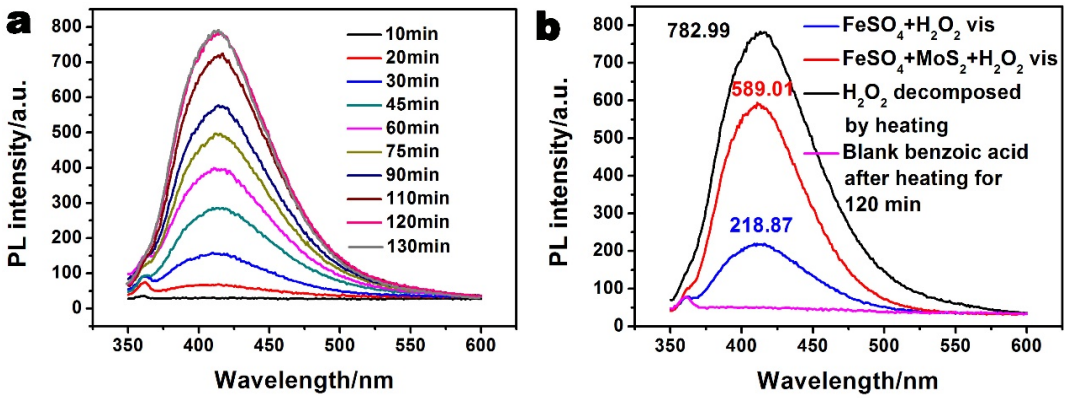

Figure 4.8 | Calculation of the conversion efficiency of H_2O_2 into •OH. a, PL spectra of the H_2O_2 mixed with benzoic acid with the increase of the heating time at 90 ^oC. 4.0 μL H_2O_2 can be completely decomposed in 100 mL aqueous solution by heating it at 90 ^oC for 120 min. **b**, PL spectra of hydroxybenzoic acid generated under different conditions. The decomposition efficiency of H_2O_2 can be obtained by the division of PL intensities.

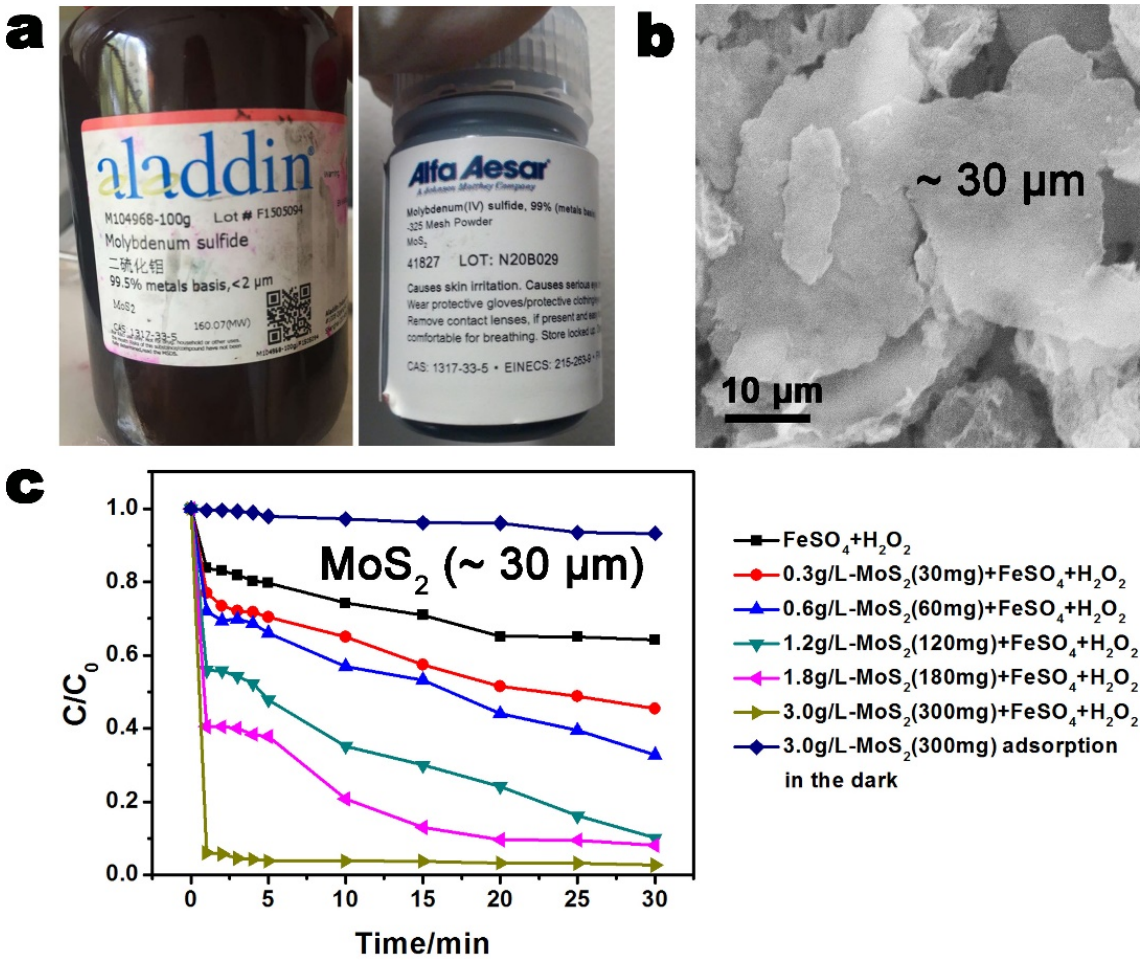

Figure 4.9 | Effect of MoS_2 size on the performance of AOPs. a, Photographs of the commercial MoS_2 purchased from different companies. **b**, SEM image for the commercial MoS_2 with the size of ~30μm purchased from Alfa Aesar. **c**, Effect of the dosage of large sized MoS_2 on the activity of AOPs for the degradation of RhB under the visible light. The dosages of $Fe(SO_4)\cdot 7H_2O$ and H_2O_2 are fixed at 0.02 g/L and 0.4 mmol/L, respectively.

Measurement of the PL intensity by addition of hydroxybenzoic acid was used to calculate the decomposition efficiency of H_2O_2 in the AOPs (Fig. 4.8). Based on the changes in the PL intensities, the conversion efficiency of H_2O_2 into •OH was calculated to be as high as 75.2% due to the promotion by MoS_2, which is much higher than the 28.0% for the conventional AOPs without MoS_2.

The co-catalytic effect of MoS_2 is size and dosage dependent, similar to the typical heterogeneous catalysts. With the same dosage of 0.3 g/L, the larger-sized MoS_2 particles (~ 30 μm, Fig. 4.9a,b) showed a much lower activity toward the degradation of RhB than the smaller ones (< 2 μm, Fig. 4.4a and Fig. 4.9c). As discussed later in detail, the size dependence of the activity can be attributed to the number of exposed edge S atoms on MoS_2 particles. On the other hand, the co-catalytic activity of large-sized MoS_2 grains can be improved by increasing their dosage while keeping the dosages of Fe^{2+} and H_2O_2 constant (Fig. 9c). More interestingly, the activity of the RhB degradation is simply proportional to the mass of added MoS_2. No poisoning effect was observed (Fig. 4.4e), which is consistent with the nature of the co-catalytic effect of MoS_2 in AOPs. Additionally, when the larger-sized MoS_2 (~ 30 μm) particles are increased to 3.0 g/L, the corresponding activity is very similar to that of the smaller MoS_2 (< 2 μm) employed at a dosage of 0.3 g/L (Fig. 4.4f). We found that the AOP activities varied for MoS_2 particles purchased from different companies due to their different size and size distribution, but all showed similar dosage dependence.

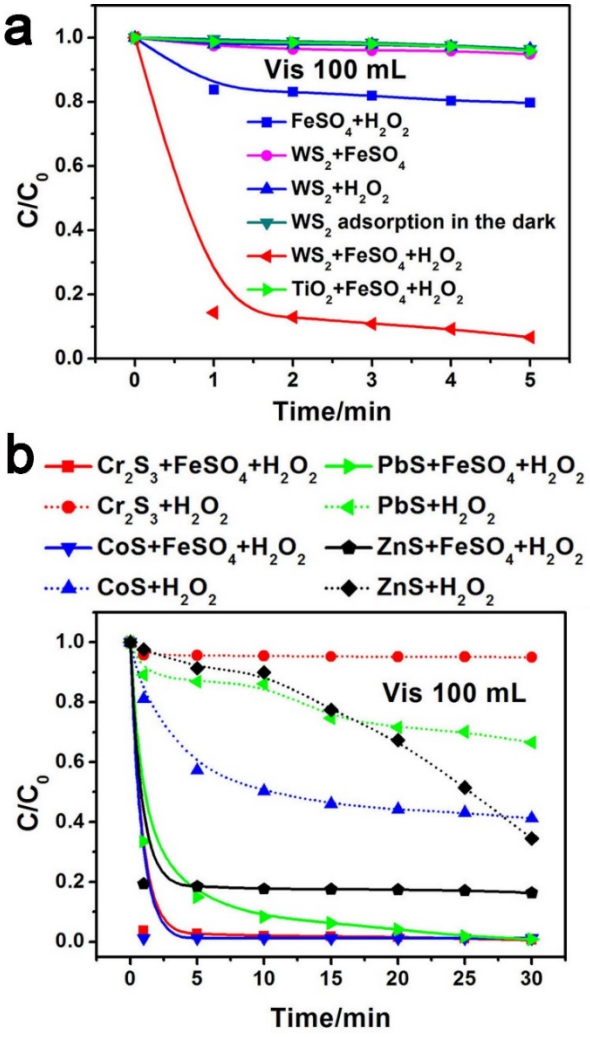

Figure 4.10 | WS_2 and other metal sulfides co-catalytic AOPs performance. a, Degradation of RhB by AOPs under visible light illumination (λ> 420 nm) with WS_2 particles as the co-catalyt: (100 mL solution including 0.02 g/L $Fe(SO_4)\cdot 7H_2O$, 3.0 g/L WS_2 or 3.0 g/L TiO_2, 0.4 mmol/L H_2O_2, and 20 mg/L RhB). **b**, Other metal sulfides (0.3 g/L) as the co-catalysts for H_2O_2 decomposition in AOPs for the degradation of RhB under visible illumination (λ> 420 nm).

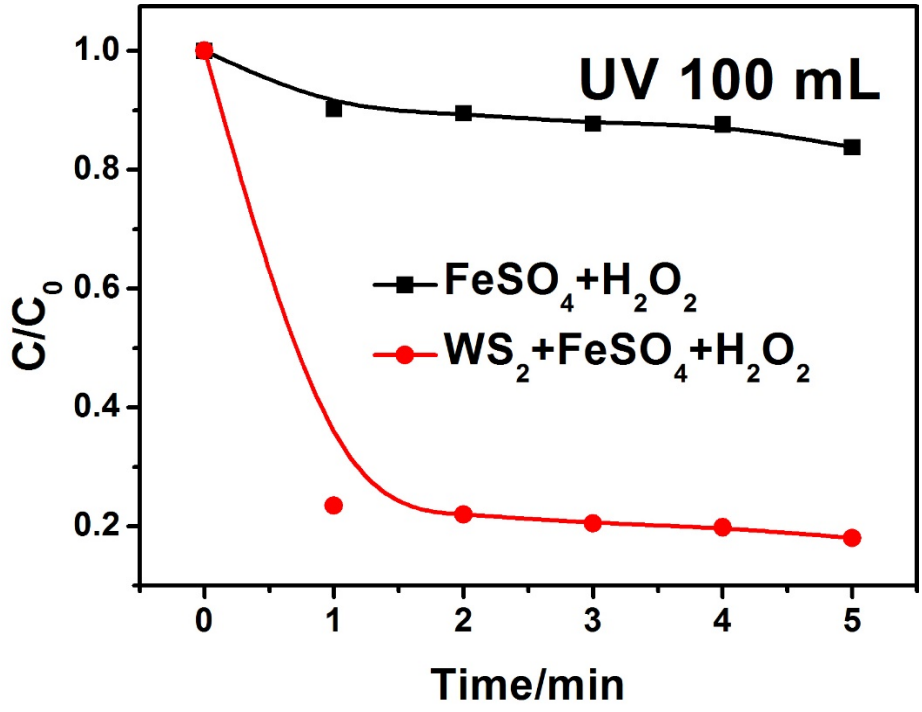

Figure 4.11 | UV light (~365 nm) driven WS_2 co-catalytic AOPs for the degradation of RhB. 100 mL solution including: 0.02 g/L $Fe(SO_4)\cdot 7H_2O$, 3.0 g/L WS_2, 0.4 mmol/L H_2O_2, and 20 mg/L RhB.

We discovered that other metal sulfides with unsaturated S atoms on their surfaces could display a similar co-catalytic effect in AOPs. For instance, WS_2 is similar to MoS_2 in many aspects including crystal structure and physical properties[203-204]. As expected, this compound could also exhibit a co-catalytic effect in AOPs for the degradation of RhB both under visible and UV light irradiation (Fig. 4.10a and Fig. 4.11), likely owing to its role in the acceleration of Fe^{3+}/Fe^{2+} cycle during AOPs. Conversely, semiconductors without the unsaturated S atoms such as the TiO_2 display a very low activity for visible-light-driven AOPs (green line in Fig. 4.10a). In addition to MoS_2 and WS_2, other metal sulfides such as Cr_2S_3, CoS, PbS and ZnS were also found to show a significant enhancement effect to the photo-degradation of RhB (Fig. 4.10b and Fig. 4.12).

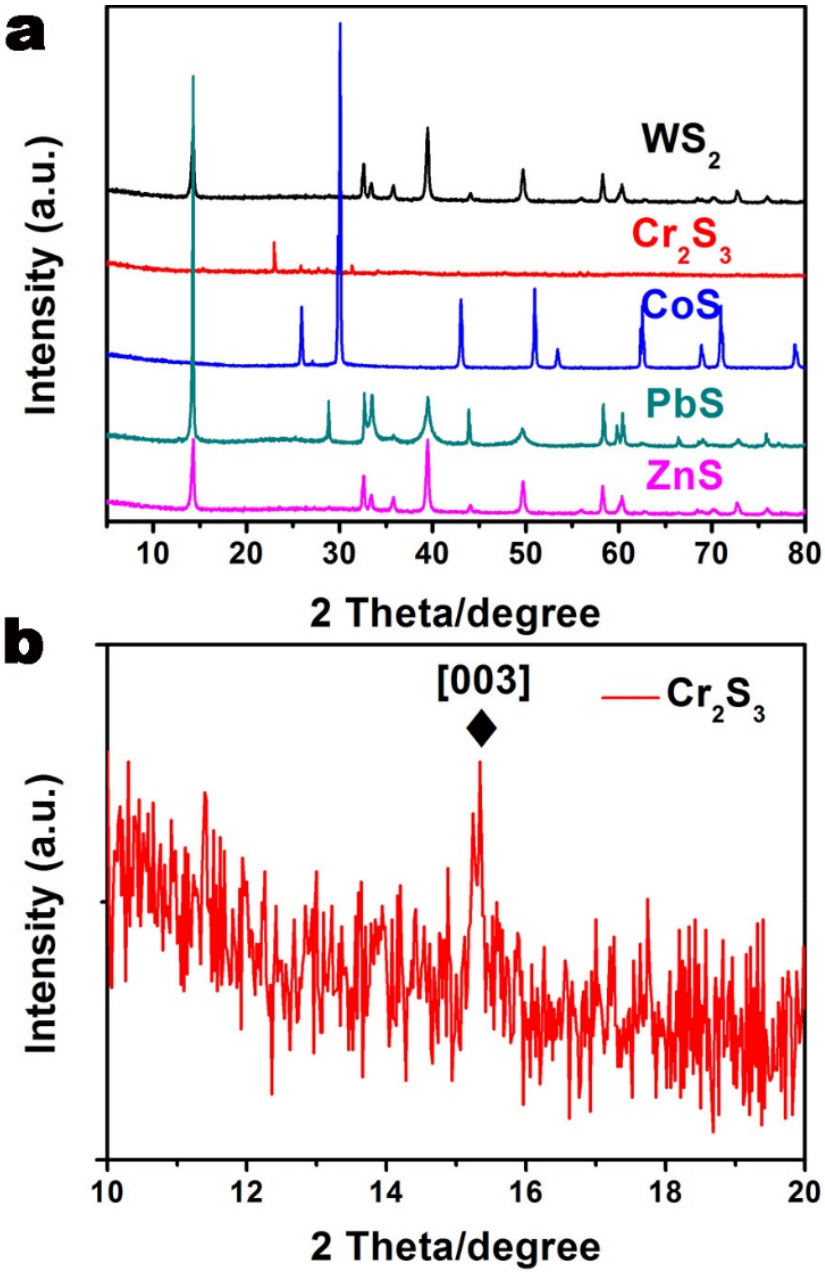

Figure 4.12 | XRD spectra for different metal sulfides. a, XRD spectra of WS_2, Cr_2S_3, CoS, PbS and ZnS. b, Amplification of XRD spectrum of Cr_2S_3 prepared by a hydrothermal method: a solution of 2.0 $Cr(NO_3)_3 \cdot 9H_2O$, 1.2 g thioacetamide and 20 mL H_2O was hydrothermal treatment at 180 ^oC for 12h to obtain the Cr_2S_3 powders.

4.3.2 Stability of the MoS_2 Co-catalytic AOPs Performance

We confirmed the stability of MoS_2 as a co-catalyst for AOPs by carrying out a 10-cycle test (Fig. 4.13a). The TOC degradation rate was found to remain at ~ 90% after the 10 cycles (Fig. 4.13b), which is much higher than that of the conventional AOPs (20%) without the assistance of MoS_2. The mass and microstructure of MoS_2 were almost unchanged after 10 cycles of catalytic reactions (Fig. 4.13c-e, ICP-OES mass loss: 0.009 wt%), a further indication of the stability of MoS_2 as a co-catalyst. The low dosage of Fe^{2+} (0.07 mmol/L) and H_2O_2 (0.4 mmol/L) used in the MoS_2 co-catalytic AOPs can effectively prevent the formation of iron cement, thus avoids catalyst poisoning.

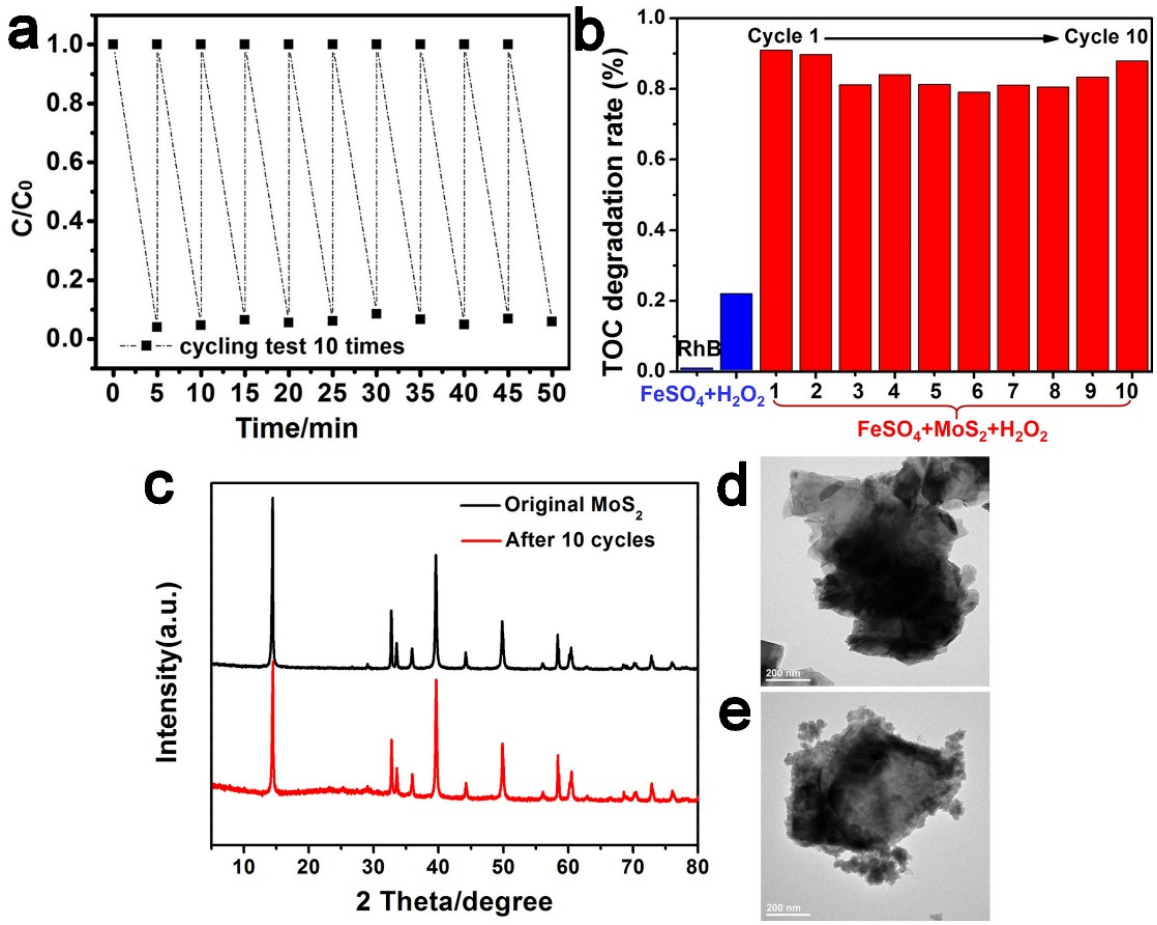

Figure 4.13 | Cycling test of the catalytic performance of AOPs with MoS_2 as the co-catalyst under visible light irradiation. **a**, Concentration change of RhB; **b**, TOC degradation rate. **c-e**, XRD patterns (**c**) and TEM images of the MoS_2 particles (< 2 μm) (**d**) before and (**e**) after the 10 cycles of AOPs.

4.3.3 Mechanism Investigation

Figure 4.14a illustrates our proposed mechanism of the catalytic reactions involving MoS_2 as the co-catalyst. The first step is the capture of protons by unsaturated S atoms on the surface of MoS_2 to form H_2S and then followed by the oxidization of the surface Mo^{4+} to Mo^{6+}. The oxidation reaction is coupled with the reduction of Fe^{3+} to Fe^{2+} (Eq. 6), thus greatly improving the reaction rate of the originally rate-limiting step Eq. (2) in the conventional AOPs. Further reduction of Mo^{6+} back to Mo^{4+} with the aid of H_2O_2 upon the Fenton reaction ensures the catalytic cycling of MoS_2 (Eq. 7).

$$Mo^{4+}+Fe^{3+} \rightarrow Mo^{6+}+Fe^{2+} \quad (6)$$

$$Mo^{6+}+H_2O_2 \rightarrow Mo^{4+}+H_2O+O_2 \quad (7)$$

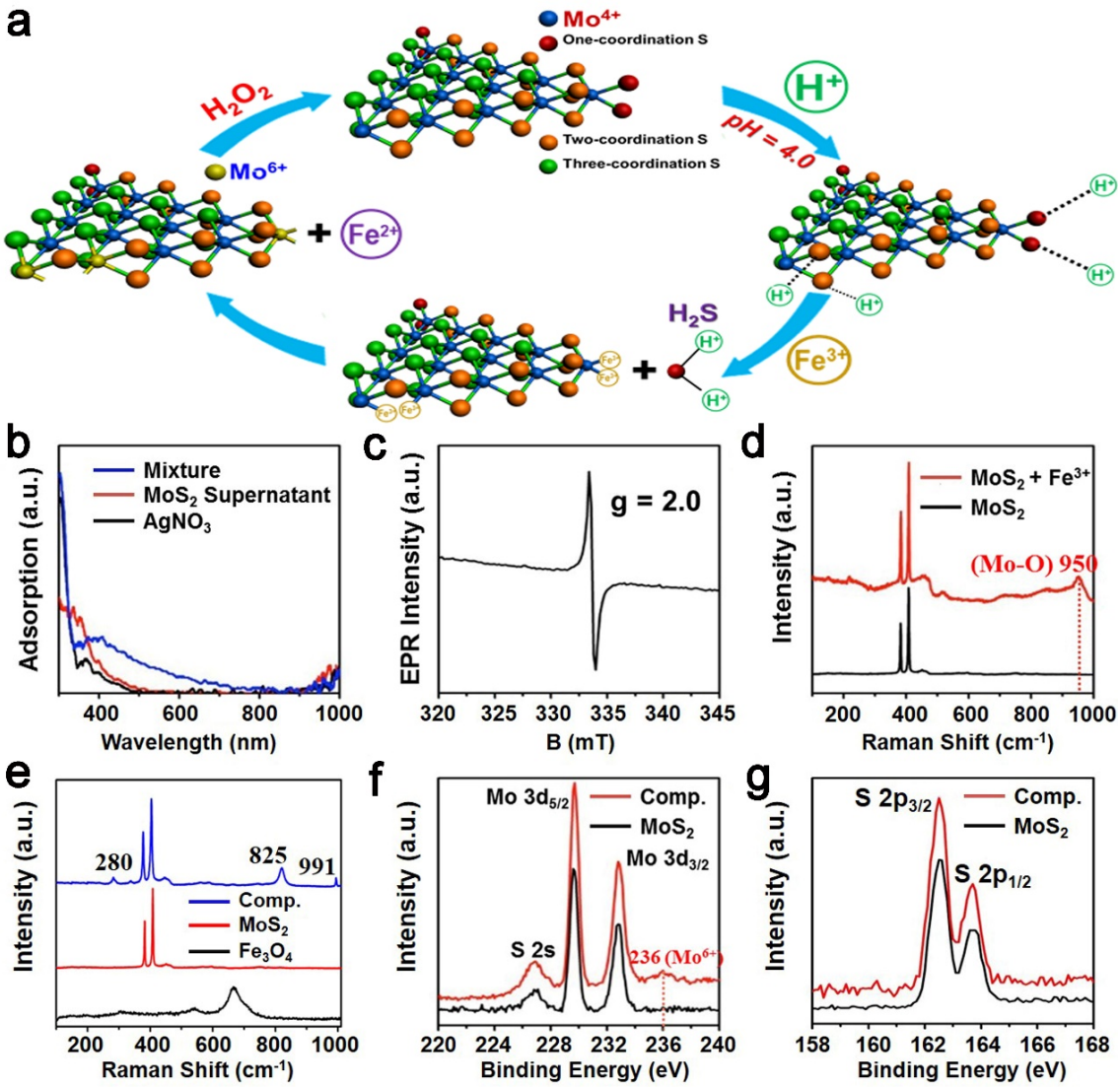

Figure 4.14 | Investigation on the mechanism of MoS_2 co-catalyzed AOPs. a, Schematic illustration of the co-catalytic mechanism of MoS_2 in AOPs. **b**, UV spectra of $AgNO_3$, MoS_2 supernatant, and their mixture. **c**, EPR spectrum of commercial MoS_2 after washing and drying. **d**, Raman spectra of MoS_2 and MoS_2 after mixing with Fe^{3+} ($FeCl_3$ solution). **e**, Raman spectra of Fe_3O_4 (commercial), MoS_2 (commercial) and MoS_2/Fe_3O_4 composite prepared through direct mixing in water. **f-g**, XPS spectra of Mo 3d (**f**) and S 2p (**g**) of MoS_2 before and after mixing with Fe_3O_4 (composite).

To confirm the proposed mechanism, we first detected the formation of H_2S by UV-vis measurements (Fig. 4.14b). We compared the extinction spectra of an aqueous solution of $AgNO_3$, the supernatant of a MoS_2 aqueous dispersion, and their mixture. The broad absorption curve in the UV range corresponding to Ag_2S was observed, indicating the existence of H_2S in the reaction solution[205]. The production of H_2S was further confirmed by pH measurement. In Fig. 4.15, the initial pH of the 0.3 g/L MoS_2 solution was 4.0~4.5, which was acidic. By washing the sample with pure water for several times, the pH value increased to near neutral due to the removal of H_2S. It is worth noting that, contrary to the previous discovery in hydrogen evolution reaction (HER) that the surface of MoS_2 could capture protons[206-208], we found that the unsaturated S atoms could be removed from the MoS_2 surface by binding with protons to form H_2S [209]. We further carried out EPR measurement to provide another evidence for the removal of S atoms from the MoS_2 surface. As shown in Fig. 4.14c, after being washed with pure water and dried, the MoS_2 powder displayed a signal at g = 2.0, indicating the presence of sulfur vacancies[210]. After the removal of S atoms, the exposed Mo^{4+} became very reactive, facilitating the reduction of Fe^{3+} to Fe^{2+} (Eq. 6).

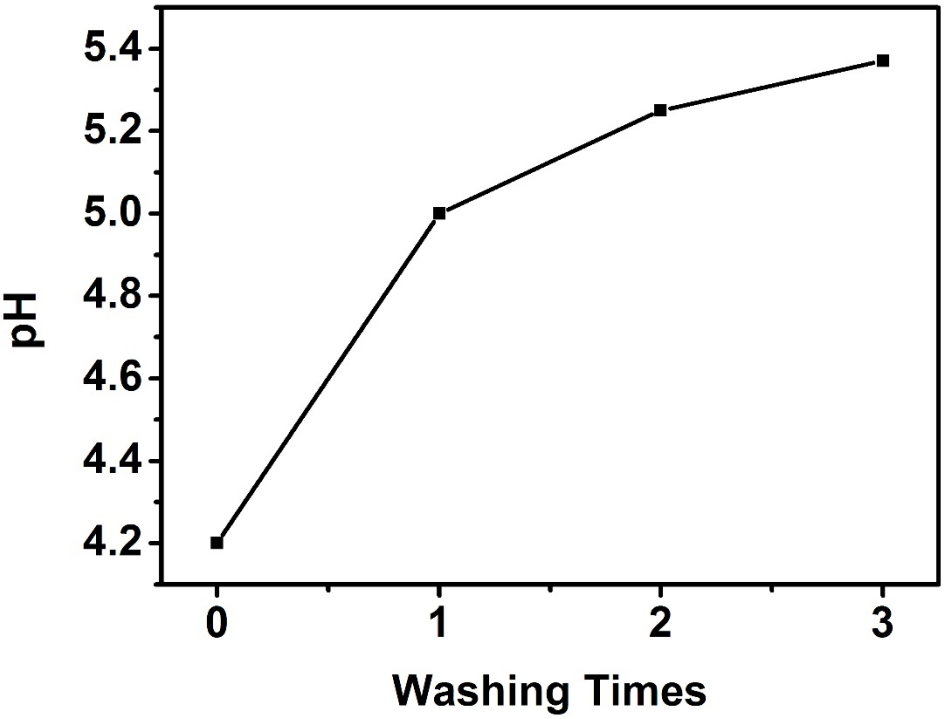

Figure 4.15 | pH value of MoS_2 solution after washing with water for different times.

The oxidation-reduction reaction proposed in (Eq. 6) was then verified by Raman measurements. As presented in Fig. 4.14d, after mixing MoS_2 and Fe^{3+} in aqueous solution, $Mo_7O_{24}^{6-}$ species were discovered with the typical Mo-O terminal bonds located at 950 cm^{-1} [211]. To further confirm the reduction capability of the exposed Mo^{4+}, more concrete evidence was acquired by analyzing the interaction between MoS_2 and Fe_3O_4 powders. As shown in Fig. 4.14e, the mixed powders displayed three Raman shifts located at 280, 825 and 991 cm^{-1}, which correspond to Mo-O (B_{2g}, B_{3g}), Mo_2-O (A_g, B_{1g}) and Mo=O (A_g, B_{1g}) modes of MoO_3, indicating the oxidation of Mo^{4+} to Mo^{6+} by forming a Mo-O-Fe bond. The bond formation can also be evidenced by the fact that the simple mixture of the MoS_2 and Fe_3O_4 powders can be completely separated by applying an external magnetic field (Fig. 4.16). As commercial MoS_2 and Fe_3O_4 powders with clean surfaces (as demonstrated by the FTIR measurement in Fig. 4.17) were used in these experiments, we can rule out the possibility of surface complexation through other species such as capping ligands. Further, as shown in Fig. 4.18, no new phases such as MoO_3 could be detected in the XRD pattern of the composite, indicating the redox reactions only occurred at the interface of the two powders. The oxidation of the exposed Mo^{4+} was further confirmed by XPS measurements. In Fig. 4.14f, the mixed powder showed a new peak at 236 eV in the XPS Mo 3d spectra, which corresponds to Mo^{6+}, further confirming the formation of MoS_2/Fe_3O_4 composite through an oxidation reaction of exposed Mo^{4+} of MoS_2 [212-213]. With no obvious change being observed in the S 2p and Fe 2p spectra, the formation of Fe-S bonds between Fe_3O_4 and MoS_2 powders could be excluded (Fig. 4.14g and Fig. 4.19). Moreover, the origin of the O during the formation

of Mo-O-Fe bond was further studied. As shown in Fig. 4.20, when the MoS_2 and Fe_3O_4 powders were mixed using propylamine as the solvent, the three typical Mo^{6+}-O bonds could still be observed in the Raman spectra, indicating that the O in Mo-O-Fe bond was originated from Fe_3O_4 rather than water, consistent with the proposed mechanism of electron transfer from Mo to Fe. In summary, the above results clearly support the proposed catalytic mechanism of the MoS_2 co-catalytic AOPs: the rate-limiting step of reduction of Fe^{3+} to Fe^{2+} is promoted by the oxidization of Mo^{4+} to Mo^{6+}, which is made possible by the removal of S atom from the surface of MoS_2 by protons in the solvent.

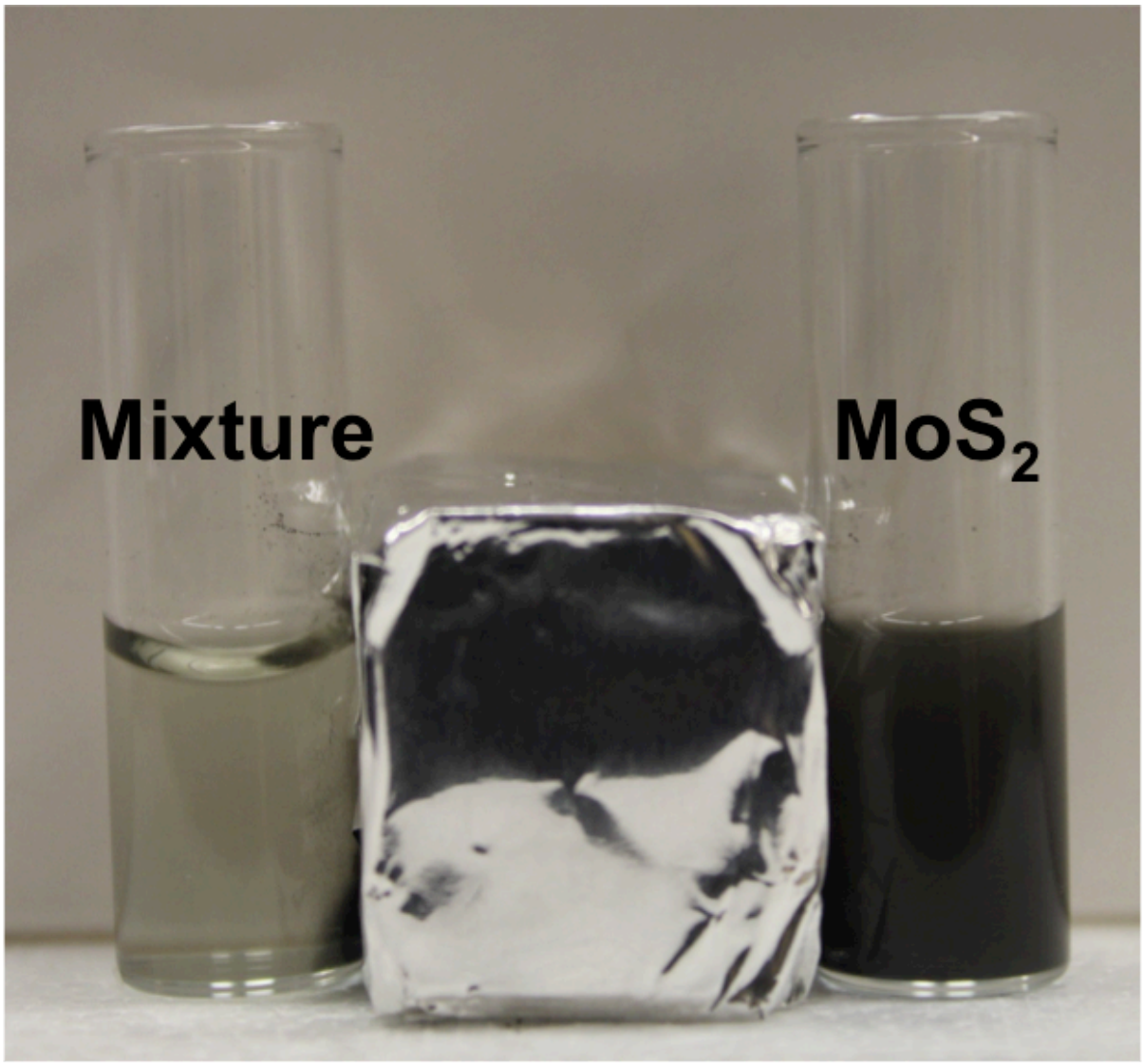

Figure 4.16 | Digital image of magnetic separation of MoS_2/Fe_3O_4 mixture and MoS_2.

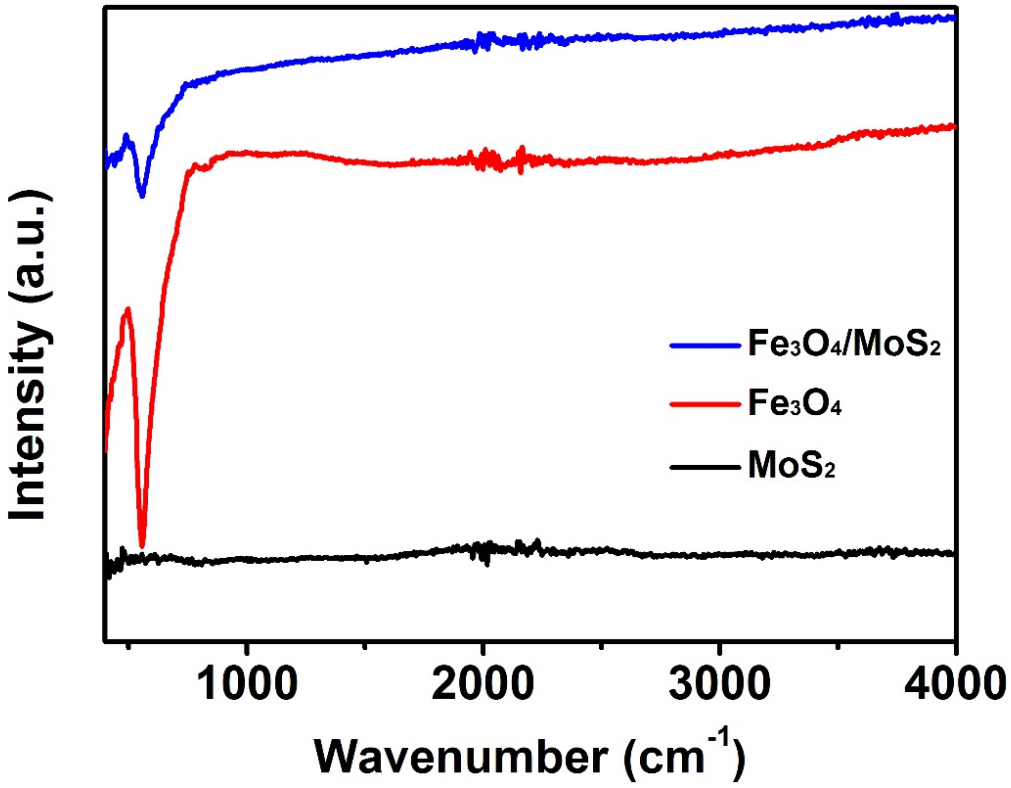

Figure 4.17 | FTIR of commercial MoS_2 and Fe_3O_4 and their mixture.

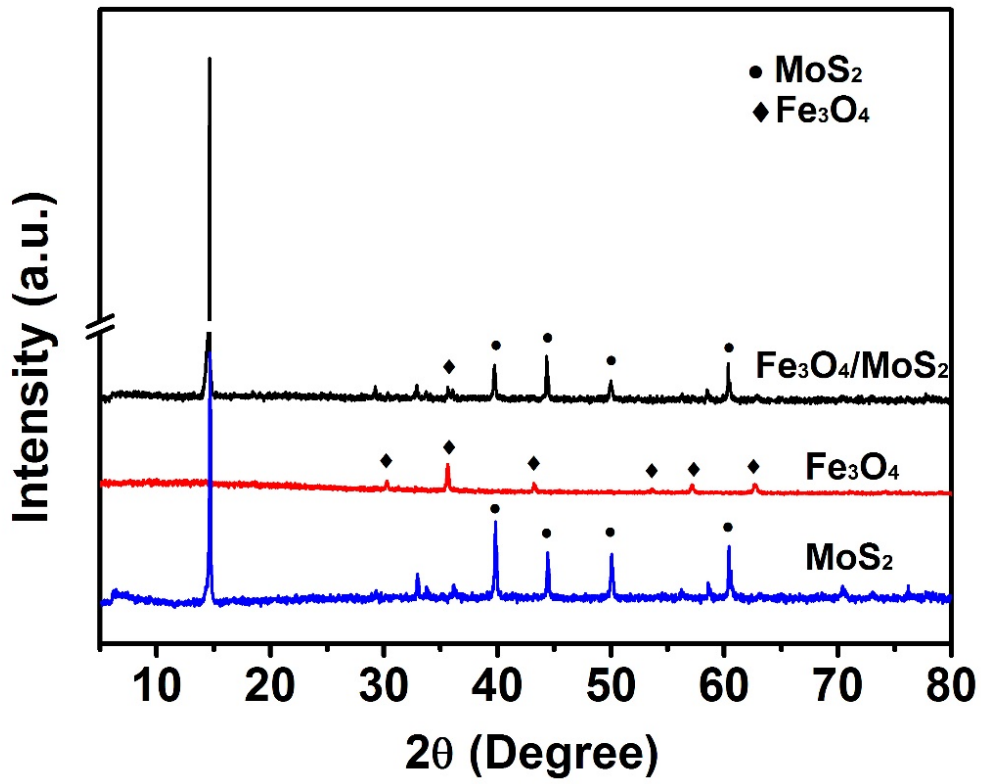

Figure 4.18 | XRD patterns of MoS_2, Fe_3O_4 and their composite (from bottom to top).

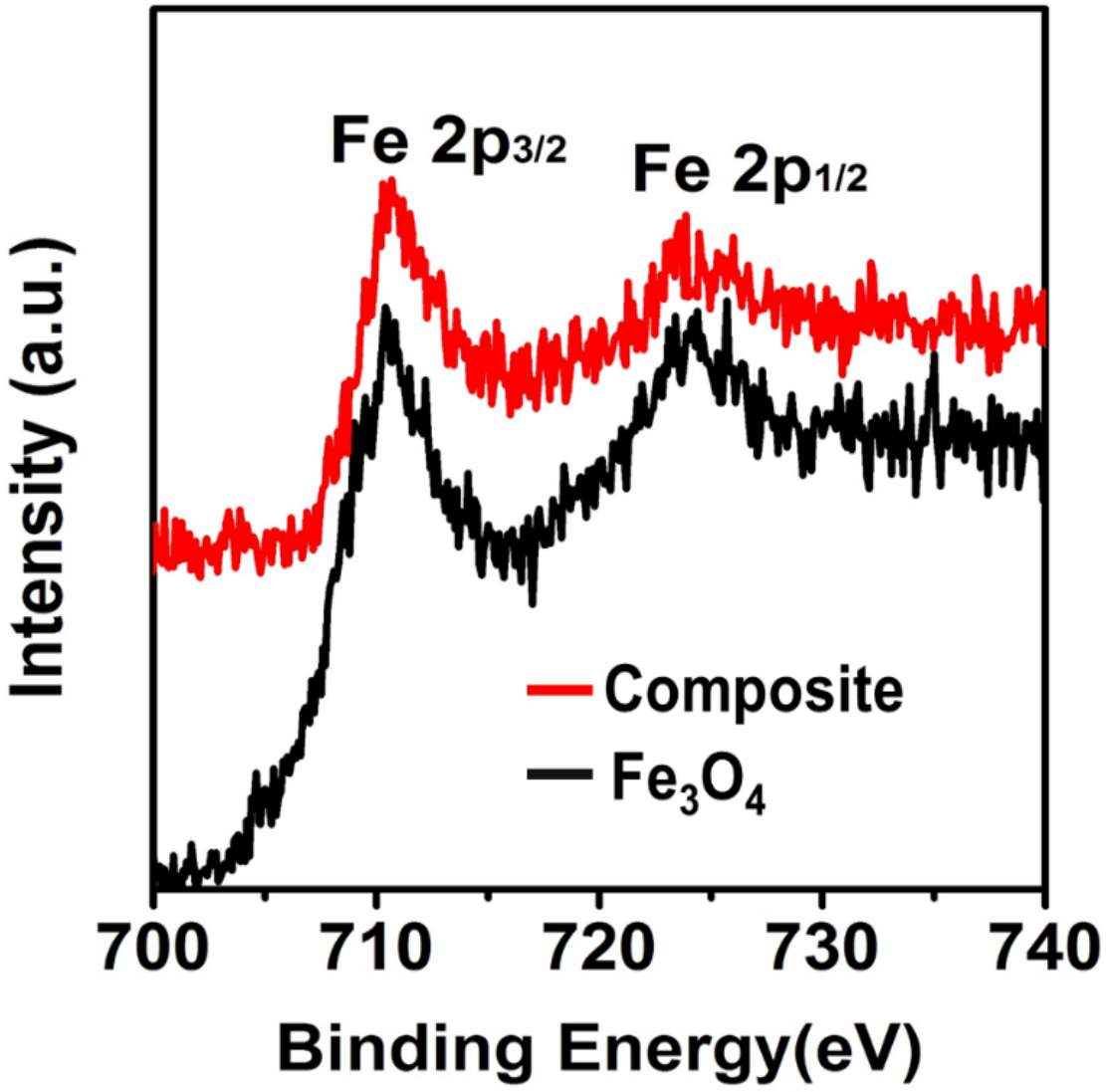

Figure 4.19 | Fe 2p XPS spectrum of Fe_3O_4 before and after mixing with MoS_2 (composite).

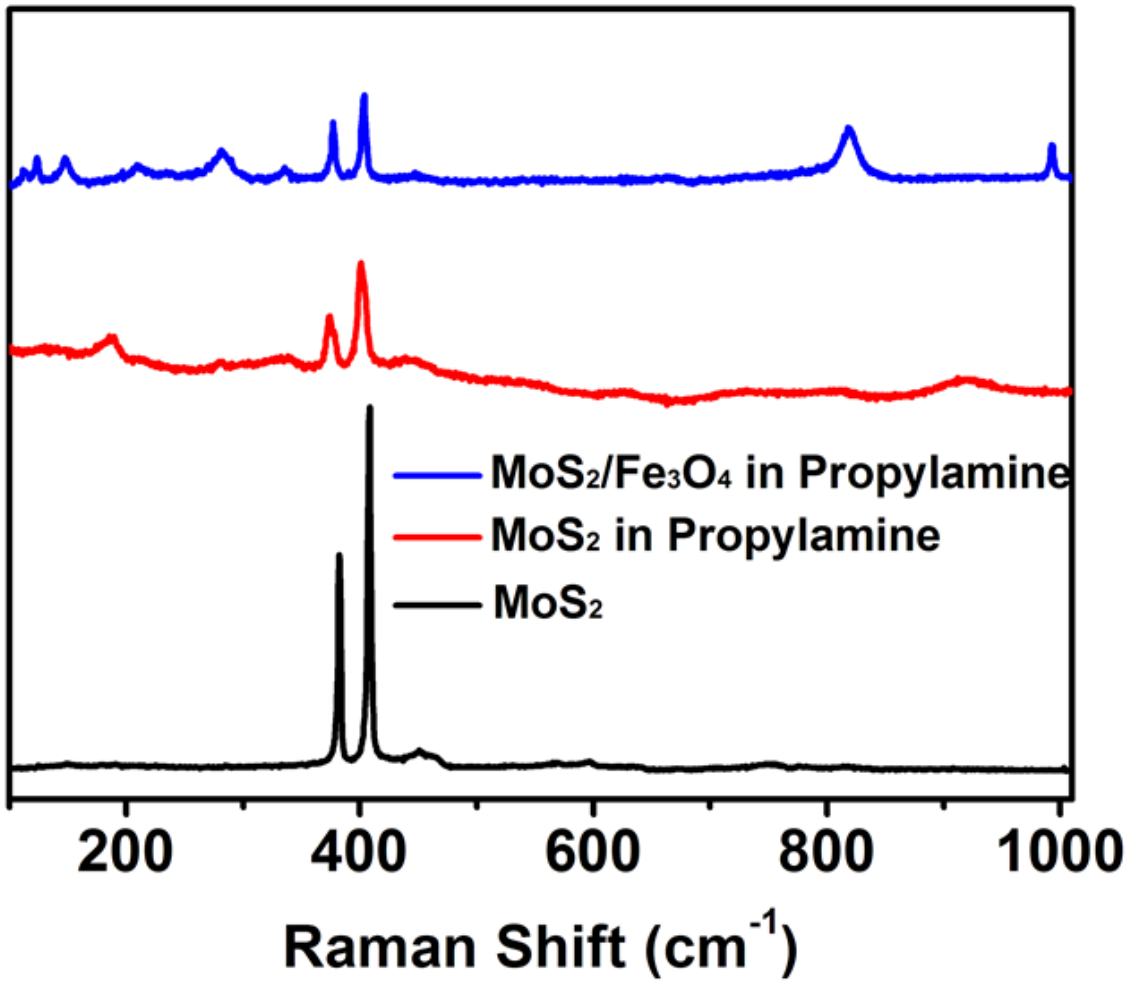

Figure 4.20 | Raman shift of dried MoS_2 powder, MoS_2 in propylamine and complexation of MoS_2 and Fe_3O_4 in propylamine.

4.3.4 Scale-up Experiment Test

To highlight the potential of the MoS_2 co-catalytic AOPs for industrial applications, we have scaled up our testing system from 100 mL to 1.0 L. As shown in Fig. 4.20a, the $FeSO_4$+MoS_2+H_2O_2 mixture still displayed excellent catalytic performance. The kinetics of the AOPs during the first 60 seconds of irradiation can be approximated as a first-order reaction (Fig. 4.20b). The reaction rate constant (Ka) value for the $FeSO_4$+MoS_2+H_2O_2 mixture is 18.5 times of that of the $FeSO_4$+H_2O_2 system ($3.7 \times 10^{-2} \cdot s^{-1}$ *vs.* $0.2 \times 10^{-2} \cdot s^{-1}$). We have varied the dosage of H_2O_2 from 0.4 to 200 mmol/L in the $FeSO_4$+H_2O_2 case (the conventional AOPs, Fig. 4.20c), and found the optimum activity at a concentration of 1.0 mmol/L (an obvious decrease could be observed when H_2O_2 was higher than 1.0 mmol/L due to the fact that H_2O_2 is also a powerful •OH scavenger at a high dosage[214]). However, even the optimal activity of the $FeSO_4$+H_2O_2 mixture (H_2O_2 = 1.0 mmol/L) is still much lower than that of $FeSO_4$+MoS_2+H_2O_2 at a lower concentration of H_2O_2 (0.4 mmol/L). Apparently, the strategy to improve the catalytic efficiency of AOPs by just increasing the concentration of H_2O_2 is as effective as by adding a co-catalyst of MoS_2. The co-catalytic effect of MoS_2 is also applicable for other cations which can catalyze AOPs in the presence of H_2O_2, such as Ni^{2+}, $Mn^{2+,}$ and Cu^{2+} (Fig. 4.20d), further suggesting the universal applicability of metal sulfides as co-catalysts in various AOPs.

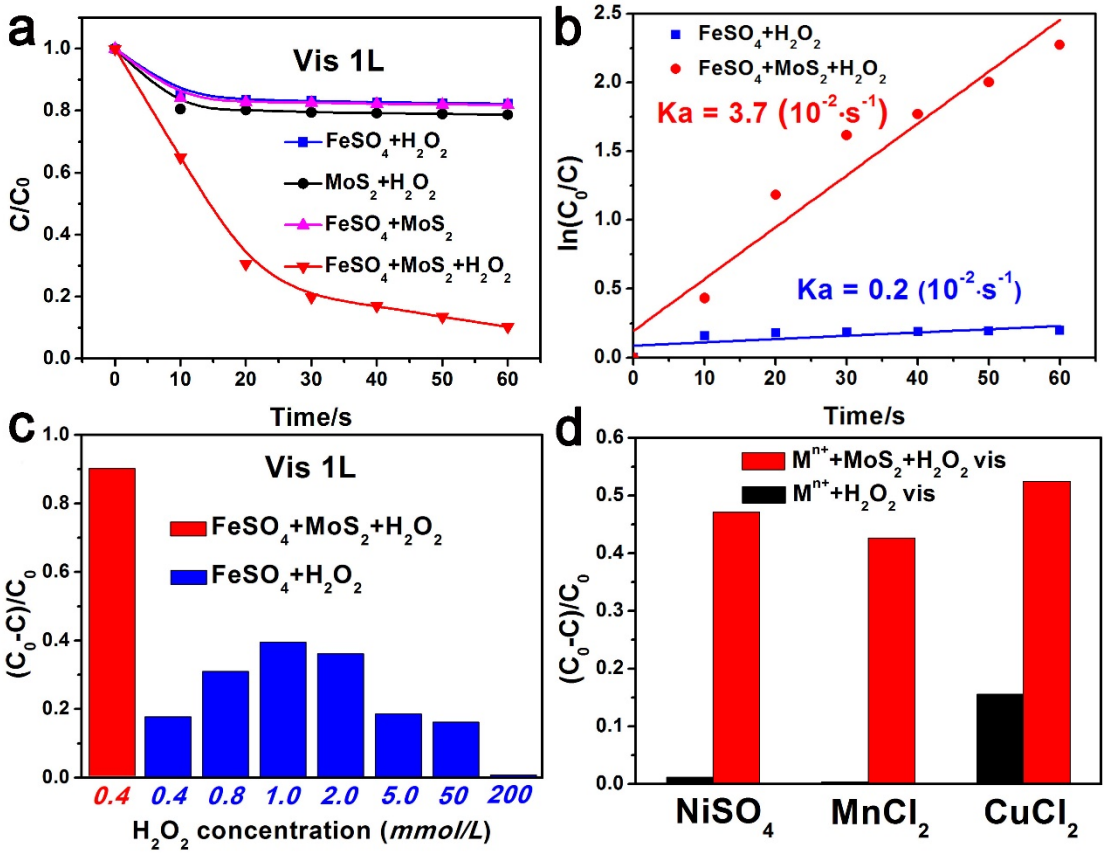

Figure 4.21 | Scale-up tests of the MoS_2 (< 2 μm) co-catalytic AOPs. a, AOPs driven by visible light (λ> 420 nm) for the degradation of RhB in a 1.0-L solution including 0.02 g/L $Fe(SO_4)\cdot 7H_2O$, 0.3 g/L MoS_2, 0.4 mmol/L H_2O_2, and 20 mg/L RhB. **b**, Comparison of the apparent rate constant (*K*a) of AOPs with and without MoS_2 for the degradation of RhB under the visible light irradiation. **c**, Comparison of the activities of AOPs for the degradation of RhB with different dosage of H_2O_2 (1.0 L solution including 0.02 g/L $Fe(SO_4)\cdot 7H_2O$, 0.4 ~ 200 mmol/L H_2O_2, and 20 mg/L RhB; red: in the presence of 0.3 g/L MoS_2, blue: in the absence of MoS_2). **d**, The co-catalytic effect of MoS_2 in AOPs catalyzed by other transition metal ions (M^{n+} = Ni^{2+}, Mn^{2+}, and Cu^{2+}) for the degradation of RhB under the visible light irradiation.

4.4 Conclusions

We have demonstrated a significant co-catalytic effect of metal sulfides for enhancing the conversion efficiency of H_2O_2 to •OH and decreasing the generation of iron cement during AOPs. By using MoS_2 as an example, we show that the co-catalytic effect works by promoting the rate-limiting step of the reduction cycle of Fe^{3+} to Fe^{2+}, which is facilitated by the removal of unsaturated sulfur atoms and the oxidation of the Mo^{4+} on the surface of MoS_2. This greatly enhanced performance is achieved by using commercial metal sulfide powders, and further optimization can be made by reducing the particle size. The co-catalytic effect of the metal sulfides is general and can be successfully applied to many kinds of AOPs involving a variety of transition metals. We believe this discovery will lead to great advances in the practical use of AOPs in the field of environmental remediation.

4.5 References

1. Pera-Titus, M.; García-Molina, V.; Baños, M. A.; Giménez, J.; Esplugas, S., Degradation of chlorophenols by means of advanced oxidation processes: a general review. *Applied Catalysis B: Environmental* **2004,** *47* (4), 219-256.

2. Zhang, C.; Ou, Y.; Lei, W.-X.; Wan, L.-S.; Ji, J.; Xu, Z.-K., CuSO4/H2O2-Induced Rapid Deposition of Polydopamine Coatings with High Uniformity and Enhanced Stability. *Angewandte Chemie* **2016,** *128* (9), 3106-3109.

3. De Laat, J.; Le, T. G., Effects of chloride ions on the iron(III)-catalyzed decomposition of hydrogen peroxide and on the efficiency of the Fenton-like oxidation process. *Applied Catalysis B: Environmental* **2006,** *66* (1–2), 137-146.

4. Pham, A. L.-T.; Doyle, F. M.; Sedlak, D. L., Kinetics and efficiency of H2O2 activation by iron-containing minerals and aquifer materials. *Water Research* **2012,** *46* (19), 6454-6462.

5. A.R., D.; N., K.; E., G.; Y., G., Removal of COD from Oil Recovery Industry Wastewater by the Advanced Oxidation Processes (AOP) Based on H_2O_2. *Global NEST Journal* **2008,** *10* (1), 31-38.

6. Ronak, S.; Shweta, V., Fenton's Reagent for the Treatment of Pharmaceutical Industry Wastewater *International Journal of Science and Research* **2015,** *4* (7), 3093-3096.

7. Li, T.; Zhao, Z.; Wang, Q.; Xie, P.; Ma, J., Strongly enhanced Fenton degradation of organic pollutants by cysteine: An aliphatic amino acid accelerator outweighs hydroquinone analogues. *Water Research* **2016,** *105*, 479-486.

8. Sekaran, G.; Karthikeyan, S.; Evvie, C.; Boopathy, R.; Maharaja, P., Oxidation of refractory organics by heterogeneous Fenton to reduce organic load in tannery wastewater. *Clean Technologies and Environmental Policy* **2013,** *15* (2), 245-253.

9. A., S.; V., K., Behavior of Steels against Corrosion in Peroxide Solutions. *J. Mater. Environ. Sci* **2011,** *3* (1), 76-84.

10. Wang, M.; Fang, G.; Liu, P.; Zhou, D.; Ma, C.; Zhang, D.; Zhan, J., Fe3O4@β-CD nanocomposite as heterogeneous Fenton-like catalyst for enhanced degradation of 4-chlorophenol (4-CP). *Applied Catalysis B: Environmental* **2016,** *188*, 113-122.

11. Ma, J. H.; Song, W. J.; Chen, C. C.; Ma, W. H.; Zhao, J. C.; Tang, Y. L., Fenton degradation of organic compounds promoted by dyes under visible irradiation. *Environmental Science & Technology* **2005,** *39* (15), 5810-5815.

12. Ma, J. H.; Ma, W. H.; Song, W. J.; Chen, C. C.; Tang, Y. L.; Zhao, J. C.; Huang, Y. P.; Xu, Y. M.; Zang, L., Fenton degradation of organic pollutants in the presence of low-molecular-weight organic acids: Cooperative effect of quinone and visible light. *Environmental Science & Technology* **2006,** *40* (2), 618-624.

13. De Luca, A.; Dantas, R. F.; Esplugas, S., Study of Fe(III)-NTA chelates stability for applicability in photo-Fenton at neutral pH. *Applied Catalysis B: Environmental* **2015,** *179*, 372-379.

14. Gazi, S.; Rajakumar, A.; Singh, N. D. P., Photodegradation of organic dyes in the presence of [Fe(III)-salen]Cl complex and H2O2 under visible light irradiation. *Journal of Hazardous Materials* **2010,** *183* (1), 894-901.

15. Qin, Y. X.; Song, F. H.; Ai, Z. H.; Zhang, P. P.; Zhang, L. Z., Protocatechuic Acid Promoted Alachlor Degradation in Fe(III)/H2O2 Fenton System. *Environmental Science & Technology* **2015,** *49* (13), 7948-7956.

16. Qian, Y.; Yin, X. P.; Lin, H.; Rao, B.; Brooks, S. C.; Liang, L. Y.; Gu, B. H., Why Dissolved Organic Matter Enhances Photodegradation of Methylmercury. *Environmental Science & Technology Letters* **2014,** *1* (10), 426-431.

17. Jiang, C.; Garg, S.; Waite, T. D., Hydroquinone-Mediated Redox Cycling of Iron and Concomitant Oxidation of Hydroquinone in Oxic Waters under Acidic Conditions: Comparison with Iron-Natural Organic Matter Interactions. *Environmental Science & Technology* **2015,** *49* (24), 14076-14084.

18. Boles, M. A.; Ling, D.; Hyeon, T.; Talapin, D. V., The surface science of nanocrystals. *Nat Mater* **2016,** *15* (2), 141-153.

19. Guo, S.; Zhu, Y.; Yan, Y.; Min, Y.; Fan, J.; Xu, Q., Holey structured graphitic carbon nitride thin sheets with edge oxygen doping via photo-Fenton reaction with enhanced photocatalytic activity. *Applied Catalysis B: Environmental* **2016,** *185*, 315-321.

20. Li, M.; Qiang, Z.; Pulgarin, C.; Kiwi, J., Accelerated methylene blue (MB) degradation by Fenton reagent exposed to UV or VUV/UV light in an innovative micro photo-reactor. *Applied Catalysis B: Environmental* **2016,** *187* (Supplement C), 83-89.

21. Hems, R. F.; Hsieh, J. S.; Slodki, M. A.; Zhou, S.; Abbatt, J. P. D., Suppression of OH Generation from the Photo-Fenton Reaction in the Presence of α-Pinene Secondary Organic Aerosol Material. *Environmental Science & Technology Letters* **2017**.

22. Mak, K. F.; Lee, C.; Hone, J.; Shan, J.; Heinz, T. F., Atomically Thin ${\mathrm{MoS}}_{2}$: A New Direct-Gap Semiconductor. *Physical Review Letters* **2010,** *105* (13), 136805.

23. Liu, C.; Kong, D.; Hsu, P.-C.; Yuan, H.; Lee, H.-W.; Liu, Y.; Wang, H.; Wang, S.; Yan, K.; Lin, D.; Maraccini, P. A.; Parker, K. M.; Boehm, A. B.; Cui, Y., Rapid water disinfection using vertically aligned MoS2 nanofilms and visible light. *Nat Nano* **2016,** *11*, 1098-1104.

24. Wiedau-Pazos, M.; Goto, J. J.; Rabizadeh, S.; Gralla, E. B.; Roe, J. A.; Lee, M. K.; Valentine, J. S.; Bredesen, D. E., Altered Reactivity of Superoxide Dismutase in Familial Amyotrophic Lateral Sclerosis. *Science* **1996,** *271* (5248), 515-518.

25. Xing, M. Y.; Zhang, J. L.; Qiu, B. C.; Tian, B. Z.; Anpo, M.; Che, M., A Brown Mesoporous TiO2-x/MCF Composite with an Extremely High Quantum Yield of Solar Energy Photocatalysis for H-2 Evolution. *Small* **2015,** *11* (16), 1920-1929.

26. Tan, C.; Zhang, H., Epitaxial Growth of Hetero-Nanostructures Based on Ultrathin Two-Dimensional Nanosheets. *Journal of the American Chemical Society* **2015,** *137* (38), 12162-12174.

27. ScraceT; TsaiY; BarmanB; SchweidenbackL; PetrouA; KioseoglouG; OzfidanI; KorkusinskiM; HawrylakP, Magnetoluminescence and valley polarized state of a two-dimensional electron gas in WS2 monolayers. *Nat Nano* **2015,** *10* (7), 603-607.

28. Jarosz, A. P.; Yep, T.; Mutus, B., Microplate-Based Colorimetric Detection of Free Hydrogen Sulfide. *Anal. Chem.* **2013,** *85* (7), 3638-3643.

29. Voiry, D.; Fullon, R.; Yang, J.; de Carvalho Castro e Silva, C.; Kappera, R.; Bozkurt, I.; Kaplan, D.; Lagos, M. J.; Batson, P. E.; Gupta, G.; Mohite, A. D.; Dong, L.; Er, D.; Shenoy, V. B.; Asefa, T.; Chhowalla, M., The role of electronic coupling between substrate and 2D MoS2 nanosheets in electrocatalytic production of hydrogen. *Nat Mater* **2016,** *15*, 1003-1009.

30. Li, H.; Tsai, C.; Koh, A. L.; Cai, L.; Contryman, A. W.; Fragapane, A. H.; Zhao, J.; Han, H. S.; Manoharan, H. C.; Abild-Pedersen, F.; Norskov, J. K.; Zheng, X., Activating and optimizing MoS2 basal planes for hydrogen evolution through the formation of strained sulphur vacancies. *Nat Mater* **2016,** *15* (1), 48-53.

31. Ye, G.; Gong, Y.; Lin, J.; Li, B.; He, Y.; Pantelides, S. T.; Zhou, W.; Vajtai, R.; Ajayan, P. M., Defects Engineered Monolayer MoS2 for Improved Hydrogen Evolution Reaction. *Nano Letters* **2016,** *16* (2), 1097-1103.

32. Tsai, C.; Li, H.; Park, S.; Park, J.; Han, H. S.; Nørskov, J. K.; Zheng, X.; Abild-Pedersen, F., Electrochemical generation of sulfur vacancies in the basal plane of MoS(2) for hydrogen evolution. *Nature Communications* **2017,** *8*, 15113.

33. Cai, L.; He, J.; Liu, Q.; Yao, T.; Chen, L.; Yan, W.; Hu, F.; Jiang, Y.; Zhao, Y.; Hu, T.; Sun, Z.; Wei, S., Vacancy-Induced Ferromagnetism of MoS2 Nanosheets. *J. Am. Chem. Soc.* **2015,** *137* (7), 2622-2627.

34. Twu, J.; Dutta, P. K., Raman spectroscopic studies of intercalated molybdate ions in layered metal hydroxides. *Chem. Mat.* **1992,** *4* (2), 398-401.

35. Guifeng, C.; Xiaolin, S.; Lixiu, G.; Jianwei, C.; Hui, Z.; Shijie, W.; Jisheng, P.; Junguang, T., Defect assisted coupling of a MoS 2 /TiO 2 interface and tuning of its electronic structure. *Nanotechnol.* **2016,** *27* (35), 355203.

36. Tang, H.; Wang, J.; Yin, H.; Zhao, H.; Wang, D.; Tang, Z., Growth of Polypyrrole Ultrathin Films on MoS2 Monolayers as High-Performance Supercapacitor Electrodes. *Adv. Mater.* **2015,** *27* (6), 1117-1123.

37. Hameed, B. H.; Lee, T. W., Degradation of malachite green in aqueous solution by Fenton process. *Journal of Hazardous Materials* **2009,** *164* (2–3), 468-472.

Chapter 5

Shape Switching Patchy Particles: Fine-Tuning of Spreading Coefficient Upon Post-Treatment

5.1 Introduction

The capability to elaborate complex shape and function of colloidal entities is particularly significant for its fundamental merits in exploration of self-assembly and for practical applications in electronic, magnetic, optical, and catalytic devices. [5, 16, 89, 215-216] Over the past decades, tremendous synthetic strategies have been developed to fabricate "colloidal molecules"[217] and "patchy particles"[86, 218-219] with complex and arbitrary structures and functionalities, comprising Janus,[87] multipod,[88] daisy,[220] raspberry[221] and ice-cream cones-like structures.[222] Although the development of synthetic tactics has achieved copious quantities of colloidal particles of good uniformity, both our current understanding of various physical phenomena and our capability to fabricate new functional material still need to be enriched.

The innovation of recent efforts, however, is that beyond the synthetic approaches of fabricating the complex and beautiful structures, intricate colloidal particles created by a

second step of post-treatment could reveal more unprecedented three-dimensional design of microstructures.[21, 223] The results of Zheng *et al.* exemplify the fruits of this technique.[90] The authors achieved shifting of the patchy shape between concave and convex features based on the swelling/deswelling of polymer matrix by different solvents. Equally impressive results published by Yoossef *et al.*,[20] Tu *et al.*[17] and Klinger *et al.*[224] showed the shape changing based on stimuli responsive polymer. Nevertheless, in direct contrast to the synthetic strategies, the ability to control the shape and functionality by post-treatment is still in its infancy. In addition to the shape feature of the patches, the tuning or switching of quantity, curvature, hydrophobicity, and function of the patches has not being realized. Moreover, the exploration of post-treatment could reveal more than just a pretty structure with future success being critical for broadening the current understanding of physical phenomena and applications ranging from drug delivery to artificial camouflage.

In this article, we proposed a post-treatment method based on the fine-tuning of spreading coefficient *S*, which enables the shape shifting of the patchy particles in highly predictable manners. In seeded emulsion polymerization, the resulting equilibrium configuration is determined by the wetting of seed surface (s) by polymer (p) in the water phase (w), which can be described in terms of interfacial tensions and spreading coefficient by Young's equation: $S_p = \gamma_{sw} - (\gamma_{sp} + \gamma_{pw})$.[225-226] When S_p is positive, the surface of seed is completely wetted by polymer, resulting in core-shell structures. Otherwise, partial wetting or dewetting happens when S_p is negative. Not limited to

synthetic process, through post-heating of the assynthesized colloidal particles above the glass transition temperature of polymer (T_g) in different solvents, γ_{sw} and γ_{pw} would be readily changed, as a result, the sign of S_p is tuned, which triggers the shape switching of the patches. In addition, since S_p represents a thermodynamic parameter aiming at minimizing the free surface energy, which means that the equilibrium configuration is only determined by the dispersion solvent, we demonstrated reversible shape switching by alternating the solvents. Moreover, kinetically, by precisely controlling the heating time, intermediate structures with controlled number of patches on the surface were captured by subsequent rapid temperature quenching before reaching the equilibrium state. At last, we demonstrated the potential of this method in fabricating multifunctional materials by growing Pt on selective area of the seeds, which was not occupied by polymer patches. Such an approach, in which colloidal particles are first formed and then develop more intriguing structures by post-heating, allows unprecedented control over the morphology of the materials, as well as enables anisotropic functionality on materials by modification of selective area in a controlled manner.

5.2 Materials and Methods

5.2.1 Materials

Anhydrous iron (III) chloride ($FeCl_3$, 98%) was purchased from Alfa Aesar and sodium hydroxide (NaOH, 98.8%), ammonium hydroxide (28%), sodium dodecyl sulfate (SDS, 99%), sodium borohydride ($NaBH_4$, 99%) and ethylene glycol (EG, 99%) were purchased from Fisher Scientific. Diethylene glycol (DEG, reagent grade), poly (acrylic acid) (PAA, M_w=1800), tetraethyl orthosilicate (TEOS, 98%), styrene (St, 99%), potassium persulfate (KPS, 99%), ascorbic acid (AA, 99%), [3-(methacryloyloxy)propyl]trimethoxysilane (MPS, 98%), , propylene carbonate (PC, 99.7%), sodium citrate dehydrate (TSC, 99%), (3-aminopropyl)triethoxysilane (APTES, 98%) and chloroplatinic acid hexahydrate were purchased from Sigma-Aldrich and ethanol (200 proof) (EtOH) was purchased form Decon Laboratories. Sodium p-styrenesulfonate hydrate (NaSS, 93%) was purchased from TCI. All chemicals were used as purchased without further purification.

5.2.2 Synthesis of Silica/PS Nanocomposite

Unless stated, all of the syntheses were carried out under standard Schlenk line operation.

5.2.2.1 Colloidal Nanocrystal Clusters (CNCs)[22]

Uniform superparamagnetic CNCs were synthesized by reacting 0.4 mmol $FeCl_3$ with NaOH at around 220 °C in a DEG solution containing 4 mmol PAA as surfactant. After several times washing with ethanol and water, the CNCs were dispersed in 3 mL of H_2O (*ca.* 8.6 mg/mL).

5.2.2.2 CNCs@SiO_2[55]

Subsequently, 1 mL $NH_3 \bullet H_2O$ and 20 mL ethanol were mixed with the CNCs dispersion under sonication. After the mixture was transferred into a three-neck flask under mechanical stirring at 600 rpm, 100 μL of TEOS was injected and stirred for one hour, after which the sample was washed with ethanol for 4 times and finally dispersed in 20 mL of EtOH.

5.2.2.3 MPS Modification of CNCs@SiO_2[31]

Certain amount of MPS was added to above solution and mechanical stirred at room temperature for 48 hours. And then the solution was centrifuged and washed with EtOH for two times and finally dispersed in 3 mL of EtOH.

5.2.2.4 CNCs@SiO_2@PS[31]

Under the mechanical stirring, 30 mL of distilled water containing 2 mmol SDS was mixed with the above solution and degassed with nitrogen for 30 min. After that, 1 mL St and 0.1 mL of 0.05 g/mL NaSS were injected, followed by degassing for another 15 min. The temperature of the solution was raised to 75 °C and 1 mL of 0.02 g/mL KPS solution was injected to initiate the polymerization. After reacting for 7 hours, the final products were washed through centrifugation and magnetic separation to remove the free PS particles, and finally, dispersed in 3 mL water.

5.2.3 Post-Treatment of CNCs@SiO_2@PS

The above solution was diluted 20 times by the selected solvent (DEG, EG or PC) followed by heating in oil bath at 160 °C for 20 min to allow the fusion of polymer and reaching the new equilibrium state. And then the particles were collected by centrifugation and washed with water and ethanol for three times.

5.2.4 Selective Growth of Pt on Patchy Particles

Unless stated, the following procedures were performed on 1/20 batch of CNCs@SiO_2@PS particles.

5.2.4.1 Pt Seed[227]

26 mL of 2.8 mM TSC solution was added to 50 mL of 0.4 mM chloroplatinic acid hexahydrate under magnetic stirring followed by adding 5 mL of 12 mM $NaBH_4$ in a drop-wise way, accompanying color change from colorless to light brown. After magnetic stirred at room temperature for 2 hours, the above solution was stored in refrigerator at 4 °C for future use.

5.2.4.2 APTES Modification[228]

The patchy particles were dispersed in 5 mL isopropanol followed by addition of 50 μL APTES. After mechanical stirred overnight, the particles were washed with isopropanol for 4 times and water for twice. Finally, the particles were dispersed in 1 mL Mili-Q water.

5.2.4.3 Pt Seed Loading

To ensure sufficient seed loading, 2 mL above Pt seed solution was added to the APTES modified patchy particles followed by sonication for 30 min. And then the particles were

washed with water for three times to remove the excess Pt seeds. Finally, the particles were dispersed in 1 mL of Mili-Q water.

5.2.4.4 Seeded Growth of Pt[229]

The mole ratio between chloroplatinic acid hexahydrate and AA is 1:10. The amount varies with the thickness requirement of Pt shell. For the thinner Pt shell coating, 10 μL of 0.01 M chloroplatinic acid and 10 μL of 0.1 M AA were used. After the addition of precursor and reducing agent, the solution was placed in oven of 65 °C and kept for 30 min. The color of the solution should turn from light yellow to dark grey or black after the seeded growth of Pt. And then the particles were washed with water for several times.

5.2.5 Removing of PS Patches

To remove the PS patches, the particles were washed with ethanol for several times to remove the water followed by addition of 1 mL toluene. After swelling for 1 min, the sample was centrifuged and washed with EtOH and water for several times.

5.2.6 Characterization

Transmission electron microscopy (TEM) studies were carried out using a Tecnai 12 microscope with an acceleration voltage of 120 kV and Fourier transform infrared spectroscopy (FTIR) spectra were collected with a Nicolet 6700. The glass transition temperature of PS was determined by differential thermal analysis (DTA) with a Seiko Instruments SII SCC/5200. The parameters of contact angle were measured by Nano Measurer and ImageJ and calculated based on a literature. [230]

5.3 Results and Discussion

5.3.1 Syntheses and Characterization of CNCs@ SiO_2@PS

We started with the synthesis of magnetic CNCs using a hydrothermal reaction followed by SiO_2 coating with a modified Stöber method. As shown in the TEM image in Figure 5.1a, the overall size of the CNCs@SiO_2 is around 190 nm with shell thickness around 28 nm. The particle surfaces were then functionalized with a monolayer of coupling agent MPS through the siloxane linkage. Each MPS molecule contains a C=C double bond, which copolymerizes with St monomers upon initiation, promoting the growth of polymer on the particle surfaces. To confirm the existence of C=C, we performed FTIR on the CNCs@SiO_2 before and after MPS modification with MPS as the reference. As illustrate in Figure 5.1b, MPS showed characteristic peaks around 1700 and 1635 cm^{-1}, corresponding to the typical stretching of C=O and C=C groups (black curve). After MPS modification, the sample only showed the typical IR peak of C=O around 1700 cm^{-1} due to the relative weak signal of C=C. However, the signal of C=O can still work as an effective indicator of its successful surface modification on CNCs@SiO_2.

After surface modification, polystyrene was then coated on the uniform CNCs@SiO_2 particles through one-step emulsion polymerization of styrene using MPS grafted CNCs@SiO_2 as seeds, SDS as surfactant and KPS as initiator. Figure 5.1c-e showed

typical TEM images of the resulting colloids with clearly distinguished three layers of Fe_3O_4, SiO_2 and PS. Interestingly, the number of PS patches on the silica and the overall morphology of the colloidal particles varied from each other, including bowtie, flower-like and core-shell structures, which can be attributed to the variation in the density of coupling agent on the surface of SiO_2. When 50 μL MPS was used during surface modification process, bowtie-like structure with two polymer patches attached to the silica core was obtained. It is because, at the initial stage of polymerization, with limited amount of double bonds modified on the silica surface, few polymer seeds were deposited on the seeds through copolymerization reaction. After absorbing styrene monomers, the polystyrene shell tends contract and reduce the surface area as a result of interfacial tension between the hydrophilic silica and hydrophobic polystyrene, resulting in asymmetric distribution of polymer around the seeds. Lacking of driving force of further combination when the two polystyrene patches occupied the South and North Pole of the seed, bowtie-like structure with the two patches opposite positioned was achieved. With increased density of coupling agent, more polymer seeds were being able to loaded at the initial polymerization state, resulting in more patches around the core with a flower-like structure. It's worth noting that, the size of the patches is more uniform in the flower particles than the bowtie case, due to the relatively uniform distribution of coupling agent with higher density. Further increased the amount of MPS to 200 μL, the reduced interfacial tension allows the fully engulfing of silica core by polymer shell. However, the core is still eccentric positioned in the polymer shell due to the low viscosity of the linear polymer network in the absence of crosslinker.[31]

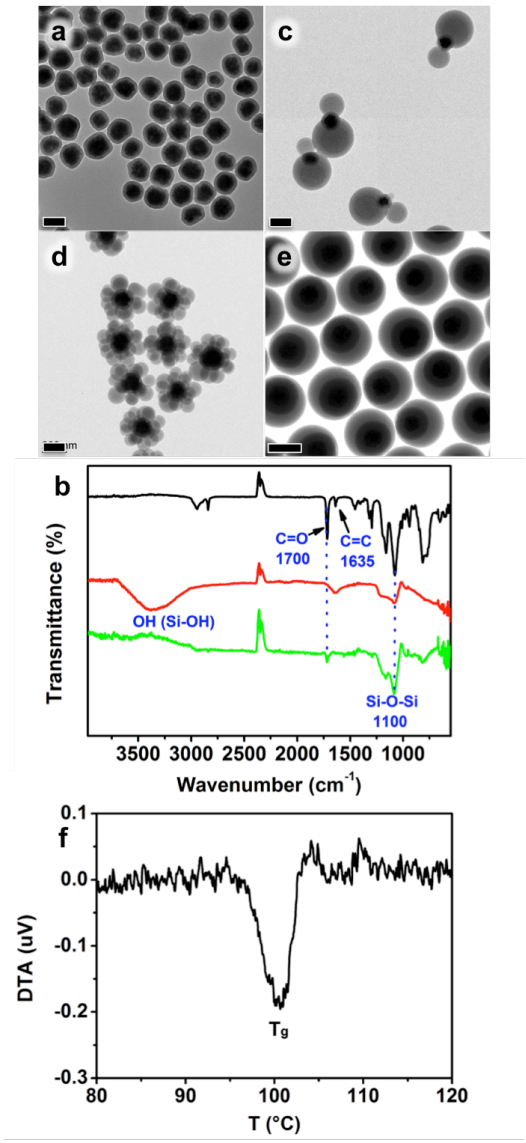

Figure 5.1. a) TEM image of CNC@SiO_2; b) FTIR of MPS (black), CNCs@SiO_2 before (red) and after (green) MPS modification; TEM images of CNCs@SiO_2@PS with different amount of MPS modification c) 50, d) 100 and e) 200 µL; f) TGA of PS on the seed particles. Scale bars: 200 nm.

To facilitate the post-treatment, the glass transition temperature (T_g) of the coated PS was examined by differential thermal analysis (DTA). As shown in Figure 5.1f, T_g of PS was determined around 100 °C. When heated above glass transition temperature, the polymer shell would be softened. Driven by the minimization of Gibbs free energy, shape changing towards equilibrium structure will be initiated.

5.3.2 Post-Treatment of Core-Shell Structure

A core-shell structured sample prepared with 200 μL MPS modification (core-shell-200) was firstly selected to perform the post-treatment. In Figure 5.2a, the core-shell-200 showed very good uniformity and dispersity with overall size of 350 nm and averaging thickness of PS coating of 30 nm. In a typical post-treatment process, the particles were firstly diluted by 20 times in the chosen solvent under sonication to avoid interparticle fusion upon heating and enable thoroughly interaction between particles and their surrounding solvent. Afterwards, the solution was heated up in a oil bath at 160 °C for 20 min, which allows the softening of polymer coating with sufficient flexibility as well as provides adequate time of shifting to the new equilibrium configuration driven by minimizing the free surface energy. After heated for 20 min in diethylene glycol (DEG), ethylene glycol (EG) and propylene carbonate (PC) respectively, the resulting morphology of the particles was characterized by TEM and showed in Figure 5.2b-d. When the post-annealing was conducted in DEG, total wetting of PS around multiple silica seeds was observed in Figure 5.2b. However, dewetting was revealed

accompanying shape shifting from full coating to half or even less coverage when EG or PC was chosen as the dispersion.

In the post-treatment process, the equation of spreading coefficient should be rewrite as: $S_p = \gamma_{s,solvent} - (\gamma_{sp} + \gamma_{p,solvent})$, with the three parameters corresponding to the interfacial tension of silica/solvent, silica/PS and PS/solvent. When the synthesized particles were dispersed in DEG solution, compared to the synthetic conditions in water, the interfacial tension between silica and DEG is larger than that with water ($\gamma_{s,DEG} > \gamma_{s,w}$) and $\gamma_{p,solvent}$ is smaller ($\gamma_{p,DEG} < \gamma_{p,w}$). As a result, wetting of PS on silica happened driven by the positive S_p. While dispersed in EG, $\gamma_{p,solvent}$ was increased, due to the relative low affinity between EG and PS compared to DEG, which resulted in a negative spreading coefficient. That's why transformation from full to half coating was observed in EG. Further increase $\gamma_{p,solvent}$ by utilizing a more PS hated solvent PC,[231] driven by the negative S_p with larger absolute value, more obvious shape switching was discovered with the only about 10% coverage of polymer on the silica core. To better describe the shifting of shape, the contact angle of PS on SiO_2 surface was carefully measured and calculated.[230] As shown in Figure 5.2e. With the decreasing of the affinity between polymer and solvent, the contact angle was increased from 0 to 10 and finally reaching around 70°. Driven by the differences of S_p when heated in different solvents, this method demonstrated good efficiency to manage the contact angle of patches of patchy particles.

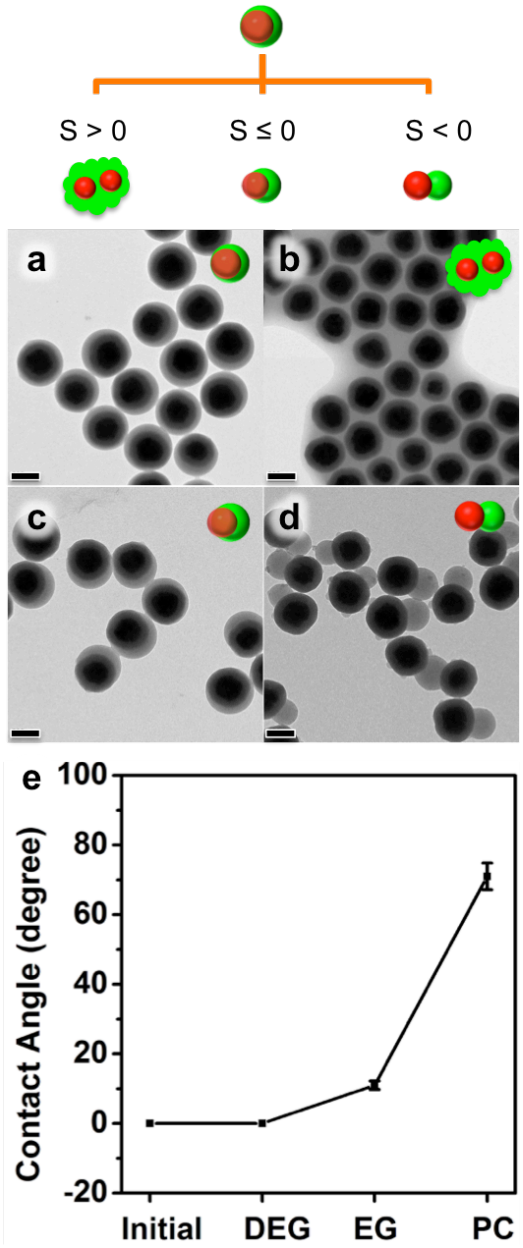

Figure 5.2. TEM images of a) The initial synthesized core-shell nanostructures of CNCs@SiO_2@PS and post-treated with b) DEG, c) EG and d) PC. Corresponding contact angle of PS on SiO_2 after fusion in different solvents was shown in e). Scale bars: 200 nm.

To further confirm the shape switching is simply determined by its dispersion solvent and achieve more precise control over the contact area, curvature or contact angle of the patches, post-heating in mixture solutions of EG and PC with different volume ratios was demonstrated. As shown in Figure 5.3a-e, with different volume fraction of PC ranging from 0 to 100%, more equilibrium states with controlled coverage area and contact angle were achieved. With only 25% of PC in the mixture, there is no obvious difference in the shifting of patches when compared to pure EG (Figure 5.3a-b). However, more predominant dewetting of polymer was discovered when the volume fraction of PC increased to 50% (Figure 5.3c). Further increasing the percentage of PC to 75% or 100%, dimer structures with less and less interfacial area were obtained (Figure 5.3d-e). Figure 5.3f illustrated the changing of contact angle in response to the volume fraction of PC in the mixture solutions, from which we can tell that with the increasing of the volume fraction of PC, the contact angle gradually increased. The phenomena can be explained in terms of Gibbs free energy. When dispersed in an environment with less and less affinity, the polymer patches tend to minimizing the surface energy by minimizing the surface area, as a result, increased contact angle was observed. It's worth noting that the uniformity and yield of the particles fabricated by post-treatment is very good, which further confirmed that the structure represents the equilibrium states with minimum surface energy. By utilizing solvent mixtures, more precise control over the contact angle was achieved as well as more structures with high yield and uniformity were fabricated.

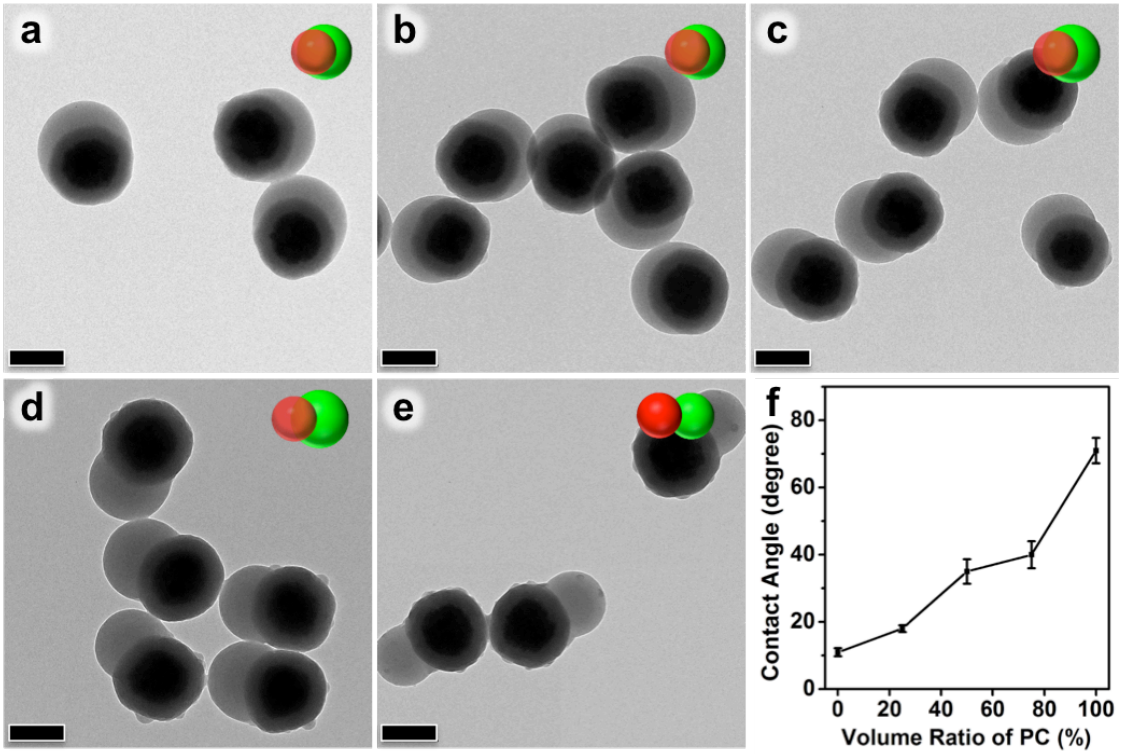

Figure 5.3. TEM images of patchy particles after fusion in mixture solutions of PC and EG with different volume ratios: a) 0, b) 25, c) 50, d) 75 and e) 100% of PC/EG. Corresponding contact angle in respond to volume ratios was presented in f). Scale bars: 200 nm.

5.3.3 Thermodynamics of the Shape Switching

To further confirm that the resulting configuration of the patchy particles represents an equilibrium state, which is determined by its corresponding S_p, aiming to minimizing the Gibbs free energy, and thus, the final structure of the patchy particles should be only related to the final dispersion environment no matter the pathways to it, the thermodynamics of the shape switching process were studied. Accordingly, we performed post-heating on the same particle by alternative PC or EG solvent and the corresponding results were shown in Figure 5.4. In detail, the particles were firstly treated with PC to achieve the dimer structure with highly curved patches followed by several times of washing and redispersed in EG for another heating treatment. And then, one more cycle of PC and EG fusion was performed. Figure 5.4a showed the structure of PC treatment alone and two-steps of PC and then EG (PC-EG) treatment was performed on the sample (Figure 5.4b). Then, result of three times heating in the order of PC-EG-PC was presented in Figure 5.4c, and finally, multiple paths of PC-EG-PC-EG were applied to the sample and showed in Figure 5.4d. However, no matter the paths that the particles been through, the final structure is only determined by the last solvent that the particles been treated. Thus, almost perfect reversibility between PC and EG determined configuration was demonstrated in the cycling process. From the results, we can tell that firstly, the reaction reached equilibrium state within the given time of 20 min; secondly, the shape switching is driven by the spreading coefficient, which is only related to the thermodynamic free energy. In such a scenario, we demonstrated that the final

configuration is the result of thermodynamic equilibrium state with the lowest energy and we realized the shape adapting and reconfiguration upon environmental stimulus, which is a prerequisite for smart materials or artificial biological system.

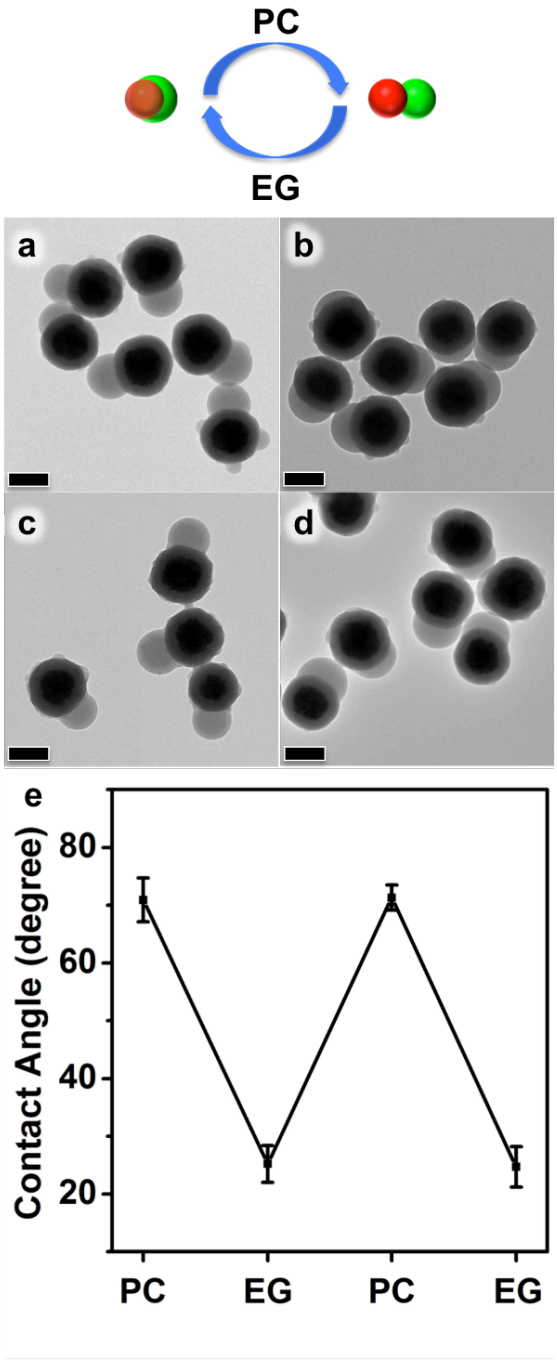

Figure 5.4. TEM images of patchy particles after alternative treatment of PC and EG: a) PC, b) EG, c) PC and d) EG. Corresponding contact angle of PS on SiO_2 after fusion in different solvents was presented in e). Scale bars: 200 nm.

5.3.4 Post-Treatment on Particles with Different PS/Seed Interfacial Tensions

In addition to varying the environment of the patchy particles in regards to changing $\gamma_{s,solvent}$ and $\gamma_{p,solvent}$, interfacial tension between PS and seeds (γ_{sp}) during the initial synthesis also played an important role in determining the value of spreading coefficient S_p. The most direct way to varying γ_{sp} is controlling the density of coupling agent on the silica cores before polymerization. Firstly, CNCs@SiO_2@PS with smaller γ_{sp} was studied, which was prepared by increasing the amount of MPS to 400 μL during surface modification process. As shown in the TEM images in Figure 5.5a, we got similar core-shell structure as the core-shell-200 sample but with thicker PS coating of around 42 nm. The sample is denoted as core-shell-400 in the following discussion for simplicity. When post-heating was carried out on core-shell-400 sample in DEG, EG and PC, we obtained different results compared to the previous case. As illustrated in Figure 5.5, no obvious change was observed in DEG and EG dispersion, whereas only PC was able to initiate shape switching to the direction of dewetting. However, the degree of dewetting in PC was not as strong as the core-shell-200 case with still almost half of the core being covered by the polymer as shown in Figure 5.5d. The possible reasons were analyzed as follows. In the equation: $S_p = \gamma_{s,solvent} - (\gamma_{sp} + \gamma_{p,solvent})$, compared to the core-shell-200 sample, $\gamma_{s,solvent}$ and $\gamma_{p,solvent}$ stay almost the same when dispersed in the same solvent and the only parameter that has been changed is γ_{sp}. From the previous studies, we know that S_p is positive in DEG for core-shell-200. When the particle is changed to core-shell-400 with a smaller γ_{sp}, S_p should still be positive by subtracting a smaller number in the

equation, as a result, the polymer patches keep wetting the surface of silica and no obvious changing was observed. Nevertheless, for the condition that S_p of core-shell-200 is negative but with a relative small absolute value in EG, the value of S_p would turn slightly positive or zero, when γ_{sp} is decreased, still resulting in the wetting structure. However, in case of a negative S_p of large absolute value in PC for core-shell-200, when switched to core-shell-400 particle, S_p remains negative even with the decrease of γ_{sp}, thus dewetting happened. Yet, the absolute value of S_p in this case would definitely been decreased, resulting in a lower degree of shape switching compared to the results shown in Figure 5.2.

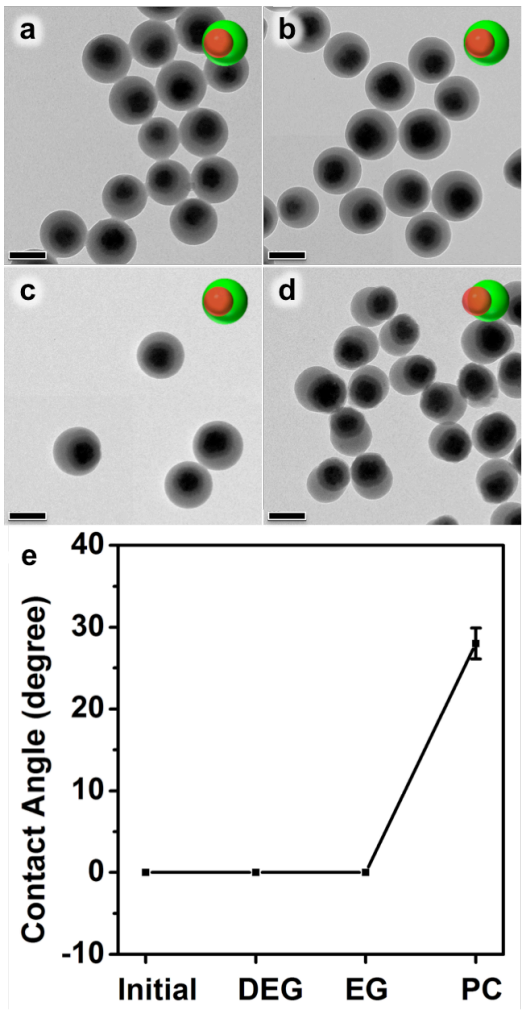

Figure 5.5. TEM images of a) CNCs@SiO_2@PS with 400 μL MPS modification and post-treated with b) DEG, c) EG and d) PC. Corresponding contact angle of PS on SiO_2 after fusion in different solvents was shown in e). Scale bars: 200 nm.

Another batch of sample with larger γ_{sp} compared to the core-shell-200 was then studied, which was realized by decreasing the density of coupling agent with less MPS modification (100 μL). Different from the previous two cases, the morphology of the patchy particles changed from core-shell to flower-like structures due to the larger interfacial tension between the polymer and silica and the sample is denoted as flower-100. As shown in Figure 5.6a, 13 patches were observed on each silica core and not only the overall size of the flower like particle but also the shape and size of the patches showed very good uniformity. And then, followed the same procedure, the flower-100 was dispersed in different solvents and heated at 160 °C for 20 min. After annealing in different solvents, the patchy particles were examined by TEM. In Figure 5.6b, completely wetting of PS on silica core was observed in DEG. Interestingly, the core is concentric positioned in the polymer shell resulting in a sunny-side up egg structure, which is quiet different from the previous case. Whereas, dewetting was observed when EG or PC was chosen as the dispersion, resulting in tripods structures with different contact angle of patches, which can be also attributed to the change of spreading coefficient with increased γ_{sp}. Specifically, with very positive S_p in DEG for core-shell 200, S_p stays positive even with larger substrate item of γ_{sp} when flower-100 was heated. However, with the initial negative S_p in EG and PC, when the particle was changed from core-shell-200 to flower-100 with a high surface tension, the new S_p becomes more negative by subtracting a larger γ_{sp}, as a result, dewetting of polymer on silica core with larger contact angle was achieved. As shown in figure 5.6e, the contact angle was increased from 0 to 70 and then 110° when the solvent was changed from DEG to EG and

then PC, the trend of which is very consistent with the previous results. It is worth noting that the contact angles of patches treated in PC were quiet different from each other by varying γ_{sp}. With increased of γ_{sp} from core-shell 400, to core-shell-200 and then flower-100, the trend of contact angle change in different solvents was summarized in Figure 5.7. With the decreasing of MPS amount during surface modification, γ_{sp} is increased, as a result, the contact angle of polymer on silica is increased when post-heated in the same solvent. For example, the contact angle in PC was increased from 30°(core-shell-400) to 70°(core-shell-200) and finally reached 110°(flower-100), which further confirmed the importance of γ_{sp} in determining the final configuration of the particles. Moreover, in the tripods structures obtained in EG and PC, the contact angles of the three patches are almost the same, which further confirmed the relative uniform distribution of the coupling agent.

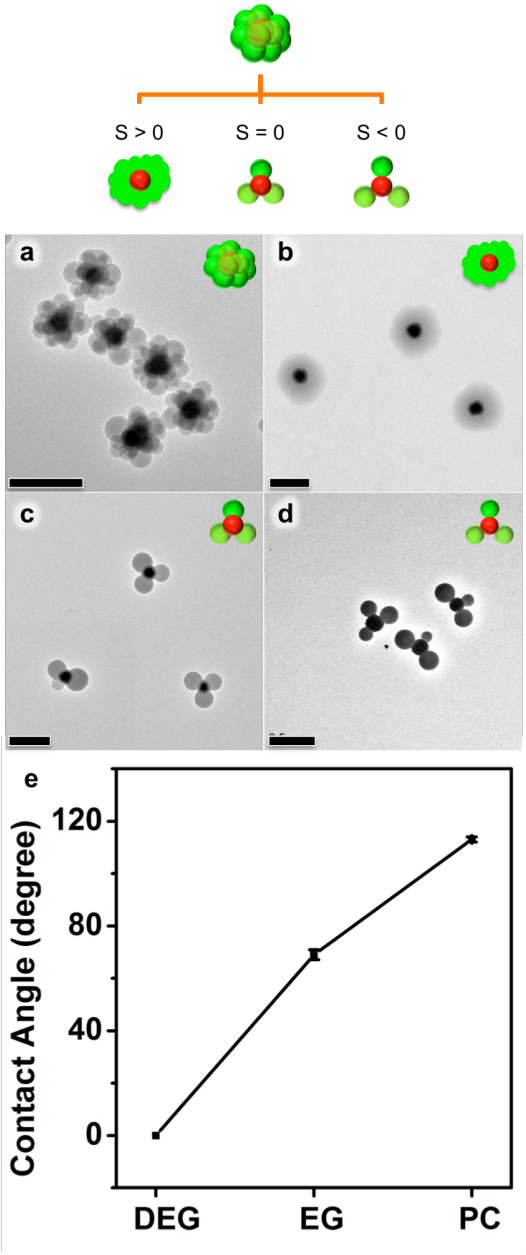

Figure 5.6. TEM images of a) The initial synthesized flower-like nanostructures of CNCs@SiO_2@PS and post-treated with b) DEG, c) EG and d) PC. Corresponding contact angle of PS on SiO_2 after fusion in different solvents was presented in e). Scale bars: 500 nm.

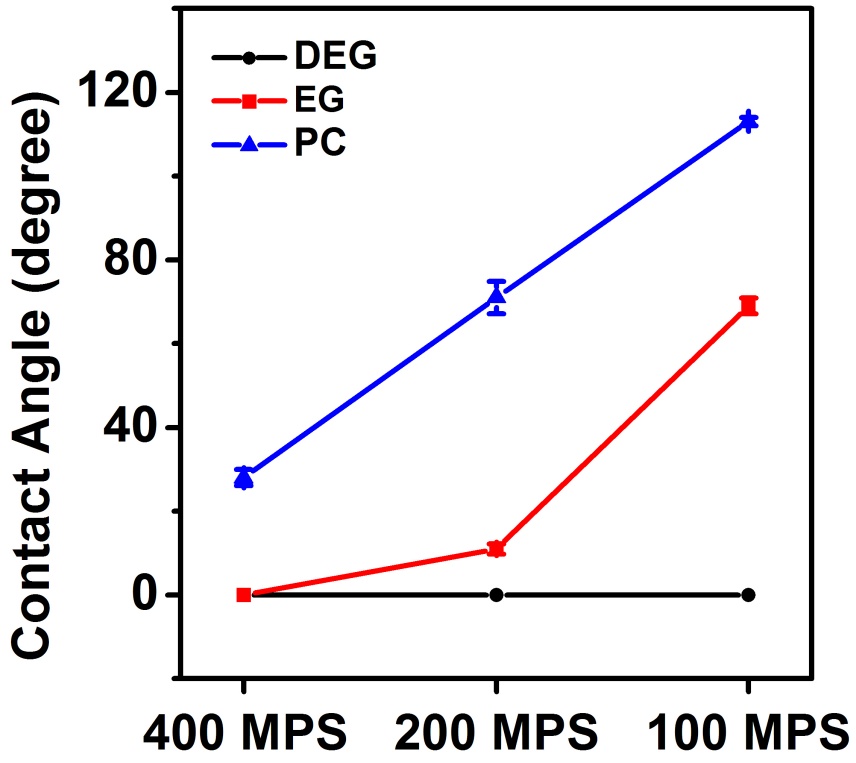

Figure 5.7. Comparison of contact angles of PS on silica for core-shell-400, core-shell-200 and flower-100 in different solvents: DEG (black curve), EG (red curve) and PC (blue curve).

3.3.5 Kinetics of Shape Switching

During the post-treatment of flower-100, in addition to the variation of contract angle, we observed obvious decrease in the number of petals on the core of the flower-like structure, which makes it a perfect system to study the kinetics of the shape switching process. When the particles were heated above glass transition temperature, the polymer is softened, turning on the shape switching towards the spreading coefficient favored direction and decreasing the number of petals to minimize the surface energy. Subsequent rapid temperature quenching at different point of time can halt the process, leaving the particle with an intermediate shape with higher energy. As shown in Figure 5.8, we started with a flower-like sample with around 13 petals surrounding the core. When only heated for about 30 seconds, the number of petals was decreased to around 9, indicating the rapid heating to the glass transition temperature. With the increasing of the heating time to 1 min, the number of petals reached 7. If quenched at 2 min, octahedron shape with six petals around the core was obtained. Within 5 min, we observed triangle bipyramid configuration with 5 patches on the silica. By further increasing the heating time to 10, 20 and 30 min, tetrapods, tripods and bowtie like structures were fabricated. It worth noting that, at the initial stage of the fusion, the reaction rate is very fast within the 5 min with quantity of patches rapidly decreased from 13 to 5. However, the reaction rate became pretty slow when attempting to further decrease the number of petals below five. It took about 30 min to achieve the structures with two patches. This phenomenon could be attributed to the density of the patches on the silica. During the chemical reaction, the

reaction rate is higher with higher concentration of the reactant; otherwise, the reaction rate slows down with the decreasing of the reactant concentration. Likewise, at the initial stage, the density of patches is higher on the surface and the interaction between petals is stronger. Upon heating, patches tend to combine with each other to minimize the surface energy. However, when the density of patches was dramatically decreased, such as tetrapods, the patches were quite detached from each other and it might take longer time for those patches to encounter with each other. In such an approach, we further demonstrated the precise control of the quantity of patches in addition to the shape control, as well as showed more complex three-dimensional configurations comprising line (2 petals), triangle (3 petals), tetrahedron (4 petals), triangular bipyramid (5 petals) and octahedron (6 petals).

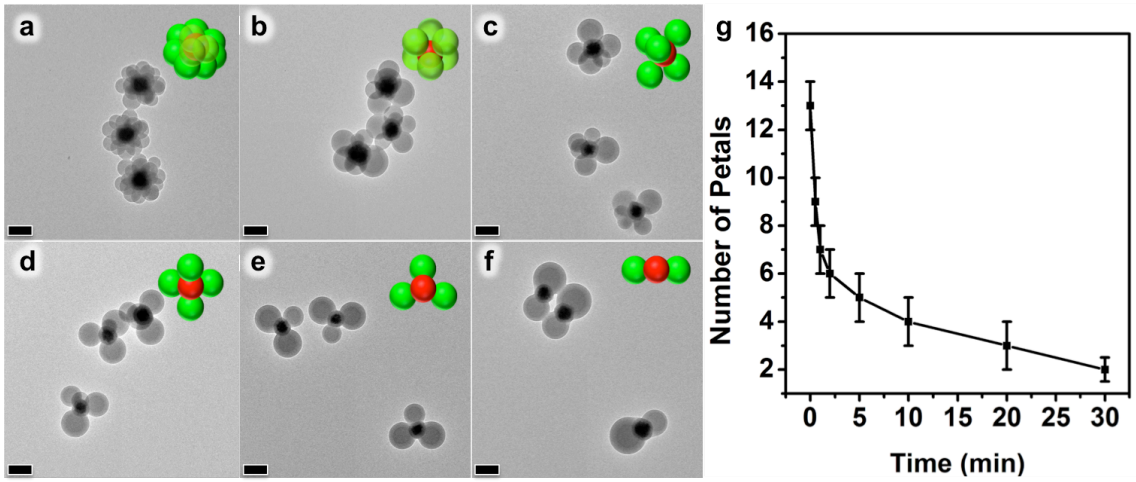

Figure 5.8. TEM images of a) The initial synthesized flower-like nanostructures of CNCs@SiO_2@PS and post-heated with EG at 160 °C for different length of time: b) 2, c) 5, d) 10, e) 20, e) 30 min. Corresponding numbers of petals on the SiO_2 core within different fusion time were shown in e). Scale bars: 200 nm.

5.3.6 Functionalization on Selective Area

Anisotropy of shape, surface property and function is always perused as it can influence crystallization and packing and contributes to structural complexities and functional varieties. To demonstrate the uniqueness of the structures fabricated through post-treatment, we performed Pt functionalization on selective area of silica core. The basic idea can be seen from the scheme in Figure 5.9. Starting with a patchy particle, amino groups were first modified on the surface through APTES modification. And then, the prepared Pt seed with average diameter around 3 nm was loaded on the surface of the particles through the interaction between noble metal and amino groups. By simply removing the polymer patches by toluene, we obtained silica particle with controlled coverage of Pt patches on the surface. To practice this design, two typical cases with silica core almost half covered by PS and about 10 % shielded were studied. As shown in Figure 5.9ai-iv, after APTES modification and Pt seed loading, both the silica core and PS patches were being able to be functionalized by Pt seed, which demonstrated the success of APTES modification. The density of Pt is high and the size and distribution of Pt seeds are quite uniform, demonstrating the high density and uniform distribution of amino groups. However, after the removal of PS patches through toluene swelling, the area that was previously occupied by PS was very clean, as a result, silica core partially patched with Pt nanoseeds was realized. By comparing the results between Figure 8a and b, controlled patchy area of Pt varying from 50% to 90% was achieved and the boundary between the patchy area and clean area can be clearly seen in the enlarged image in

Figure 5.9aiv and biv. The success of patching particles with Pt seed in a controlled manner holds great potential in the application of catalysis, biomedicine, self-assembly, and synthesis of noble metal half-shell or bowl-like structures with controlled openings.

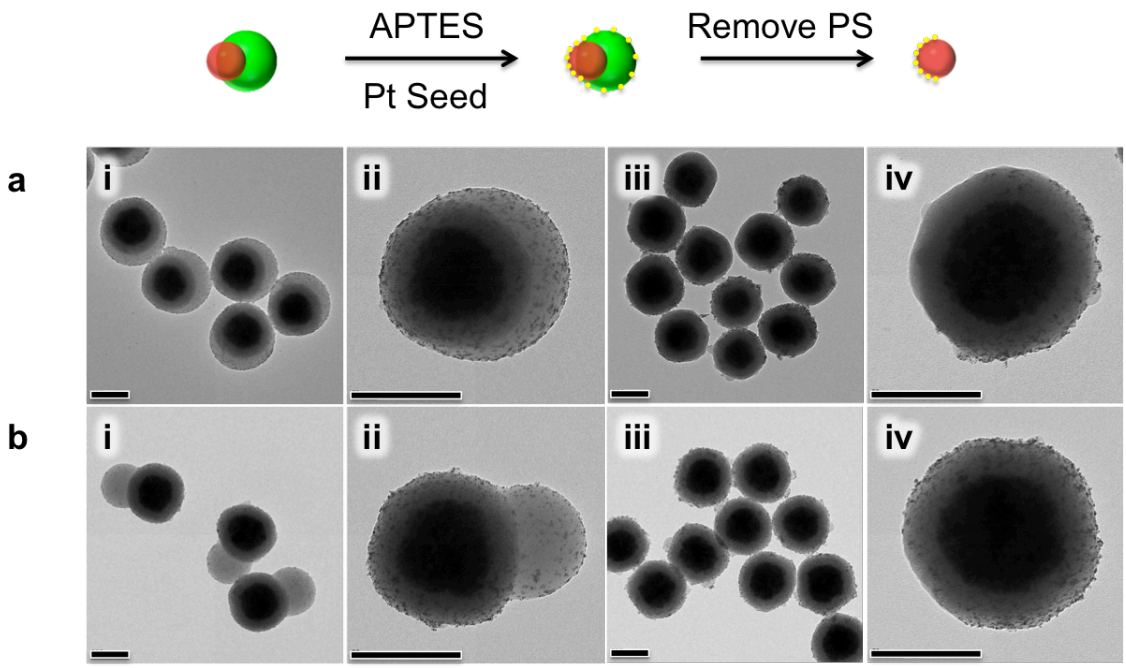

Figure 5.9. TEM images of functionalization of silica core on selective area with Pt seed for a) half coated silica and b) 10 % coated silica core and corresponding results of each steps i) right after solvent treatment, ii) after APTES modification and loading of Pt seeds, iii) after removal of PS and iv) high magnificent images after removal of PS. Scale bars: 200 nm.

We demonstrated one of the possibilities by seeded growth of Pt seed to form Pt shells with controlled thickness, depth and size of openings. The procedure was illustrated in the scheme of Figure 5.10. Firstly, the patchy particles were functionalized with Pt seeds by APTES modification and seed loading. And then, seeded growth of Pt was performed. During the seeded growth process, Pt seeds tend to simultaneously grow bigger at the initial stage. After the Pt seeds grew big enough to contact with each other, further deposition of Pt would tend to connect the particles together to form a shell structure. As illustrated in Figure 5.10, after seed loading, a thin layer of Pt shell was coated on the surface of patchy particles and the shell thickness was estimated to be less than 10 nm. And then the particles were swelled by toluene. It was found that along with the PS, Pt shells that grew on the PS were also been removed by toluene, which demonstrated that firstly, the Pt shell is porous which favors the diffusion of toluene; secondly, the connection of Pt shells on the silica core and polymer patches is very weak at such thin thickness of Pt coating. As a result, semi-spherical shells of Pt with different depth and opening were fabricated (Figure 5.10aiii, 5.10biii). Since the contrast of Pt shell is much higher than Pt seeds, the boundaries between the Pt patched area and Pt free area can be more clearly seen in the high magnificent TEM images showing in Figure 5.10aiv and 5.10biv. Here, we realized fabrication of the noble metal shell structures with controlled depth and opening size by utilizing the patchy particles with anisotropic surface functions.

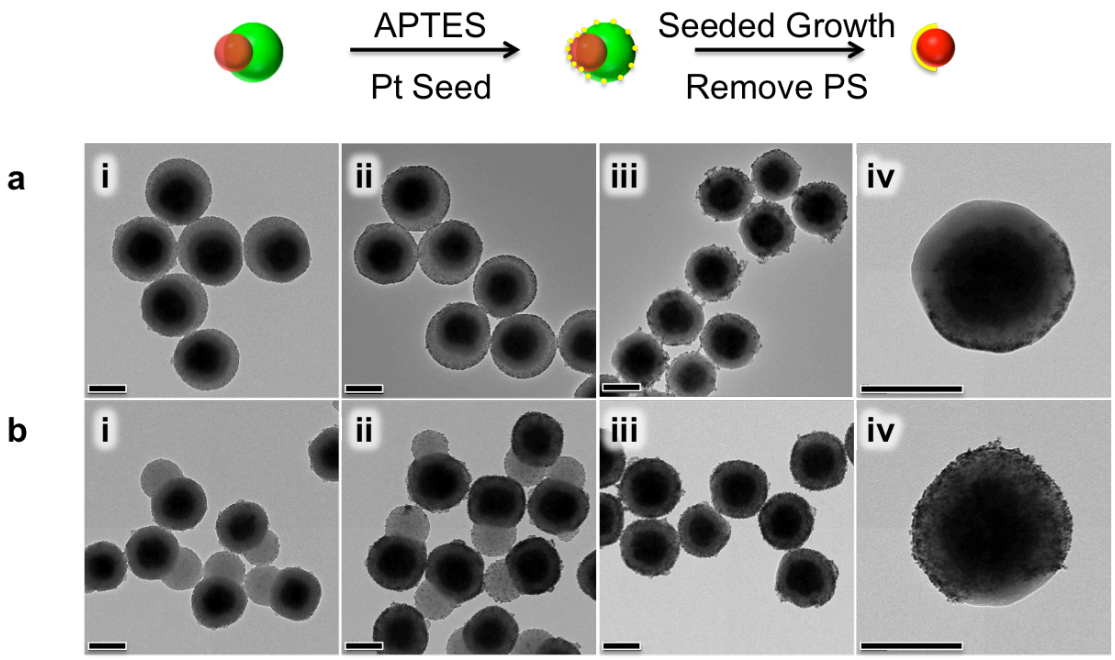

Figure 5.10. TEM images of fabrication of Pt shell template on the Pt seed functionalized patchy particles for a) 50% functionalized silica and b) 90 % functionalized silica and corresponding results of each steps i) right after seed loading, ii) after seeded growth of Pt to form a Pt shell, iii) after removal of PS and iv) high magnificent images after removal of PS. Scale bars: 200 nm.

However, if the thickness of Pt shell was increased to about 20 nm with more precursor added during the seeded growth process, after the removal of polystyrene, Pt shell on the polymer would not be removed due to the stronger connections between shells on the core and patches, resulting in snowman-like Pt shell structures with different size ratios between the head and body part (Figure 5.11). By comparing the TEM images before and after toluene treatment, a clearly higher contrast of the Pt shell on PS was observed, demonstrating the success of the removing of PS. Moreover, the success of PS removal further demonstrated that even with thicker Pt coating of approximately 20 nm, the Pt shell structure we obtained is still porous, and the porosity is still adequate for the diffusion of toluene and swelling of polystyrene. Utilizing patchy particles with controlled contact angle of PS on silica as template, snowman like Pt shell structures with different size ratios between the two parts were achieved.

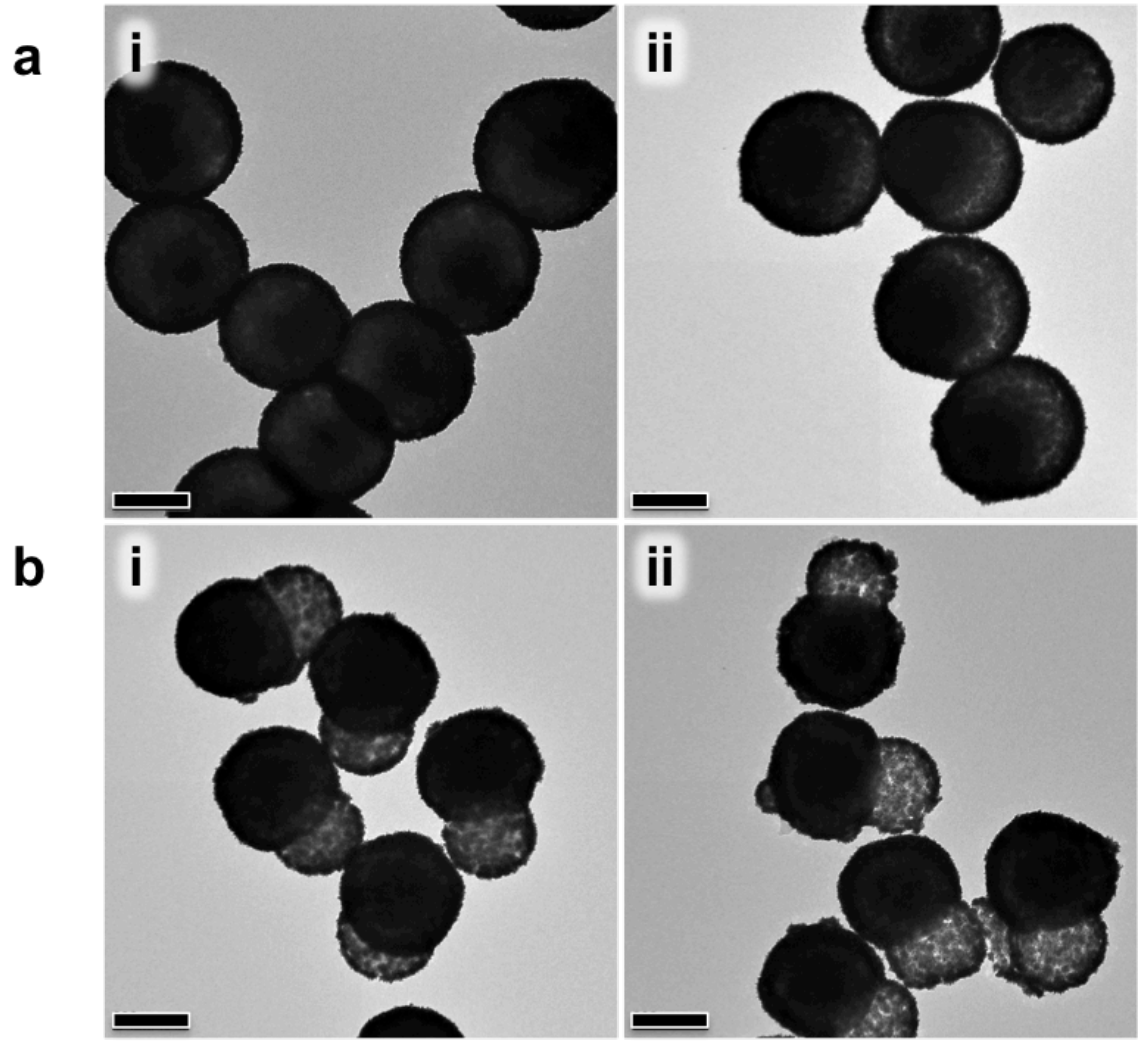

Figure 5.11. TEM images of snowman like Pt shell structures with different size ratios on a) 50% polymer patched and b) 10% polymer patched particles i) before and ii) after toluene etching.

Nevertheless, to gain Pt bowl or shell structures with thicker thickness is not a problem; minor revision just needs to be made on the experimental procedure: removal of PS was carried out right after the seed loading followed by seeded growth. As shown in Figure 5.12, uniform Pt bowl like structures with different depth and openings were fabricated and the shell thickness was estimated around 40 nm. Potentially, Pt bowls can be used in catalysis with a magnetic core inside enabling fast magnetic separation and recycling of catalysts. With partial patched with Pt, the exposed silica can also been functionalized with other possible functional materials followed in the same design. At this point, we demonstrated the success of patching functional material on selective area of the colloidal particles as well as its applications in fabricating intrinsic structures of noble metal including shell, bowl and snowman like morphology in good control.

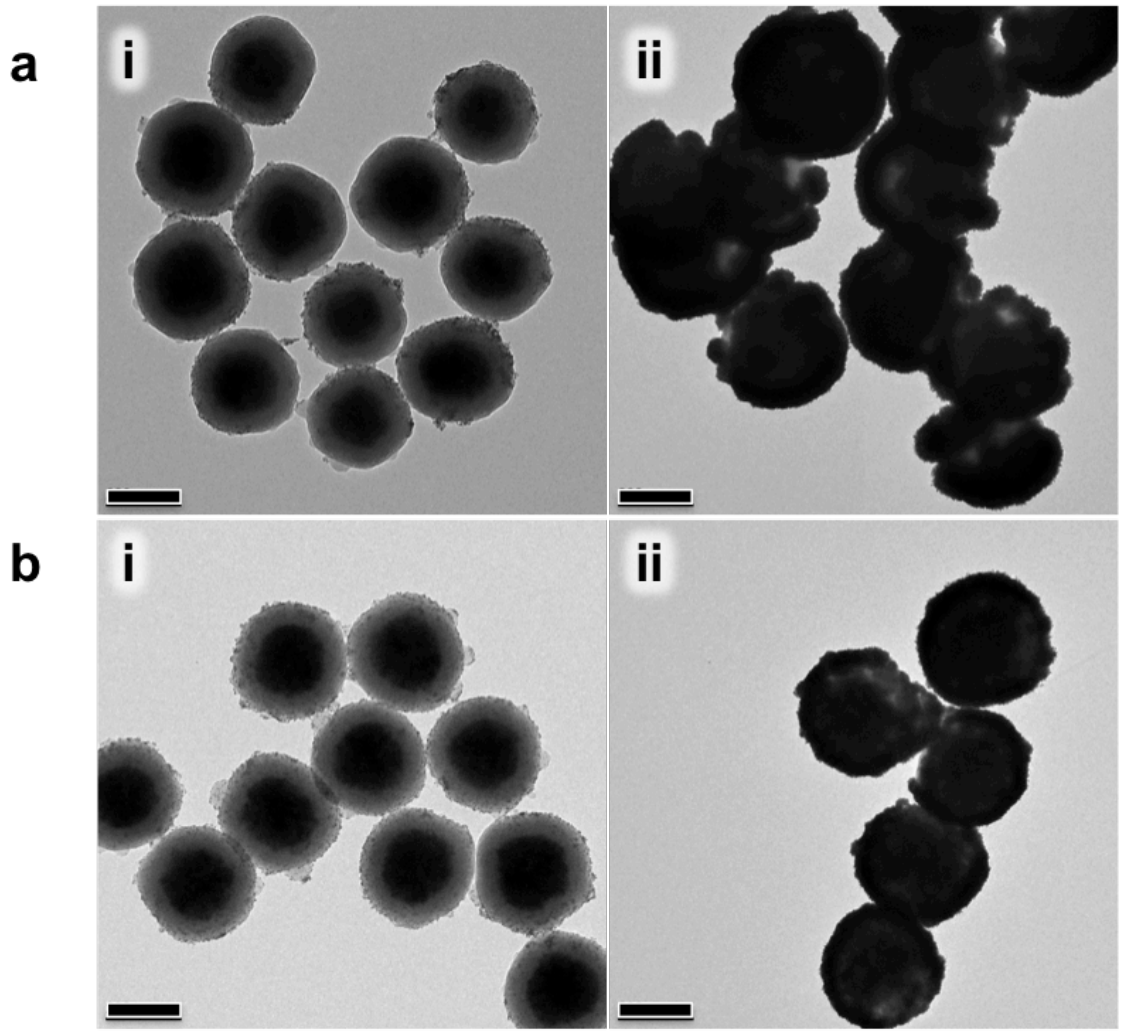

Figure 5.12. TEM images of Pt bowl structures with different depths and openings on a) 50% polymer patched and b) 10% polymer patched particles i) before and ii) after toluene etching.

5.4 Conclusion

In this article, we realized shape switching of patchy particles according to the spreading coefficient S_p of polystyrene patches on silica particles. Since S_p is determined by the three interfacial tensions--$\gamma_{s,solvent}$, $\gamma_{p,solvent}$ and γ_{sp}--between the silica seed (s), polymer (p) and dispersion environment (solvent), the reconfiguration of the building blocks was then realized by tuning $\gamma_{s,solvent}$ and $\gamma_{s,solvent}$ in different solvents and varying γ_{sp} through controlled MPS modification. As a result, fine-tuning of patchy area, curvature and contact angle of polymer coating was achieved. Next, driven by minimizing of surface energy, which is thermodynamically stable, reconfigurable and reversible shape switching of patchy particles upon different external stimuli was realized, which is of great importance in studying the biological system, considering ubiquity of adaptability in natural building blocks. In addition, kinetics studies revealed more intermediate stages with complex three-dimensional configuration including tetrahedron, triangle bipyramid and octahedron by precisely controlling the number of patches around the silica. In such a scenario, except for the shape of patches, the number of patches was achieved. Moreover, the functionality of the patches was managed through Pt seed modification on selective area of silica core, which holds great potential for application in catalysis, self-assembly or templated synthesis of noble metals with unique structures. Accordingly, Pt-shell-patched silica particles with controlled shell thickness, depth and openings were fabricated. This work has its immediate significance in providing a post-treatment

strategy for elaborating complex nanostructures, which remains challenging in their direct synthesis. Conceptually, it also renews our understanding of spreading coefficient and interfacial tensions not only in the synthetic process of polymerization or coating, but also in their post-treatment design, which reveals more variations in morphological change. More importantly, the principle of post-treatment based on spreading coefficient described there can be widely used for fabrications of complex structures and thereby greatly promote fundamental studies of self-assembly and practical applications in optical, magnetic, electronic and catalytic devices.

5.5 References

1. Boles, M. A.; Engel, M.; Talapin, D. V., Self-Assembly of Colloidal Nanocrystals: From Intricate Structures to Functional Materials. *Chem. Rev.* **2016,** *116* (18), 11220-11289.

2. Whitesides, G. M.; Grzybowski, B., Self-Assembly at All Scales. *Science* **2002,** *295* (5564), 2418-2421.

3. Velev, O. D., Self-Assembly of Unusual Nanoparticle Crystals. *Science* **2006,** *312* (5772), 376-377.

4. Wang, M.; Yin, Y., Magnetically Responsive Nanostructures with Tunable Optical Properties. *J. Am. Chem. Soc.* **2016,** *138* (20), 6315-6323.

5. Liu, Y.; Tang, A.; Zhang, Q.; Yin, Y., Seed-Mediated Growth of Anatase TiO2 Nanocrystals with Core–Antenna Structures for Enhanced Photocatalytic Activity. *J. Am. Chem. Soc.* **2015,** *137* (35), 11327-11339.

6. van Blaaderen, A., CHEMISTRY: Colloidal Molecules and Beyond. *Science* **2003,** *301* (5632), 470-471.

7. Zhang; Glotzer, S. C., Self-Assembly of Patchy Particles. *Nano Lett.* **2004,** *4* (8), 1407-1413.

8. Du, J.; O'Reilly, R. K., Anisotropic particles with patchy, multicompartment and Janus architectures: preparation and application. *Chem. Soc. Rev.* **2011,** *40* (5), 2402-2416.

9. Walker, D. A.; Leitsch, E. K.; Nap, R. J.; Szleifer, I.; Grzybowski, B. A., Geometric curvature controls the chemical patchiness and self-assembly of nanoparticles. *Nat Nano* **2013,** *8* (9), 676-681.

10. Jiang, S.; Chen, Q.; Tripathy, M.; Luijten, E.; Schweizer, K. S.; Granick, S., Janus Particle Synthesis and Assembly. *Adv. Mater.* **2010,** *22* (10), 1060-1071.

11. Perro, A.; Duguet, E.; Lambert, O.; Taveau, J.-C.; Bourgeat-Lami, E.; Ravaine, S., A Chemical Synthetic Route towards “Colloidal Molecules”. *Angew. Chem., Int. Ed.* **2009,** *48* (2), 361-365.

12. Reculusa, S.; Mingotaud, C.; Bourgeat-Lami, E.; Duguet, E.; Ravaine, S., Synthesis of Daisy-Shaped and Multipod-like Silica/Polystyrene Nanocomposites. *Nano Lett.* **2004,** *4* (9), 1677-1682.

13. Reculusa, S.; Poncet-Legrand, C.; Ravaine, S.; Mingotaud, C.; Duguet, E.; Bourgeat-Lami, E., Syntheses of Raspberrylike Silica/Polystyrene Materials. *Chem. Mat.* **2002,** *14* (5), 2354-2359.

14. Sheu, H. R.; El-Aasser, M. S.; Vanderhoff, J. W., Phase separation in polystyrene latex interpenetrating polymer networks. *J. Polym. Sci., Part A: Polym. Chem.* **1990,** *28* (3), 629-651.

15. van Blaaderen, A., Materials Science: Colloids get complex. *Nature* **2006,** *439* (7076), 545-546.

16. Wang, H.; Li, B.; Yodh, A. G.; Zhang, Z., Stimuli-Responsive Shape Switching of Polymer Colloids by Temperature-Sensitive Absorption of Solvent. *Angew. Chem., Int. Ed.* **2016,** *55* (34), 9952-9955.

17. Zheng, X.; Liu, M.; He, M.; Pine, D. J.; Weck, M., Shape-Shifting Patchy Particles. *Angew. Chem., Int. Ed.* **2017,** *56* (20), 5507-5511.

18. Youssef, M.; Hueckel, T.; Yi, G.-R.; Sacanna, S., Shape-shifting colloids via stimulated dewetting. *Nat. Commun.* **2016,** *7*, 12216.

19. Tu, F.; Lee, D., Shape-Changing and Amphiphilicity-Reversing Janus Particles with pH-Responsive Surfactant Properties. *J. Am. Chem. Soc.* **2014,** *136* (28), 9999-10006.

20. Klinger, D.; Wang, C. X.; Connal, L. A.; Audus, D. J.; Jang, S. G.; Kraemer, S.; Killops, K. L.; Fredrickson, G. H.; Kramer, E. J.; Hawker, C. J., A Facile Synthesis of Dynamic, Shape-Changing Polymer Particles. *Angew. Chem., Int. Ed.* **2014,** *53* (27), 7018-7022.

21. Brochard-Wyart, F.; Di Meglio, J. M.; Quere, D.; De Gennes, P. G., Spreading of nonvolatile liquids in a continuum picture. *Langmuir* **1991,** *7* (2), 335-338.

22. Park, J. M., Core-Shell Polymerization with Hydrophilic Polymer Cores. *Korea Polym. J.* **2001,** *9* (1), 51-65.

23. Ge, J.; Hu, Y.; Yin, Y., Highly Tunable Superparamagnetic Colloidal Photonic Crystals. *Angew. Chem., Int. Ed.* **2007,** *46* (39), 7428-7431.

24. Ge, J.; Yin, Y., Magnetically Tunable Colloidal Photonic Structures in Alkanol Solutions. *Adv. Mater.* **2008,** *20* (18), 3485-3491.

25. Ge, J.; Hu, Y.; Zhang, T.; Yin, Y., Superparamagnetic Composite Colloids with Anisotropic Structures. *J. Am. Chem. Soc.* **2007,** *129* (29), 8974-8975.

26. Bigall, N. C.; Härtling, T.; Klose, M.; Simon, P.; Eng, L. M.; Eychmüller, A., Monodisperse Platinum Nanospheres with Adjustable Diameters from 10 to 100 nm: Synthesis and Distinct Optical Properties. *Nano Lett.* **2008,** *8* (12), 4588-4592.

27. Gao, A.; Xu, W.; Ponce de León, Y.; Bai, Y.; Gong, M.; Xie, K.; Park, B. H.; Yin, Y., Controllable Fabrication of Au Nanocups by Confined-Space Thermal Dewetting for OCT Imaging. *Adv. Mater.* **2017**, 1701070-n/a.

28. Feng, L.; Wu, X.; Ren, L.; Xiang, Y.; He, W.; Zhang, K.; Zhou, W.; Xie, S., Well-Controlled Synthesis of Au@Pt Nanostructures by Gold-Nanorod-Seeded Growth. *Chem. Eur. J.* **2008,** *14* (31), 9764-9771.

29. Extrand, C. W.; Moon, S. I., Contact Angles on Spherical Surfaces. *Langmuir* **2008,** *24* (17), 9470-9473.

30. Yang, G.-W.; Wu, G.-P.; Chen, X.; Xiong, S.; Arges, C. G.; Ji, S.; Nealey, P. F.; Lu, X.-B.; Darensbourg, D. J.; Xu, Z.-K., Directed Self-Assembly of Polystyrene-b-poly(propylene carbonate) on Chemical Patterns via Thermal Annealing for Next Generation Lithography. *Nano Lett.* **2017,** *17* (2), 1233-1239.

Chapter 6

Controllable Fabrication of Au Nanocups by Confined-Space Thermal Dewetting for OCT Imaging

6.1 Introduction

Nanostructures of noble metals such as Au and Ag have received widespread interest due to their broad applications in photocatalysis,[1] photodetection,[2] electrocatalysis,[3] chemical and biological sensing,[4] biomedicine,[5] optical devices,[6] and energy storage.[7] Specifically, noble metal nanostructures with reduced morphological symmetries have recently attracted increasing attention, with Au nanocups (also known as semi-shells) being extensively studied due to their unique plasmonic properties.[8] For example, magnetoinductive modes of Au nanocups were found to be able to efficiently scatter light in a direction dependent on particle orientation; and they could also enable light-bending which is difficult to achieve by nanoparticles of other geometries.[9]

Conventionally, Au nanocups are fabricated using physical methods, which typically involve physical deposition of thin Au films on spherical templates, with the cup opening formed by the shadowing effect of deposition or additional

anisotropic etching of the Au shells.[10] While offering precise control over the size and shell thickness of the nanocups, physical fabrication methods suffer from significantly low production yield as only a monolayer of nanocups could be fabricated in each process, which has seriously hindered the further explorations of their plasmonic properties and applications. Wet-chemical syntheses, with their advantage for large scale production,[11] have also been pursued, typically based on partial blockage of the colloidal template surface and then selective deposition of Au to the remaining surface.[12] Wang et al. recently reported an interesting process using PbS nanooctahedra as the sacrificial templates for Au overgrowth.[13] Au deposition starts at one vertex of the PbS and grows along the neighbouring facets, producing Au nanocups with rough outer surface and faceted inner surface after dissolution of the PbS template. Although the feasibility of these methods has been demonstrated, it still remains a great challenge to produce high-quality Au nanocups with precise control over the dimensions such as the size of the cup opening, which has important impact on their optical properties, e.g., the light-bending behaviour.

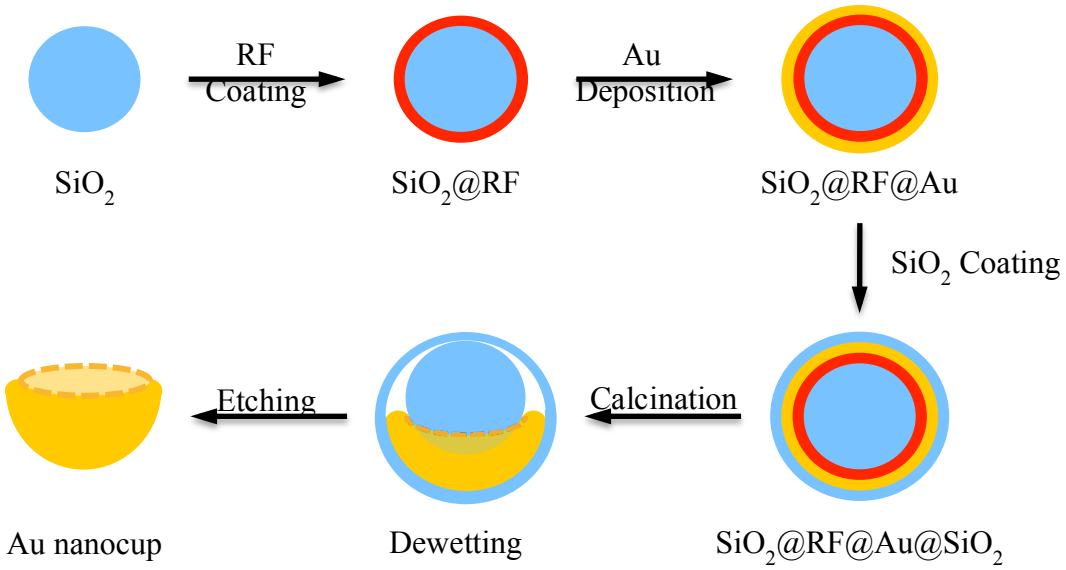

Scheme 6.1. Outline of the confined dewetting process for the fabrication of Au nanocups: silica spheres are coated sequentially with RF, Au, and SiO_2 layers, followed by calcination in air to remove RF and dewet Au from SiO_2 surface, and then etching SiO_2 templates to release Au nanocups.

In this work, we present a novel and robust method based on thermal dewetting in confined space for the fabrication of Au nanocups with high yield, well-controllable dimension, and potential scalability. As outlined in **Scheme 6.1**, the fabrication process involves multiple steps of wet chemical coating and a final step of thermal dewetting: uniform silica nanospheres are used as starting templates, coated sequentially with a layer of resorcinol-formaldehyde resin (RF), a layer of Au, and an additional layer of protective silica, followed by calcination of the dried powder of the core-shell particles at 800 °C and a final step of etching of silica to release Au nanocups. It is worth noting that the multiple steps of coating are performed through simple solution reactions under ambient condition so the overall process can be carried out conveniently and efficiently. In this design, the original silica template determines the overall dimension of the nanocups, and the thickness of the RF layer determines the extra space available for thermal dewetting and therefore the size of opening of the nanocups. By taking advantage of their controllable surface plasmon resonance in near infrared (NIR), we further demonstrate the use of the as-synthesized Au nanocups as efficient contrast agents for spectral-domain optical coherence tomography (OCT) imaging.

6.2 Materials and Methods

6.2.1 Synthesis of SiO_2@RF Nanospheres

Colloidal silica nanospheres were prepared through a modified Stöber method.[30] In a typical synthesis for ~350 nm particles, 4.5 mL of TEOS was mixed with 45.5 mL of ethanol, and then added into another mixture containing 28 mL of ethanol, 15 mL of water and 7 mL of aqueous solution of ammonia (28 %). After stirring for 2 hours at room temperature, the silica particles were collected by centrifugation, washed with ethanol and water, and then re-dispersed in 24 mL of water. A layer of RF was coated on the surface of silica according to a modified version of a reported procedure.[31] In a typical process, 1 mL of the as-prepared silica spheres was mixed with 22 mL of water and 2 mL of aqueous solution of PVP (5 wt %). After stirring overnight, the silica spheres were collected by centrifugation and re-dispersed in 28 mL of water, then mixed with resorcinol (0.05 g), an aqueous solution of formaldehyde (37 %, 0.07 mL), and 0.1 mL of dilute aqueous ammonia solution (2.8 %). After heating the solution at 60 ℃ for 3 hours, SiO_2@RF particles with 25 nm RF were collected by centrifugation, washed with ethanol and isopropanol, and finally re-dispersed in 5 mL of isopropanol. For RF thickness of 18 nm and 12 nm, 0.025 g of resorcinol, 0.035 mL formaldehyde

solution and 0.0125 g of resorcinol, 0.0175 mL of formaldehyde solution were added, respectively.

For silica particles around 80 nm, 98 mL of ethanol and 10 mL of water was firstly mixed together, followed by adding 1.25 mL of ammonia (28 %) and 5 mL of TEOS. After stirring for 16 hours at room temperature, the silica particles were collected by centrifugation, washed with ethanol and water, and then re-dispersed in 27 mL of water. For silica particles around 250 nm, the volume of ethanol, water, ammonium and TEOS was 92, 16, 2.6 and 3.44 ml, respectively. After washing, the silica particles were dispersed in 18.5 mL of water. For 80 nm silica with RF thickness of around 20 nm, 1 mL of the above silica solution was coated with 0.02 g of resorcinol and 0.028 mL of formaldehyde solution. For 250 nm silica with RF thickness of around 20 nm, 2 mL of the above silica solution was coated with 0.03 g of resorcinol and 0.042 mL of formaldehyde solution. Other procedures were the same as the above.

6.2.2 Synthesis of SiO_2@RF@Au Nanospheres

The Au layer was deposited by following a modified method reported by Halas et al.[32] The SiO_2@RF particles were firstly functionalized with APTES to obtain an amine coated surface. Typically, 1 mL of the above SiO_2@RF solution was added into 19 mL of isopropanol, followed by introducing 50 μL of APTES under vigorous stirring. The mixture was allowed to reflux for 3 hours. The resulting

particles were centrifuged and washed four times with ethanol and twice with water to remove excess APTES, then dispersed in 15 mL of water. The Au seeds were synthesized using Baiker's method:[33] A mixture of 1.35 mL of 0.2 M NaOH, 41 mL of water, 0.9 mL of 1.2 mM tetrakis-(hydroxymethyl)-phosphonium chloride (THPC) aqueous solution was prepared and stirred for 10 min, to which 1.8 mL of 25 mM aqueous solution of chloroauric acid was added quickly. The final solution was aged at 4 ℃ for at least 2 weeks before use. The as-prepared THPC Au seeds (1-2 nm in diameter, 5 mL) were added to the above SiO_2@RF solution and kept overnight under stirring. Then the samples were collected by centrifugation, washed several times with water to remove the isolated Au particles and dispersed in 50 mL of water.

The seed-mediated growth was then carried to deposit additional Au to the Au seeds attached to the SiO_2@RF particles. A plating solution was firstly prepared by adding 7.5 mL of 25 mM $HAuCl_4$ in 500 mL of 1.8 mM KCO_3 aqueous solution and stored for a minimum of 24 h before use. The above SiO_2@RF/Au seed solution (20 mL) was added to 200 mL of the plating solution, stirred for 5 min, and mixed with 2 mL of 100 mM TSC and 0.5 mL of formaldehyde (37 %). The color of the solution changed from pink to red, purple, blue and at last green, indicating the end of the reaction. This solution was treated with 5 mL of 5 wt % PVP overnight to allow for the adsorption of PVP onto the Au surface.

6.2.3 Synthesis of SiO_2@RF@Au@SiO_2 Nanospheres

The above SiO_2@RF@Au nanospheres were separated from solution by centrifugation and re-dispersed in 3 mL of water, then sequentially mixed with ethanol (20 mL), aqueous ammonia (28 %, 1 mL) and TEOS (30 μL). After stirring for 40 min at room temperature, the SiO@RF@Au@SiO particles were centrifuged, washed three times with ethanol and dried under vacuum.

6.2.4 Thermal Dewetting and Template Removal

The powder was heated in the muffle oven to the predetermined temperature at a rate of 3°C/min then held for 3 h and then cooled to room temperature. To release Au nanocups, the calcined powder was dispersed in an aqueous HF solution (20 ml, 1%) and aged overnight to remove the silica core and shell. The etched samples were centrifuged, washed with water for 3 times and dispersed in 5 mL of water. The concentration of Au was 15 mM.

6.2.5 Synthesis of Au nanoshells

The above SiO_2@RF@Au sample was dispersed in 30 mL of water, mixed with 1 mL of 2.5 M NaOH solution, stirred overnight, collected by centrifugation, washed with water for 3 times, and dispersed in 5 mL of water. The concentration of Au was 15 mM.

6.2.6 Preparation of Au nanospheres

Au nanospheres were synthesized using a method we developed previously.[34] Au seeds were firstly prepared by using sodium borohydride as the reducing agent and trisodium citrate dehydrate as the capping agent. Typically, 1 mL of $HAuCl_4$ (5mM) and1 mL of TSC (5mM) were added to 18 mL of water in sequence, followed by quick injection of 600 μL of freshly prepared $NaBH_4$ solution (0.1 M) into the solution under vigorous stirring. After aging 4 h, 5 μL of such seed solution was then quickly injected into a freshly prepared Au growth solution containing 500 μL of PVP (5 wt%, K30), 250 μL of ascorbic acid (0.1 M), 200 μL of KI (0.2 M), 60 μL of $HAuCl_4$ (0.25 M) and 2 mL of water. After 10 minutes of vigorous stirring, the Au nanoparticles were collected by centrifugation and redispersed in 1 mL of water. The concentration of Au was 15 mM.

6.2.7 Characterization

The sample morphology was characterized by a Tecnai 12 transmission electron microscopy and a FEI Nova Nano 450 scanning electron microscopy (SEM). UV-Vis spectra were measured with an Ocean Optics HR2000 CG-UV-NIR spectrometer. UV-Vis-NIR spectra were measured with a Cary 500 UV- Vis-NIR spectrophotometer. Size measurements were performed using a Beckman Coulter Delsa Nano C Size Analyzer. Powder X-ray diffraction analysis was collected using a Bruker D8-Advance powder diffractometer operating with Cu-Kα radiation (λ=1.5406Å).

6.2.8 OCT Imaging

The obtained Au nanostructures were tested both in water and chicken tissue as contrast agents for OCT imaging. For water samples, the Au nanostructure solutions were diluted into half of their original concentration. For the chicken samples, 6 μL of the water samples was injected separately into a piece of chicken tissue using a syringe pump at an injection rate of 30 μL/min. The injection depth was around 1 mm. OCT image acquisition was performed using a spectral-domain system centered at 1300 nm, using a similar procedure as described in literature.[35]

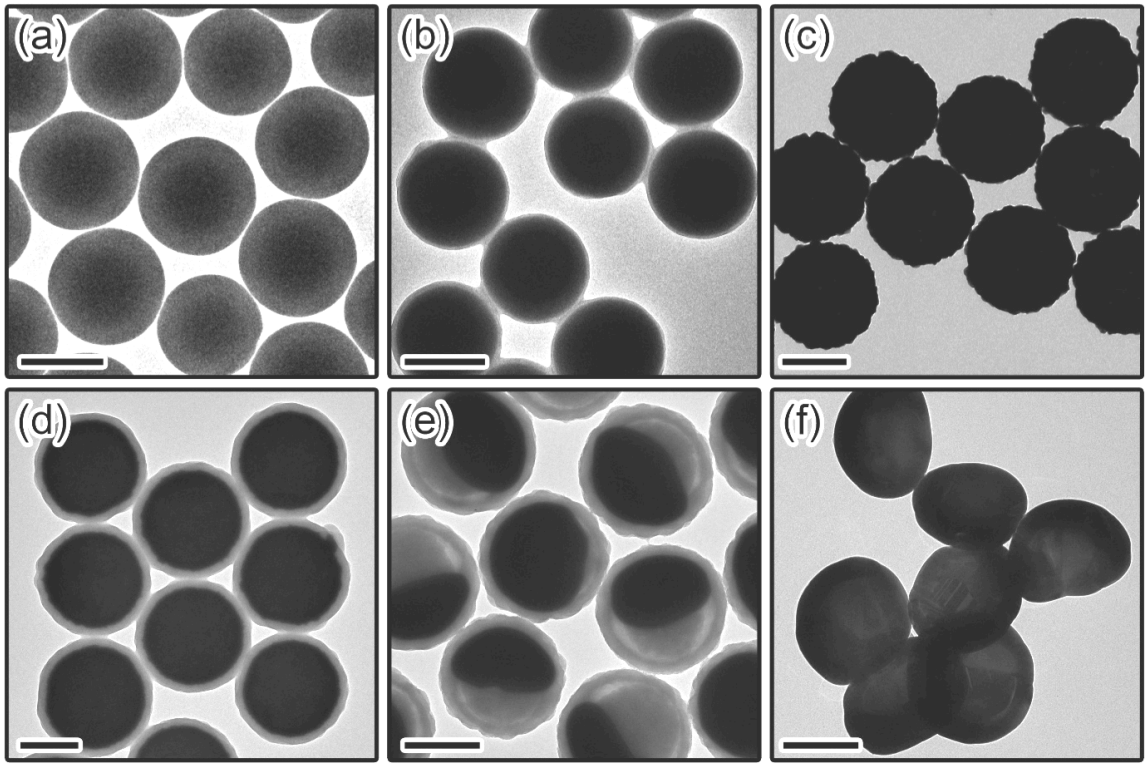

Figure 6.1. TEM images of (a) SiO_2 nanospheres; (b) SiO_2@RF nanospheres; (c) SiO_2@RF@Au nanospheres; (d) SiO_2@RF@Au@SiO_2 nanospheres; (e) SiO_2@RF@Au@SiO_2 nanospheres after calcination in air at 800 °C for 3 h; and (f) Au nanocups after removal of the SiO_2 templates. All scale bars are 200 nm.

6.3 Results and Discussion

6.3.1 Fabrication of Au Nanocups

Figure 6.1 shows the transmission electron microscopy (TEM) images of a typical sample of Au nanocups and their synthesis intermediates. The first step involved the formation of a uniform resin film on silica cores through a sol-gel process.[14] The diameter of the silica core was 250 nm and thickness of RF coating ~ 10 nm (Figure 6.1a and b). The RF thickness could be adjusted by easily changing the amount of resorcinol and formaldehyde during the sol-gel coating. Then the outer surface of RF was modified with amino groups by introducing 3-aminopropyltriethoxysilane (APTES), followed by the attachment of 1～2 nm Au seeds and additional seed-mediated growth to produce a continuous, multicrystalline Au layer.[15] The control over the thickness of Au shells can be achieved by tuning the ratio of gold growth solution to seeds. The formation of a continuous Au layer could be monitored by UV-Vis extinction spectrum, as shown in **Figure 6.2**. With the increase of the growth solution, the peak of the optical response gradually shifted from 560 nm towards a higher wavelength until a complete shell was obtained. Further thickening of the gold shell caused a blue shift of the plasmon resonance. For the gold nanoshells with a core diameter of 270 nm and shell thickness of 25 nm (Figure 6.1c), the plasmon resonance peak

was measured at ~ 700 nm. After the formation of the continuous Au shell, a layer of silica was coated on the core/shell nanoparticles, forming SiO_2@RF@Au@SiO_2 multilayer nanostructures (Figure 6.1d). Here the additional silica coating plays two roles: it serves as a protector to prevent interparticle aggregation during high-temperature calcination, and also affords a confined space for the Au dewetting process.

The RF layer was removed by calcination in air at or above 500 °C.[16] To ensure the complete removal of RF and dewetting of the Au shells, the hybrid nanoparticles were calcined in air at 800 °C for 3 h. Figure 6.1e shows the TEM image of the resulting SiO_2@RF@Au@SiO_2 nanoparticles. A gap between the inner silica core and outer silica shell could be clearly observed, which was caused by the removal of RF. Calcination at such a high temperature also greatly increased the mobility of Au atoms, causing significant dewetting of the Au due to its low affinity to silica surface.[17] The thermal dewetting thus led to the formation of Au nanocups as shaped by the geometric confinement of the silica templates, with their opening size dependent on the space made available by the sacrificial RF layer. Understandably, the calcination temperature may also contribute to the opening size of the nanocups as it affects the dewetting kinetics.

Finally, freestanding Au nanocups could be obtained after removing the silica core and shell by HF etching, as shown in Figure 6.1f. The unique combination of

seeded growth and confined-space thermal dewetting processes ensured a high production yield and a high uniformity in both size and morphology, as demonstrated in the low magnification TEM image in **Figure 6.3**.

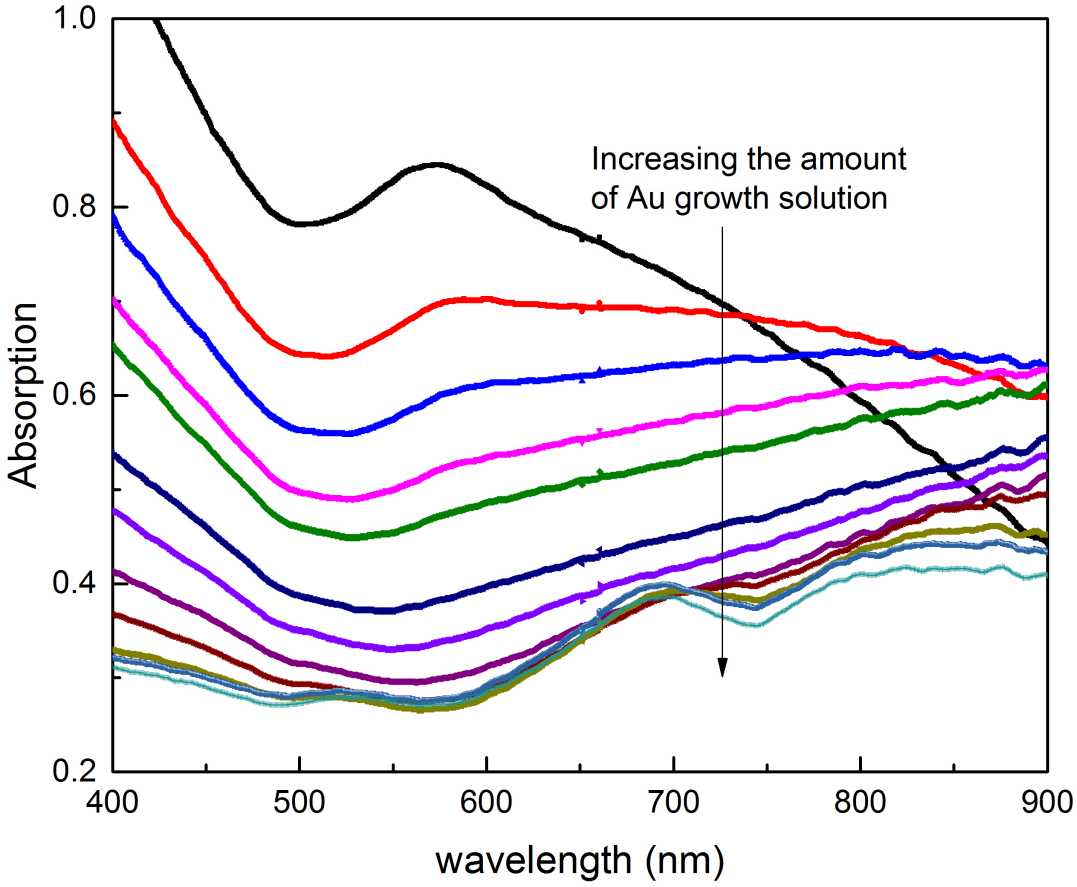

Figure 6.2. Experimentally measured absorption spectrum of SiO_2@RF@Au during seed-mediated growth process.

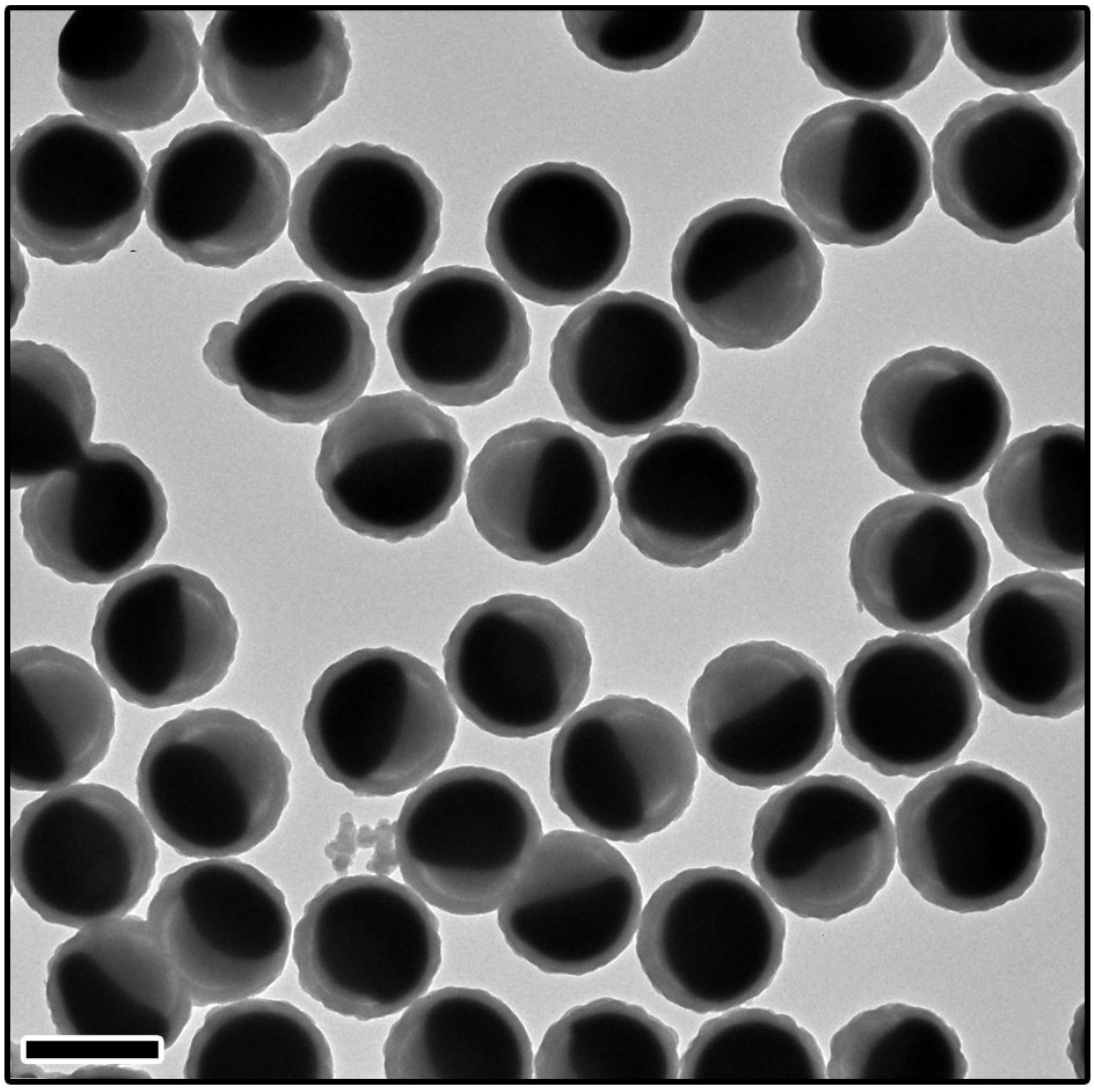

Figure 6.3. Low magnification TEM image of Au nanocups before silica etching, indicating the uniform size and high yield of the dewetting method. The scale bar is 500 nm.

6.3.2 Shape Tuning by Confined Space

The success of this fabrication method should be attributed to two key points. The first one is the creation of a confined space by removing the sacrificial RF layer through calcination in air,[16] which is essential for reshaping the Au layer. The size of the space can be tuned by changing the thickness of RF coating. The second important point is the thermal dewetting of Au nanoshells from silica surfaces during calcination at high temperatures. While thermal dewetting has been used previously in reconstruction of metal thin films into microcrystals of equilibrium shapes,[18] in this work such a process was confined in a limited space, allowing the production of non-equilibrium shapes, i.e. nanocups. Accordingly, the morphologies of the products were determined by both the dewetting process and shape/size of the confined space.

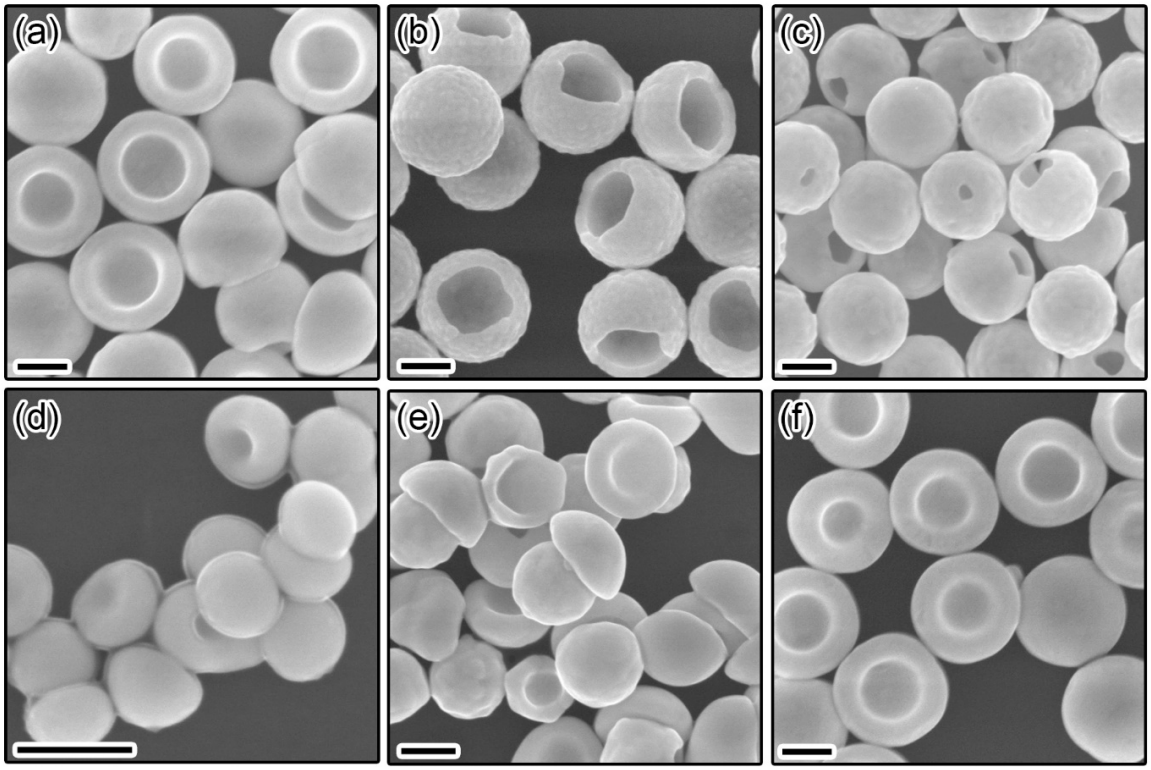

Figure 6.4. (a-c) SEM images of the Au nanocups prepared using templates of 350-nm silica coated with RF thickness of (a) 25 nm, (b) 18 nm, and (c) 12 nm, demonstrating the convenient control over cup opening by the thickness of the RF layer; (d-f) SEM images of Au nanocups obtained using silica cores with diameters of ~80, ~250 and ~350 nm. All scale bars are 200 nm.

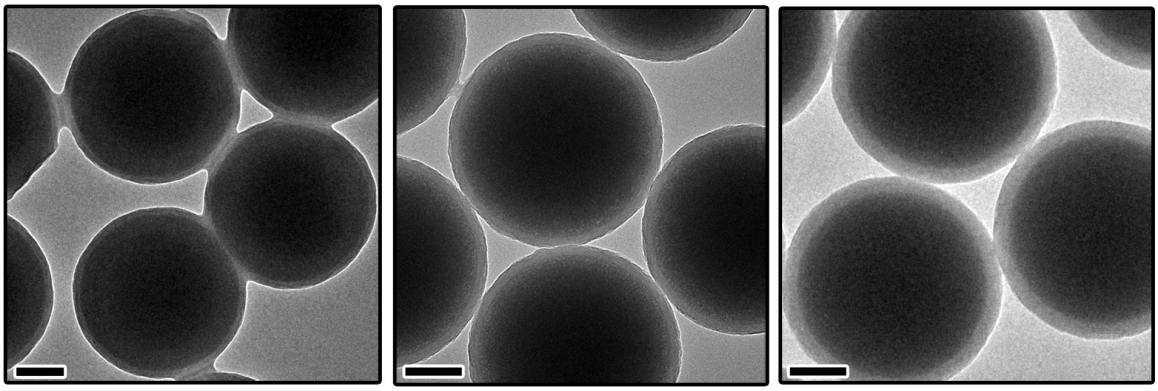

Figure 6.5. 350 nm SiO2 with different thickness of RF coating:(a) 12 nm; (b) 18 nm; (c) 25 nm. All scale bars are 100 nm.

This method is versatile in affording Au nanocups with different height, size of cup opening, and the overall diameter, which can be conveniently achieved by controlling the thickness of RF coating and size of the silica templates. As discussed above, we can easily tune the height and cup opening by controlling the thickness of the RF layer, which determines the confined space for thermal dewetting. **Figure 6.4**a-c shows the scanning electron microscopy (SEM) images of a series of Au nanocups prepared by using SiO_2@RF templates with core diameter of ~ 350 nm and RF thickness of 25, 18 and 12 nm (**Figure 6.5**). With the decrease in RF thickness, the height of Au nanocups increased and the size of the cup opening decreased. The overall size of the Au nanocups could also be controlled by changing the size of the silica templates. Figure 6.4d–f shows the Au nanocups with size of ~ 120, 300 and 400 nm prepared using silica templates with diameter of ~ 80, 250 and 350 nm.

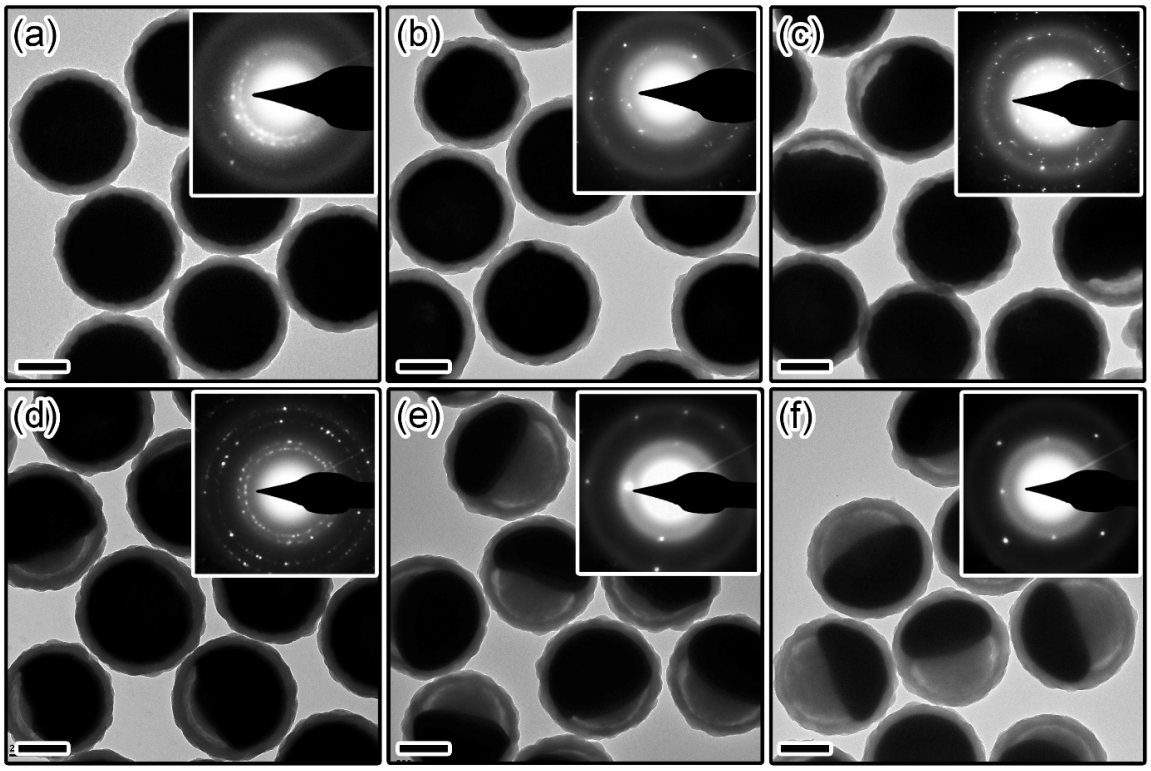

Figure 6.6. TEM images showing the morphology evolution during the confined-space thermal dewetting of SiO_2@RF@Au@SiO_2 nanospheres: (a) before calcination; and (b-f) after calcination at 500 °C (b), 600 °C (c), 700 °C (d), 800°C (e), and 900 °C (f). All scale bars are 200 nm. Insets are the corresponding SAED patterns.

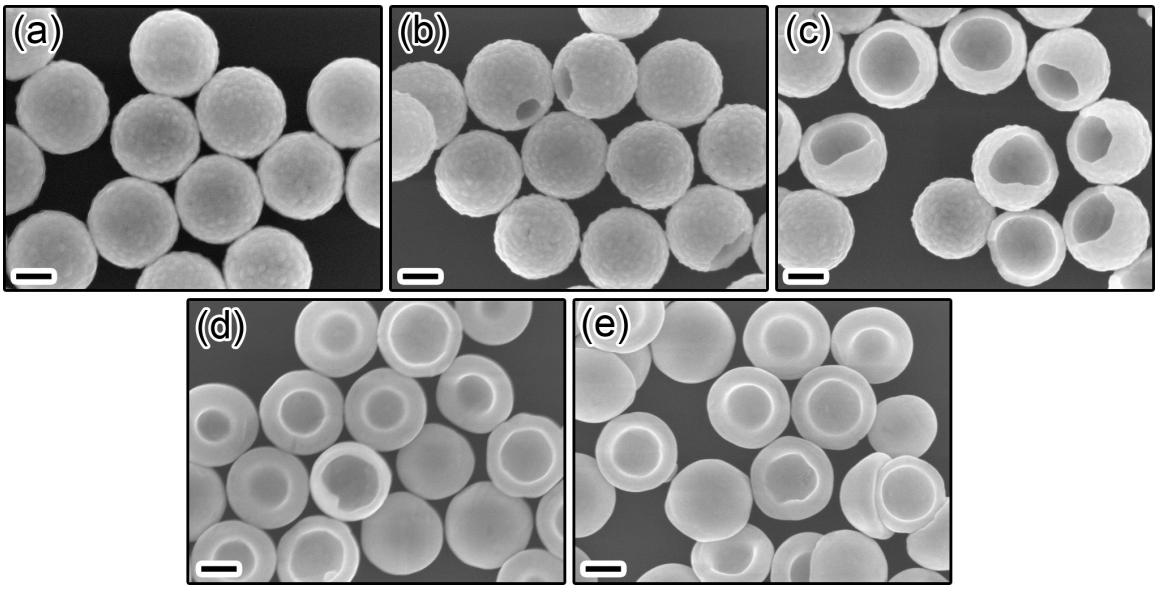

Figure 6.7. SEM images of products of silica@RF@Au@silica after calcination at (a) 500 °C; (b) 600 °C; (c) 700 °C; (d) 800 °Cand (e) 900 °C after silica etching. All scale bars are 200 nm.

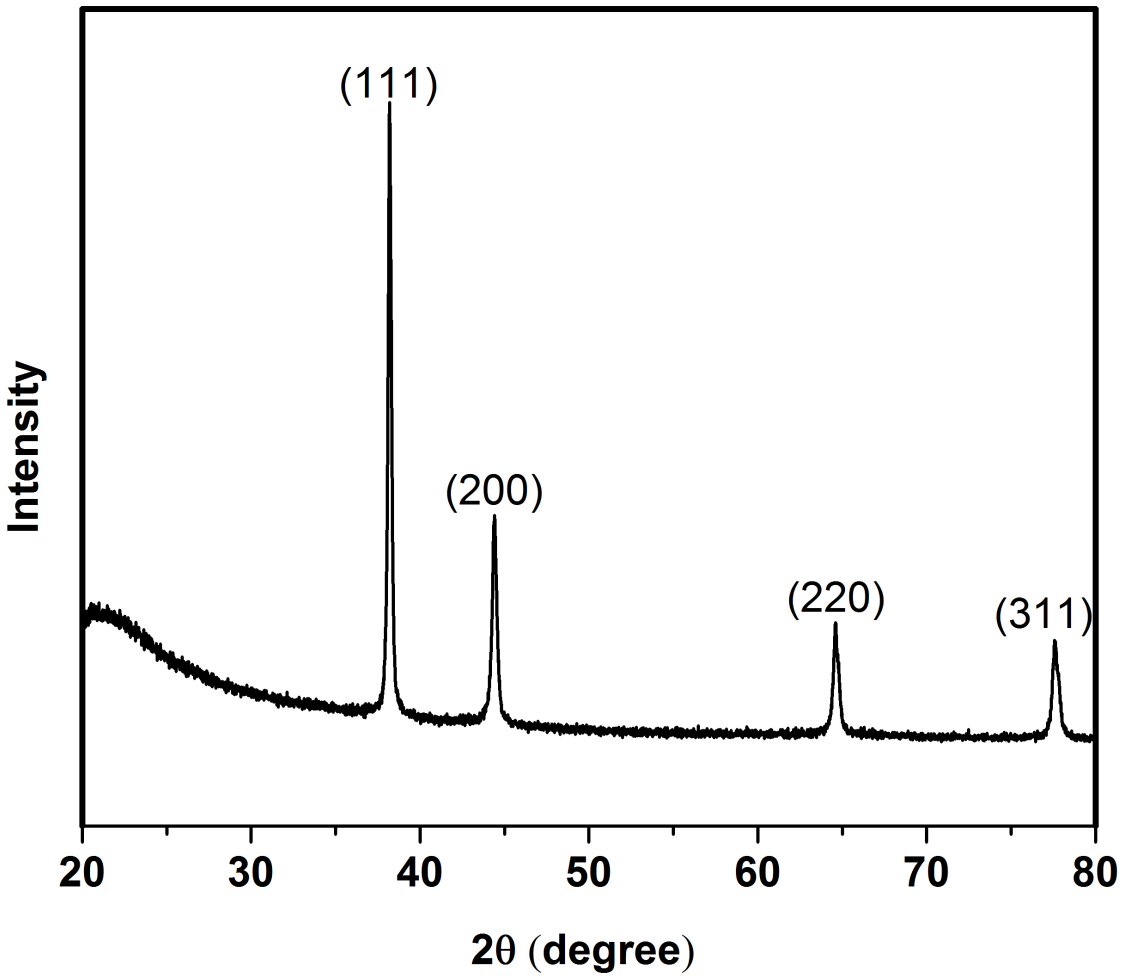

Figure 6.8. XRD pattern taken from the same sample as Fig. 6.1d, indicating that the Au nanocups were highly crystalline.

6.3.3 Shape Tuning by Temperature

As the dynamics of dewetting is controlled by macroscopic hydrodynamic flows,[17] the calcination temperature is a crucial factor for the formation of nanocups. We have experimentally confirmed the strong temperature dependence, and found that the degree of dewetting could be controlled from minimal to partial and complete dewetting by adjusting the calcination temperature, resulting in different morphologies of the products. **Figure 6.6** shows the TEM images of the samples after calcination under air for 3 h at different temperatures from 500 to 900 °C by starting with the same material shown in Figure 3a. Particles prepared by calcination at a relatively low temperature (e.g. 500 °C) were still complete shell structures (Figure 6.6b and **Figure 6.7**a, Supporting Information), indicating that minimal dewetting occurred, which could be attributed to the low mobility of Au atoms at this temperature. When the temperature was raised to 600 °C, as shown in Figure 6.6c, a small gap appeared between gold and the outer silica shell, indicating partial dewetting of Au. Such a deformation was accompanied by the formation of Au nanocups with very small cup opening (Figure 6.7b). Further increasing the calcination temperature to 700 °C induced more obvious dewetting, resulting in Au nanocups with larger cup opening (Figure 6.6d and 6.7c). When the calcination temperature reached 800 °C, as shown in Figure 6.6e, the cup opening was even larger. Further increase of the calcination temperature to 900 °C brought a similar result to the case at 800 °C (Figure 6.6f), both of which formed

Au nanocups with a large cup opening (Figures 6.7d and 6.7e). Based on this observation, we believe that calcination at 800 °C for 3 h is enough for fully dewetting a typical sample, and nanocups with smaller openings or complete nanoshells could be obtained by calcining the samples at lower temperatures.

It has been proved in our previous study that calcination at high temperatures could effectively enhance the atomic mobility and remove most of the crystallographic defects, achieving single crystalline metal nanoparticles.[19] A similar observation was obtained in the current work, as confirmed by the selected area electron diffraction (SAED) pattern shown in the insets in Figure 6.6 and the X-ray diffraction (XRD) pattern in **Figure 6.8**.

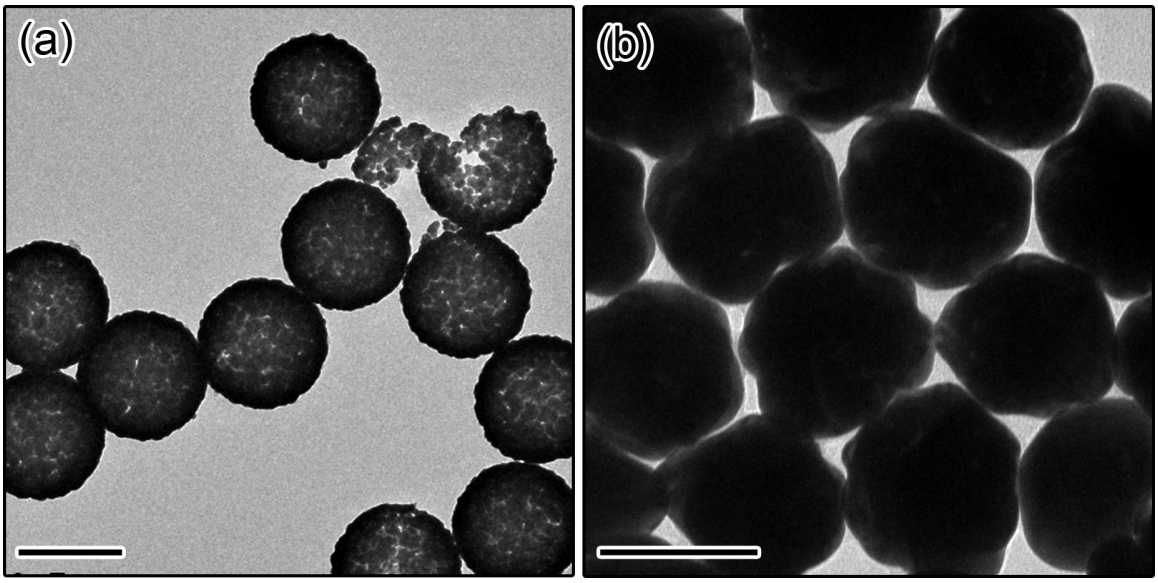

Figure 6.9. TEM images of (a) Au nanoshells and (b) Au nanospheres used for OCT imaging. All scale bars are 100 nm.

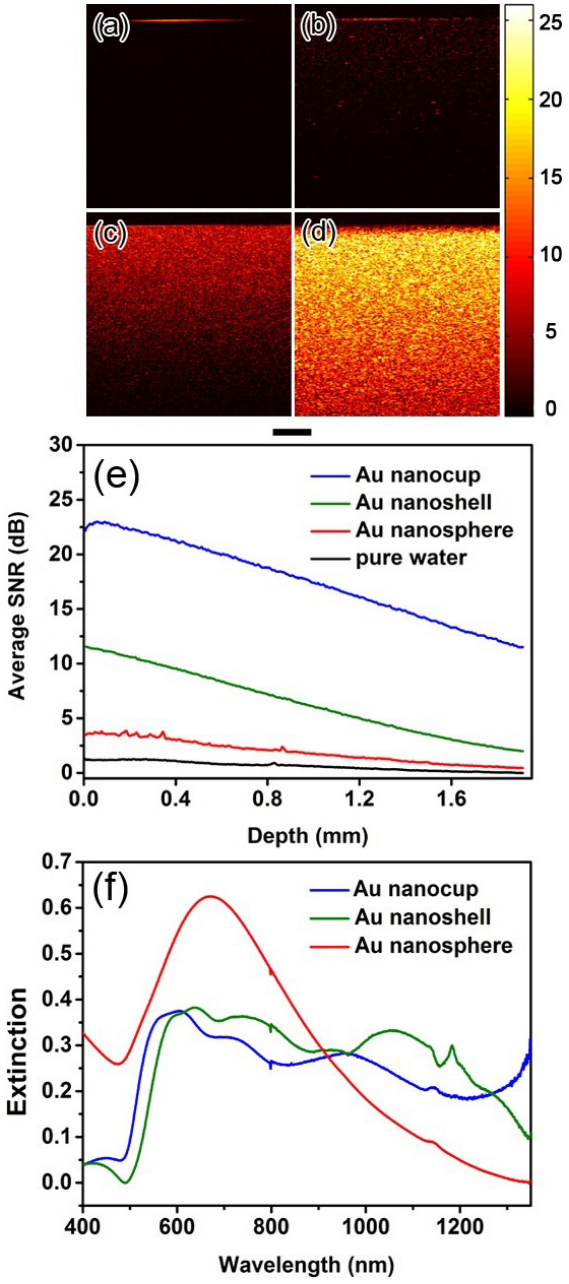

Figure 6.10. (a-d) OCT B-scan images of (a) pure water and aqueous dispersions containing (b) solid Au nanospheres, (c) Au nanoshells, (d) Au nanocups; (e) A-scan profile of these Au nanostructures in water; (f) Extinction spectra of these Au nanostructures in water. The scale bar is 400 μm and applies to all the images.

6.3.4 OCT Performance

OCT is an optical tomographic imaging technique capable of capturing cross-sectional images of scanned objects in a non-invasive manner.[20] With the use of low-coherence interferometry of near-infrared light, OCT is able to achieve better spatial resolution (3-20 μm) than other imaging modalities including magnetic resonance imaging (MRI) and ultrasonic imaging (USG) but with a depth of penetration limited to 2-3 mm.[21] Benefiting from its relatively high resolution, non-invasive and real-time nature, and the involvement of non-ionization radiation, OCT has been widely used in ophthalmology, cardiology, and dermatology.[22] However, visualization of some structures with OCT can be limited by poor contrast, an issue that has been addressed in the past with exogenous contrast agents, including typically air-filled microbubbles and engineered microspheres.[23] Given the low cytotoxicity, high stability, and unique localized surface plasmon resonance, Au nanoparticles of different morphologies, such as nanospheres, nanoshells, or nanocages, show great potential for OCT contrast enhancement.[24] Previous results suggest that contrast enhancement of gold nanoparticles with different geometries and sizes can be improved if their plasmon resonance matches the central wavelength of OCT system.[25] Also, a good OCT contrast agent would prefer particles of small sizes (typically less than 150 nm) which permit extravasation into the tissue, and resonant scattering centered in NIR which allows deep tissue penetration. By these criteria, Au nanoparticles with anisotropic

shapes are more desirable than spherical ones, as their plasmonic resonance can be tuned to NIR region by controlling the shape anisotropy.[26] Some previous studies have examined Au nanorods as they exhibit plasmon resonance dependent on their aspect ratio.[27] However, their broad application in optical imaging has suffered from the toxicity of cetyltrimethyl-ammonium bromide (CTAB), a typical capping ligand that is essential in Au nanorod synthesis but quite difficult to be completely removed. Here we demonstrate the use of Au nanocups with sub-120 nm dimension as an effective contrast agent in both water and chicken tissue for a spectral-domain OCT system with a central wavelength at 1300 nm. To show the efficiency of Au nanocups in OCT, we compared their performance with that of Au solid nanospheres and nanoshells with the same concentration and similar sizes. The TEM images of Au nanospheres and nanoshells used in the OCT imaging are shown in **Figure 6.9**.

Figure 6.10 shows the OCT B-scan images for the cases of different Au nanoparticles in Millipore water. The image of water without any Au particles (Figure 6.10a), as might be expected, has little to no back-reflected intensity. The presence of solid nanospheres improved the contrast, albeit still with limited enhancement (Figure 6.10b). Compared with the case of Au nanospheres, the B-scan images of water with Au nanoshells and nanocups show significant enhancement in intensity. The A-scan profile shown in Figure 6.10e was calculated by averaging 1024 A-scans that compose an average B-scan image for

different cases: pure water, and water with Au nanospheres, Au nanoshells and Au nanocups, respectively. From Figure 6.10e, we can see more clearly the efficiency of different types of Au nanoparticles as contrast agents for OCT imaging. Au nanocups show the highest contrast enhancement, while Au nanospheres show the lowest, indicating the high activity of Au nanocups as a contrast agent for OCT imaging. This enhancement means that Au nanoshells and nanocups scatter light more efficiently at the wavelength near that of the OCT light source. This can be explained from the extinction spectra of Au nanospheres, nanoshells and nanocups in Figure 6.10f. The central wavelength of the OCT light source is 1300 nm, around which the optical extinction of Au nanospheres is almost zero. While the low scattering intensity of the Au nanospheres resulted in low contrast enhancement in OCT imaging, the Au nanoshells and nanocups display much higher extinction intensity. Consequently, more obvious contrast enhancement could be observed for OCT imaging in water with nanoshells and nanocups, as OCT detects the backscattered light and scattering makes the main contribution to the extinction spectra at wavelengths above 1000 nm for both types of particles.[28] The much better backscattered intensity achieved by nanocups than nanoshells could be attributed to the higher extinction of the nanocups than that of the nanoshells in most of the OCT spectral bandwidth (which runs from about 1250-1350), as well as the increased heterogeneity of the nanocups with respect to the optical beam (in comparison to that of the nanoshells, which have a symmetric shape).

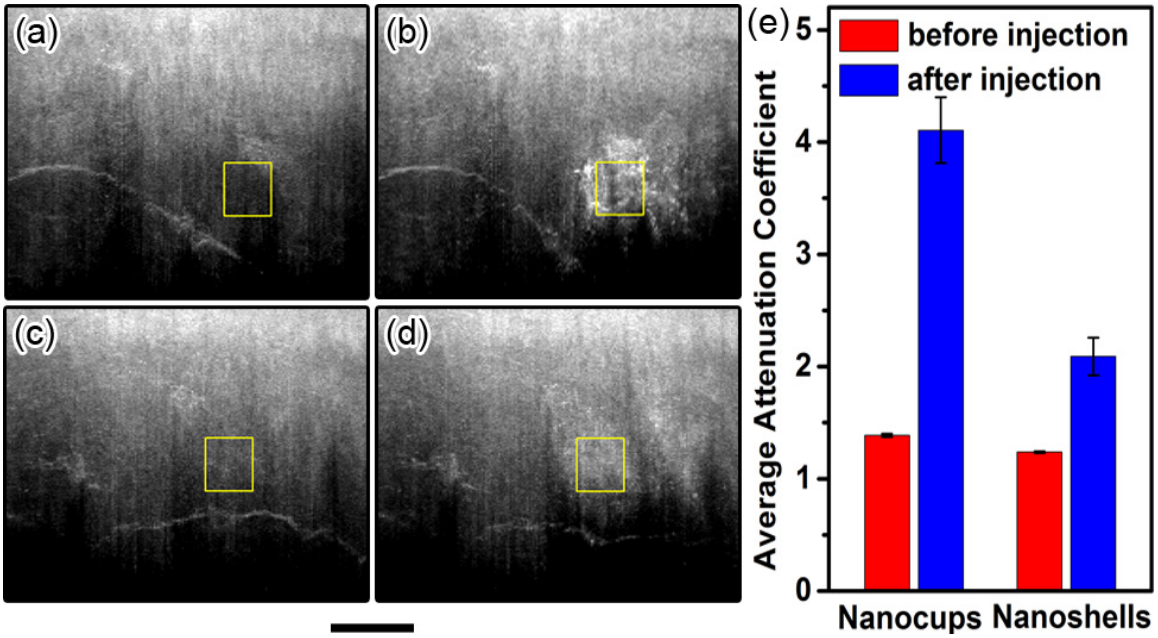

Figure 6.11. (a-d) Cross-sectional view of chicken tissue before (a, c) and after (b, d) injection of Au nanocups (a, b) and Au nanoshells (c, d); (e) Comparison of the average attenuation coefficient before and after injection of Au nanocups and Au nanoshells, calculated by averaging the time-dependent attenuation coefficient. The squares drawn on the images indicate the areas used for calculating the average attenuation coefficient. The scale bar is 160 μm and applies to all the images.

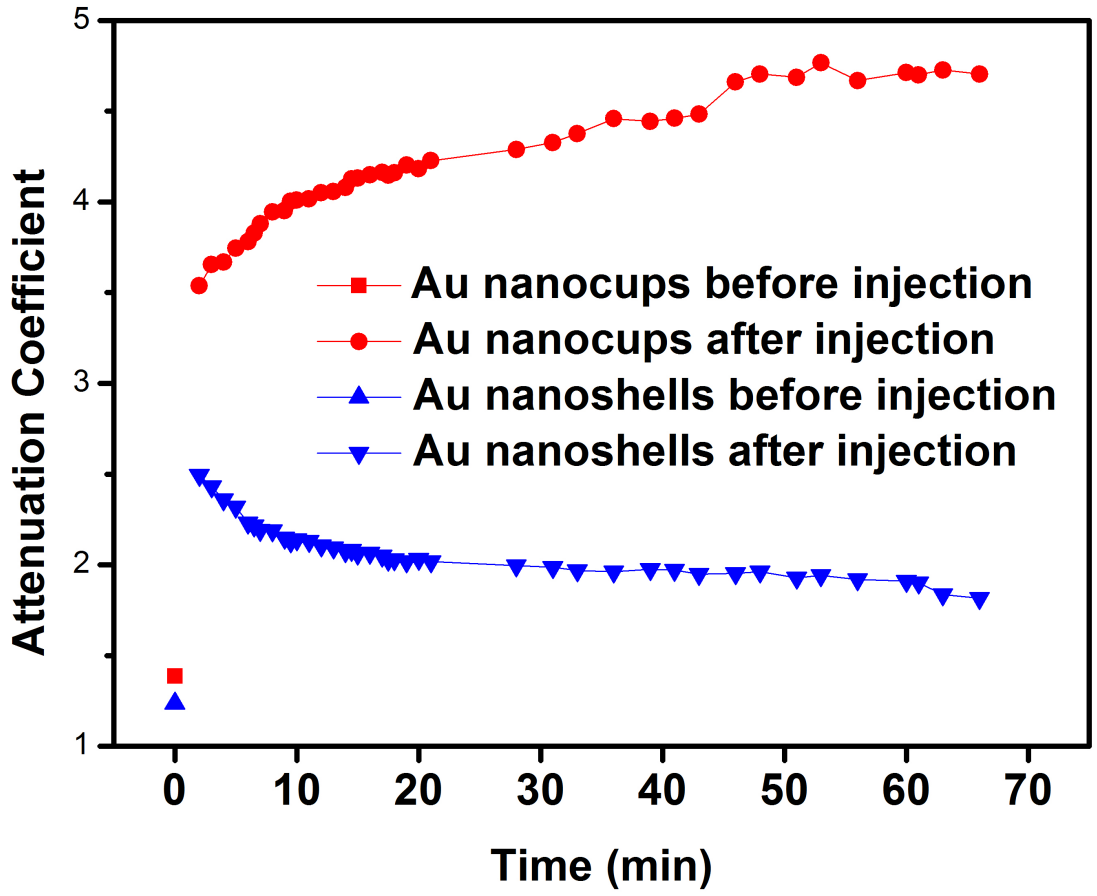

Figure 6.12. Time-dependent attenuation coefficient of Au nanocups and Au nanoshells before and after injection in chicken tissue.

6.3.5 Application for Bio-imaging

To show the usefulness of Au nanocups as a contrast agent for biological systems, we tested their efficiency of contrast enhancement in chicken tissue, and compared the performance of Au nanocups and Au nanoshells. **Figure 6.11**a-d shows the cross-sectional view of chicken tissues before (a, c) and after (b, d) injection of 6 μL of the dispersions of Au nanocups (a, b) and nanoshells (c, d) diluted to half of their original concentrations. The frames drawn on the images represent the area used for calculating the average attenuation coefficient as proposed by Vermeer et al.[29] It can be observed that the OCT images displayed obvious variation in backscattered light intensity of the chicken tissues. Both Au nanocups and nanoshells showed contrast enhancement but the enhancement of Au nanocups was more significant than that of nanoshells, as suggested by both the cross-sectional view images in Figure 6.11b, d and the time-dependent attenuation coefficient in **Figure 6.12**. Figure 6.11e was obtained by averaging the attenuation coefficient before or after injection of the Au contrast agents, showing an intensity increase from 1.39 and 1.24 for nanocups and nanoshells before injection to 4.10 and 2.08 after injection, respectively. With an increment in attenuation coefficient of 2.95 times versus 1.68 times for Au nanoshells, the Au nanocups demonstrated a higher efficiency as a contrast agent in biological tissues.

6.4 Conclusion

In summary, we have developed a novel confined-space thermal dewetting strategy for the fabrication of Au nanocups with controlled morphologies. The process involves sequential steps of colloidal coating and final calcination, and affords Au nanocups with tunable diameter, height and size of cup opening. The key to the success of this strategy is the creation of a well-defined space confined in silica templates that can allow controlled thermal dewetting of Au into the desired nanocup morphology. With strong NIR plasmon resonance, the Au nanocups exhibit superior efficiency as contrast agents for spectral-domain OCT imaging. This confined-space thermal dewetting strategy is scalable and general, and can be potentially extended to the synthesis of novel anisotropic nanostructures of various compositions that are difficult to produce by conventional wet chemical or physical methods, thus opening up opportunities for extensive applications.

6.5 References

1. a) S. Linic, P. Christopher, D. B. Ingram, *Nat. Mater.* **2011**, *10*, 911; b) A. Marimuthu, J. Zhang, S. Linic, *Science* **2013**, *339*, 1590; c) C. Wang, D. Astruc, *Chem. Soc. Rev.* **2014**, *43*, 7188.

2. a) C.-C. Chang, Y. D. Sharma, Y.-S. Kim, J. A. Bur, R. V. Shenoi, S. Krishna, D. Huang, S.-Y. Lin, *Nano Lett.* **2010**, *10*, 1704; b) M. W. Knight, H. Sobhani, P. Nordlander, N. J. Halas, *Science* **2011**, *332*, 702.

3. a) H. Ataee-Esfahani, L. Wang, Y. Nemoto, Y. Yamauchi, *Chem. Mater.* **2010**, *22*, 6310; b) L. Wang, Y. Yamauchi, *Chem. Mater.* **2011**, *23*, 2457.

4. a) K. Saha, S. S. Agasti, C. Kim, X. Li, V. M. Rotello, *Chem. Rev.* **2012**, *112*, 2739; b) J. N. Anker, W. P. Hall, O. Lyandres, N. C. Shah, J. Zhao, R. P. Van Duyne, *Nat. Mater.* **2008**, *7*, 442.

5. a) N. L. Rosi, C. A. Mirkin, *Chem. Rev.* **2005**, *105*, 1547; b) X. Huang, S. Neretina, M. A. El-Sayed, *Adv. Mater.* **2009**, *21*, 4880.

6. a) M.-C. Daniel, D. Astruc, *Chem. Rev.* **2004**, *104*, 293; b) H. Ataee-Esfahani, L. Wang, Y. Yamauchi, *Chem. Commun.* **2010**, *46*, 3684; c) C. Li, Ö. Dag, T. D. Dao, T. Nagao, Y. Sakamoto, T. Kimura, O. Terasaki, Y. Yamauchi, *Nat. Commun.* **2015**, *6*.

7. Y. Valadbeigi, V. Ilbeigi, H. Farrokhpour, *Res. Chem. Intermed.* **2016**, *42*, 4921.

8. N. S. King, Y. Li, C. Ayala-Orozco, T. Brannan, P. Nordlander, N. J. Halas, *Acs Nano* **2011**, *5*, 7254.

9. N. S. King, M. W. Knight, N. Large, A. M. Goodman, P. Nordlander, N. J. Halas, *Nano Lett.* **2013**, *13*, 5997.

10. a) P. Van Dorpe, J. Ye, *ACS nano* **2011**, *5*, 6774; b) J. C. Love, B. D. Gates, D. B. Wolfe, K. E. Paul, G. M. Whitesides, *Nano Lett.* **2002**, *2*, 891; c) J. Ye, L. Lagae, G. Maes, G. Borghs, P. Van Dorpe, *Opt. Express* **2009**, *17*, 23765.

11. L. H. Tan, S. Xing, T. Chen, G. Chen, X. Huang, H. Zhang, H. Chen, *Acs Nano* **2009**, *3*, 3469.

12. a) C. Charnay, A. Lee, S.-Q. Man, C. E. Moran, C. Radloff, R. K. Bradley, N. J. Halas, *J. Phys. Chem. B* **2003**, *107*, 7327; b) Y. Ridelman, G. Singh, R. Popovitz-Biro, S.

G. Wolf, S. Das, R. Klajn, *Small* **2012**, *8*, 654; c) D. Rodríguez-Fernández, J. Pérez-Juste, I. Pastoriza-Santos, L. M. Liz-Marzán, *ChemistryOpen* **2012**, *1*, 90.

13. R. Jiang, F. Qin, Y. Liu, X. Y. Ling, J. Guo, M. Tang, S. Cheng, J. Wang, *Adv. Mater.* **2016**, *28*, 6322.

14. N. Li, Q. Zhang, J. Liu, J. Joo, A. Lee, Y. Gan, Y. Yin, *Chem. Commun.* **2013**, *49*, 5135.

15. B. E. Brinson, J. B. Lassiter, C. S. Levin, R. Bardhan, N. Mirin, N. J. Halas, *Langmuir* **2008**, *24*, 14166.

16. H. Liu, J. B. Joo, M. Dahl, L. Fu, Z. Zeng, Y. Yin, *Energy Environ. Sci.* **2015**, *8*, 286.

17. C. Redon, F. Brochard-Wyart, F. Rondelez, *Phys. Rev. Lett.* **1991**, *66*, 715.

18. a) Y. Lu, H. Xiong, X. Jiang, Y. Xia, M. Prentiss, G. M. Whitesides, *J. Am. Chem. Soc.* **2003**, *125*, 12724; b) J. Huang, F. Kim, A. R. Tao, S. Connor, P. Yang, *Nat. Mater.* **2005**, *4*, 896.

19. C. Gao, Y. Hu, M. Wang, M. Chi, Y. Yin, *J. Am. Chem. Soc.* **2014**, *136*, 7474.

20. D. Huang, E. A. Swanson, C. P. Lin, J. S. Schuman, W. G. Stinson, W. Chang, M. R. Hee, T. Flotte, K. Gregory, C. A. Puliafito, *Science (New York, NY)* **1991**, *254*, 1178.

21. J. G. Fujimoto, M. E. Brezinski, G. J. Tearney, S. A. Boppart, B. Bouma, M. R. Hee, J. F. Southern, E. A. Swanson, *Nat. Med.* **1995**, *1*, 970.

22. a) W. Drexler, U. Morgner, F. Kärtner, C. Pitris, S. Boppart, X. Li, E. Ippen, J. Fujimoto, *Opt. Lett.* **1999**, *24*, 1221; b) G. J. Tearney, M. E. Brezinski, B. E. Bouma, S. A. Boppart, C. Pitris, J. F. Southern, J. G. Fujimoto, *Science* **1997**, *276*, 2037.

23. K. M. Au, Z. Lu, S. J. Matcher, S. P. Armes, *Adv. Mater.* **2011**, *23*, 5792.

24. a) R. John, E. J. Chaney, S. A. Boppart, *IEEE J. Sel. Top. Quant.* **2010**, *16*, 691; b) M. A. Hahn, A. K. Singh, P. Sharma, S. C. Brown, B. M. Moudgil, *Anal. Bioanal. Chem.* **2011**, *399*, 3; c) A. L. Oldenburg, V. Crecea, S. A. Rinne, S. A. Boppart, *Opt. Express* **2008**, *16*, 11525.

25. Y. P. De León, J. Pichardo-Molina, N. A. Ochoa, D. Luna-Moreno, *J. Nanomater.* **2012**, *2012*, 128.

26. A. L. Oldenburg, M. N. Hansen, D. A. Zweifel, A. Wei, S. A. Boppart, *Opt. Express* **2006**, *14*, 6724.

27. a) A. Zerda, S. Prabhulkar, V. L. Perez, M. Ruggeri, A. S. Paranjape, F. Habte, S. S. Gambhir, R. M. Awdeh, *Clin. Exp. Ophthalmol.* **2015**, *43*, 358; b) J. Tucker-Schwartz, T. Meyer, C. Patil, C. Duvall, M. Skala, *Biomed. Opt. Express* **2012**, *3*, 2881.

28. J. Ye, P. Van Dorpe, W. Van Roy, K. Lodewijks, I. De Vlaminck, G. Maes, G. Borghs, *J. Phys. Chem. C* **2009**, *113*, 3110.

29. K. Vermeer, J. Mo, J. Weda, H. Lemij, J. de Boer, *Biomed. Opt. Express* **2014**, *5*, 322.

30. a) W. Stöber, A. Fink, E. Bohn, *J. Colloid Interf. Sci.* **1968**, *26*, 62; b) Q. Zhang, T. Zhang, J. Ge, Y. Yin, *Nano Lett.* **2008**, *8*, 2867.

31. N. Li, Q. Zhang, J. Liu, J. Joo, A. Lee, Y. Gan, Y. Yin, Chem. Commun. **2013**, *49*, 5135.

32. B. E. Brinson, J. B. Lassiter, C. S. Levin, R. Bardhan, N. Mirin, N. J. Halas, Langmuir **2008**, *24*, 14166.

33. D. G. Duff, A. Baiker, P. P. Edwards, Langmuir **1993**, *9*, 2301.

34. C. Gao, J. Vuong, Q. Zhang, Y. Liu, Y. Yin, Nanoscale **2012**, *4*, 2875.

35. C. L. Rodriguez, J. I. Szu, M. M. Eberle, Y. Wang, M. S. Hsu, D. K. Binder, B. H. Park, Neurophotonics **2014**, *1*, 025004.

Chapter 7

pH Dependent Bistability of Colloidal Assembly

7.1 Introduction

The self-assembly of colloidal particles into ordered, macroscopic structures has greatly promote the design and fabrication of next generation functional materials.[110, 216, 232-234] Driven by short-range attractions, including entropic, chemical and nonequilibrium forces, a number of binding schemes have been explored.[20, 90, 235] Most of these building blocks and assembled architectures, however, are static in nature and posses only one stable equilibrium state with respect to minimum of potential energy, which limits the ability to adapt and reconfigure their shape and structures upon external stimuli.[236-238] While, with two local minima of potential energy separated by a local maximum, the intrinsic bistability is ubiquitous in the building blocks of nature, such as decision-making processes in cell cycle progression, cellular differentiation and apoptosis.[239] Although tremendous efforts have been put into nanoparticles assembly, it remains a great challenge to develop stimuli-responsive systems with bistable properties.

The stability of colloidal suspension is determined by the forces between colloidal particles. The classic Derjaguin-Landau-Verwey-Overbeek (DLVO) theory, which

considers the sum of van der Waals attraction and electrostatic repulsion, has been widely used to explain and predict the stability of colloidal dispersion.[240-243] The van der Waals attraction mainly depends on the properties of the nanoparticles, such as density, shape and volume, the electrostatic interaction, however, relies not only on their surface properties but also on their dispersion properties such as dielectric constant, ionic strength, pH and temperature.[64, 244-245] Opposite to colloidal stabilization with the aim to avoid aggregation and flocculation, self-assembly intends to aggregate nanoparticles through overcoming the energy barrier of electrostatic repulsive interactions.[63-64, 72] Most of these assembled structures, however, are dominated by van der Waals attractive force and lack the ability to recover to initial state upon external stimulus, which is a prerequisite for bistable system that can adapt on demand, or to environmental cues, to perform a required function.

A bistable colloidal system should behave like “light-switch”, which is designed to rest in the “on” or “off” position with minimal energy. Once turned “on” by an external stimulus, the colloidal nanoparticles readily stabilized in assembled state. While when another stimulus switches the system to “off” position, disassembly of the ordered structures should be initiated and the system would rest in the dispersion state. In this scenario, we developed a bistable system with amine-functionalized superparamagnetic nanoparticles as the building block. Upon exposure to external magnetic stimuli, the magnetic nanoparticles assemble into chain structure and remain stable at assembled state until another stimuli is imposed to trigger the disassembly of the nanoparticles to

dispersion. The assembled state is favored under magnetic stimulus, owing to the NH_2-catalyzed formation of siloxane bonds between silanol groups during the encounter between nanoparticles. Since the repulsive electrostatic force is countered by magnetic dipolar attraction, the interparticle distance can be readily controlled by the strength of the magnetic stimulus. Moreover, compared to other methods such as screening the electrostatic force to shorten the interparticle distance, our design could prevent the close contact, in which short-range van der Waals attractive force starts dominant and induces permanent aggregation. Upon thermal agitation, the siloxane bonds are easily broken and the collision of silanol groups is barred by electrostatic repulsion, thus the dispersion state is favored. Beneficial from the easy formation and breaking of the siloxane bonds, which indicates a lower energy barrier between the two stable states, a bistable system is established, which can effectively switch between assembly and dispersion upon external stimuli. Since protonation and deprotonation of amine functional group is highly dependent on the pH of the dispersion, which greatly affects the surface charge and in return changes the electrostatic force, as a result, the interparticle distance and bistability is regulated.

7.2 Materials and Methods

7.2.1 Synthesis of Bistable Nanoparticles

Uniform superparamagnetic CNCs were synthesized by reacting 0.4 mmol $FeCl_3$ with NaOH at around 220°C in a DEG solution containing 4 mmol polyacrylate acid (PAA) as surfactant. After several times washing with ethanol and water, the CNCs were dispersed in 3 mL of H_2O (*ca.* 8.6 mg/mL). Subsequently, 1 mL NH4OH and 20 mL ethanol were mixed with the CNCs dispersion under sonication. After the mixture was transferred into a three-neck flask under mechanical stirring at 600 rpm, 50 μL of TEOS was injected. After 20 min, certain amount of APTES was injected and stirred for one hour, after which the sample was washed with ethanol for 4 times and finally dispersed in 10 mL of H_2O. Following the same recipe, CNCs@C=C-SiO_2 was fabricated with addition of 5 μL of MPS after TEOS.

7.2.2 Characterization

The morphologies of CNCs@NH_2-SiO_2, CNCs@SiO_2 and CNCs@C=C-SiO_2 were characterized using Tecnai T12 transmission electron microscope (TEM). Fourier transform infrared (FTIR) spectrum to confirm the amine group was performed by Brucker Alpha FT-IR spectrometer in form of powder. A Zeiss AXIO Imager optical microscope connected to a digital camera was used to observe the in situ assembly and disassembly of colloidal samples. The pH was measured by Fisher Scientific accumet AB15 pH meter. Zeta potential and dynamic light scattering (DLS) were measured by Beckman Coulter Delsa NanoC particle analyzer.

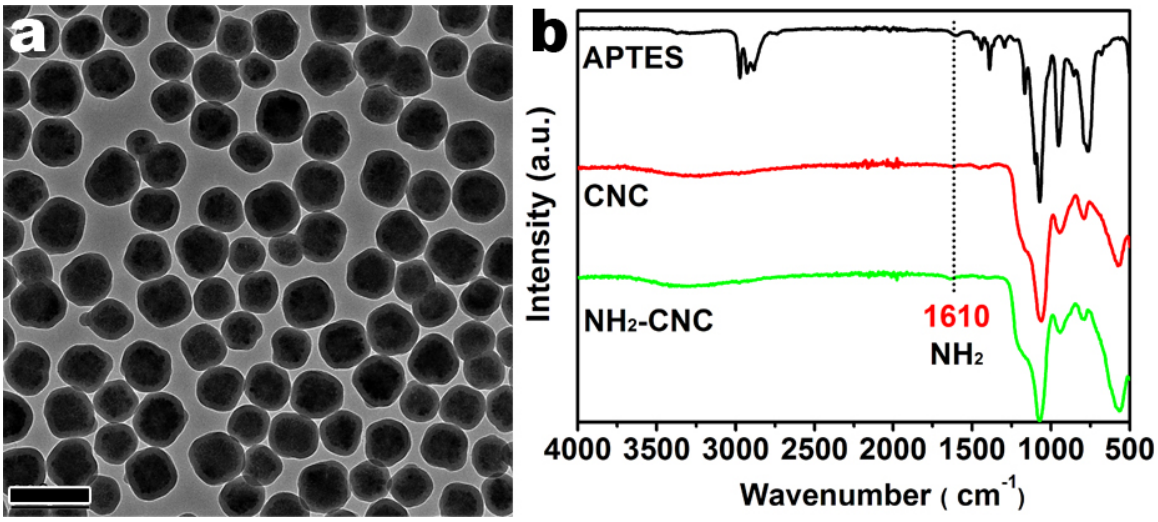

Figure 7.1. a) TEM image of NH_2-CNCs; b) FTIR spectra of APTES, CNCs before and after APTES coating. Scale bar: 200 nm

7.3 Results and Discussion

7.3.1 Synthesis of Bistable Particles

Amine-functionalized superparamagnetic nanoparticles (CNCs@NH_2-SiO_2) were prepared by firstly synthesis of the magnetic core using a high-temperature hydrolysis reaction that we reported previously and then coted with a silica layer through a modified Stöber method with the mixture of (3-aminopropyl)trithoxylsilane (APTES) and tetraethyl orthosilicate (TEOS) as precursor.[22] As shown in the transmission electron microscope (TEM) image in Figure 7.1a, the overall size of the CNCs@NH_2-SiO_2 is around 130 nm with shell thickness around 20 nm. To confirm the existence of amine functional group, we performed Fourier transform infrared spectroscopy (FTIR) on the magnetic CNCs before and after NH_2-SiO_2 coating with APTES as the reference. As illustrated in Figure 7.1b, APTES showed a characteristic peak around 1610 cm^{-1}, corresponding to the typical stretching of amine groups (black curve). As synthesized CNCs showed a characteristic peak at 560 cm^{-1} due to the Fe-O stretching mode of tetrahedral and octahedral sites of magnetite (red curve).[1] After coating with APTES, CNCs@NH_2-SiO_2 sample showed typical IR peaks of both amine groups and Fe-O stretching (green curve), indicating its successful surface binding to the CNCs surface.

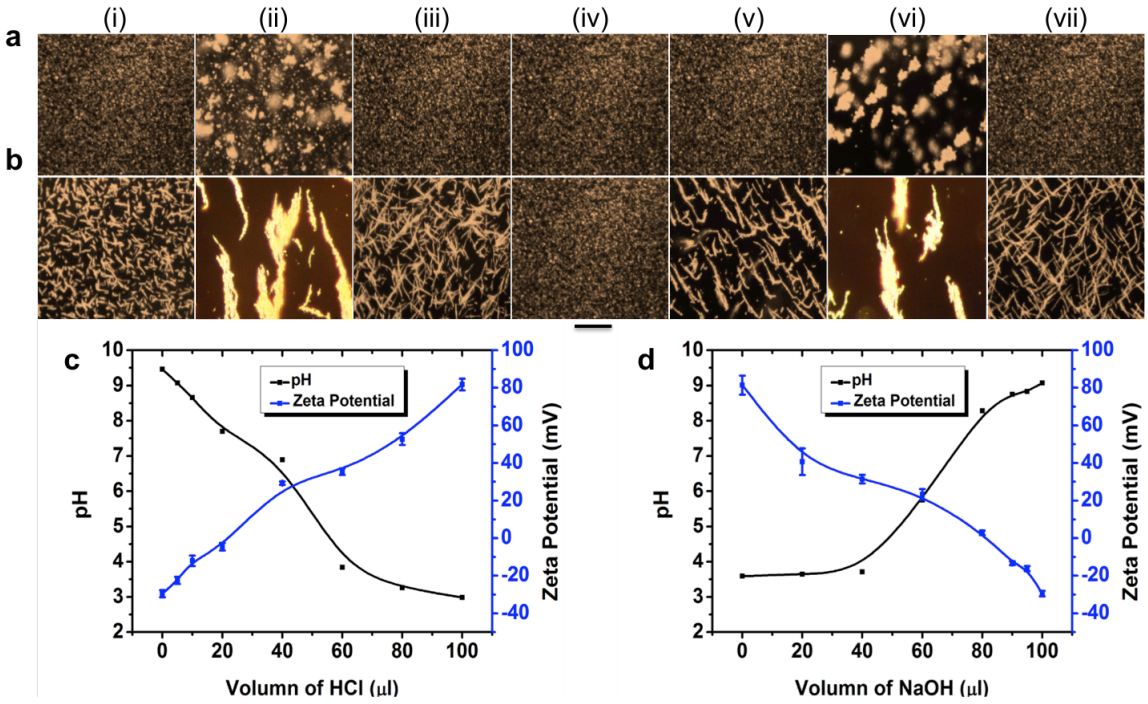

Figure 7.2. Optical microscope images of the CNCs@NH_2-SiO_2 dispersion a) before and b) after exposing to magnetic stimulus under different pH: (i), (ii), (iii) and (iv) are with addition of 0, 20, 40 and 100 μL of 0.1 M HCl; (v), (vi) and (vii) are with addition of 60, 80 and 100 μL of 0.1 M NaOH. c) and d) show the corresponding pH value and zeta potential. Scale bar corresponds to 60 μm.

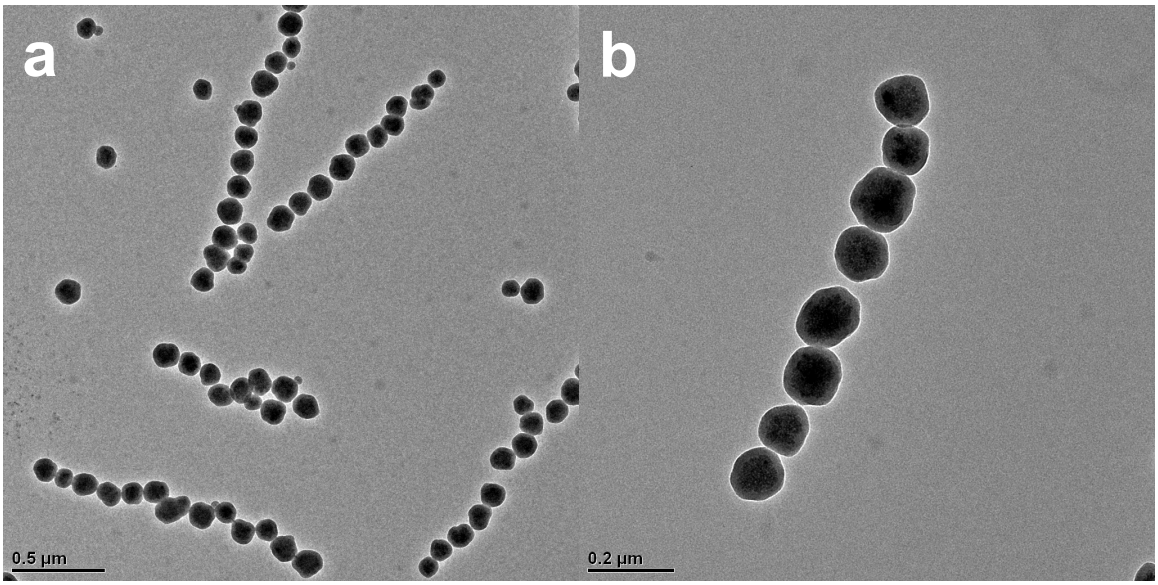

Figure 7.3. TEM images of the assembled chain structures.

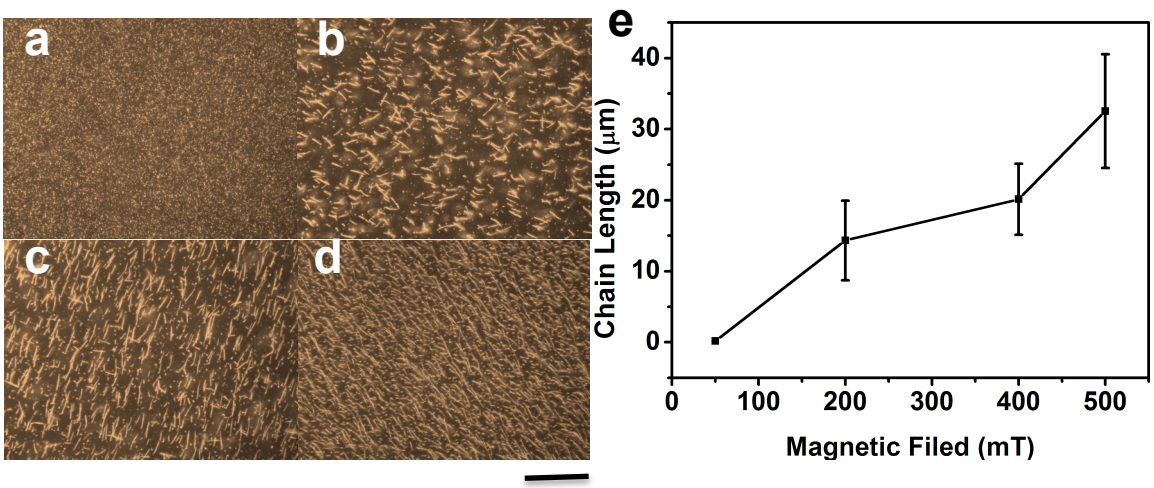

Figure 7.4. Optical microscope images after exposing to magnetic stimuli of different magnetic strength a) 50, b) 200, c) 400 and d) 500 mT and the corresponding chain length were shown in e. Scale bar: 60 μm.

7.3.2 pH Dependent Bistability

The bistability of colloidal assembly is high dependent on the pH value of the dispersion. Figure 7.2 showed optical microscope (OM) images of CNCs@NH_2-SiO_2 before and after magnetic stimulus under different pH values. The dispersion of assythesized nanoparticles possesses a pH value of about 9.5 owing to the protonation of amine groups and leaving more hydroxide ions in water. The zeta potential of the dispersion was then measured around – 30 mV, which enables good dispersion by providing energy barrier from aggregation. Upon treating with a magnetic pulse of 50 mT for 1 second, the dispersion of CNCs@NH_2-SiO_2 immediately switched to assembled mode. The assemblies were characterized by TEM to confirm the single chain structure (Figure 7.3). Different from our previously reported CNCs@SiO_2, which would disassemble right after the removal of the external magnetic field,[22, 55] the magnetic chain structures of CNCs@NH_2-SiO_2 were well maintained without the aid of magnetic field as illustrated in Figure 7.2bi. When 20 μL of 0.1 M HCl solution was added to the dispersion, we observed aggregation even before exposing to magnetic stimulus, owing to the screening of the surface charge with zeta potential near 0 mV. Once the addition amount of HCl reached to 40 μL, the good dispersion was recovered with zeta potential of 30 mV. Further decreasing the pH of the solution to 3 with addition of 100 μL HCl, the assembled state could not be achieved due to the high surface charge of 80 mV, which was hardly countered by the magnetic dipolar attraction in the range that silanol groups between particles could reach to each other. However, by increasing the strength of the

external magnetic field from 50 mT to 500 mT, the bistability was recovered as shown in Figure 7.4, which demonstrates the importance of interparticle distance. Alternatively, adjusting the pH of the dispersion can also restore the bistability by adding equivalent amount of NaOH to neutralize the HCl as shown in Figure 7.2v-vii. In summary, with the decreasing of the pH value of the dispersion, zeta potential would increase due to the protonation of amine groups. With higher surface charge, the interparticle distance would increase to establish new balance between the magnetic potential and electrostatic potential until silanol groups between nanoparticles cannot encounter with each other, as a result the system loses the bistability.

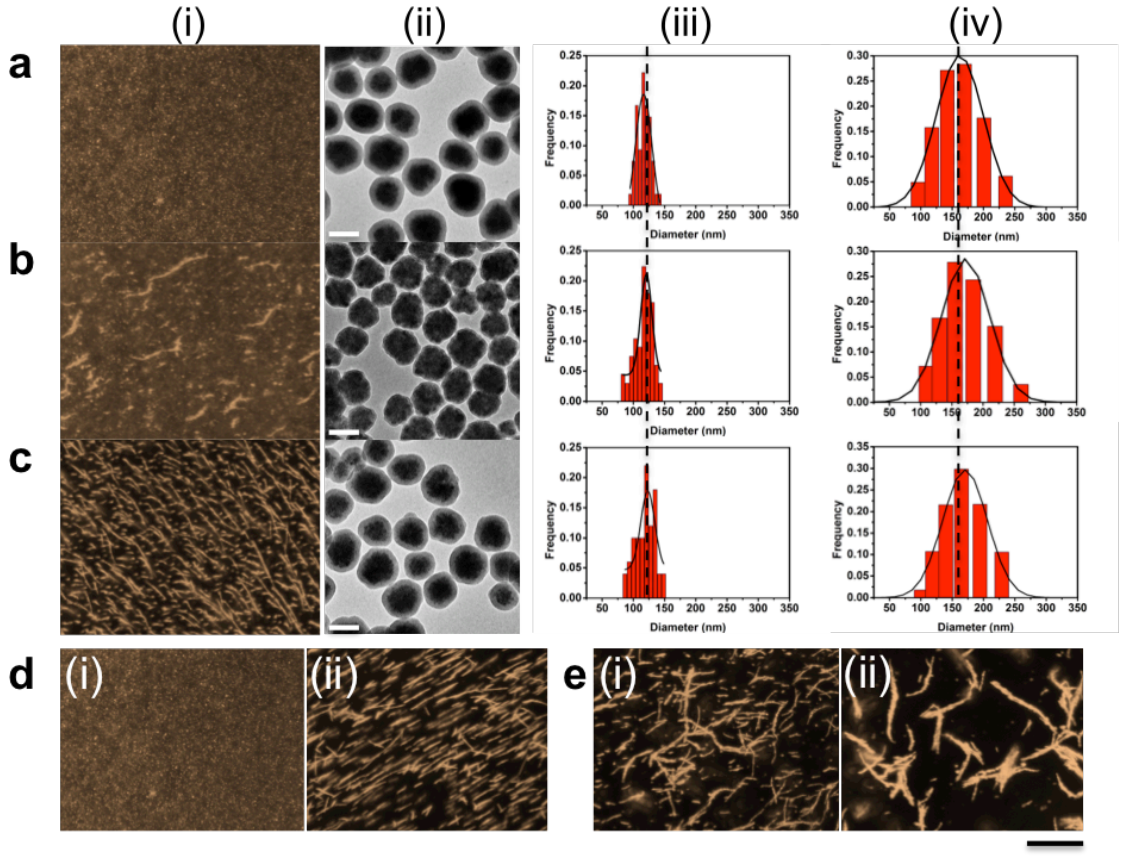

Figure 7.5. a) CNCs@SiO_2, b) CNCs@ C=C-SiO_2 and c) CNCs@NH_2-SiO_2. (i) Optical microscope images after magnetic stimuli of 500 mT for 1s, (ii) TEM images of the nanoparticles, histograms of size distribution measured with (iii) TEM images and (iv) DLS. d) Optical images of CNC@C=C-SiO_2 (i) before and (ii) after magnetic stimulus with addition of 1 µL 1.5 M NH_3•H_2O. e) Optical images after magnetic stimulus of samples with (i) 20 and (ii) 30% volume fraction of APTES to TEOS coating. Scale bars of optical microscope and TEM are 60 µm and 200 nm respectively.

7.3.3 Mechanism of Bistability

Subsequently, we investigated the formation mechanism of bistability. Our initial studies focused on the formation of siloxane bonds. Distance and catalyst are two key points for the formation of siloxane bonds. The interparticle distance is determined by the sum of electrostatic and magnetic potential. However, with fixed interparticle distance, the length of the silanol ligands on the surface governs the collision of silanol groups. The bistability of CNCs coated with TEOS, [3-(methacryloyloxy)propyl]trimethoxysilane (MPS) (CNC@C=C-SiO_2) and APTES were compared in Figure 7.5a-c. With the similar surface charge and the same magnetic stimulus, no connection between particles were found in CNCs@SiO_2 dispersion, relatively low yield of bonding was formed in CNCs@C=C-SiO_2, whereas only CNCs@NH_2-SiO_2 showed the strongest interaction with almost complete conversion to assemblies, which could be attributed to the differences between polymer chain length. To investigate the polymer chain length in each sample, particle sizes were examined by TEM and dynamic light scattering (DLS). By comparing the size difference between the dry state (TEM) and hydrated state (DLS), the polymer chain length on the surface of each sample can be roughly compared. With four silanol groups after hydrolysis, TEOS tends to form more condensed network with shorter polymer chains on the surface with a size difference of 20 nm between the TEM and DLS measurement. However, MPS and APTES can only provide three silanol positions for crosslinking, as a result, less condensed network with longer polymer chains stretched out was produced with variance of about 40 nm. Thus, longer polymer chains

enable contact of silanol groups between the nanoparticles. With longer polymer chains, CNCs@C=C-SiO_2, however, still yielded much lower bondings between particles compared to the CNCs@NH_2-SiO_2 due to the lack of catalyst for the formation of siloxane bonds. To reveal the importance of catalyst, 1 μL of 1.5 M ammonia hydroxide was added to 1 mL of CNCs@C=C-SiO_2 dispersion to promote the bonding. As shown in Figure 7.5d, with the addition of ammonia hydroxide, the nanoparticles were well dispersed. After magnetic stimulating, the assembly was greatly enhanced under the catalyzing of ammonia hydroxide. The effect of ionic strength change by adding ammonia hydroxide was then excluded by comparing the dispersions with addition of the same amount of sodium chloride and 2000 times of ammonia hydroxide. As shown in Figure 7.6, 1 μL of 1.5 M NaCl induced aggregation by screening the surface charge, with 2000 times of concentrated ammonia hydroxide however, the nanoparticles were still well dispersed. Thus, we can conclude that the enhanced bonding is caused by catalytic contribution rather than ionic-strength. It is worth noting that the addition of ammonia hydroxide still could not induce bonding between CNCs@SiO_2 nanoparticles (Figure 7.7), which further confirmed the lack of interaction due to shorter silanol ligands. The synergetic effect of longer uncrosslinked polymer chain and self-catalyst of amine group was then further confirmed by coating CNCs with increasing amount of APTES. When the volume ratio of APTES/TEOS was increased from 10 to 20 and 30%, although the surface charge kept increasing (Figure 7.8), longer chains and even bundles were formed, indicating more effective bondings between particles.

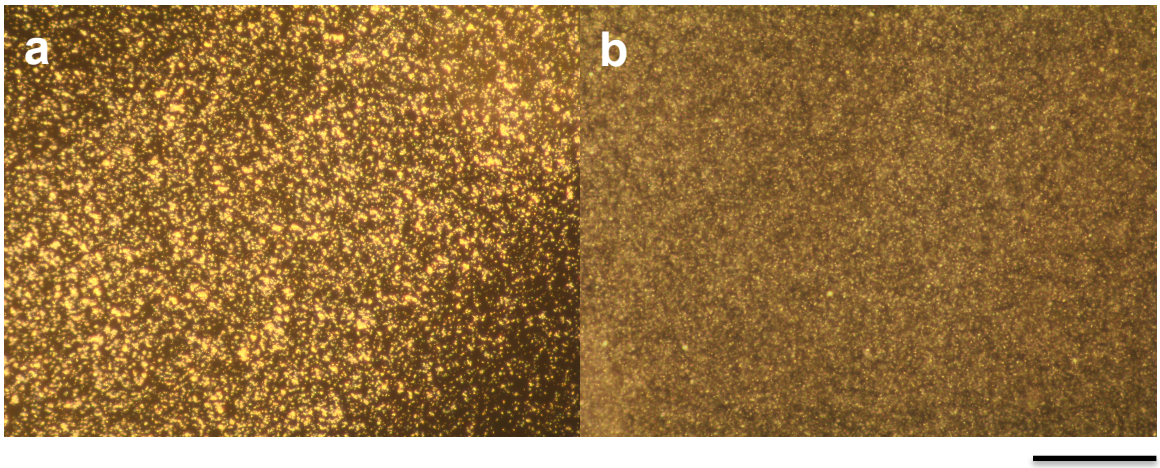

Figure 7.6. Optical microscope images of CNCs@C=C-SiO_2 with addition of a) 1 µL of 1.5 M NaCl and b) 200 µL of 15 M NH_3•H_2O. Scale bar: 60 µm.

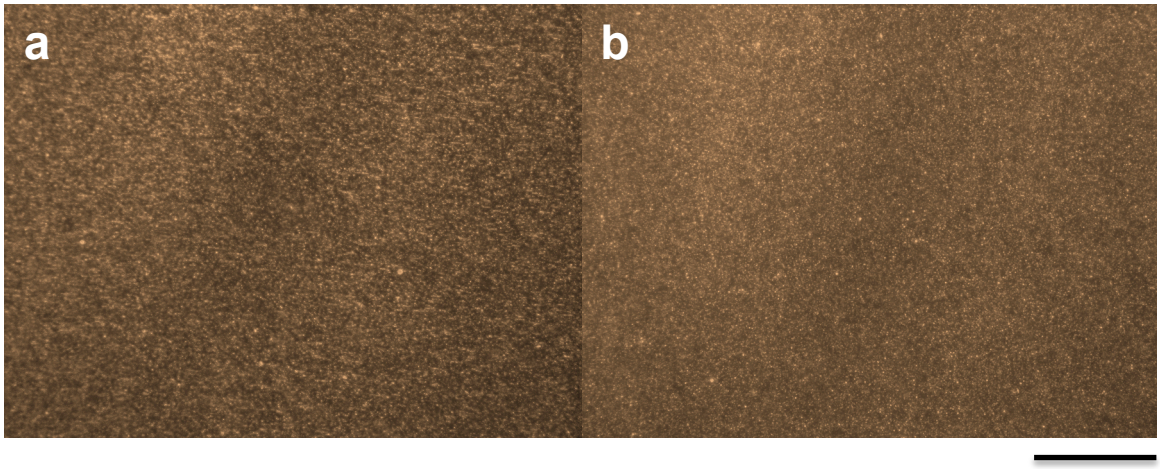

Figure 7.7. Optical images of CNC@SiO_2 with addition of 1 µL 1.5M ammonia hydroxide a) before and b) after magnetic stimulus.

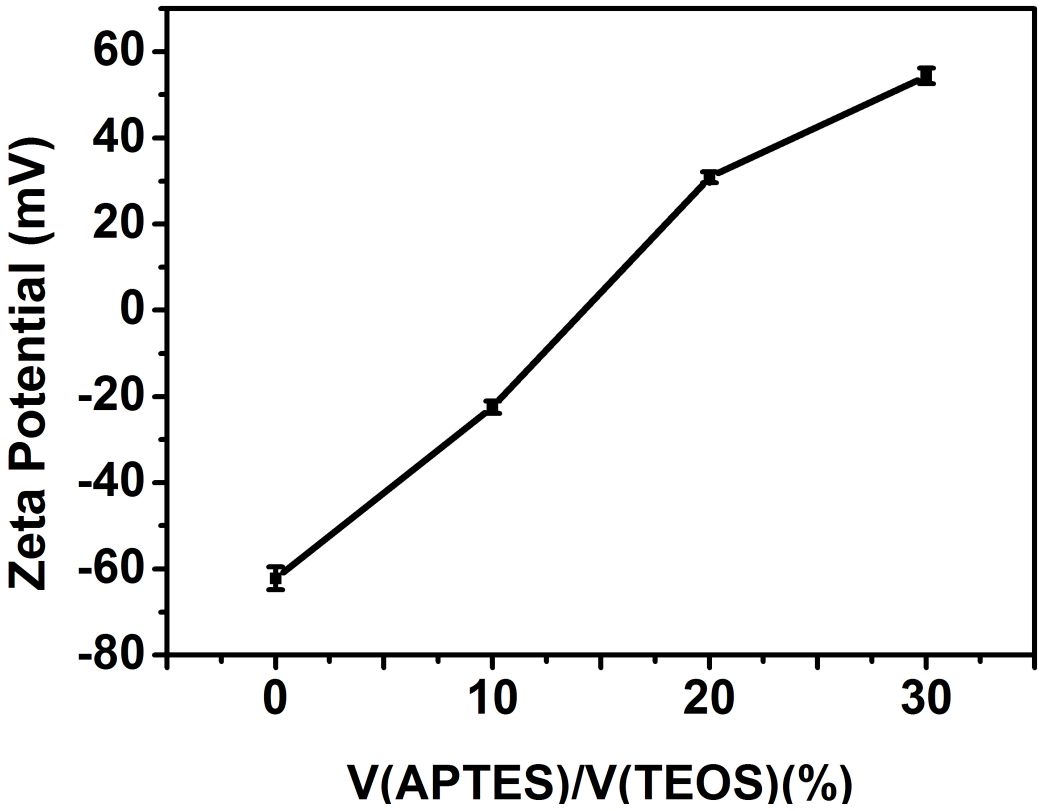

Figure 7.8. Zeta potentials for CNCs@NH_2-SiO_2 with different amount of APTES coating.

7.3.4 Switching Between Bistable States

We also studied the breaking of siloxane bonds with external stimuli. Between the two energy minima, an energy barrier needs to be overcome to switch the system from assembled state to dispersed state. Chemically, 100 μL of 0.1 M HCl was added to break the established equilibrium. As shown in Figure 7.9, the chain length of the assemblies gradually decreased to the size of isolated particles within 15 min owing to the increasing of surface charge upon the addition of HCl, which teared the particles apart through repulsive electrostatic interaction. Mechanically, sonication, infrared radiation (IR) and rotational magnetic field were applied to agitate the assemblies. As illustrated in Figure 7.10, sonication and IR could disassemble the assemblies to complete dispersion while magnetic stirring at 1200 rpm could break the longer assemblies into shorter fragments. We also tried managing the interparticle distance by screening the electrostatic interaction with salt, during which severe aggregation was observed with the addition of NaCl (Figure 7.11). However, through diluting or sonication, the particles could not restore to dispersion state since short-range van der Waals force was dominant, which further demonstrated the necessity to avoid close contact when designing bistable system.

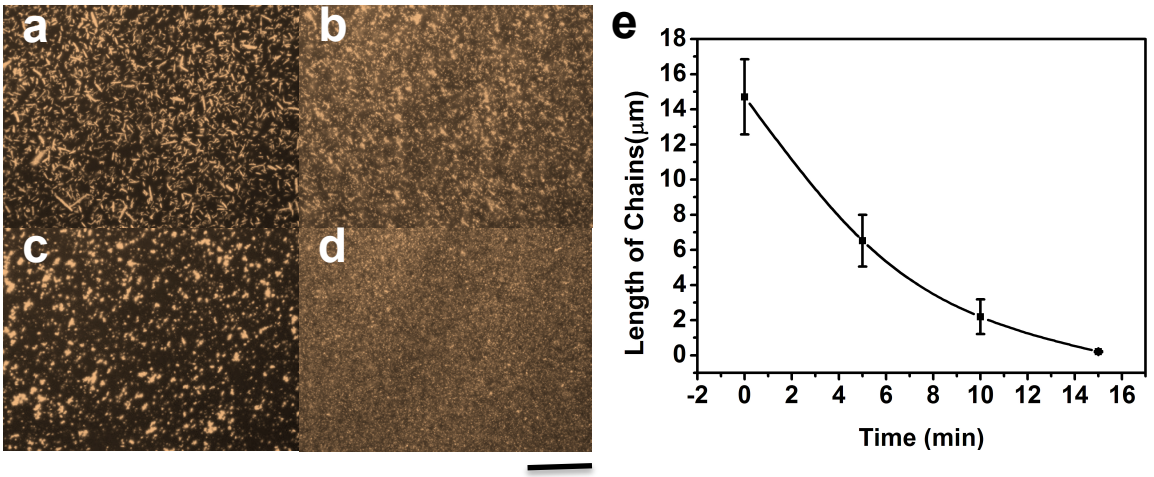

Figure 7.9. Optical microscope images of CNCs@NH_2-SiO_2 after addition of 100 μL 0.1 M HCl at different point of time a) 0, b) 5, c) 10 and d) 15 min and e) corresponding measured chain lengths. Scale bar: 60 μm.

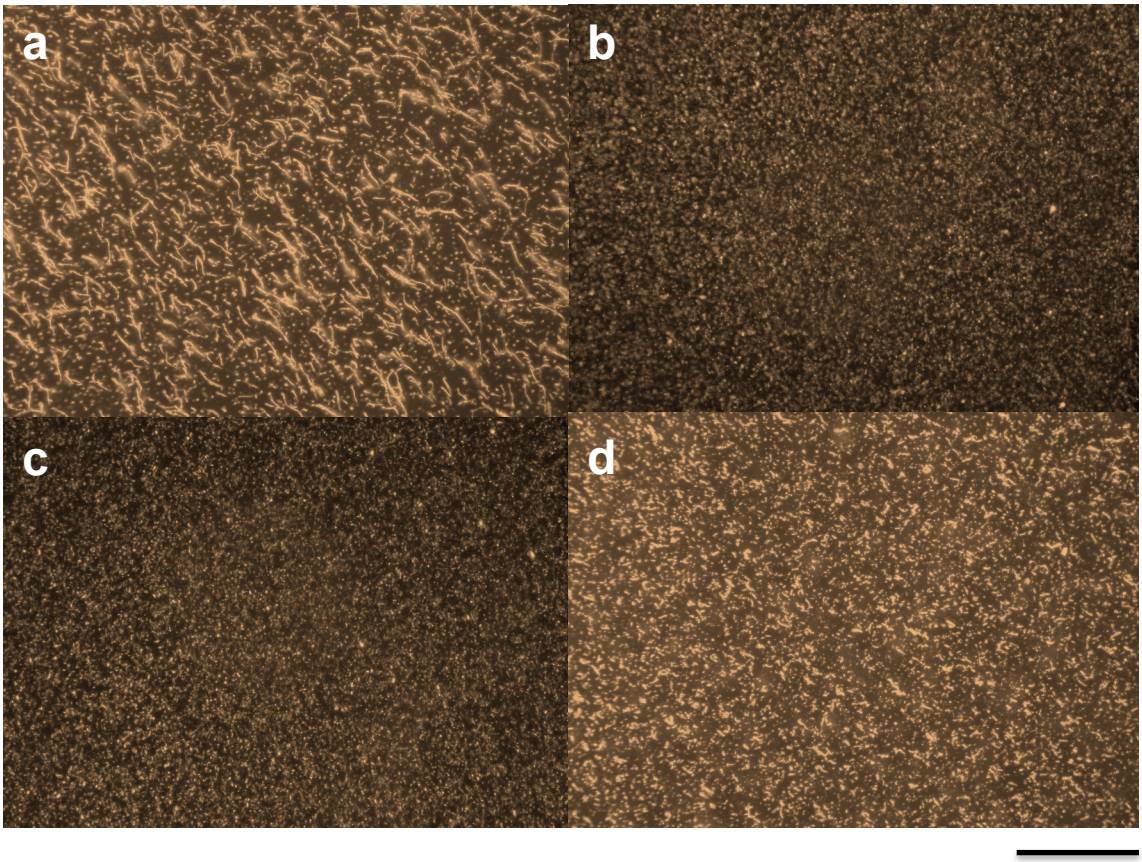

Figure 7.10. Optical microscope images of the assemblies a) before disturbance and after b) sonication, c) IR irradiation and d) rotational magnetic field with 1200 rpm. Scale bar: 60 μm.

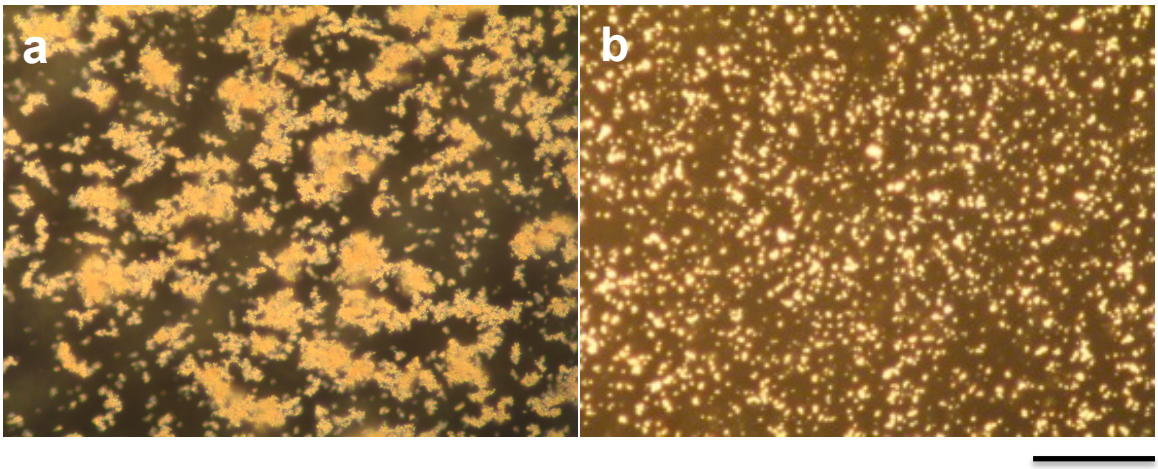

Figure 7.11. Optical microscope images of CNCs@SiO_2 a) with 1.5 M of NaCl and b) after 10 times dilution with sonication. Scale bar: 60 μm.

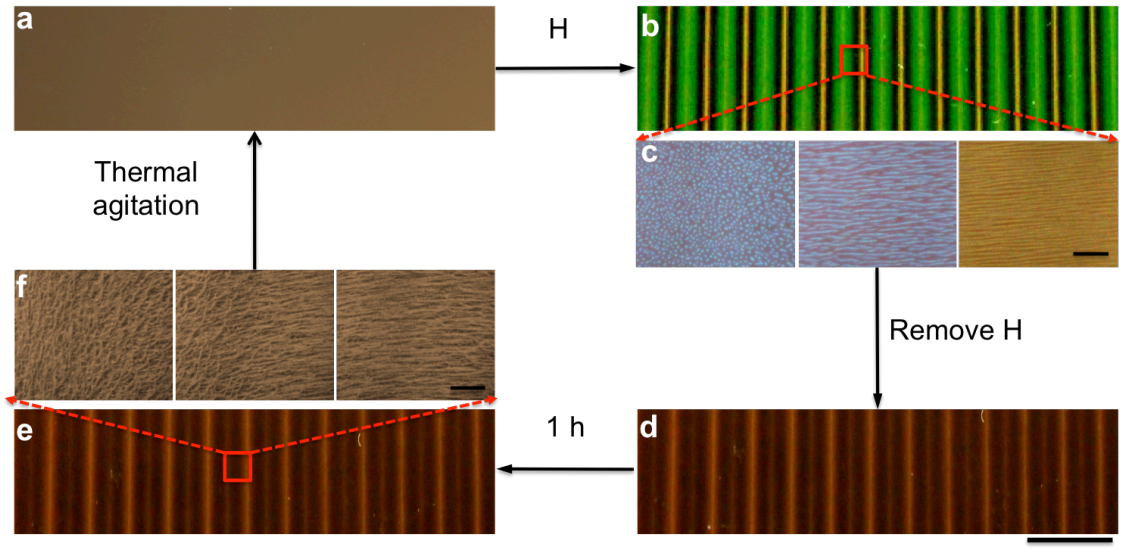

Figure 7.12. Digital photo showing the photonic response of CNCs@NH_2-SiO_2 encapsulated in a flat glass tube a) original, b) under a non-ideal linear Halbach array, d) after removal of magnet and e) after sitting for 1 h. c) and f) corresponding selective area optical microscope images of b and d. The scale bar of digital image corresponds to 2 cm and 60 μm for OM images.

7.3.5 Application of Bistability

To further illustrate the applications of the bitable system, a simple display unit was fabricated by dispersing CNCs@NH_2-SiO_2 nanoparticles in water and encapsulating in a flat glass capillary tube with a thickness of 100 μm. A refrigerator magnet with Halbach-array-patterned field was used to test the bistability of the display tablet. As illustrated in Figure 7.12, upon application of the magnetic field, alternative green or brown stripes formed owing to the various orientations of the photonic chains in accordance with the local magnetic field. Although the field of the refrigerator magnet can be treated as alternating vertical and horizontal, the orientation and gradient of the local magnetic field are more complicated.[60, 246] Selected area OM images in Figure 7.12c showed that the orientation of the chains was vertical, titled and horizontal in green, black and brown regions respectively. After the removal of the magnet, the alternating stripes maintained and remained visually unchanged for 1 hour (Figure 7.12d-e), indicating a good stability in assembled mode. However, the structural color was lost right after the removing of the magnetic field, owing to the rotational movements of the assemblies. As illustrated in the select area OM images in Figure 7.12f, the assembled chains in the initial green region were randomly leaning on each other, breaking the established periodicity, thus only showing lighter contrast. With no much change in the tilted and horizontal regions, we can still observe the black and brown stripes. With the aid of thermal agitation including sonication, IR or rotational magnetic field, the information can be completely erased from the display tablet and fully recovered to the starting point, which demonstrated the good

bistability of the system. Since the bistability is realized by switching between energy valleys, there is no decay during the recycling. Without bistablity as shown in Figure 7.13, the display showed patterns with magnetic field on and restored to dispersion right after the removal of the magnet. Not limited to aqueous solution, the bistability of CNCs@NH_2-SiO_2 were successfully demonstrated in other solvent such as ethanol and diethylene glycol (Figure 7.14), which provides potential applications of the bistability in other systems.

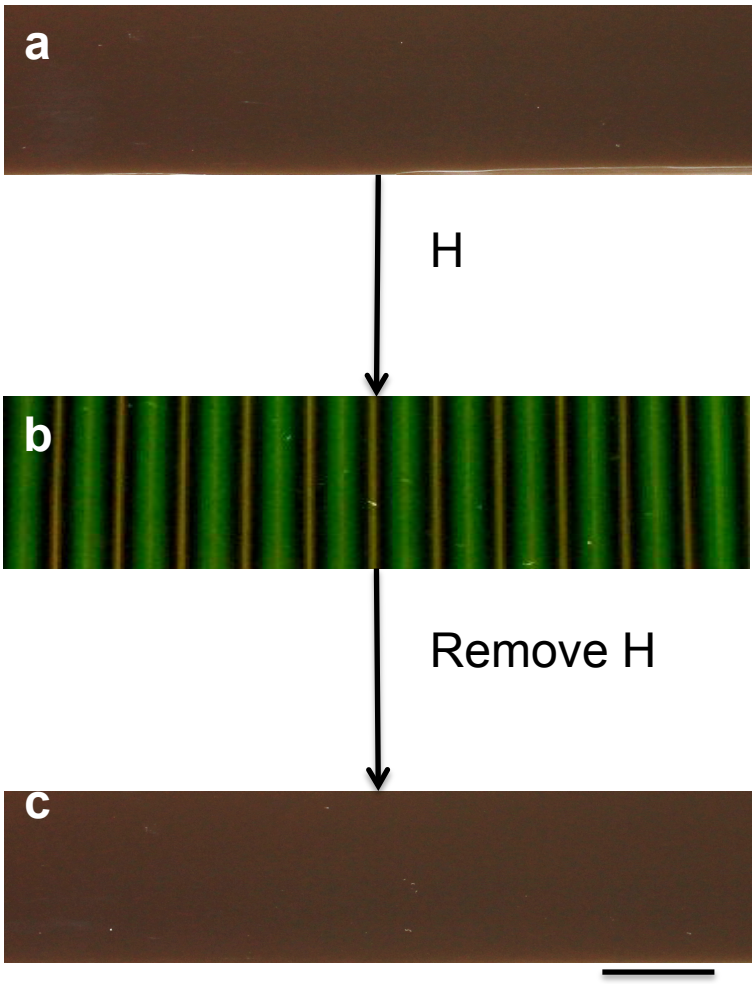

Figure 7.13. Digital photo images of CNCs@SiO_2 without bistability: a) original, b) under a non-ideal linear Halbach array and c) after removal of magnet. Scale bar: 5 mm.

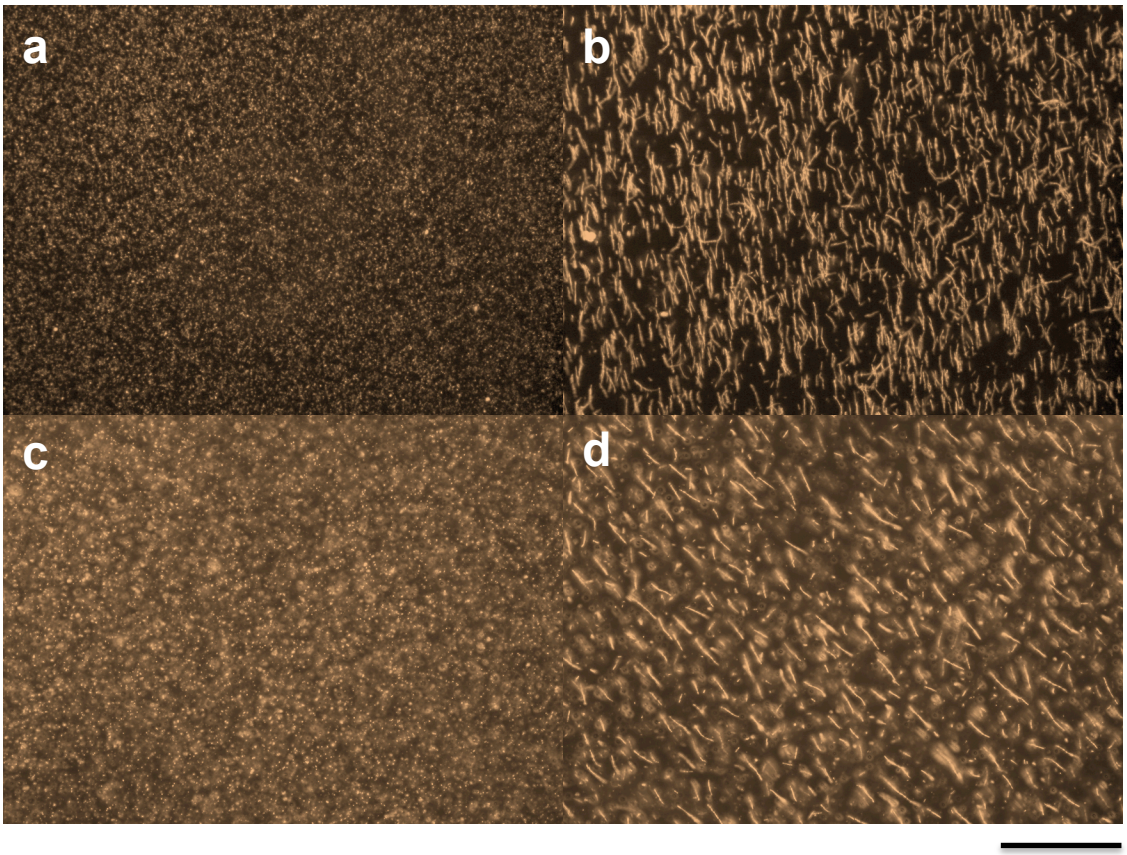

Figure 7.14. Optical microscope images of demonstration bistability a) before and b) after magnetic stimulus in ethanol; c) before and d) after magnetic stimulus in DEG. Scale bar: 60 μm.

7.4 Conclusion

In conclusion, we have developed a bistable colloidal system based on the condensation of silanol groups between particles to form siloxane bonds and hydrolysis of siloxane bonds back to silanol groups. By utilizing the amine-functionalized superparamagnetic nanoparticles as the building block, the interaction between particles is readily controlled by tuning the external magnetic field. When the particles are pushed to the range that silanol groups start interacting with each other, catalyzed by amine, nanoparticles tend to assemble into chain structures and remain stable unless the energy barrier between the two energy minima is overcome. Upon disturbing with sonication, IR or rotational magnetic field, nanochains disassemble to isolated particles driven by the repulsive elelctrostatic interaction. Highly dependent on pH during the condensation and hydrolysis reaction, the bistability is tuned by pH. The switching between the two stable states is very effective with no decay, making it a good candidate for information storing and erasing. This system renews our understanding of the stability of colloidal systems, which holds potential applications in information storage, display and electronics.

7.5 References

1. Whitesides, G. M.; Grzybowski, B., Self-Assembly at All Scales. *Science* **2002**, *295* (5564), 2418-2421.

2. Xia, Y.; Gates, B.; Yin, Y.; Lu, Y., Monodispersed Colloidal Spheres: Old Materials with New Applications. *Adv. Mater.* **2000**, *12* (10), 693-713.

3. Yin, Y.; Xia, Y., Self-Assembly of Spherical Colloids into Helical Chains with Well-Controlled Handedness. *J. Am. Chem. Soc.* **2003**, *125* (8), 2048-2049.

4. Wang, M.; He, L.; Xu, W.; Wang, X.; Yin, Y., Magnetic Assembly and Field-Tuning of Ellipsoidal-Nanoparticle-Based Colloidal Photonic Crystals. *Angew. Chem., Int. Ed.* **2015**, *54* (24), 7077-7081.

5. Wang, J.; Hu, Y.; Deng, R.; Xu, W.; Liu, S.; Liang, R.; Nie, Z.; Zhu, J., Construction of multifunctional photonic crystal microcapsules with tunable shell structures by combining microfluidic and controlled photopolymerization. *Lab on a Chip* **2012**, *12* (16), 2795-2798.

6. Youssef, M.; Hueckel, T.; Yi, G.-R.; Sacanna, S., Shape-shifting colloids via stimulated dewetting. *Nat. Commun.* **2016**, *7*, 12216.

7. Zheng, X.; Liu, M.; He, M.; Pine, D. J.; Weck, M., Shape-Shifting Patchy Particles. *Angew. Chem., Int. Ed.* **2017**, *56* (20), 5507-5511.

8. Grzelczak, M.; Vermant, J.; Furst, E. M.; Liz-Marzán, L. M., Directed Self-Assembly of Nanoparticles. *ACS Nano* **2010**, *4* (7), 3591-3605.

9. Steinbach, G.; Nissen, D.; Albrecht, M.; Novak, E. V.; Sanchez, P. A.; Kantorovich, S. S.; Gemming, S.; Erbe, A., Bistable self-assembly in homogeneous colloidal systems for flexible modular architectures. *Soft Matter* **2016**, *12* (10), 2737-2743.

10. Hu, Y.; He, L.; Yin, Y., Magnetically Responsive Photonic Nanochains. *Angew. Chem., Int. Ed.* **2011**, *50* (16), 3747-3750.

11. Zhang, Q.; Janner, M.; He, L.; Wang, M.; Hu, Y.; Lu, Y.; Yin, Y., Photonic Labyrinths: Two-Dimensional Dynamic Magnetic Assembly and in Situ Solidification. *Nano Lett.* **2013**, *13* (4), 1770-1775.

12. Mirkin, C. A.; Letsinger, R. L.; Mucic, R. C.; Storhoff, J. J., A DNA-based method for rationally assembling nanoparticles into macroscopic materials. *Nature* **1996**, *382* (6592), 607-609.

13. Derjaguin, B., On the repulsive forces between charged colloid particles and on the theory of slow coagulation and stability of lyophobe sols. *J. Chem. Soc. Faraday Trans.* **1940,** *35* (0), 203-215.

14. Carman, P. C., Constitution of colloidal silica. *J. Chem. Soc. Faraday Trans.* **1940,** *36* (0), 964-973.

15. Verwey, E. J. W., Theory of the Stability of Lyophobic Colloids. *J. Phys. Colloid Chem.* **1947,** *51* (3), 631-636.

16. Depasse, J.; Watillon, A., The stability of amorphous colloidal silica. *J. Colloid Interface Sci.* **1970,** *33* (3), 430-438.

17. Zhang, H.; Wang, D., Controlling the Growth of Charged-Nanoparticle Chains through Interparticle Electrostatic Repulsion. *Angew. Chem.* **2008,** *120* (21), 4048-4051.

18. Wang, Y.; Chen, G.; Yang, M.; Silber, G.; Xing, S.; Tan, L. H.; Wang, F.; Feng, Y.; Liu, X.; Li, S.; Chen, H., A systems approach towards the stoichiometry-controlled hetero-assembly of nanoparticles. *Nat. Commun.* **2010,** *1*, 87.

19. Han, X.; Liu, Y.; Yin, Y., Colorimetric Stress Memory Sensor Based on Disassembly of Gold Nanoparticle Chains. *Nano Lett.* **2014,** *14* (5), 2466-2470.

20. He, L.; Hu, Y.; Wang, M.; Yin, Y., Determination of Solvation Layer Thickness by a Magnetophotonic Approach. *ACS Nano* **2012,** *6* (5), 4196-4202.

21. Liu, Y.; Han, X.; He, L.; Yin, Y., Thermoresponsive Assembly of Charged Gold Nanoparticles and Their Reversible Tuning of Plasmon Coupling. *Angew. Chem., Int. Ed.* **2012,** *51* (26), 6373-6377.

22. Ge, J.; Hu, Y.; Yin, Y., Highly Tunable Superparamagnetic Colloidal Photonic Crystals. *Angew. Chem., Int. Ed.* **2007,** *46* (39), 7428-7431.

23. Xu, W.; Wang, M.; Li, Z.; Wang, X.; Wang, Y.; Xing, M.; Yin, Y., Chemical Transformation of Colloidal Nanostructures with Morphological Preservation by Surface-Protection with Capping Ligands. *Nano Lett.* **2017,** *17* (4), 2713-2718.

24. Ge, J.; Yin, Y., Magnetically Tunable Colloidal Photonic Structures in Alkanol Solutions. *Adv. Mater.* **2008,** *20* (18), 3485-3491.

25. He, L.; Hu, Y.; Han, X.; Lu, Y.; Lu, Z.; Yin, Y., Assembly and Photonic Properties of Superparamagnetic Colloids in Complex Magnetic Fields. *Langmuir* **2011,** *27* (22), 13444-13450.

26. Wang, M.; He, L.; Hu, Y.; Yin, Y., Magnetically rewritable photonic ink based on superparamagnetic nanochains. *J. Mater. Chem. C* **2013,** *1* (38), 6151-6156.